Magnetic Resonance Imaging of Diffusion in the Presence of Physiological Motion

by

Hákon Gudbjartsson

Submitted to the Department of Electrical Engineering and Computer Science
in partial fulfillment of the requirements for the degree of

Doctor of Philosophy

at the

MASSACHUSETTS INSTITUTE OF TECHNOLOGY

February 1996

© Massachusetts Institute of Technology 1996. All rights reserved.

Author .....
Department of Electrical Engineering and Computer Science
January 31, 1996

Certified by .....
Samuel Patz
Assistant Professor, Harvard Medical School
Thesis Supervisor

Certified by .....
Martha Gray
Associate Professor, M.I.T.
On Campus Thesis Supervisor

Accepted by .....
Frederic R. Morgenthaler
Chairman, Departmental Committee on Graduate Students

MASSACHUSETTS INSTITUTE OF TECHNOLOGY
APR 11 1996
LIBRARIES ARCHIVES

Magnetic Resonance Imaging of Diffusion in the Presence of Physiological Motion

by

Hákon Gudbjartsson

Submitted to the Department of Electrical Engineering and Computer Science
on January 31, 1996, in partial fulfillment of the
requirements for the degree of
Doctor of Philosophy

Abstract

The influence of physiological motion on magnetic resonance diffusion imaging techniques is studied. First, the applicability of the steady-state free precession (SSFP) imaging sequence for imaging of diffusion is studied with a novel, fast, and highly accurate computer simulation based on conditional random walk. By using measurements of *in vivo* brain motion, it is shown that the SSFP sequence cannot provide accurate measurements of *in vivo* diffusion attenuation. Next, the use of navigator echo for correction of motion artifacts in the pulsed-gradient spin-echo sequence is studied. The navigator technique is also extended for the fast spin-echo (FSE/RARE) sequence. However, it is shown that the navigator technique cannot provide accurate measurements of diffusion in three orthogonal directions and needs cardiac gating to minimize the influence of spatially varying motion. Finally, the major result of this work is a novel line scan diffusion imaging technique (LSDI). The LSDI technique is inherently insensitive to motion artifacts because it does not use phase encoding. It is shown, that high quality diffusion maps can be obtained rapidly with the LSDI technique on both 0.5T and 1.5T systems without the use of head restraints or cardiac gating. Furthermore, it is shown that these diffusion maps compare very well with diffusion maps obtained using diffusion weighted echo-planar imaging (EPI). In contrast to the EPI technique, LSDI does not require modified gradient hardware and can easily be implemented on conventional scanners. The main disadvantage of the LSDI technique is that multi-slice imaging is considerably slower than with EPI. However, the feasibility of using the LSDI technique for clinical evaluation of acute ischemic stroke in less than ten minutes is demonstrated. Thus, LSDI should increase the general availability of robust clinical diffusion imaging dramatically.

Thesis Supervisor: Samuel Patz
Title: Assistant Professor, Harvard Medical School

On Campus Thesis Supervisor: Martha Gray
Title: Associate Professor, M.I.T.

Til Magneu

Acknowledgments

I am most grateful to my advisor Samuel Patz for his constant support, motivation, and kindness throughout the whole time we worked on this project together. I am also deeply indebted to Stephan E. Maier for his friendship and his invaluable contribution to the line scan technique and to Ferenc A. Jolesz for allowing me to freely operate the scanners at the Brigham and Women's Hospital as well as for financial support in the summer of 1995.

The members of my thesis committee - Martha Gray, William C. Karl, Robert Weisskoff, and Jacob White - deserve many thanks for their feedback and discussion.

It has been my fortune to be associated with the LMRC MRI research group and I would like to thank all the colleagues there for their friendship during my time there. In particular, I would like to thank Sharon Peled and Pisti Mórocz for pleasant conversations and useful collaboration, Larry Panych for the many walks we took in k-space, and Charles Guttmann and Bob Mulkern for their willfulness to help.

This work could never have been completed or so much as started without the enormous support and guidance I have always got from my parents. Let's just hope that upon completion of this work, that I have become half as much of an "engineer" as my father and that I am finally capable of changing the plug in the kitchen!

Finally, I would like to thank my little Bjartur and my dearest wife for being an everlasting inspiration and for always being there for me when I needed.

Brookline, January 31st
Hákon Gudbjartsson

Preface

This thesis summarizes most of my doctoral work at the LMRC lab at the Brigham and Women's Hospital from the beginning of March 1993 and the chapters reflect in some way the chronological order of this work. However, all the source code I wrote for computer simulations and to control the Signa has been left out.

The analysis of the SSFP sequence may seem very long and detailed. As a matter of fact, the original name of this thesis was "Steady State Free Precession Magnetic Resonance Imaging of Flow and Diffusion". It is my belief, however, that understanding of the issues that come up in the analysis of the SSFP sequence provides insight into the whole field of MRI.

Contents

Chapter 1

Overview

1.1 Motivation

STROKE is one of the most devastating and costly health problems in the western world. After heart disease and cancer, stroke is the third most common cause of death and each year over 400,000 Americans suffer from stroke [122]. Up to 80% of acute infarctions are thromboembolic in origin and the remaining are caused by intracerebral hemorrhage. Mortality at three months after onset of ischemic infarct and hemorrhage stroke is approximately 20% and 60%, respectively, taking about 150,000 American lives each year.

Currently, limited acute therapeutic interventions are available and there is no direct treatment to reduce the extent of the neurologic injury. In the last 15 years, the rationale for early intervention in acute stroke has been changed by the concept of *ischemic penumbra* [41]. This term refers to the zone of brain tissue in which ischemic neuronal paralysis has occurred but where there is sufficient cerebral blood flow to maintain cell membrane integrity. Until recently, most available imaging modalities such as CT and MRI have not been very sensitive in the early phase of cerebral ischemia. This lack of ability to identify the penumbra may be one of the reasons why few therapeutic strategies have been developed for acute stroke.

Recently, a five year clinical study, conducted by the National Institute of Neurological Disorders and Stroke, has shown that a treatment with the clot-dissolving drug t-PA is an effective emergency treatment for acute ischemic stroke despite some risk from bleeding [122]. The main difference of this trial, and other studies of intravenous t-PA for stroke where no conclusive evidence of efficacy was found, is the extent to which the time to treatment was minimized. For each patient, the treatment, which included CT scanning and other studies, was accomplished in 90-180 minutes from stroke onset. As compared with patients given placebo, patients treated with t-PA

were at least 30% more likely to have minimal or no disability at three months from onset. In other words, there is a narrow window of opportunity, several hours in duration, depending on the severity of the ischemia, beyond which neither reperfusion nor brain protective agents will have any effect. Therefore, the aim of the radiologist should be to identify the ischemic penumbra or the brain area which is still accessible for acute intervention as well as screen for intracerebral bleeding. Early detection of the location and the size of tissue involved in acute ischemia should make any treatment aimed at reducing morbidity and mortality more effective. Furthermore, it should enable the monitoring of therapeutic interventions.

Unfortunately, changes on CT and conventional MRI images only reflect already infarcted brain tissue and not the potentially salvageable area of the ischemic penumbra. Earliest changes on T_1 and the more sensitive T_2 weighted MRI scan cannot be reliably visualized within the first 8 hours after the onset of ischemia [80, 135]. Radiological cerebral blood flow techniques like positron emission tomography (PET), Xenon-CT and SPECT [138] can show decreased cerebral perfusion earlier. These imaging modalities are less readily available, too expensive, cause some discomfort to the patient, or lack the high contrast resolution of MRI. Also, these methods require radiation exposure and are therefore of limited value for repetitive clinical research.

Fast MRI techniques combined with contrast enhancers have in recent years been used to monitor perfusion [110]. By the application of tracer kinetic theory, a series of these images allow the calculation of haemodynamic parameters such as regional cerebral blood volume (rCBV) and regional cerebral blood flow (rCBF) [41, 140]. Therefore, perfusion deficits are visible immediately after vessel occlusion. Because of the time resolution that is needed for these sequential perfusion images, until now, most of the few reports in patients have described a single-slice technique. This is because of the technical limitations of most available scanners. This makes it impossible to visualize all the ischemic tissue. Also, equipment is required for reliable bolus injection [41]. New ultrafast echo-planar (EPI) MR techniques make multi-slice measurements practical for acute stroke patients [136], who often are not able to stay still for a long time. However, EPI hardware is expensive and still not widely available.

Moseley *et al.* showed that diffusion weighted MRI can detect ischemic stroke within minutes after vascular occlusion [90]. Since then, water self-diffusion has become a well established contrast mechanism on MR images and has shown to be of great value in early detection and characterization of cerebral ischemia in animal studies of acute stroke [22, 23, 121, 133]. Until now, limited number of diffusion stroke studies have been done of in humans [20, 135]. Diffusion imaging of humans, especially stroke patients, has been hampered by severe motion artifacts which make evaluation of the data unreliable. With the advent of diffusion weighted EPI, motion artifacts have become much less of a problem [137], however, as mentioned before, most MR

scanners do not have EPI capabilities.

Not only is it possible to identify ischemia with diffusion weighted MRI, but also, it has been shown, that there is a strong correlation between the apparent diffusion coefficient (ADC) and cerebral blood flow in animal models of stroke [39,69,79]. In a recent study by Warach *et al.* [136], it was found that diffusion weighted EPI images were highly accurate in identifying acute ischemic stroke and in distinguishing patients who would improve from those who would not.

Thus, it is of great interest and value to have a robust, fast, and accurate diffusion imaging technique for conventional MR scanners. With such a technique, the number of clinical sites that would have a tool for early identification and evaluation of acute stroke would be greatly increased.

1.2 MRI Perfusion Techniques

The term *perfusion* has attracted some controversy in the MR community but its biological meaning refers to the delivery of oxygen and nutrients to the cells. It is therefore related to the amount of fresh oxygenated arterial blood delivered to the tissue capillary network. Conventional perfusion measurements techniques based on the uptake of radionuclide tracers have led to the identification of perfusion with *blood flow* in the tissue, measured in milliliters per minute per 100g of tissue.

A technique of reference for measurement of perfusion uses radiolabeled microspheres, such as albumin microspheres labeled with ^{68}Ga. The microsphere deposition pattern is then determined after injection by a nuclear imaging technique or sacrifice followed by autoradiography counting or microscopy.

Invasive MRI perfusion techniques which use tracers can be divided into two main groups. One group which uses exogenous tracers such as ^{19}F, ^{17}O, and D_2O which exchange with the tissue. The other group uses tracers such as Gd-DTPA and Dy-DTPA which are pure intravascular tracers and do not cross the capillary wall in the brain.

The methods which use the non-proton exogenous tracers, ^{19}F [3], ^{17}O [59], and D_2O [112] generally suffer from low signal-to-noise ratio (SNR) because of the relative low concentration of the contrast, although, the signal is not masked by the large background proton signal. Most of the measurements have therefore been done at higher field strength than those currently used clinically.

Imaging techniques which use intravascular paramagnetic agents such as Gd-DTPA have shown good results [9,110] for imaging of cerebral perfusion. The susceptibility of the contrast agent produces steep localized magnetic field gradients that cause a decrease in T_2^*. Because the gradients extend well beyond the capillary wall, the signal from very many spins outside of the capillaries is influenced by the pas-

sage of the agent bolus. Second, in these same pulse sequences, the variations in the magnetic field can lead to a net displacement in the resonance frequency throughout a whole voxel which can be measured [25]. Fast imaging techniques such as EPI and Turbo-FLASH are usually applied to measure the change in T_2^* but SSFP has also been applied for this purpose [68].

It has been shown [95, 104, 124], that magnetic susceptibility of blood changes dramatically when it becomes deoxygenated. This blood oxygenation level dependent (BOLD) effect is strongly dependent on field strength and was originally demonstrated at 7T although it can also be observed at lower field. In principle, this method is based on the same effect as the perfusion techniques which use paramagnetic agents, however, it is non-invasive. The BOLD contrast has been used extensively in functional imaging of the brain in recent years [82].

Another non-invasive MRI perfusion technique uses water as an endogenous diffusible tracer. The method is based on spin labeling in a labeling plane [30]. These labeled spins are then allowed to perfuse into a detection plane where the steady-state longitudinal magnetization will be affected by the labeled spins. This results in a apparent change in T_1 which can be related to the perfusion. Successful quantitative results have been reported in rat hearts [143] and rat brain [148] at 4.7T. The high field is important because T_1 increases with the magnetic field strength and larger T_1 values give larger perfusion sensitivity [77].

Intravoxel incoherent motion (IVIM) introduced by Le Bihan *et al.* is another non-invasive method which has been used to measure perfusion [8, 71, 74, 128]. Its concept is based on pseudo-diffusion. The microcirculation of blood in capillaries is regarded as random, incoherent motion at the voxel scale. The blood is assumed to change direction several times during the measurement and the apparent diffusion coefficient (ADC) can be shown to be related to the blood flow. The data analysis is based on the bi-exponential nature of the signal as a function of the b-factor (see section 3.4). Given that the pseudo-diffusion coefficient is much larger than the water diffusion, it can be estimated from the initial slope of the curve which shows the signal as a function of the b-factor. The main problem with this technique is that the signal from the static tissue is not suppressed and only a small fraction of the signal carries the microcirculation information. The SNR requirement is thus difficult to achieve.

1.3 Prior Art in Diffusion Imaging

NMR has been used to study water self-diffusion [18, 55, 126] since shortly after its discovery, but only in recent years has it been used for *in vivo* diffusion imaging.

The basic principle of most NMR diffusion experiments can be understood from the pulsed gradient spin-echo (PGSE) sequence, first demonstrated by Stejskal and

Tanner [118]. The PGSE sequence is shown in Fig. 1-1a) and the stimulated echo version of PGSE it in Fig. 1-1b). The initial RF pulse produces transverse magnetization which is dephased by the strong magnetic field gradient and rephased at a later time. If the spins are static, the dephasing and rephasing gradients compensate each other. However, for nucleuses in liquid state molecules, some translational motion is inevitable during the time Δ because of molecular self-diffusion. Therefore, in the spin ensemble, there will be a distribution of residual phase shifts leading to attenuation in the total NMR signal.

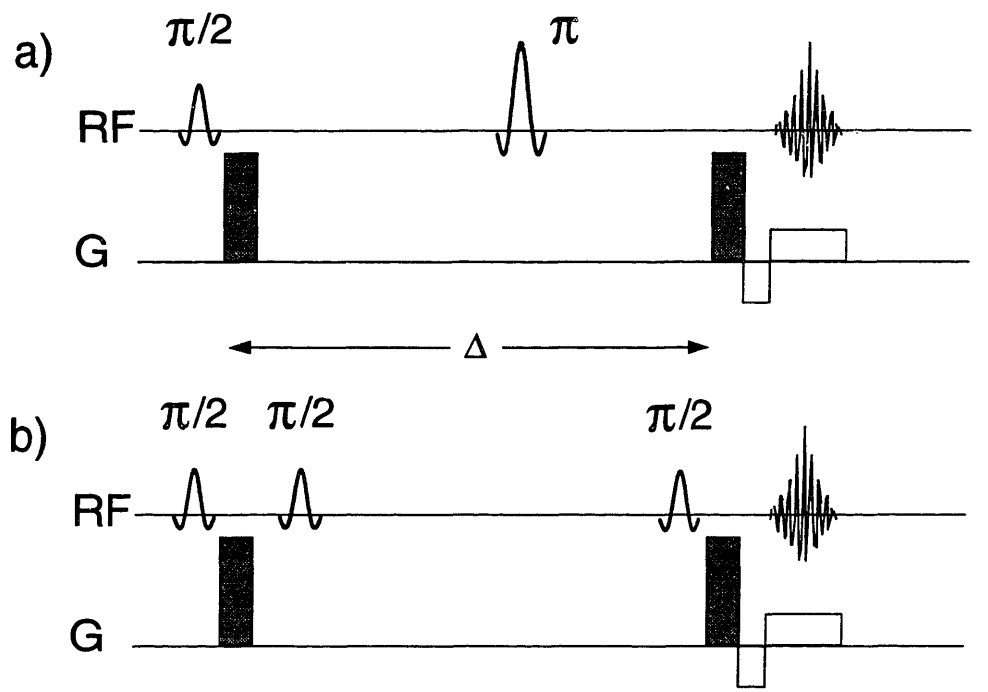

Figure 1-1: a) Pulsed gradient spin-echo (PGSE) sequence. **b)** Stimulated echo version of the PGSE sequence which is beneficial when T_2 is short and T_1 is long. See also Fig. 3-5.

All current diffusion imaging sequences are based on the same principle as PGSE, however, they differ in the way they encode the the spatial information of the object. The encoding scheme is very important because, it is precisely the imaging part which determines whether the diffusion sequence is useful in the presence of physiological motion.

Some of the initial attempts for *in vivo* imaging of diffusion were by PGSE spin-warp Fourier imaging [72, 73]. However, this technique is hampered by severe bulk motion artifacts which make it problematic for accurate assessment of *in vivo* diffus-

ivity. Usually, the artifacts appear as a terrible ghost in the phase encoding direction (see Fig. 6-4).

Imaging techniques that are faster than PGSE such as steady-state free precession (SSFP) [74] have been proposed for diffusion imaging. In SSFP, ghost artifacts are also present, however, this ghost can be minimized by using a frame-by-frame averaging scheme [27, 150]. As our results in chapter 5 show, such a scheme only hides the problem and signal cancelation occurs nevertheless.

Another fast MRI technique that has been tried for diffusion imaging is Turbo-STEAM [135]. This imaging sequence is based on the stimulated echo sequence shown in Fig. 1-1b). It has been reported, however, that with stroke patients, the lack of patient cooperation makes the results with this technique unreliable [136]. Furthermore, its diffusion sensitivity is not very well defined because of the different diffusion weighting on each echo.

The advent of diffusion weighted echo-planar imaging (EPI), made it possible to quantitatively measure diffusion while minimizing physiological motion artifacts [1] [4, 128, 137]. Currently, EPI is not a very widespread technique, because of its need for a specialized and expensive gradient hardware. Furthermore, EPI diffusion images are sensitive to large field inhomogeneities and chemical shift artifacts and fat suppression pulses are usually needed. This has motivated ongoing research to find techniques which will allow accurate and reliable *in vivo* diffusion studies on conventional MR scanners.

Several approaches have been proposed such as reduction of patient motion with customized head restraints [20]. This is generally uncomfortable and inconvenient, especially for patients with head injuries. Also, pulsatile brain motion cannot be eliminated in this way.

Cardiac gating can be used to greatly reduce artifacts from cardiac induced motion along with gradient moment nulling [12]. The gradient strength on most whole body imaging systems is however not large enough to make moment nulling an attractive solution, due to consequent fourfold reduction in diffusion-weighting. Also, as we see from section 5.8, effects from rapidly pulsatile motion are not fully removed by using bipolar gradients alone.

The problem of rigid body translational motion in PGSE has been dealt with by post-processing techniques. An elegant approach is the use of a "navigator echo" [32, 97]. This approach has also been extended to correct for rigid in-plane rotation [2]. Recently, fast imaging sequences which employ multiple echoes have also been augmented with navigator echo [13, 14, 50]. In principle, however, corrections for rotation work only when the diffusion sensitivity is applied in the phase encoding direction [2, 24]. Furthermore, cardiac gating is crucial to minimize cardiac induced

[1] The reason why diffusion weighted EPI is immune to motion is explained in chapter 6.

motion which is spatially varying [78] and cannot be corrected by using a navigator.

A technique related to the navigator technique is the spiral scan diffusion sequence [127]. This technique uses a phase correction scheme without the need for a navigator, because it samples the center of k-space in each shot. Hence, the signal from the center of the k-space can be used as a reference. Most recently, a reference phase map has been introduced to correct diffusion weighted images [132]. This method is essentially identical with the navigated PGSE technique [97] except that the phase information is acquired in a separate scan. The reference phase map technique can therefore neither correct for rotational bulk motion nor spatially varying pulsatile motion.

Another technique that is known to be less sensitive to motion artifacts (in terms of ghosts) is projection reconstruction (PR). PR has been used for diffusion imaging [92] and a modified version which uses the magnitude of the projections has been proposed to reduce the motion artifacts [46, 64]. However, this technique can only correct for motion in the form of bulk displacement and, from the analysis in chapter 6, it cannot give accurate measurements of *in vivo* diffusivity. As expected, the reported values for ADC in brain tissue [64] are very high as compared with our results in chapter 7.

1.4 Summary

This work studies magnetic resonance imaging of diffusion in the presence of physiological motion, i.e. problems with diffusion imaging of human patients in clinical setting. We focus on techniques that may work on conventional scanners which do not have specialized gradient hardware for echo planar imaging.

The first chapters provide the theoretical tools that are needed to understand the most important issues of MRI diffusion imaging as well as some of the signal-to-noise considerations that relate to accuracy and sensitivity.

Since much of the analysis was done by a computer simulation, we took a close look at the intrinsic properties of several simulation techniques for diffusion in NMR. In chapter 3, we extend the random walk model for diffusion and show how a conditional random walk model can be used to modify existing simulation techniques. This improves the speed and the accuracy in simulation of free diffusion and allowed us to develop an extremely fast and accurate simulation technique based on the discrete Fourier transform (DFT). This technique is particularly useful in the simulation of the SSFP sequence. We also show how the concept of random walk can be used as a simple analytical tool for calculating the diffusion sensitivity in various pulse sequences.

The SSFP sequence, being fast and known for its high diffusion sensitivity, is studied in detail in chapter 5. The DFT simulation technique is used to show that

SSFP is not able to provide accurate diffusion maps. Furthermore, we show that a recently proposed modification of the SSFP sequence which uses bipolar gradients is also inaccurate.

After the disappointing results with the SSFP sequence, we experiment with a recently proposed navigated spin-echo diffusion sequence in chapter 6 and extend it to the fast spin-echo sequence. Although, motion artifacts can be greatly reduced by this technique, residual motion artifacts still exist. This technique therefore requires cardiac gating and some patient cooperation. Furthermore, accurate diffusion weighting cannot be achieved in three orthogonal directions. However, it is important to measure the diffusivity in three orthogonal directions, since, cell membranes and other oriented molecular structures lead to anisotropic water displacement. Anisotropy can be used to determine nerve fiber orientation within brain white matter [6, 7, 19, 123]. It also permits distinction of relative hyper-intensity in white matter due to acute ischemic lesions from that due to orientation of axons perpendicular to the direction of the applied diffusion gradient [133,137]. Recently, diffusion anisotropy has also been exploited to improve image contrast among the various uterine tissue types [147].

This has led us to develop a novel diffusion imaging technique that does not use phase encoding. This technique is therefore insensitive to motion artifacts and for brain imaging, neither head restraints nor cardiac gating is needed. By insensitivity to motion artifacts we mean, that any tissue displacement that is small compared with the image voxel size but large compared with the diffusion displacement of the spin bearing particles does not cause significant increase in signal loss or other image artifacts.

In chapter 7, we describe our ultimate solution, i.e. Line Scan Diffusion Imaging (LSDI). The key to the success of LSDI is that each line is self-contained and the phase information is discarded. Therefore, each line can be considered a one-dimensional EPI image. Also, line scan and diffusion imaging make a perfect fit, because, problems related to the secondary echoes disappear by alternating between high and low diffusion sensitivity. Then, by using an interleaving scheme with a "dummy sweep", uniform image intensity is ensured as well as high quality diffusion maps.

We believe the LSDI technique is an excellent alternative to EPI diffusion imaging. Our results show, that it is possible to use the LSDI technique to acquire accurate diffusion maps on conventional 1.5T and 0.5T systems. This can have great clinical impact because reliable stroke studies with diffusion imaging, which previously required scanners with expensive gradient hardware for EPI, can now be done on most conventional scanners. Hence, this increases the number of clinical sites capable of doing stroke and other diffusion studies dramatically.

Chapter 2

Background

2.1 Introduction

THIS chapter serves to provide the reader with some insight into basic Nuclear Magnetic Resonance (NMR) and NMR imaging (MRI). A much more thorough discussion can be found in the following references: [16, 35, 36, 75, 115].

2.2 Fundamentals of NMR

Nuclear Magnetic Resonance is a phenomena which depends on the internal structure of the nucleus in atoms. The nucleus possesses a total angular momentum $\mathbf{J}$ and a total magnetic moment $\mathbf{m}$ which are related by the *gyromagnetic ratio*

$$\mathbf{m} = \gamma \mathbf{J} \tag{2.1}$$

The angular momentum can be related by *Planck's constant*, $\hbar$, to the dimension-less angular momentum or *spin*, $\mathbf{I}$, by $\mathbf{J} = \hbar \mathbf{I}$ where $\mathbf{I}$ takes only integer of half-integer values. The spin states of the nuclei are inherently quantum mechanical in their behavior and their dynamics are described by the *commutation relationship* of the spin operators, the *Schrödinger equation*, and the corresponding *Hamiltonian operator*. The Hamiltonian for the spin is due to the static magnetic field, B_0, which is usually taken to be along the z-axis, and is given by

$$\mathcal{H} = -\gamma \hbar B_0 \mathbf{I}_z \tag{2.2}$$

This form of interaction is known as a Zeeman interaction. Calculations with the *density operator* show that for uncoupled spin-1/2 nuclei such as protons, the motion of the ensemble of spins may always be described in terms of a magnetization vector

precessing in the magnetic field. This semi-classical description of NMR has equations of motion that are analogous to those of an electron orbiting around a nucleus in a magnetic field. The rate of change of the angular momentum equals the torque and by using Eq. (2.1) this can be written as

$$\frac{d\mathbf{M}}{dt} = \gamma \mathbf{M} \times \mathbf{B} \tag{2.3}$$

The solution to this equation corresponds to precession of the magnetization, $\mathbf{M}$, about the magnetic field, $\mathbf{B}$, at a rate $\omega = \gamma B$, known as the *Larmor frequency.* The precession does not go on forever because, due to tumbling of the molecules, there are fluctuations in the local magnetic field that causes the net magnetization to align with the thermal equilibrium value of the magnetization, $\mathbf{M}_0$. This process is called *relaxation.* The thermal equilibrium value of the average magnetization is given by *Curie's law*

$$\mathbf{M}_0 = \frac{\gamma^2 \hbar^2 \mathbf{B}_0}{4kT} \tag{2.4}$$

where kT is the *Boltzmann energy* and $\mathbf{B}_0$ is the main static magnetic field. By applying and external magnetic field B_1 with an RF pulse excitation, the magnetization is perturbed from its thermal equilibrium value, $\mathbf{M}_0$. Relaxation makes the transverse part of the magnetization, which is orthogonal to the main magnetic field $\mathbf{B}_0$, decay to zero and the magnetization will align back towards the thermal equilibrium, $\mathbf{M}_0$, which is purely longitudinal.

In liquids, the relaxation can be modeled as an irreversible first order process where T_1 and T_2 represent the spin-lattice (longitudinal) and spin-spin (transverse) relaxation times, respectively. Furthermore, movements of spins because of flow and diffusion affect the local magnetization if it is not spatially uniform. All these changes can be incorporated into Eq. (2.3) resulting in the well known *Bloch-Torrey equation*

$$\frac{d\mathbf{M}}{dt} = \gamma \mathbf{M} \times \mathbf{B} - \hat{x}\frac{M_x}{T_2} - \hat{y}\frac{M_y}{T_2} - \hat{z}\frac{(M_z - M_0)}{T_1} + \nabla \cdot \mathbf{v}\mathbf{M} + \nabla \cdot \mathbf{D}\nabla\mathbf{M} \tag{2.5}$$

where $\mathbf{v}$ denotes the flow and $\mathbf{D}$ is the diffusion coefficient or the diffusion tensor in anisotropic material.

2.3 Spin Manipulation and Signal Detection

In order to detect the NMR signal, a coil is placed around the sample with its symmetry axis transverse to the polarizing magnetic field $\mathbf{B}_0$. The detection process is governed by *Faraday's law* and depends on the motion of the magnetization vectors within the coil. Any transverse magnetization precessing at the Larmor frequency will

induce an oscillatory e.m.f. at frequency ω_0. The receivers work by mixing the signal e.m.f. with the output from a reference RF oscillator, a process known as heterodyning. This gives low-frequency quadrature output signals which are each respectively proportional to orthogonal phases of the transverse magnetization. It turns out that it is most convenient to describe the dynamics of the magnetization in a *rotating reference frame* which rotates with the frequency ω_r. This is equivalent with changing from the *Schrödinger picture* to the *Heisenberg picture* in quantum mechanics. Equation (2.3) can then be rewritten as

$$\frac{d\mathbf{M}}{dt} = \gamma \mathbf{M} \times \mathbf{B}_{\text{eff}} \tag{2.6}$$

where the effective magnetic field is given by

$$\mathbf{B}_{\text{eff}} = \hat{z}\,(B_0 + \omega_r/\gamma) + \mathbf{B}_1 \tag{2.7}$$

and $\mathbf{B}_1$ represents the amplitude of the RF magnetic field which carrier frequency is ω_r. If the reference frequency is chosen to be $\omega_r = -\gamma B_0$ then the effective field is simply $\mathbf{B}_1$. Hence, by choosing the correct amplitude and duration, τ, it is possible to design RF pulses that rotate the magnetization vector by an angle α from its value prior to the RF pulse

$$\alpha = \gamma \mathbf{B}_{\text{eff}}\, \tau \tag{2.8}$$

If $\mathbf{M}$ is defined as $\hat{x}M_x + \hat{y}M_y + \hat{z}M_z$, then the rotation around the x-axis can be described by a rotation matrix, $\mathbf{R}$, which is given by

$$\mathbf{R} = \begin{bmatrix} 1 & 0 & 0 \\ 0 & \cos\alpha & \sin\alpha \\ 0 & -\sin\alpha & \cos\alpha \end{bmatrix} \tag{2.9}$$

The magnetization following the RF pulse, $\mathbf{M}^+$, is related to the magnetization prior to the RF pulse, $\mathbf{M}^-$, by

$$\mathbf{M}^+ = \mathbf{R}\mathbf{M}^- \tag{2.10}$$

This equation assumes influence of relaxation to be negligible, which is usually the case for short RF pulses.

Spins which are off resonance, i.e. not rotating with the reference frequency γB_0, will precess and accumulate phase, ϕ, according to their spatial dependent magnetic field offset, $\Delta B_z(\mathbf{r}) = (\mathbf{B}(\mathbf{r}) - \mathbf{B}_0) \cdot \hat{z}$

$$\phi(t) = \int_0^t \gamma \Delta B_z \, d\tau \tag{2.11}$$

Furthermore, due to relaxation the transverse and the longitudinal magnetization will decay according to T_2 and T_1, respectively. The free induction decay (FID) following an RF pulse at $t = 0$ is then most easily described by

$$\mathbf{M}(t) = \mathbf{P}(t)\mathbf{M}(0) + \hat{z}(1 - E_1(t))M_0 \tag{2.12}$$

where

$$\mathbf{P}(t) = \begin{bmatrix} E_2(t)\cos\phi(t) & -E_2(t)\sin\phi(t) & 0 \\ E_2(t)\sin\phi(t) & E_2(t)\cos\phi(t) & 0 \\ 0 & 0 & E_1(t) \end{bmatrix} \tag{2.13}$$

and $E_1(t) = \exp(-t/T_1)$ and $E_2(t) = \exp(-t/T_2)$.

2.4 Principles of MRI

2.4.1 K-space Formalism

Spin-warp Fourier imaging is the most common MR imaging technique today. It uses linear magnetic field gradients, $\nabla B_z = \mathbf{G}$, to modify the static magnetic field, $\mathbf{B}_0$. Thereby, the spatial location of the magnetization is frequency encoded. The magnetization precesses with a frequency that is different from the reference frequency of the receiver and the offset can be related to the spatial location. It is most convenient to use a complex notation to describe the precession of the transverse magnetization. By defining $m_{xy} = M_x + iM_y$, the precession can be written as

$$m_{xy}(t) = m_{xy}(0)E_2(t)e^{i\phi(t)} \tag{2.14}$$

where

$$\phi(t) = \gamma \int_0^t \mathbf{G}(\tau) \cdot \mathbf{r}\, d\tau \tag{2.15}$$

Frequency encoding is only a special case of phase encoding with constant gradients, i.e. $\phi(t) = \omega t = \gamma \mathbf{G} \mathbf{r} t$. In this case, the phase varies linearly with time which is equivalent to a frequency shift. For a more general imaging experiment with complex gradients, it is better to think in terms of phase encoding.

By recognizing that the precession angle in Eq. (2.15) can be written as $\phi(t) = \mathbf{k}(t) \cdot \mathbf{r}$ it is possible to view the MR imaging experiment in the spatial frequency domain, or what is usually referred to as k-space. The wavenumber, $\mathbf{k}$, is defined by the "area" of the gradients

$$\mathbf{k}(t) = \gamma \int_0^t \mathbf{G}(\tau)\, d\tau \tag{2.16}$$

Now ignore transverse relaxation for the moment. The received signal, $\tilde{S}(t) = S(\mathbf{k}(t))$, from magnetization which has been tilted into the transverse plane is given by

$$S(\mathbf{k}(t)) = \iiint \rho(\mathbf{r}) \exp\left[i\mathbf{k}(t) \cdot \mathbf{r}\right] d\mathbf{r} \tag{2.17}$$

where ρ represents the proton density of the object. This is clearly the Fourier transform of the proton density. By collecting sufficient data in the k-space, by varying the gradients properly, the image can be reconstructed by the inverse Fourier transform

$$\rho(\mathbf{r}) \propto \sum_{n_x} \sum_{n_y} \sum_{n_z} S(\mathbf{k}(n_x, n_y, n_z)) \exp\left[-i\mathbf{k}(n_x, n_y, n_z) \cdot \mathbf{r}\right] \tag{2.18}$$

Note that the integral has been replaced by a sum because of the finite number of data points collected from the k-space. The point-spread function (PSF) is determined by the number and the location of the k-space data points[1].

In conventional MRI imaging, one line in the k-space is acquired after applying an RF pulse which tilts the magnetization into the transverse plane. It depends on how long time passes from the RF pulse excitation to the data collection at the echo time, TE, how much the magnetization has decayed from transverse relaxation, T_2. The RF pulses are separated by the repetition time TR. If the magnetization has not reached its equilibrium value, M_0, before the next RF pulse, the magnetization will also depend on the longitudinal relaxation, T_1. This is called T_1 and T_2-weighting. Furthermore, as will be shown in later chapters, by proper use of extra gradients before the data collection, it is possible to make the phase and the amplitude of the received signal reflect flow and diffusion.

2.4.2 Slice Selection

Unlike imaging techniques such as ultrasound and X-ray computerized tomography, MRI is inherently a volume imaging technique because of the long RF wavelength. It is possible, however, to image only a fraction of the object at the time by using volume selective excitation. This is important in order to reduce imaging time and often only a part of the object is of interest. Because of the important role volume selection plays in chapter 7 its major concepts will be outlined here.

The key insight can be drawn from Eq. (2.7). If the spins are irradiated in the presence of a linear magnetic field gradient $\mathbf{G}$ by an RF wave which frequency is ω, the effective magnetic field will vary with location according to

[1]The PSF depends also on the transverse relaxation and the order in which the data points are sampled. To simplify the discussion we have ignored the influence of T_2 here.

$$\mathbf{B}_{\text{eff}} = \hat{z}\mathbf{G}\cdot\mathbf{r} + \hat{x}B_1 \tag{2.19}$$

Spins which are on resonance, $\mathbf{G}\cdot\mathbf{r} = 0$, will rotate toward the xy-plane according to the field $\hat{x}B_1$. Spins which are far away from the resonance location, $|\mathbf{G}\cdot\mathbf{r}| \gg |B_1|$, will see an effective magnetic field which is almost entirely aligned towards the z-axis. These spins will therefore not tilt toward the xy-plane.

This simplistic analysis can now be generalized to include time varying RF excitation, i.e. short duration pulses. Each such pulse can be represented by a sum of infinitely many continuous waves which frequencies, phases, and amplitudes are different. Because of the magnetic field gradient, there is a distinct resonance location for each of the frequencies. Therefore, the flip angle at each location (the slice profile) will depend on the frequency spectrum of the RF pulse. The width of the slice is proportional to the bandwidth of the RF pulse and inversely proportional to the gradient strength. Furthermore, the location of the slice is determined by the carrier frequency of the RF pulse.

For small flip angles, it turns out that previous analysis is exact and the slice profile is directly related to the Fourier transform of the RF pulse. Consider the real zero order hold (ZOH) RF pulse shown in Fig. 2-1a and its corresponding fictitious discrete time RF pulse. The *small flip angle approximation* assumes that each of the discrete time hard pulses produces transverse magnetization without perturbing the longitudinal magnetization "reservoir", i.e. $\sin\alpha \approx \alpha$ and $\cos\alpha \approx 1$. As a consequence, the transverse magnetization produced by each of the hard pulses is not affected by the trailing hard pulses.

It is easy to verify, by using Eq. (2.7), that if the sampling rate of the RF pulse is high enough, the total rotation of the tip of the magnetization vector during each sampling interval is the same if: a) it rotates according to the effective field of the ZOH RF pulse waveform, b) it first rotates instantaneously due to the hard pulse and then due to the gradient. This is demonstrated in Fig. 2-1b.

Each hard pulse creates a small transverse magnetization which is uniform over space and its amplitude depends only on the strength of the pulse. The area of the gradient that follows the pulse will then determine the modulation of this transverse magnetization. As shown in Fig. 2-1a, at time t_e the transverse magnetization produced by the hard pulse at time t_a is uniform over space, because the area of the gradient from t_a to t_e is zero, whereas, the magnetization produced by the pulse at time t_b is spatially modulated at time t_e. The modulation wavenumber for the harmonic created by the RF pulse at time t is given by

$$\mathbf{k}(t) = \gamma \int_t^{t_e} \mathbf{G}(\tau)\, d\tau \tag{2.20}$$

Clearly, the total transverse magnetization, from the whole train of hard pulses, is the

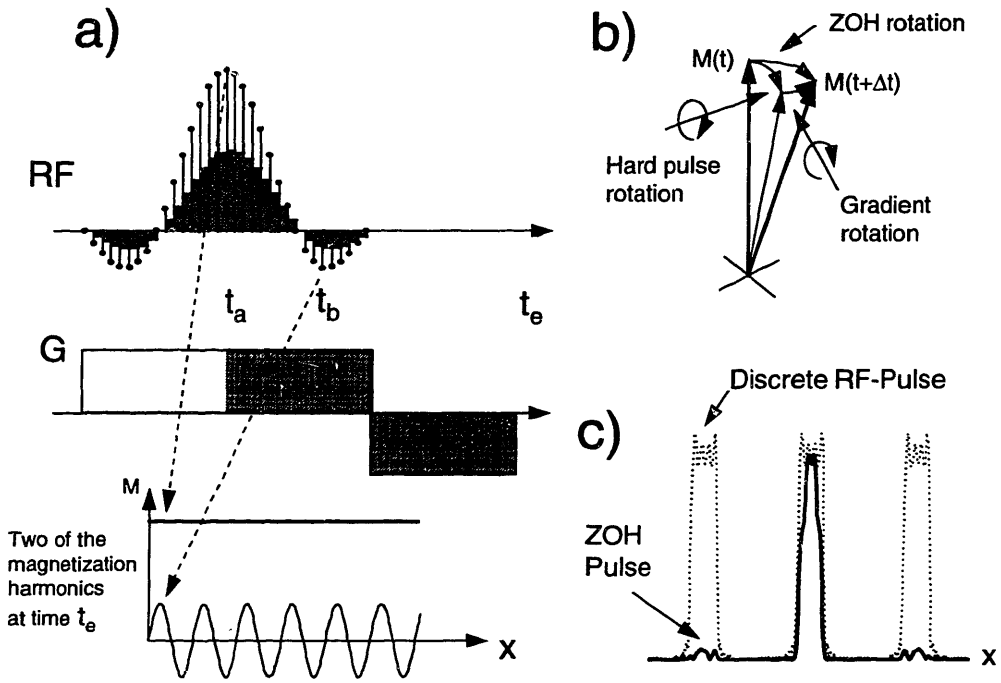

Figure 2-1: a) A zero-order hold sinc RF pulse and the corresponding fictitious discrete time pulse. The harmonics created by the hard pulses at time t_a and t_b are shown as they are at time t_e. **b)** The effective rotation of the magnetization vector according to the ZOH pulse and the discrete pulse is the same. **c)** The magnitude of the magnetization profiles excited by the ZOH pulse and the discrete pulse.

discrete Fourier transform of the RF pulse. This is demonstrated in Fig. 2-1c. For the real ZOH pulse, it is no longer true that the transverse magnetization produced at a given time in the RF pulse is uniform over space, because the gradient causes the effective magnetic field to vary with location. The real slice profile is therefore not periodic in space as the one predicted by the discrete Fourier transform of the fictitious discrete time RF pulse. Indeed, the sidelobes can be determined from the Fourier transform of the ZOH waveform, and they can easily be made negligible for one-dimensional selective pulses. For two-dimensional or frequency-spatial selective pulses, the finite duration of the RF pulse limits the coverage of the k-space and side-lobes become a much bigger problem. The longer RF pulses get, the more important it is to correct for transverse relaxation during the excitation pulse. From Fig. 2-1 and the previous discussion, it is easy to see that the envelope of the RF pulse at time t should be multiplied by $\exp\left[(t_e - t)/T_2\right]$ to correct for the T_2 decay.

The Fourier shift theorem, $\mathcal{F}\{M(\mathbf{r}-\mathbf{r}_0)\} = \exp[-i\mathbf{k}\mathbf{r}_0]\mathcal{F}\{M(\mathbf{r})\}$, shows that in order to shift the location of the selective excitation, the phase of the RF pulse has to be adjusted according to the wavenumber. In the case of one-dimensional RF-pulses which use linear gradients, the wavenumber changes linearly with time. Hence, the linear phase variation is equivalent to changing the carrier frequency of the RF pulse.

The previous discussion holds only for RF pulses with small flip angles and for an accurate analysis and design of RF pulses with large flip angles the Shinnar-LeRoux algorithm has to be used. The small flip angle approximation is still surprisingly accurate even for moderately large flip angles.

2.4.3 Pathway Diagrams

Pathway diagrams are an extremely useful tool for understanding MR imaging experiments. These diagrams are easily drawn and they provide good information about the properties of the most complex pulse sequences. There are two equivalent ways to think about pathway diagrams: a) as representing the phase of the magnetization at a particular location (an isochromat), or, b) as representing the spatial frequencies of the magnetization. The equivalence is due to the fact that $\phi(t) = \mathbf{k}(t) \cdot \mathbf{r}$.

There are two things that are essential for understanding how pathway diagrams are drawn. First, the RF rotation in Eq. (2.9) has to be written for complex notation. The magnetization prior to the RF pulse is denoted by (m_{xy}^-, m_z^-) and after the RF pulse by (m_{xy}^+, m_z^+). The RF rotation is then given by

$$\begin{aligned} m_{xy}^+ &= \frac{1+\cos\alpha}{2}\, m_{xy}^- + \frac{1-\cos\alpha}{2}\, \overset{*}{m}_{xy}^- + i \cdot \sin\alpha\, m_z^- \\ m_z^+ &= \frac{i \cdot \sin\alpha}{2}\, m_{xy}^- - \frac{i \cdot \sin\alpha}{2}\, \overset{*}{m}_{xy}^- + \cos\alpha\, m_z^- \end{aligned} \tag{2.21}$$

The asterisk is used to represent the complex conjugate, i.e. the opposite phase. Second, at the time when the RF pulses are applied, each component of the magnetization vector is decomposed into three new components (pathways). Therefore, the number of components grows exponentially with the number of RF pulses and the total magnetization vector is the sum of all the pathways.

Between the RF pulses, the phase of the transverse pathways changes according to Eq. (2.14), whereas, the longitudinal pathways maintain a constant phase. The transverse and the longitudinal pathways decay according to $E_2(t)$ and $E_1(t)$, respectively.

Figure 2-2 shows an example of the pathways formed by three RF pulses applied during a constant gradient. After the first RF pulse, the local transverse magnetization can be described by a single transverse pathway which phase increases according to the area of the gradient. In terms of the total magnetization, this is a single spatial wave which wavenumber is increasing. The next RF pulse mixes the pathways as

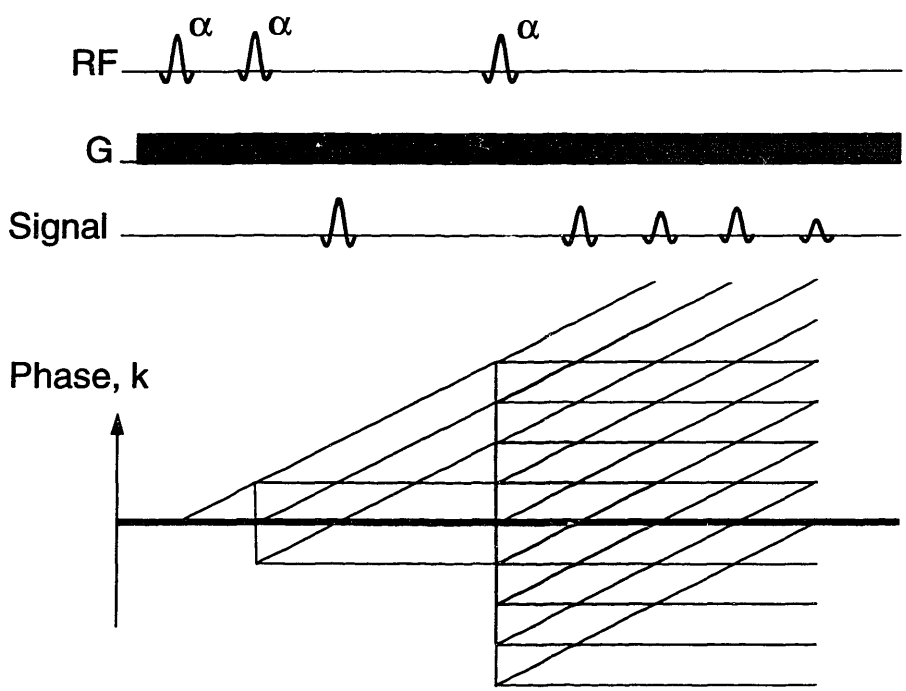

Figure 2-2: Pathway diagram example. The RF pulses mix the spatial harmonics according to Eq. (2.21). The phase of the transverse magnetization pathways increases because of the gradient but the phase of the longitudinal pathways remains constant. The RF pulses split each pathway into three new pathways.

described in Eq. (2.21). The pathway which starts out with the negative phase will eventually have zero phase. Hence, an echo will be formed because its average value of the pathway is nolonger zero[2], as is the case for the other two transverse pathways. The horizontal lines are the undetectable longitudinal pathways. According to Eq. (2.21), m_z^+ is a mixture of m_{xy}^- and its conjugate. Therefore, m_z^+ is represented by two lines with opposite phase[3]. After the third RF pulse, there are four more occurrences where pathways cross the zero phase line. Therefore, the three RF pulses form 5 echoes. The FIDs that immediately follow the RF pulses have been ignored here. They occur at locations where a pathway departs the zero phase line.

Finally, it should be mentioned that the echo signals that are drawn according to the pathway diagram should be delta pulses in time. This is because the spatial waves with $\mathbf{k} = 0$ integrate to a nonzero number, whereas, spatial waves with any nonzero

[2]Spatial waves with zero wavenumber have nonzero average

[3]By thinking in terms of wavenumbers, Eq. (5.28) makes this obvious.

wavenumber integrate to zero. This assumes that the magnetization extents over an infinite region in space. For real life situations this is not so. The the spatial waves of the magnetization must be *multiplied* by the proton density of the object (or any other contrast function). Therefore, according to the convolution theorem (Eq. (A.27)), the pathways should be *convolved* with the spatial frequencies of the object. For the simple example shown in Fig. 2-2 the RF pulses are slice selective. From section 2.4.2 it is known that the magnetization they excite does have spatial frequencies which amplitudes are identical to the shape of the RF pulse (assuming small flip angles). The received echo signal should therefore have a shape similar to the RF pulses.

Chapter 3

Diffusion in NMR

3.1 Introduction

SELF-DIFFUSION is a phenomena caused by random motion of the molecules. This random motion, named *Brownian motion* in honor of its discoverer, was first explained by Einstein in 1905 [33] from the molecular-kinetic theory of heat. Since Hahn's invention of spin echoes [55] NMR has become a very important tool in measuring diffusion. Carr and Purcell [18] first described, using a *random walk* model, how the dephasing of spins caused by diffusion can be partly refocused. Torrey [126] then introduced a diffusion term in the phenomenological equations of Bloch and provided a very useful theoretical tool for predicting diffusion effects in pulse sequences [117]. Since then, many different alternatives have been developed for diffusion measurements for a variety of different applications.

Restricted diffusion is much harder to analyze than free diffusion, even for simple geometries, and correct analytical results have only been obtained in a limited number of cases. In order to study restricted diffusion, numerical analysis is therefore often the only possible choice [5]. There are also cases where it is very hard to obtain analytical solutions for free diffusion, such as in steady state free precession imaging. Numerical simulations have also been found to be a useful tool for studying dephasing behavior in an inhomogeneous magnetic field [40].

The Monte Carlo (MC) method, which is motivated by the random walk model, is one of the most common simulation methods in NMR because it is flexible and easy to implement on modern computers. In this method, an ensemble of spins are randomly moved in space and their phase accumulated according to the local magnetic field at certain time instances.

The finite difference (FD) method applied to the Bloch-Torrey differential equation is also commonly used [149]. Recently Wong *et al.* [144] presented a deterministic

convolution method for diffusion simulation in NMR which is a combination of the two previous methods. The magnetization is discretized in space as in the FD method. The movements, however, are calculated by the theoretical probability distribution of the particle displacement similar to the MC method.

Although these simulation techniques are widely used in the NMR literature, little has been published on their intrinsic properties. In this chapter, we will extend the results obtained by Carr and Purcell [18] by deriving a relationship between the change in the precession angle and the spin displacement, using a conditional random walk. Since the problem is very complex for a nonlinear inhomogeneous magnetic field, we limit ourselves to a constant linear gradient and free diffusion. These results are then used to modify existing algorithms for both the MC and convolution methods. We prove it is possible to simulate free diffusion in a constant linear gradient such that the outcome does not depend on the time steps used in the simulation algorithm.

The conditional random walk model provides good insight into the diffusion related attenuation. We shown how the MC algorithm can be used as an analytical tool to evaluate the diffusion sensitivity or the so called b-factor in a pulsed gradient spin-echo (PGSE). Finally, we show how the apparent diffusion coefficient and anisotropic diffusion can be understood from the random walk model.

3.2 Theory

3.2.1 Random Walk Process

The displacement of freely diffusing spins can be modeled as a "random walk" process. To simplify the discussion we will consider a spin diffusing in one dimension only; however, the results are readily generalized because contributions to the phase resulting from displacements in orthogonal directions are independent. We denote the position of the spin by X and its phase by Φ. Then we let x denote the displacement of a spin due to diffusion during time Δt. Similarly we let ϕ denote the difference in the phase of a freely diffusing spin and a static spin, after some time step Δt. Carr and Purcell [18] showed, by using a *Einstein-Smoluchowski* random walk model [1], that x and ϕ can be written as

$$x = \xi \sum_{i=1}^{N} a_i \tag{3.1}$$

and

[1] Diffusion can also be described by the *Langevin theory* of Brownian motion which gives the relation between the mobility B and the diffusion coefficient $D = BkT$ [38,99]

$$\phi = G\gamma\tau\xi \sum_{j=1}^{N} \sum_{i=1}^{j} a_i = G\gamma\tau\xi \sum_{j=1}^{N} j a_{(N+1-j)} \tag{3.2}$$

where ξ is a small instantaneous displacement and $a_i \in (-1, 1)$ is a discrete zero mean random variable which governs the direction of the motion. The gradient strength is denoted by G and γ is the gyro-magnetic ratio. The time Δt is defined by the very small time step τ and the number of steps N; that is $\Delta t = N\tau$. The mean of x and ϕ is zero and their variance is given by

$$\sigma_x^2 = \overline{\left(\xi \sum_{i=1}^{N} a_i\right)\left(\xi \sum_{j=1}^{N} a_j\right)} = \xi^2 N \tag{3.3}$$

and

$$\begin{aligned} \sigma_\phi^2 &= \overline{G^2\gamma^2\tau^2\xi^2 \left(\sum_{i=1}^{N} i a_i\right)\left(\sum_{j=1}^{N} j a_j\right)} \\ &= G^2\gamma^2\tau^2\xi^2 \sum_{j=1}^{N} j^2 = G^2\gamma^2\tau^2\xi^2 \frac{N(N+1)(2N+1)}{6} \end{aligned} \tag{3.4}$$

For every practical simulation time step, Δt, N will be a large number. By using the well known relation for the diffusion coefficient [33]

$$D = \frac{\xi^2}{2\tau} \tag{3.5}$$

one obtains

$$\sigma_x^2 = 2D\Delta t \qquad \text{and} \qquad \sigma_\phi^2 = 2\gamma^2 G^2 D \Delta t^3/3 \tag{3.6}$$

When N is large, both x and ϕ depend on a sum of a large number of random variables. The *central limit theorem* can then be used to argue that the probability densities $\Pr(x)$ and $\Pr(\phi)$ are Gaussian and therefore completely described by their mean and their variance as

$$\Pr(x, t) = \frac{1}{\sqrt{2\pi 2Dt}} \exp\left[\frac{-x^2}{2 \cdot 2Dt}\right] \tag{3.7}$$

$$\Pr(\phi, t) = \sqrt{\frac{3}{2\pi 2G^2\gamma^2 D t^3}} \exp\left[\frac{-3\phi^2}{2 \cdot 2G^2\gamma^2 D t^3}\right] \tag{3.8}$$

3.2.2 Conditional Random Walk

In a computer simulation both the position and the phase of the spins have to be updated. If we assume the displacement x at time $t + \Delta t$ caused by the diffusion of some particular spin to be known, then we are restricted to a subset of random variables. Consider a set $\mathcal{X}$ of random variables $(a_1, a_2, \ldots, a_N)$ where $a_i \in (-1, 1)$ such that

$$\mathcal{X} = \left\{ (a_1, a_2, \ldots, a_N) \mid \xi \sum_{i=1}^{N} a_i = x \right\} \tag{3.9}$$

To calculate the expectation value $\overline{\phi_{|x}}$ Eq. (3.2) is used. But first consider the number of positive and negative a_i's which are N_p and N_n, respectively. We must have that

$$\begin{aligned} N_p + N_n &= N \\ (N_p - N_n)\xi &= x \end{aligned} \tag{3.10}$$

Because Eq. (3.2) is linear in terms of a_j, we can simply substitute a_j by its mean given the set $\mathcal{X}$ which is $(N_p - N_n)/N$. We then get

$$\begin{aligned} \overline{\phi_{|x}} &= \overline{G\gamma\tau\xi \left(\sum_{j=1}^{N} j a_j \mid \mathcal{X} \right)} \\ &= G\gamma\tau\xi \frac{N(N+1)}{2} \frac{(N_p - N_n)}{N} = G\gamma\tau \frac{N+1}{2} x \end{aligned} \tag{3.11}$$

where $\mid \mathcal{X}$ means that the random variable, $(a_1, a_2, \ldots, a_N)$, is a member in the set $\mathcal{X}$. As expected, the conditional average $\overline{\phi_{|x}}$ depends on x. Similarly, the variance $\sigma^2_{\phi|x}$ should depend on x and the variance should decrease by increasing x. The variance can be expressed as

$$\begin{aligned} \sigma^2_{\phi|x} &= \overline{\left(G\gamma\tau\xi \sum_{i=1}^{N} i a_i \mid \mathcal{X} \right) \left(G\gamma\tau\xi \sum_{j=1}^{N} j a_j \mid \mathcal{X} \right)} - \overline{\phi_{|x}}^2 \\ &= \overline{G^2\gamma^2\tau^2\xi^2 \left(\sum_{i=1}^{N} a_i^2 i^2 + \sum_{i=1}^{N} \left(i a_i \sum_{j \neq i}^{N} j a_j \right) \right) \mid \mathcal{X}} - \overline{\phi_{|x}}^2 \end{aligned} \tag{3.12}$$

The first term in Eq. (3.12) becomes

$$\overline{G^2\gamma^2\tau^2\xi^2 \left(\sum_{i=1}^{N} a_i^2 i^2 \mid \mathcal{X} \right)} = G^2\gamma^2\tau^2\xi^2 \frac{N(N+1)(2N+1)}{6} \tag{3.13}$$

Now consider the other terms in Eq. (3.12) by dividing them into two cases, i.e. $a_i = 1$ and $a_i = -1$. Again, using the fact that these terms are now linear in a_j gives

$$\overline{\left(ia_i \sum_{j\neq i}^{N} j a_j \mid \mathcal{X}\right)} = i \cdot \left[\frac{\binom{N-1}{\frac{x/\xi+N}{2}-1}\left(\frac{N(N+1)}{2}-i\right)\frac{(x/\xi-1)}{N-1}}{\binom{N}{\frac{x/\xi+N}{2}}} - \frac{\binom{N-1}{\frac{x/\xi+N}{2}}\left(\frac{N(N+1)}{2}-i\right)\frac{(x/\xi+1)}{N-1}}{\binom{N}{\frac{x/\xi+N}{2}}} \right] \tag{3.14}$$

where we have used standard combinatorial probability notation. After some tedious algebra (see Appendix A.1), the variance can be expressed as

$$\sigma^2_{\phi|x} = G^2\gamma^2\tau^2\xi^2 \left[\frac{N(N+1)(2N+1)}{6} - \left(\frac{N+1}{2}x/\xi\right)^2 + \left(2(x/\xi)^2 - 2N\right)\frac{(N+1)}{(N-1)}\frac{(3N^2-N-2)}{24} \right] \tag{3.15}$$

As expected, the variance is found to depend upon x. However, here we are interested in the limit of large N.

$$\lim_{N\to\infty} \sigma^2_{\phi|x} = G^2\gamma^2\tau^2\xi^2\frac{N^3}{12} \tag{3.16}$$

By using Eq. (3.5) this becomes

$$\sigma^2_{\phi|x} = \frac{1}{4}2G^2\gamma^2 Dt^3/3 = \frac{1}{4}\sigma^2_{\phi} \tag{3.17}$$

Similarly, in the limit of large N, Eq. (3.11) becomes

$$\overline{\phi_{|x}} = G\gamma\frac{t}{2}x \tag{3.18}$$

The final result is therefore

$$\Pr(\phi \mid x, t) = \sqrt{\frac{6}{2\pi G^2\gamma^2 Dt^3}} \exp\left[\frac{-6\left(\phi - \gamma G t x/2\right)^2}{2 \cdot G^2\gamma^2 Dt^3}\right] \tag{3.19}$$

One thing to note is that the angle's conditional average, $\overline{\phi_{|x}}$, is the same as Larmor's equation gives for a spin moving with a constant velocity

$$\int_0^t G\gamma(v\tau)d\tau = \frac{G\gamma v t^2}{2} = \frac{G\gamma x t}{2} \tag{3.20}$$

It is somewhat surprising, that $\sigma^2_{\phi|x}$ does not depend on x in the limit of very large N. This motivates a different approach to calculate $\Pr(\phi \mid x,t)$ which is given in Appendix A.2.

3.2.3 Diffusive Attenuation

Here, the attenuation associated with diffusion will be considered. Diffusive attenuation is also analyzed in section 3.4.

There are two extreme limits for diffusive attenuation in a spatially inhomogeneous magnetic field. The first case is where the magnetic field has a linear spatial variation and the second case where the variations are highly nonuniform.

Spins which move due to diffusion in a linear gradient G will acquire an additional precession angle, ϕ. The expectation value of the transverse magnetization, $m_{xy} = m_x + i \cdot m_y$, at location X at time $t+\Delta t$ can be described in terms of the magnetization at time t by

$$\overline{m_{xy}(X,t+\Delta t)} = \int_{-\infty}^{\infty} m_{xy}(X-x,t)e^{i\gamma G(X-x)\Delta t}\Pr(x)\int_{-\infty}^{\infty} e^{i\phi}\Pr(\phi \mid x)d\phi dx \qquad (3.21)$$

This equation explains how the magnetization at X will be influenced by the fraction of magnetization which diffuses from adjacent regions to X. Equation (3.18) shows that the magnetization from spins that move through a distance x precess as if the velocity was constant. As Eq. (3.17) shows, the magnetization is also attenuated. This attenuation comes from dephasing and is due to the fact that there are many different path trajectories leading to the same displacement x. Mathematically this result is obtained by evaluating the second integral in Eq. (3.21) using Eqs. (A.26), (3.17) and (3.18) as well as the fact that $\Pr(\phi \mid x)$ is a Gaussian distribution

$$\overline{m_{xy}(X,t+\Delta t)} = \int_{-\infty}^{\infty} m_{xy}(X-x,t)e^{i\gamma G(X-x)\Delta t}\Pr(x)e^{i\gamma G\frac{x}{2}\Delta t}dx \cdot e^{\frac{-\gamma^2G^2D\Delta t^3}{12}} \qquad (3.22)$$

This dephasing term ($e^{\frac{-\gamma^2G^2D\Delta t^3}{12}}$) represents irreversible relaxation. This result depends on the fact that all the spins experience the same linear gradient. Each spin is statistically equivalent and the system is therefore *ergodic*.

In the so called *motionally-narrowed* regime, the magnetic field is highly nonuniform over the average path through which each spin diffuses. By using a simple random walk model similar to that described in previous sections, it is easy to show that for this case the diffusive attenuation causes extra irreversible transverse relaxation. This extra relaxation depends on the strength of the magnetic field inhomogeneities,

their size and their densities as well as the diffusion coefficient [45]. However, unlike the case for attenuation in a linear magnetic field gradient, this extra transverse relaxation reduces with increasing diffusion. Similarly, one can show that for highly restricted diffusion in a linear magnetic field gradient, the diffusive attenuation decreases with increasing diffusion. Then the diffusive related relaxation increases as the square of the ratio of the restriction size and the average diffusion displacement [109]. This may seem counterintuitive at first but the explanation lies in the fact that all correlation between the displacement and the magnetic field strength, a spin experiences, is lost in the motionally-narrowed regime. A highly restricted spin in a linear gradient will experience the same magnetic field as a freely diffusing spin moving in a gradient with the shape of a saw-tooth. With increasing diffusion the effect of each saw-tooth peak, or minima, on the total precession angle is diminished. This is because with larger diffusion each spin will pass by a greater number of gradient peaks and minima, therefore reducing the average effect on the precession angle. Also the influence of each gradient perturbation is reduced since the spins pass by more quickly when the diffusion is high.

The impact of starting position can also be neglected if the total diffusion trajectory of each spin is much larger than the size of the restriction. Statistically the highly restricted system is therefore ergodic. The distribution of the precession angles will also be Gaussian as in the case of freely diffusing spins in linear gradient, however, the variance in these two cases will be very different and hence very different diffusion attenuation characteristics.

We have not considered the intermediate case when neither the linear gradient free diffusion nor the motionally-narrowed approximation can be applied. This case is of practical interest, such as in the study of cerebral perfusion [40]. It turns out to be difficult to analyze [57] because the distribution on precession angles will not, in general, be Gaussian and the spins will not be statistically equivalent. It is therefore not sufficient to know the mean and the variance to deduce the distribution in the precession angles. For such complex cases numerical simulation has been found to be very useful [142].

3.3 Computer Algorithms

By using the theory in the previous section we can modify two of the existing algorithms for diffusion in NMR. These are the convolution and the Monte Carlo methods.

3.3.1 Monte Carlo Method

The MC simulation algorithm is a straightforward application of Eqs. (3.6) and (3.18). We will use Normal() to denote a function which returns a random value from a Gaussian distribution with zero mean and unit variance. Between the RF pulses, the following steps are then repeated for each spin:

1. $\phi_s = \gamma G \cdot X \cdot \Delta t$ (Static precession)
2. $x = \sqrt{2D \cdot \Delta t} \cdot \mathbf{Normal}()$ (Diffusion displacement)
3. $\phi_{|x} = \gamma G \cdot x/2 \cdot \Delta t + \gamma G \sqrt{D\Delta t^3/6} \cdot \mathbf{Normal}()$ (Conditional phase correction)
4. $\Phi \rightarrow \Phi + \phi_s + \phi_{|x}$ (Precess the spin)
5. $X \rightarrow X + x$ (Move the spin)
6. goto step 1.

In a conventional MC algorithm step no. 3 is not included and $\phi_{|x}$ is therefore always zero.

It is also straightforward to include transverse and longitudinal relaxation in the algorithm. This simulation algorithm uses two calls to Normal() in each loop. Equation (3.22) shows that the variation in the conditional phase causes attenuation. Therefore we can remove the call to Normal() from step no. 3 and substitute this attenuation into the transverse relaxation

$$E_2' = \exp\left[-\Delta t/T_2 - \gamma^2 G^2 D \Delta t^3/12\right] \tag{3.23}$$

The kind of implementation which is best for the simulation depends on the type of the problem. For a one-dimensional problem, there are only four parameters that describe a particular spin. The two bases $\mathcal{A} : (X, m_x, m_y, m_z)$ and $\mathcal{B} : (X, m_l, m_t, \Phi)$ are equivalent. The solution to the Bloch equation for a static spin in a constant magnetic field is a simple rotation about the z-axis. In the $\mathcal{A}$ basis this can be expressed by a precession matrix. However, in basis $\mathcal{B}$ this is much simpler because the rotation becomes just an addition to the precession angle.

Usually RF pulses are considered as being instantaneous and can therefore be represented by a rotation for all spins in a particular volume. In basis $\mathcal{A}$ a rotation can be expressed by rotation matrix but in basis $\mathcal{B}$ this is more complicated because of the nonlinear relationship between the two bases.

When the first pulse is an α pulse and all the following pulses are 180°, it is better to use the $\mathcal{B}$ basis because the use of trigometric functions is reduced. This is especially true when results from intermediate time steps are not needed. Also, because the

precession angle is proportional to the deviation of the magnetic field from B_0, then by simple scaling of each spin's precession angle, one obtains the result for different magnetic field gradients [40]. Thus results for different magnetic field gradients can be calculated from only one simulation experiment, which saves computation time. This is very useful when doing an experiment where the phase distribution is not Gaussian and it is hard to predict the magnetic field dependence [40,57]. For Gaussian distributions, the relationship between the magnetic field strength and the diffusion attenuation can however be expressed analytically, by Eq. (A.26).

The accuracy of the method depends on the number of spins used in the simulation. If the model is assumed unbiased then the accuracy increases proportionally with the square root of the number of spins. The relative accuracy, however, depends on the diffusion attenuation. A simple way to estimate the accuracy is to divide the spins into sub-batches and then use the mean and the variance, obtained from simulation of these sub-batches, to estimate the accuracy of the mean [5]. For this to be a good estimate, however, the results from each sub-batch have to be independent. Care must be taken with the random number generator to ensure this [107].

3.3.2 Convolution Method

Equation (3.22) is the motivation for the convolution method. The dynamics of the spins are updated by the Larmor equation as if they were static and then a complex diffusion propagator, which we will refer to as the *correction kernel*, is used to account for the dynamics during the time step. For a constant gradient, the simulation algorithm is given by:

i) Precess spins as if static; multiply the transverse magnetization by $\exp[i\gamma GX \cdot \Delta t]$

ii) Convolve the magnetization with the correction kernel $c(x, \Delta t)$, to account for the diffusion

iii) Repeat step **i**

The correction kernel for the transverse magnetization can be found from inspection of Eq. (3.22) and the fact that $\Pr(x)$ is a Gaussian distribution. It is given by:

$$c(x, \Delta t) = \frac{1}{\sqrt{2D\Delta t 2\pi}} \exp\left[\frac{-x^2}{2 \cdot 2D\Delta t} - \gamma^2 G^2 D \frac{\Delta t^3}{12} + i\gamma G \frac{x}{2} \Delta t\right] \tag{3.24}$$

Note that the correction kernel for the longitudinal magnetization is identical but with the gradient set to zero (no precession).

The minimum number of time steps is determined by the conditions that a) the gradient is constant during any particular step and b) RF pulses occur between time

steps. A correction kernel for a linearly ramped gradient can also be derived and is given in ref. [49].

Time Step Size Invariance

We want to show that the size of the time steps does not affect the outcome of the simulation. In other words: simulation from time t to time $t+\alpha\Delta t$ and then from $t+\alpha\Delta t$ to $t+(\alpha+\beta)\Delta t$ yields the same results as a simulation directly from t to the time $t+(\alpha+\beta)\Delta t$.

We start with some arbitrary magnetization $m_{xy}(x) = m_x(x) + i \cdot m_y(x)$. The signal measured from this magnetization is given by

$$\int_{-\infty}^{\infty} m_{xy}(x)dx = \mathcal{F}\{m_{xy}(x)\}(k=0) = M(0) \tag{3.25}$$

where $\mathcal{F}$ denotes the Fourier transform. We also define $C(k,\Delta t)$ as $\mathcal{F}\{c(x,\Delta t)\}$. According to our modified convolution algorithm, the one step simulation gives

$$\begin{array}{rcl} m_{xy}(x,t+(\alpha+\beta)\Delta t) & = & \left(m_{xy}(x,t)\cdot e^{i\gamma Gx(\alpha+\beta)\Delta t}\right) * c(x,(\alpha+\beta)\Delta t) \\ \mathcal{F} \Downarrow & & \Uparrow \mathcal{F}^{-1} \\ M(k,t+(\alpha+\beta)\Delta t) & = & M(k-\gamma G(\alpha+\beta)\Delta t,t)C(k,(\alpha+\beta)\Delta t) \end{array} \tag{3.26}$$

where we have used the convolution theorem as well as the scaling and modulation properties of the Fourier transform (Eqs. (A.27) and (A.28) in the Appendix). The two step simulation can be written in the Fourier domain as

$$\begin{array}{rcl} M(k,t+\alpha\Delta t) & = & M(k-\gamma G\alpha\Delta t,t)C(k,\alpha\Delta t) \\ M(k,t+(\alpha+\beta)\Delta t) & = & M(k-\gamma G\beta\Delta t,t+\alpha\Delta t)C(k,\beta\Delta t) \end{array} \tag{3.27}$$

Now one can show, by comparing Eqs. (3.26) and (3.27) and then using Eq. (3.25), that both of these simulations yield the same outcome if and only if

$$C(0,(\alpha+\beta)\Delta t) = C(-\gamma G\beta\Delta t,\alpha\Delta t)C(0,\beta\Delta t) \tag{3.28}$$

By using the definition of the correction kernel and Eq. (A.26) to calculate the Fourier transform of the correction kernel, one can easily verify the equality in Eq. (3.28)

$$C(-\gamma G\beta\Delta t,\alpha\Delta t)C(0,\beta\Delta t) = \exp\left[\frac{-\gamma^2G^2\Delta t^2\left(\beta+\alpha/2\right)^2 2D\Delta t\alpha}{2}\right]\cdot\exp\left[\frac{-\gamma^2G^2D\Delta t^3\alpha^3}{12}\right]$$

$$\begin{aligned} &\cdot \exp\left[\frac{-\gamma^2 G^2 \Delta t^2 (\beta/2)^2 2D\Delta t\beta}{2}\right] \cdot \exp\left[\frac{-\gamma^2 G^2 D\Delta t^3 \beta^3}{12}\right] \\ = \;& \exp\left[-\gamma^2 G^2 D\Delta t^3 \left(\left(\beta^2 + \beta\alpha + \frac{\alpha^2}{4}\right)\alpha + \frac{\alpha^3}{12} + \frac{\beta^3}{4} + \frac{\beta^3}{12}\right)\right] \\ = \;& \exp\left[-\gamma^2 G^2 D\Delta t^3 \frac{(\alpha+\beta)^3}{3}\right] = C(0, (\alpha+\beta)\Delta t) \end{aligned} \tag{3.29}$$

Hence, the size of the time steps does not affect the total magnetization. As shown in section 3.3.2, the finite grid size used in the implementation of the convolution algorithm will set limitations on the minimum time step.

As an example, one can easily calculate the result in a spin-echo (SE) sequence with a constant gradient. By keeping in mind that the 180° refocusing pulse conjugates the magnetization, $m_{xy}(\mathrm{TE}/2_+) = m^*_{xy}(\mathrm{TE}/2_-)$, we can write

$$m_{xy}(x, \mathrm{TE}) = \left(\left(\left(m_{xy}(x,0) \cdot e^{i\gamma G x \mathrm{TE}/2}\right) * c(x, \mathrm{TE}/2)\right)^* \cdot e^{i\gamma G x \mathrm{TE}/2}\right) * c(x, \mathrm{TE}/2) \tag{3.30}$$

The echo is then calculated as the total transverse magnetization. By applying Eq. (A.26) twice and then using Eq. (3.25), one easily gets the echo intensity

$$M(t = \mathrm{TE}) = M^*(t=0) \exp\left[\frac{-\gamma^2 G^2 D \mathrm{TE}^3}{6 \cdot 2}\right] \tag{3.31}$$

This is exactly the well known result first derived by Carr and Purcell [18].

Comparison with the Double Step FD Method

An important factor in the implementation of the convolution method is the sampling of the correction kernel. We will argue, by using our numerical results, that the ratio between the time step and the average time it takes a spin to diffuse between adjacent grid points, $\Delta t/(\Delta x^2/2D)$, is a good estimate of whether the sampling of the kernel is sufficiently fine. If the time step is much smaller than the average time it takes to diffuse between the grid points, the only data point in the kernel considerably different from zero is the center point of the kernel. Obviously this will lead to errors because no magnetization will propagate to adjacent cells. To understand this better we will now consider the finite difference method. We will now show that the Double Step FD method is equivalent to a convolution with a kernel consisting of three points.

Zientara *et al.* [149] have shown that the corresponding FD equations for the transverse Bloch equation can be written as

$$\frac{dm_{xy}(t)}{dt} = [i\mathbf{\Omega} + \mathbf{W}]\, m_{xy}(t) \tag{3.32}$$

where $\mathbf{\Omega}$ is a diagonal matrix whose elements equal $\gamma G x_i$ and $\mathbf{W}$ is a tridiagonal matrix which diagonals are given by $-2D/\Delta x^2$ and the first off-diagonals by $D/\Delta x^2$. Furthermore, they introduce the *double step* method to solve this equation, because the theoretical exponential solution becomes impractical for large matrices. The double step procedure is given by

$$\tilde{m}_{xy}(t+\Delta t) = [\mathbf{1} + \mathbf{W}\Delta t]\, m_{xy}(t) \tag{3.33}$$

$$m_{xy}(t+\Delta t) = \exp[i\mathbf{\Omega}\Delta t]\, \tilde{m}_{xy}(t+\Delta t) \tag{3.34}$$

These two equations can be thought of as convolution and precession and can just as well be written in the reverse order. The corresponding correction kernel would have three elements, $1 - 2D\Delta t/\Delta x^2$ in the center and $D\Delta t/\Delta x^2$ off-center. We see that the correction kernel has only real elements and therefore does not account for precession due to diffusion during the time step. The off-center elements can be thought of as the probability of a spin diffusing to an adjacent grid point. When the time step becomes larger than $\Delta x^2/2D$ the probability of staying at the same grid point becomes negative. The reason is that more elements are needed to represent $\mathbf{W}$ as the time step increases. These matrix elements can easily be found by inspection of the correction kernel in Eq. (3.24).

3.3.3 Simulation Results

To demonstrate the algorithms we simulated a Spin Echo (SE) pulse sequence with a constant magnetic field gradient. The RF pulses are a 90° excitation pulse and a single 180° refocusing pulse. The theoretical diffusion attenuation of the echo is given by Eq. (3.31).

Figure 3-1 shows the simulation results for a conventional MC algorithm and our modified version. The echo amplitude is plotted as a function of the ratio of the echo time and the simulation time step, $\mathrm{TE}/\Delta t$. The average of 10 simulations is plotted, each using 50000 spins, $G = 0.032\mathrm{T/m}$, $D = 3.0\mu\mathrm{m}^2/\mathrm{msec}$ and $\mathrm{TE} = 0.05\mathrm{sec}$. The theoretical echo amplitude from Eq. (3.31) is plotted as a straight line independent of the time step. Clearly the conventional MC algorithm yields incorrect results for larger time steps, however, our version is not affected by the size of the time step.

We also compared the convolution method with the Double Step FD method [149]. Figures 3-2 - 3-4 show the time history of the x- and the y-magnetization in the SE pulse sequence. The initial magnetization is a slice in the yz-plane. Note from Fig. 3-4 how the refocusing pulse, which occurs at the midpoint of the time axis, changes the sign of the y-magnetization. This is, however, harder to see on Figs. 3-2 and 3-3 due to the large time steps and the interpolation done by the plot program. The theoretical echo amplitude is obtained from Eq. (3.31) and found to equal $0.2305M_0$.

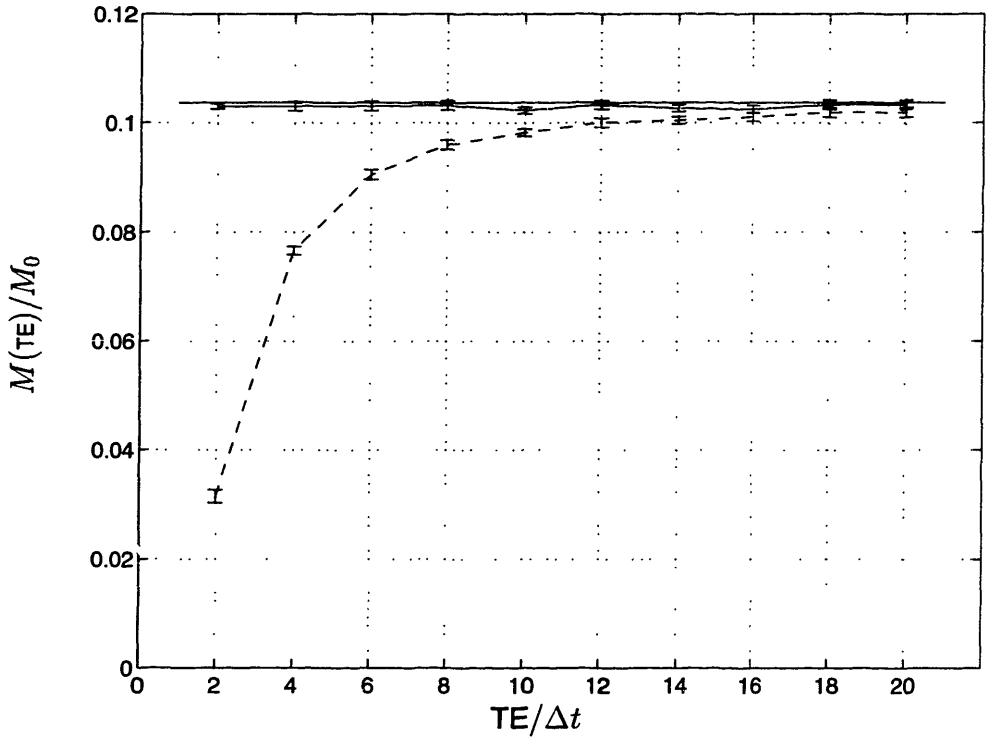

Figure 3-1: Conventional MC (dashed) and our modified MC (solid) methods compared in a SE sequence using different time steps.

This echo amplitude is calculated as the average of the magnetization at the end of the simulation. The average is printed on each plot, for both the convolution and the FD method. It can be seen that for both $\Delta t = \text{TE}/2$ (Fig. 3-2) and $\Delta t = \text{TE}/6$ (Fig. 3-3) the convolution method gives correct results whereas the FD method is either unstable or inaccurate. When a much smaller time step is used, as in Fig. 3-4, the FD method becomes more accurate, however, the time step is now too small for the convolution method, given the grid size in the x-direction. The ratio between the time step and the average time it would take a spin to diffuse between adjacent grid points (denoted by t on the figures) is a good indicator of the accuracy of the methods. When the ratio is larger than one, the convolution method is always exact but the FD method is unstable. Figure 3-4 shows that for ratios less than one, the convolution method loses accuracy because of insufficient sampling of the correction kernel, however the FD method gives fairly accurate results.

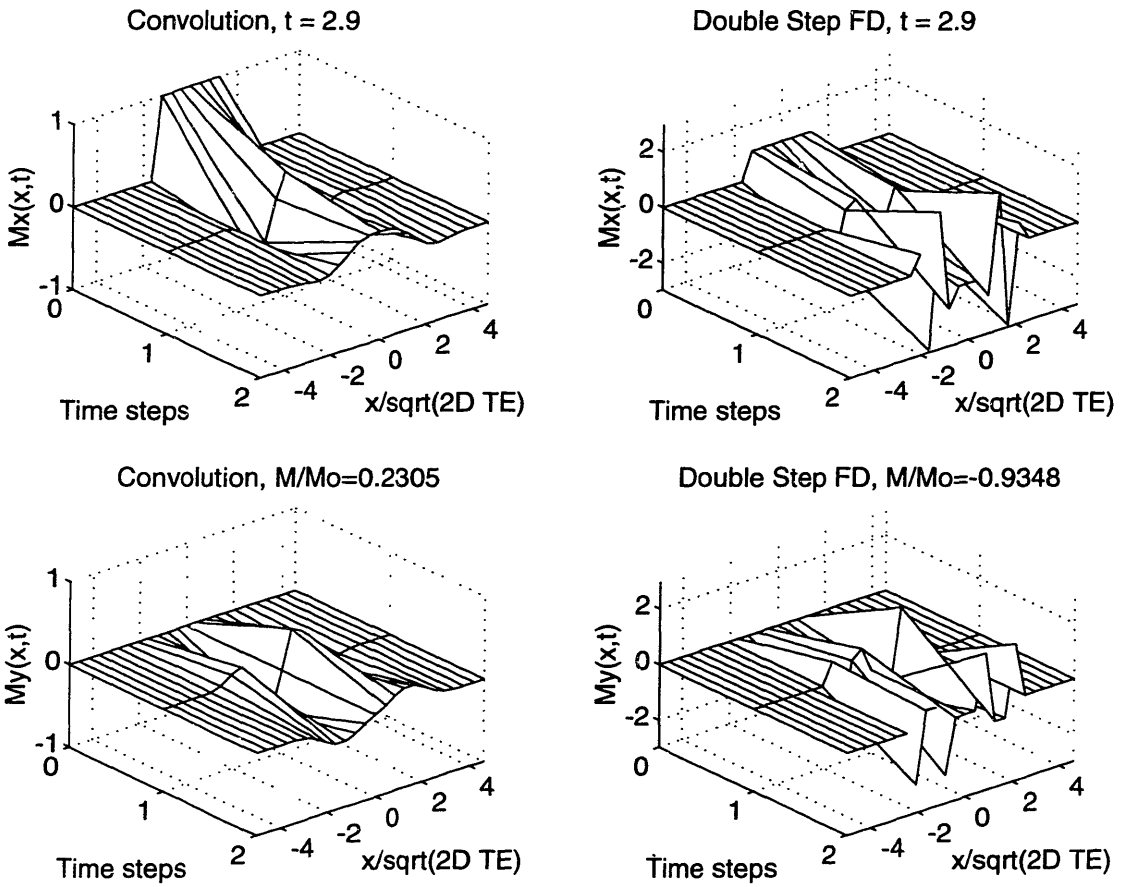

Figure 3-2: Convolution versus the Double Step FD in a SE sequence. Theoretical $M/M_0 = 0.2305$, Δt = TE/2.

3.3.4 Boundary Conditions

For a restricted region with impenetrable boundaries, the Brownian motion can be obtained by augmenting the random walk with reflecting boundary conditions [5]. This is easily done for the MC method but can be done as well in the convolution method.

If the boundary is at χ and the spin starts at position X, then it will be reflected to $\chi - (X + x - \chi)$, where x is the displacement caused by the diffusion. It is very important to point out that the spin distribution resulting from the reflection method in one dimension gives the true distribution for time steps of any size [98, pg. 612]. This means that the size of the simulation time step will not affect the distribution of the particle displacement near the boundary. The same will hold true in two and three dimensions for any rectangular region. For curved surfaces, the reflection method will be a good approximation as long as the displacement is small compared to the radius

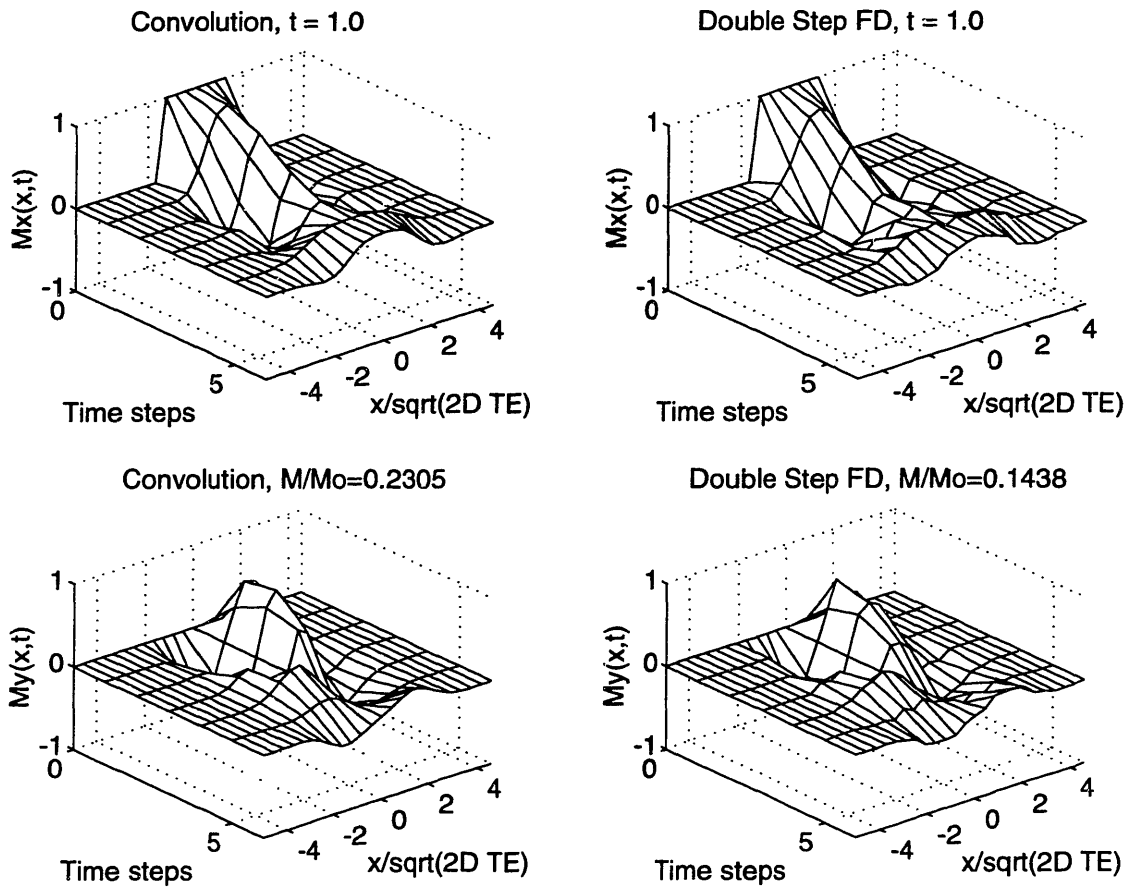

Figure 3-3: Convolution versus the Double Step FD in a SE sequence. Theoretical M/M_0 = 0.2305, Δt = TE/6.

of curvature of the surface. Then displacements in orthogonal directions will be almost independent and thus can be treated separately.

When the boundaries are perfectly absorbing, a similar reflection procedure can be used. The sign of the reflected magnetization, however, has to be inverted. As for the case of perfectly reflecting boundaries, the reflection method will give a spin distribution which is independent of the size of the time step.

Although the spin distribution near the boundary does not depend on the time step, the integration of the spins precession angle will. Therefore, if the gradient is on, the time steps have to be small to ensure correct phase integration.

For the case of restricted diffusion, the volume can be divided into several subregions, in which the time steps are chosen according to the proximity to the nearest boundary. Often only a small fraction of the spins are close to the boundary with the majority located far away from the boundary. This majority can therefore be treated

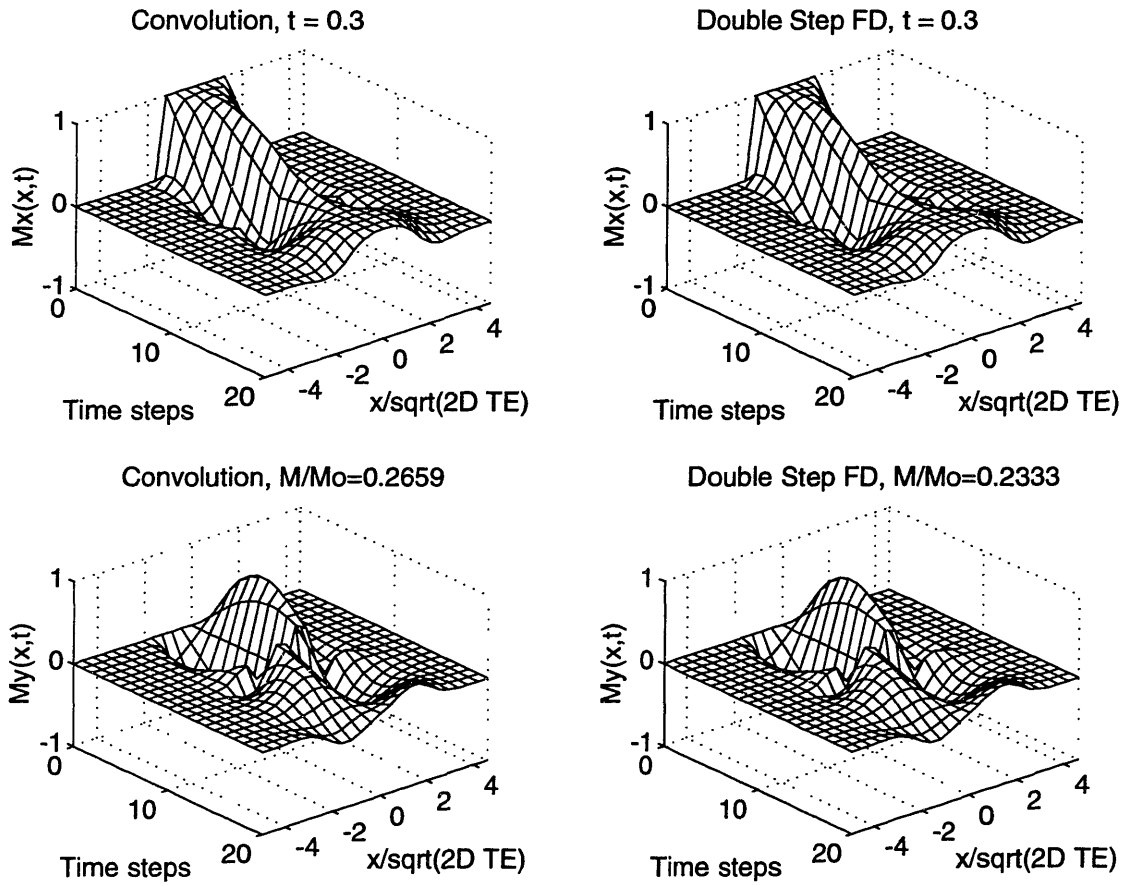

Figure 3-4: Convolution versus the Double Step FD in a SE sequence. Theoretical $M/M_0 = 0.2305$, Δt = TE/20.

by the statistics of free diffusion. To save computation time, we use time steps as large as possible in the simulation of these spins. When these spins eventually come close to the boundary their dynamics will be updated by much smaller time steps, to minimize the error from the free diffusion model at the boundary and ensure correct phase integration. The size of this time step, $\Delta t_{\min}$, will depend on the gradient strength, because the phase change is proportional to $\Delta t_{\min} G\sqrt{2D\Delta t_{\min}}$. The time steps in a given subregion near the boundary are chosen such that the r.m.s. diffusion distance during the time step is less than the shortest distance to the boundary from the particular subregion. The number of regions depends on the restriction size, R, and the minimum time step needed at the boundaries. By using a fixed ratio (some integer factor such as 2) between the time steps in adjacent subregions the number of regions is found to be proportional to $\log_2(R^2/2D\Delta t_{\min})$. When the number of regions is larger than 4 the simulation time is found to be approximately proportional

to $\sqrt{1/\Delta t_{\min}}$. For comparison, in the conventional MC method the simulation time is proportional to $1/\Delta t_{\min}$. If only a few subregions "fit into" the volume of restriction, the computational savings are less. It is therefore only when the gradient is strong and the restriction size is large compared with the diffusion distances that the overhead of using the subregions is beneficial.

Many numerical studies involve analysis of the influence of finite duration gradient pulses in the study of restricted diffusion [5, 11]. Often the gradient is only active during part of the measurement. For such cases, it is possible to use the FD method, with small time steps, when the gradient is on, and then use the convolution method, with larger time steps, when the gradient is off. Both methods would have to be augmented with reflecting boundary conditions [11] in order to insure correct particle distribution.

It is interesting to note that according to Eq. (3.18) the average spin moving in a linear gradient acquires additional phase, $\overline{\phi_{|x}}$, which is the same as if the spin had moved with constant velocity. This is also the same phase that would have been obtained by using trapezoidal integration. By using trapezoidal integration for free diffusion, the error according to Eq. (3.23) is exactly $\exp(-\gamma^2 G^2 D \Delta t^3/12)^{\#\text{steps}}$, where $\Delta t \cdot \#\text{steps}$ is the total simulation time. Hence, by reducing the time step the error can be made arbitrarily small.

If a spin is reflected at a boundary, it is clear that $\overline{\phi_{|x}}$ will be different than given by Eq. (3.18) and the variance of the phase distribution will be less than for the freely diffusing spins. The problem of finding the phase distribution for reflected spins is nontrivial, and the distribution, which will not necessarily be Gaussian, will depend on the distance from the boundary. It might, however, be possible to reduce the error in the phase integration by modifying $\overline{\phi_{|x}}$ such that it reflects the magnetic field over the trajectory of the reflected spin.

One can speculate about specific interesting areas where the formalism presented here would be useful. For example one area is in evaluating T_2^* effects in functional imaging [142]. Microscopic susceptibility variations cause high spatially varying gradients, which lead to increased dephasing of spins. By breaking up space into a number of small regions where the gradient is approximately linear in each region, our diffusion simulation method may be applied.

3.4 Diffusion Sensitivity

3.4.1 The b-factor

For free diffusion and linear magnetic field gradients, the attenuation of the NMR signal is most easily described in terms of a single number which is usually referred

to as the b-factor. The b-factor depends on the RF pulse sequence. Here we will give an example how the Monte Carlo conditional random walk model can be used to calculated the b-factor in a very simple but the single most important pulse sequence for diffusion imaging, namely the pulsed gradient spin echo (PGSE) shown in Fig. 3-5.

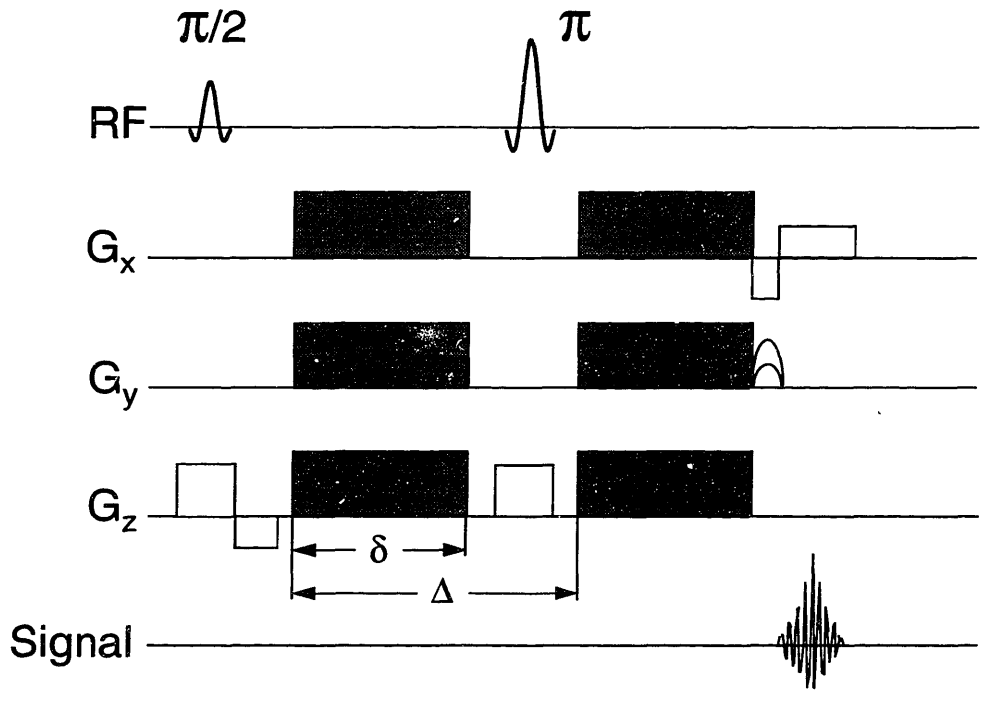

Figure 3-5: The regular spin-warp pulsed gradient spin-echo (PGSE) sequence. The amplitude of the diffusion gradient is varied to change the diffusion sensitivity.

Unlike the more general approach we took in section 3.2.3, we will only be interested in the signal attenuation once the magnetization has been refocused. This attenuation will only depend on the phase dispersion cause by random motion during and between the gradient pair shown in Fig. 3-5. In section 3.2.3, we argued that a system of spins diffusing freely in a linear magnetic field gradient is ergodic. Independent of location, the attenuation is therefore given by

$$A = \int_{-\infty}^{\infty} e^{i\Phi} \Pr(\Phi)\, d\Phi = \exp\left[\frac{-\sigma_\Phi^2}{2}\right] = \exp\left[-bD\right] \tag{3.35}$$

where we have used Eqs. (3.8) and (A.26) for the evaluation of the integral.

Clearly, we only need to know the variance of the phase distribution to calculate the diffusion attenuation, A. We will now use the MC algorithm to calculate the

variance of the phase distribution for the sequence shown in Fig. 3-5. We will ignore the slice selection gradient which is usually much smaller in amplitude and shorter in duration than the diffusion gradients. Obviously, minimum of three time steps are needed for this sequence: the first gradient pulse $\Delta t_1 = \delta$, the separation of the gradients $\Delta t_2 = \Delta - \delta$, and the second gradient pulse $\Delta t_3 = \delta$.

Any initial location can be chosen for the spin and to simplify the calculations we make it the origin, i.e. $X_0 = 0$. This makes the initial static precession $\phi_s = 0$. After the first time step the spin will be located at $X_1 = x_1$. It is most convenient to denote the conditional phase correction $\phi_{|x}$ by $\gamma\delta G x_1/2 + \Delta\phi_1$ where $\Delta\phi_1$ is the trajectory dependent part of the phase. Therefore, $\Phi_1 = \gamma\delta G x_1/2 + \Delta\phi_1$. At the start of the second time step the spin is located at X_1, but since no gradient is on, the only phase change occuring is due to the inversion pulse, i.e. $\Phi_2 = -\Phi_1$ and $X_2 = X_1 + x_2$. In the third time step, it has to be remembered to include the static precession: $\Phi_3 = \Phi_2 + \gamma\delta G X_2 + \gamma\delta G x_3/2 + \Delta\phi_3$. By substituting the values for Φ_2 and X_2 this becomes

$$\Phi_3 = \gamma G\delta(x_1/2 + x_2 + x_3/2) - \Delta\phi_1 + \Delta\phi_3 \tag{3.36}$$

Notice that because of the refocusing pulse, we get $x_1/2$ instead of $3x_1/2$ in the expression for Φ_3. This can be referred to as partial refocusing. As mentioned in section 3.2.3, the phase dispersion resulting from $\Delta\phi_1$ and $\Delta\phi_3$ is irreversible. This is because these are two independent random variables.

Now the only thing left is to evaluate the variance of Φ_3. This done by using Eqs. (3.6) and (3.17)[2]

$$\begin{aligned} \mathrm{var}(\Phi_3) &= \gamma^2 G^2\delta^2 \mathrm{var}(x_1/2 + x_2 + x_3/2) + \mathrm{var}(\Delta\phi_1) + \mathrm{var}(\Delta\phi_3) \\ &= 2\gamma^2 D G^2\delta^2(\Delta - \delta/3) \end{aligned} \tag{3.37}$$

From Eq. (3.35), it is clear that the b-factor is given by

$$b = \gamma^2 G^2\delta^2(\Delta - \delta/3) \tag{3.38}$$

In practice, the gradient amplifiers will have a finite slew rate. It is possible to use Eqs. (A.24) and (A.25), derived for ramped gradients, to calculate the b-factor in such situations. These calculations are however much more elaborate since they involve seven time steps instead of three as in the previous analysis. Because of this, we only give the final result

$$b = \gamma^2 G^2 \left[\delta^2(\Delta - \delta/3) + \frac{8a^3}{15} - \frac{7a^2\delta}{6} + \delta^2 a + a^2\Delta - 2\Delta\delta a\right] \tag{3.39}$$

[2]It is important to realize, that since x_1, x_2, and x_3 represent the particle displacement and not the location, they are independent random variables.

Here, a denotes the duration of the gradient's attack and decay periods. By comparing Eqs. (3.38) and (3.39), the error from using Eq. (3.38) can be calculated. This error can easily be made insignificant (less than 0.5%) for the ratio of a/δ as large as 0.2, if the gradients are separated by Δ and it is ensured that their area is equal to $G\delta$.

3.4.2 Effective and Anisotropic Diffusion

Until now, we have only considered diffusion in one-dimension. For isotropic medium such as liquids, the extension to three-dimensions is trivial. However, in liquid crystals or tissues such as brain white matter and skeletal muscle, the diffusion can no longer be considered isotropic because of membrains and other tissue mechanism. Because of restrictions, the diffusivity will actually depend upon position, i.e. heterogeneous at a cellular length scale. Often such a system can be modeled on macroscopic or image voxel length scale as homogeneous but anisotropic. It must be kept in mind, however, that the diffusion attenuation can then no longer accurately be described in terms of a single b-factor because the duration of the NMR pulse sequence will become important.

The Apparent Diffusion Coefficient

A highly revealing example is the case when molecular motion is confined to one-or two-dimensional local elements as discussed in ref. [16]. These elements have r.m.s length of λ and are interconnected such that the diffusion particle migrates from one randomly oriented element to another, hence tracing out a random walk in the laboratory frame. This is different from regular free self-diffusion because of the lack of branch points. In the free diffusion random walk model it is the time which determines the number of random variables a_i in Eq. (3.1). In this situation, however, it is the displacement due to free diffusion within the elements, x, which determines the number of randomly oriented elements each particle has passed through. The time (N) should therefore be replaced by the r.m.s. displacement according to Eq. (3.6) in section 3.2.1. Similarly, the instantaneous displacement ξ should be replaced by the length of the elements, λ. The expected number of elements passed is $N = x/\lambda = \sqrt{2Dt}/\lambda$. The mean square displacement in the laboratory frame is then

$$\overline{R^2} = \lambda^2 N = 2Dt/N = \lambda\sqrt{2Dt} \tag{3.40}$$

If we compare this with Eqs. (3.3) and (3.6), we see that the mean square displacement is no longer proportional to the time t but the square root of the time. A key factor for this result is that there are no branch points.

If the diffusing molecule has a choice of paths after moving N elements, comprising mean square distance R^2 in the laboratory frame over a time τ, the motion can be

considered as Brownian motion on macroscopic scale. However, the effective diffusion coefficient will be different from the diffusion coefficient of the free molecules within the elements. According to Eq. (3.5)[3], the effective diffusion coefficient should be $R^2/6\tau$. By using Eq. (3.40) to express R^2 and equating $t = \tau$ we get

$$D_{\text{eff}} = (2D\tau/N)/6\tau = \frac{D}{3N} \tag{3.41}$$

It is clear from the previous discussion, that the geometrical structure of the tissue will determine the effective diffusion coefficient. Also, the attenuation of the NMR signal will depend on the finite duration of the gradient pulses [5, 11, 109] and if there are multiple compartments with different diffusion coefficients and relaxation parameters, the situation get even more complex [120]. It is therefore necessary to define the term "apparent diffusion coefficient" from the NMR diffusion attenuation, A, and the b-factor as

$$A = \exp\left[-b \cdot \text{ADC}\right] \tag{3.42}$$

Anisotropic Diffusion

The influence of anisotropic diffusion can easily be studied with the Bloch-Torrey equation (Eq. (2.5)) [117,126]. Here, however, we show how anisotropic diffusion can be understood from the random walk model presented in section 3.2.1.

Consider the definition of the displacement, x, in Eq. (3.1)

$$x = \xi_x \sum_{i=1}^{N} a_i \tag{3.43}$$

where $a_i \in (-1, 1)$ are independent discrete zero mean random variables. From this definition and the definition of $D_{xx} = \xi_x^2/2\tau$ and $t = N\tau$, it is straight forward to show that

$$\overline{x(t_1)x(t_2)} = \overline{\xi_x^2 \left(\min(t_1, t_2)\right)/\tau} = 2D_{xx}\min(t_1, t_2) \tag{3.44}$$

Similarly we define

$$y = \xi_y \sum_{i=1}^{N} b_i \tag{3.45}$$

where $b_i \in (-1, 1)$ are independent discrete zero mean random variables. However, we will assume that b_i and a_i are correlated and the correlation coefficient is denoted by c. For instance, if particles collide with permeable membranes that are tilted with respect to the principal axes of the coordinate system, the particle displacements in orthogonal

[3]The number 2 has to be replaced by 6 because the mean square displacement is 3 times larger in three-dimensions than in one-dimension.

directions will be correlated. Analogous to Eq. (3.44), the correlation between x and y becomes

$$\overline{x(t_1)y(t_2)} = \overline{c\xi_x\xi_y \left(\min(t_1,t_2)\right)/\tau} = 2D_{xy}\min(t_1,t_2) \tag{3.46}$$

where we have defined $D_{xy} = c\xi_x\xi_y/2\tau$. From this definition follows reciprocality, i.e. $D_{xy} = D_{yx}$.

Now consider the phase dispersion of anisotropic diffusion in linear magnetic field gradients. For mathematical simplicity, we will replace the discrete Larmor equation in Eq. (3.2) with its continuous counterpart

$$\phi(t) = \int_0^t \gamma(G_x(\tau)x(\tau) + G_y(\tau)y(\tau))d\tau \tag{3.47}$$

The variance of $\phi(t)$ is expressed as[4]

$$\begin{aligned}
\sigma_\phi^2(t) &= \overline{\int_0^t \gamma(G_x(\tau')x(\tau')+G_y(\tau')y(\tau'))\,d\tau' \cdot \int_0^t \gamma(G_x(\tau'')x(\tau'')+G_y(\tau'')y(\tau''))\,d\tau''} \\
&= \int_0^t\int_0^t \gamma^2 G_x(\tau')G_x(\tau'')\overline{x(\tau')x(\tau'')}\,d\tau'd\tau'' \\
&\quad + 2\int_0^t\int_0^t \gamma^2 G_x(\tau')G_y(\tau'')\overline{x(\tau')y(\tau'')}\,d\tau'd\tau'' \\
&\quad + \int_0^t\int_0^t \gamma^2 G_y(\tau')G_y(\tau'')\overline{y(\tau')y(\tau'')}\,d\tau'd\tau''
\end{aligned} \tag{3.48}$$

We have yet to specify the shape of the gradients. If the time course of the gradients is specified, the expectation value of the integrals in Eq. (3.48) can be calculated by using Eqs. (3.44) and (3.46). However, for the pulsed gradient spin echo (PGSE) sequence shown in Fig. 3-5, we already know from Eq. (3.37), that the first term in Eq. (3.48) yields $2\gamma^2 D_{xx}G_x^2\delta^2(\Delta - \delta/3)$. By inspection of Eq. (3.48), it should be obvious that the total phase variance is given by

$$\sigma_\phi^2 = 2\gamma^2\delta^2(\Delta - \delta/3)\left[G_x^2 D_{xx} + G_y^2 D_{yy} + 2G_xG_yD_{xy}\right] \tag{3.49}$$

This can be written in a more general form for three-dimensions in terms of the diffusion attenuation, A, as

$$\ln(A) = -\gamma^2\delta^2(\Delta - \delta/3)\ \mathbf{GDG}^T \tag{3.50}$$

where $\mathbf{D}$ is the diffusion tensor

$$\mathbf{D} = \begin{bmatrix} D_{xx} & D_{xy} & D_{xz} \\ D_{yx} & D_{yy} & D_{yz} \\ D_{zx} & D_{zy} & D_{zz} \end{bmatrix} \tag{3.51}$$

[4]The mean of ϕ is obviously zero.

Similarly, in the spirit of Eq. (3.7), the probability distribution for the diffusion displacement $\mathbf{r} = \hat{x}x + \hat{y}y + \hat{z}z$ can be written as

$$\Pr(\mathbf{r}, t) = \frac{1}{\sqrt{(2\pi \cdot 2t)^3 |\mathbf{D}|}} \exp\left[\frac{-\mathbf{r}\ \mathbf{D}^{-1}\ \mathbf{r}^T}{2 \cdot 2t}\right] \tag{3.52}$$

The diffusion tensor is a symmetric matrix. It follows from a fundamental theorem in linear algebra, that there exist a coordinate transformation which diagonalizes the diffusion tensor

$$\mathbf{D}' = \mathbf{U}^{-1}\ \mathbf{D}\ \mathbf{U} = \begin{bmatrix} D_{x'} & 0 & 0 \\ 0 & D_{y'} & 0 \\ 0 & 0 & D_{z'} \end{bmatrix} \tag{3.53}$$

The columns of $\mathbf{U}$ are the eigenvector of $\mathbf{D}$. The new primed coordinates are related to the laboratory coordinates by $\mathbf{r}' = \mathbf{U}^{-1}\mathbf{r}$. The nonzero elements of $\mathbf{D}'$ are the eigenvalues of $\mathbf{D}$ and the largest eigenvalue represents the principal direction of the diffusion. In the laboratory frame, this direction is given by the eigenvector which corresponds to the particular eigenvalue. Because the trace of the diffusion tensor is independent of the choice of coordinate system, by calculating ADC-trace maps, the dependance of tissue orientation in the magnet is removed.

Chapter 4

MRI Noise Characteristics

4.1 Introduction

IN this chapter we will review the theoretical distributions for the noise in magnitude images and then we supplement it with the exact expression for the noise distribution in phase images as well. A very simple post-processing scheme is proposed to correct for the bias due to the Rician distribution of the noisy magnitude data. The statistical properties of the correction scheme are studied and compared to a similar correction scheme for power images, proposed earlier independently by Miller and Joseph [85] and McGibney and Smith [81].

Noise can influence both the accuracy and the precision of parameters that are estimated from MR images, such as the diffusion coefficient. Therefore, the problem of fitting exponential curves is studied for both high and low signal-to-noise ratios.

4.2 Theory

Magnitude images are most common in MRI since they avoid the problem of phase artifacts by deliberately discarding the phase information. The signal is measured through a quadrature detector which gives the real and the imaginary signals. We will assume the noise in each signal to have a Gaussian distribution with zero mean and each channel will be assumed to be contaminated with white noise.

The real and the imaginary images are reconstructed from the acquired data by the complex Fourier transform. Since the Fourier transform is a linear and orthogonal transform, it will preserve the Gaussian characteristics of the noise. Furthermore, the variance of the noise will be uniform over the whole field of view and, due to the Fourier transform, the noise in the corresponding real and imaginary voxels can be assumed uncorrelated.

There are many factors which influence the final signal-to-noise ratio (SNR) in the real and the imaginary images. Not only is the noise associated with the receiving coil resistance, but also with inductive losses in the sample [61]. Which one is the dominant source will depend on the static magnetic field (B_0) and the sample volume size. Furthermore, the final image noise will depend on the image voxel size, the receiver bandwidth (BW) and the number of averages in the image acquisition. By using similar arguments as Edelstein *et al.* [31], one can write

$$\mathrm{SNR} \propto \frac{B_0^2}{\sqrt{B_0^2 + \alpha\sqrt{B_0}}} \cdot V \cdot \sqrt{\frac{\mathrm{NEX}}{N_x \cdot N_y \cdot \mathrm{BW}}} \tag{4.1}$$

where α is a factor whose size depends on the sample size [31], V is the slice volume, NEX is the number of excitations used for averaging, and N_x and N_y are the resolution in the readout and phase direction, respectively. Equation (4.1) can be used to compare the relative SNR in two 2D imaging experiments with the same relaxation parameters, repetition (TR) and echo time (TE). If the sampling time and the total imaging time are kept constant, Eq. (4.1) shows that the SNR is proportional to the image voxel volume[1].

4.2.1 Magnitude Images

The magnitude images are formed by calculating the magnitude, pixel by pixel, from the real and the imaginary images.

$$M = \sqrt{(I_r + n_r)^2 + (I_i + n_i)^2} \tag{4.2}$$

I_r and I_i are the pixel values of the real and the imaginary images and n_r and n_i are the corresponding noise components. The noise is assumed to be Gaussian with zero mean and variance σ^2. This is a nonlinear mapping and therefore the noise distribution in M is no longer Gaussian.

The image pixel intensity in the absence of noise is denoted by A and the measured pixel intensity by M. In the presence of noise, the probability distribution for M can be shown to be given by [70, 108]

$$p_M(M) = \frac{M}{\sigma^2} e^{-(M^2+A^2)/2\sigma^2} I_0\left(\frac{A \cdot M}{\sigma^2}\right) \tag{4.3}$$

where I_0 is the modified zeroth order Bessel function of the first kind. This is known as the *Rice* density and is plotted in Fig. 4-1 for different values of the SNR, A/σ.

[1] If the resolution is increased by a factor of two in both directions while keeping the signal sampling time and the total imaging time constant, the bandwidth has to be doubled and it is only possible to average half as much as before.

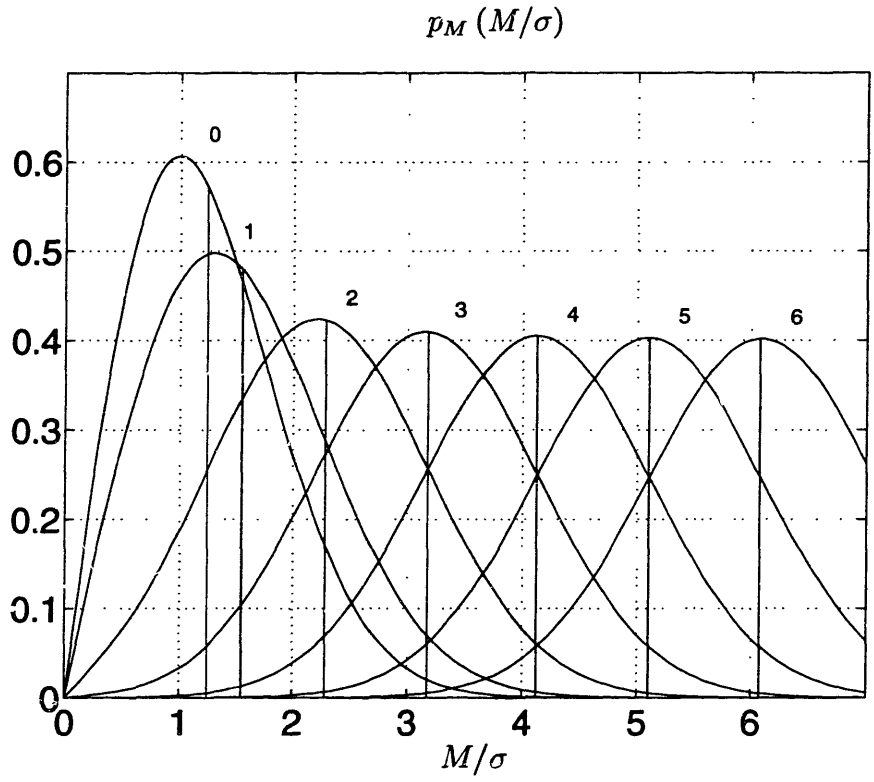

Figure 4-1: The Rician distribution of M for several signal to noise ratios, A/σ, and the corresponding means.

As can be seen the Rician distribution is far from being Gaussian for small SNR ($A/\sigma \leq 1$). For ratios as small as $A/\sigma = 3$, however, it starts to approximate the Gaussian distribution.

Note that the mean of the distributions, $\overline{M}/\sigma$, which is shown by the vertical lines in Fig. 4-1 is not the same as A/σ. This bias is due to the nonlinear transform of the noisy data.

A special case of the Rician distribution is obtained in image regions where only noise is present, $A = 0$. This is better known as the *Rayleigh* distribution and Eq. (4.3) reduces to

$$p_M(M) = \frac{M}{\sigma^2} e^{-M^2/2\sigma^2} \tag{4.4}$$

This Rayleigh distribution governs the noise in image regions with no NMR signal. The mean and the variance for this distribution can be evaluated analytically and are given by [98]

$$\overline{M} = \sigma\sqrt{\pi/2} \quad \text{and} \quad \sigma_M^2 = (2 - \pi/2)\sigma^2 \tag{4.5}$$

These relations can be used to estimate the "true" noise power, σ^2, from the magnitude

image. Another interesting limit of Eq. (4.3) is when the SNR is large.

$$p_M(M) \approx \frac{1}{\sqrt{2\pi\sigma^2}} e^{-\left(M-\sqrt{A^2+\sigma^2}\right)^2/2\sigma^2} \tag{4.6}$$

This equation shows that for image regions with large signal intensities the noise distribution can be considered as a Gaussian distribution with variance σ^2 and mean $\sqrt{A^2+\sigma^2}$. This trend is clearly seen for large ratios, A/σ, in Fig. 4-1.

4.2.2 Phase Images

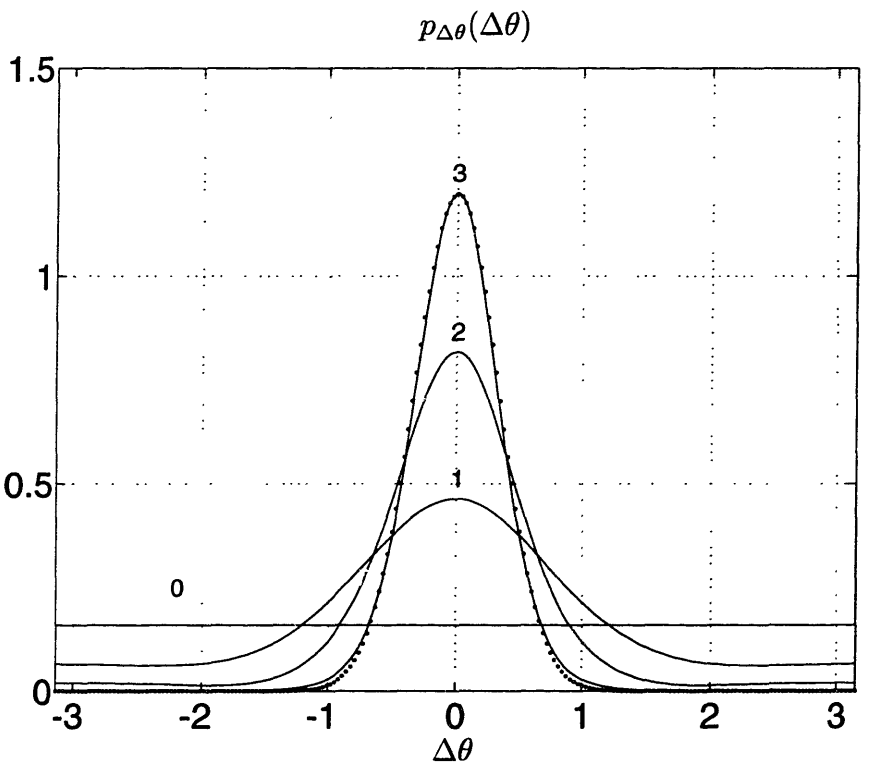

Figure 4-2: The distribution of the phase noise for several signal to noise ratios, A/σ. The Gaussian approximation is shown with a dotted line for A/σ = 3.

Phase images, which are commonly used in flow imaging, are reconstructed from the real and the imaginary images by calculating pixel by pixel the arctangent of their ratio. This is a nonlinear function and therefore we no longer expect the noise distribution to be Gaussian. Indeed, the distribution of the phase noise, $\Delta\theta = \theta - \overline{\theta}$,

is given by [70]

$$p_{\Delta\theta}(\Delta\theta) = \frac{1}{2\pi}e^{-A^2/2\sigma^2}\left[1+\frac{A}{\sigma}\sqrt{2\pi}\cos\Delta\theta\; e^{A^2\cos^2\Delta\theta/2\sigma^2}\cdot\frac{1}{\sqrt{2\pi}}\int_{-\infty}^{\frac{A\cos\Delta\theta}{\sigma}} e^{-x^2/2}\,dx\right] \tag{4.7}$$

Although the general expression for the distribution of $\Delta\theta$ is complicated, the two limits of A, $A = 0$ and $A \gg \sigma$, turn out to yield simple distributions.

In image regions where there is only noise, $A = 0$, Eq. (4.7) reduces to

$$p_{\Delta\theta}(\Delta\theta) = \begin{cases} \frac{1}{2\pi} & \text{if } -\pi < \Delta\theta < \pi \\ 0 & \text{otherwise} \end{cases} \tag{4.8}$$

This result is obvious since the complex data, which only consists of the noise, "points in all directions" with the same probability.

For large SNR, $A \gg \sigma$, it is easy to see that the deviation in the phase angle, $\Delta\theta$, due to the noise will be small. The integral in Eq. (4.7) will therefore be close to 1 and the second term in the brackets will therefore dominate the constant 1. Equation (4.7) therefore reduces to

$$\begin{aligned} p_{\Delta\theta}(\Delta\theta) &\approx \frac{A\cos\Delta\theta}{\sigma\sqrt{2\pi}}\exp\left[\frac{-A^2(1-\cos^2\Delta\theta)}{2\sigma^2}\right] \\ &\approx \frac{1}{\sqrt{2\pi(\sigma/A)^2}}\exp\left[\frac{-\Delta\theta^2}{2(\sigma/A)^2}\right] \end{aligned} \tag{4.9}$$

The noise distribution in the phase angle can therefore be considered as a zero mean Gaussian distribution, when $A \gg \sigma$. This result is not surprising because when the pixel intensity is large, all deviations parallel to the complex pixel intensity can be ignored. Also the phase variations, due to the noise which is orthogonal to the complex pixel intensity, can be linearized as σ/A, where σ represents the orthogonal part of the noise.

The standard deviations for the phase noise can in general be calculated by using Eq. (4.7), however, for the two special cases in Eqs. (4.8) and (4.9) it is given by

$$\sigma_{\Delta\theta} = \begin{cases} \frac{\sigma}{A} & \text{if } A \gg \sigma \\ \sqrt{\frac{\pi^2}{3}} & \text{if } A = 0 \end{cases} \tag{4.10}$$

Figure 4-2 shows the distribution in the phase noise, evaluated by Eq. (4.7), for several signal to noise ratios. The Gaussian approximation is also shown by the dotted line

for $A/\sigma = 3$. Clearly the Gaussian approximation is very good even for fairly small signal-to-noise ratios.

Phase images are sometimes weighted by the magnitude data, in order to reduce phase variations in regions with no signal. The general noise distribution for such images is nontrivial. For regions with large SNR one can show that the distribution approaches a Gaussian distribution whose standard deviation is σ.

4.3 Bias Reduction in Magnitude Data

For large SNR Eq. (4.6) shows that the mean of M is not the true image intensity A, but approximately $\sqrt{A^2+\sigma^2}$. This is a small deviation for large SNR, however, when the SNR is small this bias has to be considered. We will continue to approximate the mean by the simple expression $\sqrt{A^2+\sigma^2}$ for all SNR, but for an exact analytical evaluation of the mean of Eq. (4.3) see refs. [10, 108]. Figure 4-1 shows the mean of the Rician distribution for several values of A/σ plotted as a straight vertical line. Henkelman suggested a look-up table correction scheme to correct for this bias [58]. We suggest a much simpler correction scheme.

To reduce the bias the following post-processing correction scheme is suggested:

$$\tilde{A} = \sqrt{|M^2 - \sigma^2|} \tag{4.11}$$

The probability distribution for the corrected signal, $\tilde{A}$, is then given by

$$p_{\tilde{A}}\left(\tilde{A}\right) = \begin{cases} \frac{\tilde{A}\cdot p_M(\sqrt{\sigma^2+\tilde{A}^2})}{\sqrt{\sigma^2+\tilde{A}^2}} + \frac{\tilde{A}\cdot p_M(\sqrt{\sigma^2-\tilde{A}^2})}{\sqrt{\sigma^2-\tilde{A}^2}} & \text{if } \tilde{A} < \sigma \\ \frac{\tilde{A}\cdot p_M(\sqrt{\sigma^2+\tilde{A}^2})}{\sqrt{\sigma^2+\tilde{A}^2}} & \text{if } \tilde{A} \geq \sigma \end{cases} \tag{4.12}$$

where p_M is defined by Eq. (4.3). The distribution of $\tilde{A}$ is shown in Fig. 4-3 for several signal-to-noise ratios. We see that the bias is greatly reduced, however, the corrected distribution is not Gaussian. For ratios of $A/\sigma > 2$ the corrected distribution is however very close to being a Gaussian. Table 4.1 lists the mean and the standard deviation of the corrected and uncorrected distributions.

A different, but somewhat similar, correction scheme has been proposed for power images, independently by Miller and Joseph [85] and McGibney and Smith [81], to perform quantitative analysis on low SNR images and as an unbiased SNR estimate respectively. It is interesting to compare this with our correction scheme, described above.

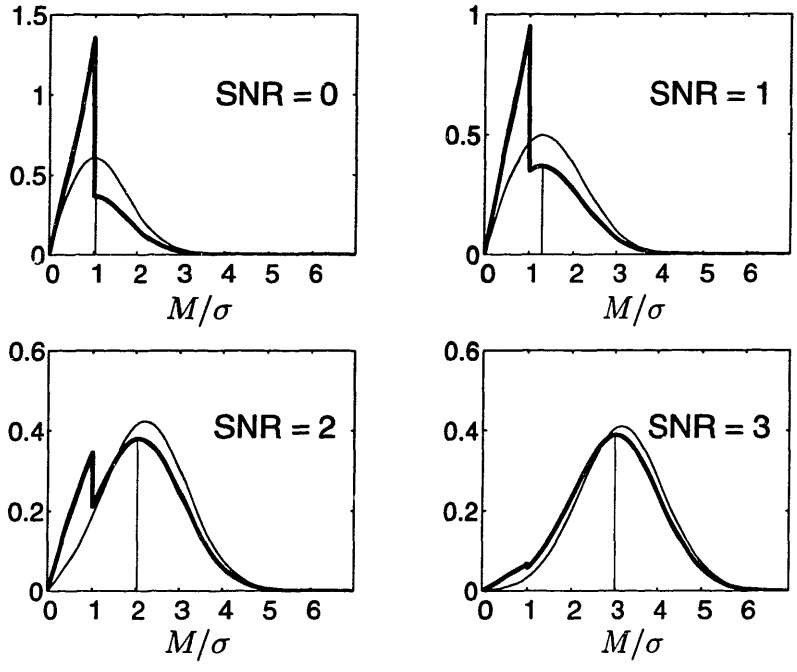

Figure 4-3: The distribution of the corrected pixel intensity, $\tilde{A}$ (bold), compared with the Rician distribution of M for several signal-to-noise ratios. The mean of the corrected distribution, $\overline{\tilde{A}}$, is shown with a vertical line.

Their correction scheme is based on the simple relationship between the mean of the measured power and the true image power, namely $\overline{M^2} = A^2 + 2\sigma^2$ [58,85]. Their correction scheme is therefore simply

$$\tilde{A}^2 = M^2 - 2\sigma^2 \tag{4.13}$$

We have found that the resulting distribution for the corrected power, $\tilde{A}^2$, is given by

$$p_{\tilde{A}^2}(\tilde{A}^2) = \frac{1}{2\sigma^2} e^{-(\tilde{A}^2+2\sigma^2+A^2)/2\sigma^2} I_0\left(\frac{A \cdot \sqrt{\tilde{A}^2 + 2\sigma^2}}{\sigma^2}\right) \tag{4.14}$$

The mean of $\tilde{A}^2$ gives an unbiased estimate of A^2. We have calculated the variance of $\tilde{A}^2$ and found it to be given by

$$\sigma^2_{\tilde{A}^2} = 4A^2\sigma^2 + 4\sigma^4 \tag{4.15}$$

Figure 4-4 shows the distribution of M^2 and $\tilde{A}^2$ as the original and the corrected image power respectively. The distributions are clearly far from being Gaussian at low SNR

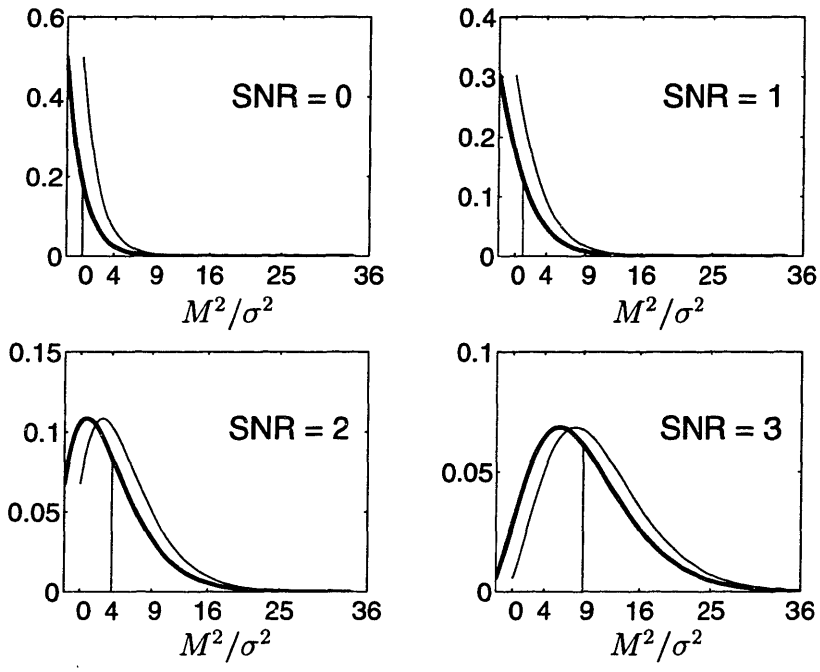

Figure 4-4: The distribution of the corrected pixel power, $\tilde{A}^2$ (bold), compared with the distribution of the measured power, M^2, for several signal-to-noise ratios. The mean of the corrected distribution, $\overline{\tilde{A}^2} = A^2$, is shown with a vertical line.

although their mean is always the true mean, A^2. This can lead to some ambiguities, when information is extracted from corrected power data, since least-squares fitting techniques, such as nonlinear chi-square minimization, assume Gaussian deviation which is fully characterized by its standard deviation. For large SNR, however, one can show that the distribution for $\tilde{A}^2$ becomes approximately a Gaussian distribution of $\sqrt{\tilde{A}^2}$ with a mean A^2 and variance given by Eq. (4.15). The variance dependence on the power strength is an issue which has to be taken into account, for accurate fitting. Unlike ours, their correction scheme, originally proposed to fit mono-exponentials [85], cannot be used when the signal has a multi-exponential nature. Finally, analysis based on statistics from a region of interest will be sensitive to any variations in A, because the mean of the distribution is a function of A^2.

4.4 Fitting Exponential Curves

In section 3.4 it is shown that for spin echo, the diffusion related attenuation can be described in terms of an exponential decay curve, i.e. $\exp(-bD)$. Similarly, the free

A/σ	$\overline{\tilde{A}}/\sigma$	$\sigma_{\tilde{A}}/\sigma$	$\overline{M}/\sigma$	σ_M/σ
0	1.03	0.35	1.25	0.43
0.5	1.10	0.42	1.33	0.48
1	1.30	0.59	1.55	0.60
1.5	1.61	0.79	1.87	0.73
2	2.03	0.96	2.27	0.84
2.5	2.50	1.04	2.71	0.90
3	3.00	1.07	3.17	0.93

Table 4.1: Some statistical properties of the Rician distribution and the correction scheme for several signal-to-noise ratios.

induction decay due to transverse relaxation can be modeled as $\exp(-t/T_2)$. Therefore, it is of great importance in MRI to accurately estimate data from exponential decay curves. Because of its simplicity and the availability of fast algorithms, linear least-squares is the most commonly used technique for fitting data with Gaussian measurement noise. We will therefore only focus on this particular technique.

4.4.1 High Signal-to-Noise Ratio

In the following discussion, it is assumed that the measured signal decay can be described by a mono-exponential

$$y'_m = M \exp(-b_m D) + n'_m \tag{4.16}$$

where y'_m denotes the measured signal, b_m is the m'th b-factor applied and n'_m is the measurement noise which variance is σ^2. Also, M is the signal strength measured with zero diffusion sensitivity. To cast this into a linear least-square problem, the logarithm is applied on both sides

$$y_m \approx \ln M - b_m D + \frac{n'_m}{M \exp(-b_m D)} = C - b_m D + n_m \tag{4.17}$$

This first order Taylor approximation is good if the signal variations due to noise are small, i.e. sufficient SNR. Clearly, the noise, n_m, has no longer fixed variance, σ^2. When many measurements are taken, it is more convenient to write Eq. (4.17) in vector notation

$$\mathbf{y} = \mathbf{B}\,[C \;\; D]^T + \mathbf{N} \tag{4.18}$$

where

$$\mathbf{B} = \begin{bmatrix} 1 & -b_1 \\ \vdots & \vdots \\ 1 & -b_m \end{bmatrix} \tag{4.19}$$

By defining $\mathbf{x} = [C \;\; D]^T$ the weighted least-square solution can be written as [42]

$$\begin{aligned} \tilde{\mathbf{x}} &= \left(\mathbf{B}^T\mathbf{W}\mathbf{B}\right)^{-1}\mathbf{B}^T\mathbf{W}\mathbf{y} \\ &= \mathbf{P}\mathbf{y} \end{aligned} \tag{4.20}$$

where $W_{ii} = \exp(-b_i \cdot D)$ and the off-diagonals are zero. The matrix $\mathbf{P}$ is referred to as the pseudo-inverse.

Multiple b values

The diffusive attenuation is often measured with b-values distributed evenly from the minimum b-factor to the maximum b-factor. It is interesting to consider the case when three measurements are taken with $b_1 = b_{\text{min}}$, $b_2 = (b_{\text{min}} + b_{\text{max}})/2$, and $b_3 = b_{\text{max}}$. According to Eq. (4.20), the diffusion estimate is given by

$$\tilde{D} = \frac{[1 \;\; 0 \;\; -1]}{b_{\text{max}} - b_{\text{min}}}\,\mathbf{y} \tag{4.21}$$

Therefore, the second measurement has no affect on the estimated diffusion coefficient. A better estimate, with smaller variance, is obtained if the second b-factor is b_{max}. In general, with multiple b-factor the measurements from the center b-values influence the diffusion estimate much less than the measurements taken with b-values close to b_{min} and b_{max}. Also, as shown in Eq. (4.17), the log-transformed noise is higher in data points of measurements taken with high b-values. Hence, it is more important to average those measurement than those taken with low b-values.

Two b values

Time constraints often limit the number of possible measurements. It is important to choose the b-factor such that the estimate of the diffusion coefficient is as precise as possible. Consider the case when only two measurements are taken with b_1 and b_2. Clearly it is always optimal to choose the lower b-value as small as possible, i.e. $b_1 = 0$. The second b-factor should be chosen such that the variance of $\tilde{D}$ is as small as possible. From Eq. (4.20), the estimate is given by

$$\tilde{D} = \frac{[1 \;\; -1]}{b}\,\mathbf{y} \tag{4.22}$$

where $b = b_2 - b_1$. The variance is therefore given by

$$\begin{aligned} \mathrm{var}\left\{\tilde{D}\right\} &= \frac{\mathrm{var}\{y_1\} + \mathrm{var}\{y_2\}}{b^2} \\ &= \frac{\sigma^2 + \exp(2bD)\sigma^2}{M^2 b^2} \end{aligned} \tag{4.23}$$

Solving for the minimum gives

$$\frac{\partial\left(\mathrm{var}\left\{\tilde{D}\right\}\right)}{\partial b} = 0 \implies bD\exp(2bD) = 1 + \exp(2bD) \tag{4.24}$$

The solution to this equation shows that $b_{\mathrm{opt}} \approx 1.1/D$. This expression does not take into account the T_2 relaxation of the signal. Because of the finite gradient strength, the echo time needs to be long enough to fit in the diffusion gradients. From Eq. (3.38) it is clear, that the minimum echo time is given by

$$\mathrm{TE} = \left(\frac{3b}{2\gamma^2 G_{\max}^2}\right)^{1/3} \tag{4.25}$$

If the transverse relaxation is known, it is easy to use a computer simulation to estimate the precision of $\tilde{D}$ (σ_D) in a two point log-linear least-square fit. Similarly, the relative precision, σ_D/D, can be estimated. Since the optimal b-factor is a function of the diffusion coefficient, it is more logical to use a range of diffusion coefficients. The figure of merit is then defined as the average precision of the diffusion coefficients in the specified range. We set the range to be: $0.1\,\mu\mathrm{m}^2/\mathrm{ms} < D < 1\,\mu\mathrm{m}^2/\mathrm{ms}$. Three different relaxation parameters, which can be expected in white and gray brain tissue, were used in the simulation. Also, two maximum gradient amplitudes were tried, 1G/cm and 1.5G/cm. The results are shown in Fig. 4-5. The optimal b-factor is clearly close to $1000\,\mathrm{s/mm}^2$, however, it is also obvious that by using a b-factor larger than $500\,\mathrm{s/mm}^2$, one gets precision which is very close to the optimal precision.

4.4.2 Low Signal-to-Noise Ratio

When the SNR is low, the analysis in previous section does not apply. This is because the logarithm is a nonlinear function and the first order approximation is no longer accurate. The nonlinearity of the logarithm in combination with the measurement noise introduces bias into the data, y_m. Furthermore, the original magnitude data, y'_m, is biased because of the Rician distribution. Hence, the diffusion estimate in Eq. (4.20) will be a biased estimate of the diffusion.

Averaging can be used to minimize the noise. However, averaging does not eliminate the bias. Here, the correction schemes studied in section 4.3 will be analyzed

in combination with a *two-point* log-linear least-square fit and data averaging. The following four schemes will be compared:

I: $\tilde{D} = [0\ \ 1]\,\mathbf{P}\ln(\overline{\mathbf{y}})$, i.e. estimate D from the average of the data points.

II: $\tilde{D} = [0\ \ 1]\,\mathbf{P}\ \overline{\ln(\mathbf{y})}$, i.e. estimate D as the average of the independent noisy estimates.

III: $\tilde{D} = [0\ \ 1]\,\mathbf{P}\ln\left(\ \overline{\sqrt{|\mathbf{y}^2 - \sigma^2|}}\ \right)$, i.e. correct for the Rician bias using Eq. (4.11), then average, and finally estimate D using the logarithm.

IV: $\tilde{D} = [0\ \ 1]\,\mathbf{P}\ln\left(\ \overline{\mathbf{y}^2 - 2\sigma^2}\ \right)/2$, i.e. use power data and correct for the Rician bias using Eq. (4.13), then average, and finally estimate D using the logarithm.

A computer simulation is used to compare these four schemes. Without of loss of generality, D and b are defined such that $D = 1$ and $bD = 1$. The data $\mathbf{y}$ is then defined such that $y_1 = \sqrt{(1 + n_{1r})^2 + n_{1i}^2}$ and $y_2 = \sqrt{(\exp(-bD) + n_{2r})^2 + n_{2i}^2}$ where n_{1r}, n_{2r}, n_{1i}, and n_{2i} are zero mean Gaussian random variables with variance σ^2. The signal-to-noise is then defined from the smaller data point, i.e. $\sigma = \exp(-bD)/\mathrm{SNR}$. In this way, both y_1 and y_2 have Rician distribution.

For each of the estimation schemes, the bias or the accuracy of D is defined as $\tilde{D} - 1$ and the precision of the estimate as the standard deviation of $\tilde{D}$. The results are shown in Fig. 4-6 for different number of averages and as a function of the SNR. It is clear, that all these schemes give very similar results for SNR$>$ 3. For very low SNR, SNR$<$ 2, scheme I is clearly worst because of the strong bias it produces. When only four data points are averaged, scheme II and III are the best because they combine low bias and high precision. Although scheme IV has the smallest bias for SNR$<$ 1, it gives very unprecise estimate. This is in good agreement with Eq. (4.15) which shows, that for low SNR the relative variance is larger in power images than in magnitude images. This variance is then emphasized by the singularity of the logarithmic function. However, if 256 data points are averaged, scheme IV yield almost an unbiased estimate in accordance with section 4.3. Most surprising is the similarity between the results obtained with schemes II and III. One might even speculate whether they yield identical results in the limit of infinite averages. No attempt will be made here to prove this hypothesis. Scheme II and III provide good compromise between accuracy and precision for few averages. Scheme II, however, is much simpler and it does not require a prior estimate of the noise, σ. It is as if the bias from the Rician distribution is in part opposed by the bias from the logarithmic function. Also, the bias in the Rician distribution avoids the singularity of the logarithmic function.

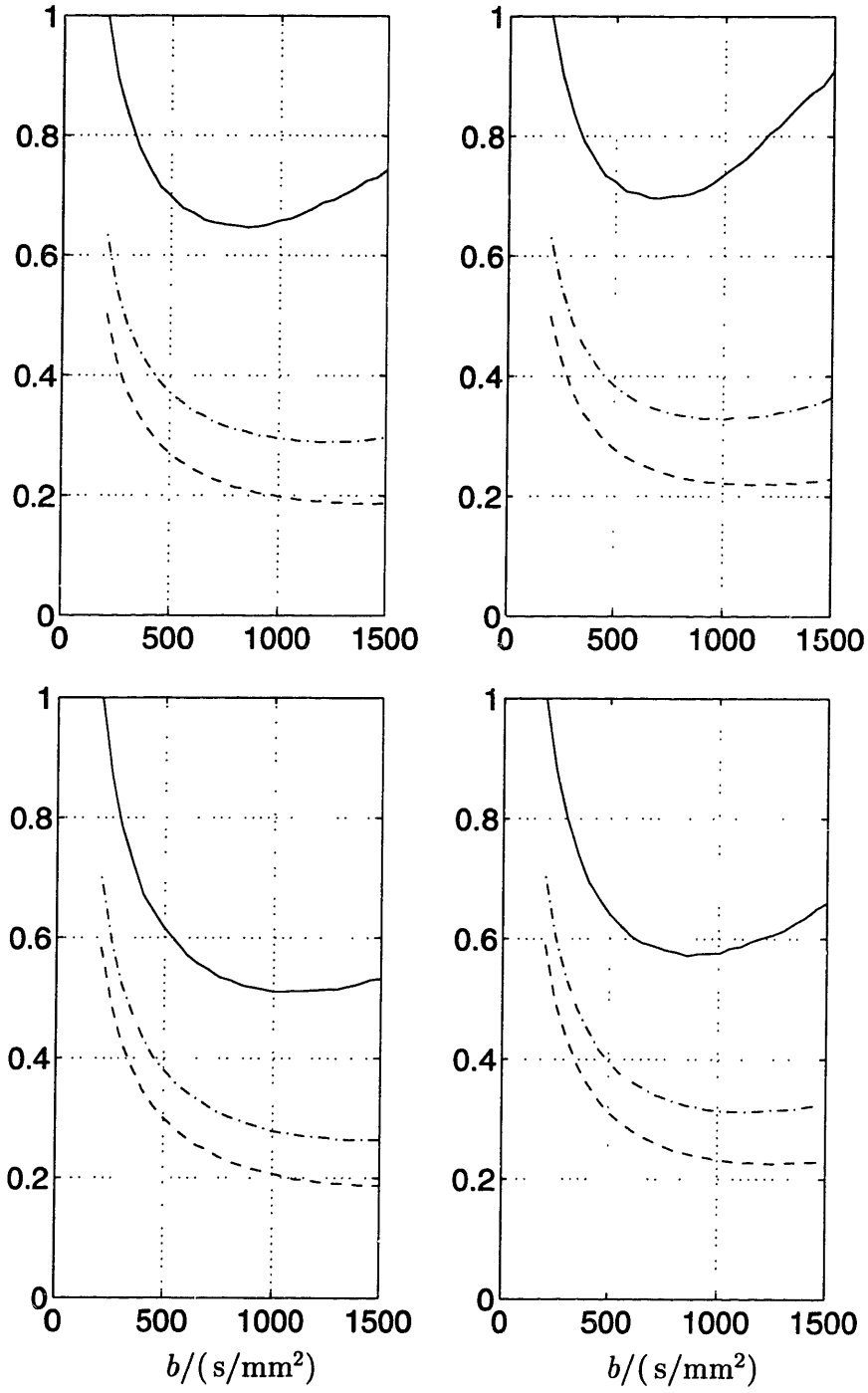

Figure 4-5: Left: The average precision, σ_D. **Right:** The average relative precision, σ_D/D. Averages taken over the range $0.1\,\mu\mathrm{m}^2/\mathrm{ms} < D < 1\,\mu\mathrm{m}^2/\mathrm{ms}$. **Above:** $G_{\max} = 1\mathrm{G/cm}$. **Below:** $G_{\max} = 1.5\mathrm{G/cm}$. The solid line is for $T_2 = 50\mathrm{ms}$, the dot-dashed line is for $T_2 = 75\mathrm{ms}$, and the dashed line is for $T_2 = 100\mathrm{ms}$. The curves have been normalized by the maximum value of the dashed line because their actual value is noise dependent.

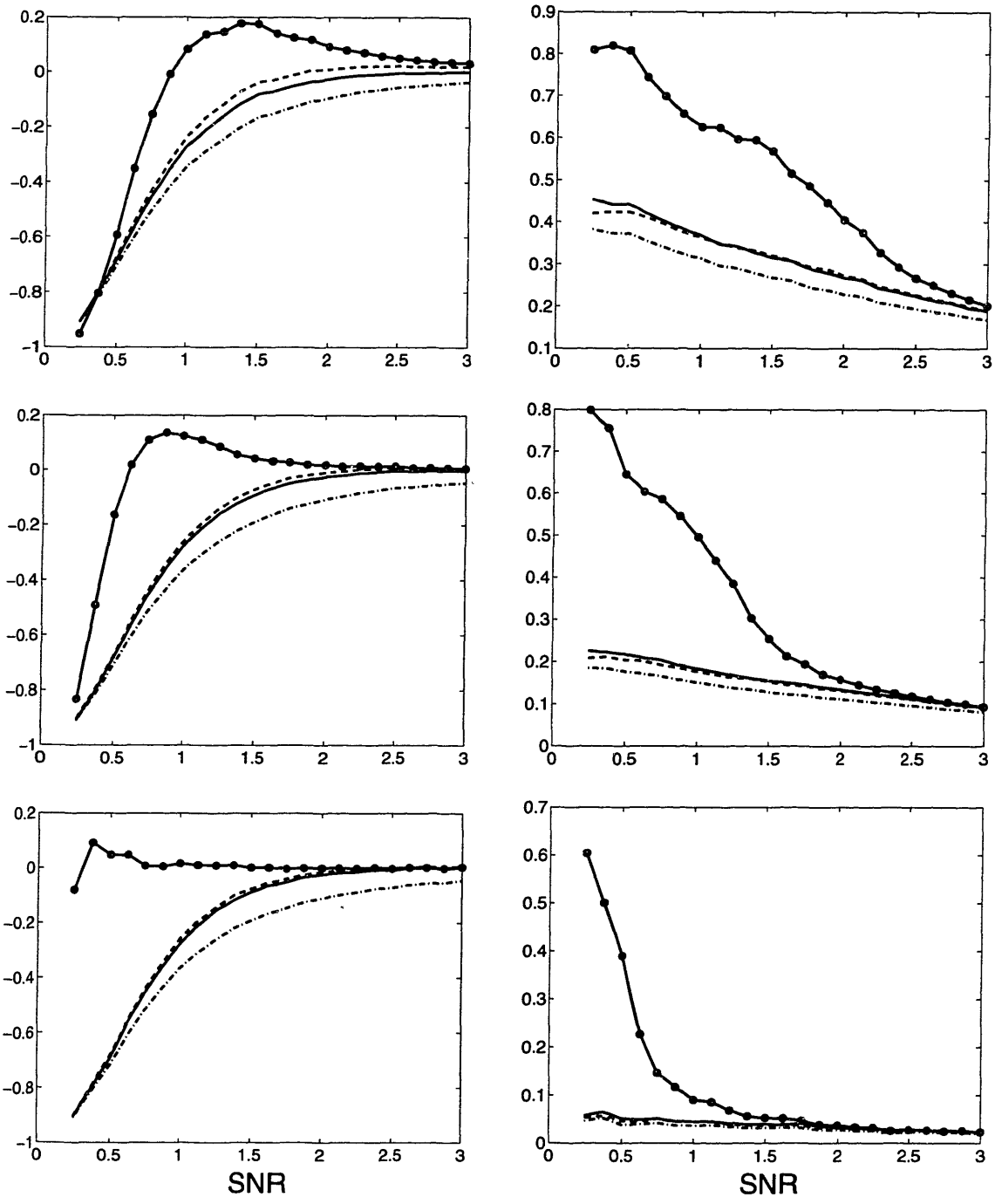

Figure 4-6: Comparing four schemes for log-linear least-squares fitting of exponential data curves as a function of SNR. **Left:** accuracy (bias) and **right:** precision. Scheme I (dash dotted), II (solid), III (dashed), IV (solid circles). **Top:** Four averages, **middle:** 16 averages, and **bottom:** 256 averages.

4.5 Artificial Diffusion Weighting

As shown in chapter 7, it can be useful to enhance the contrast between healthy tissue and ischemic tissue by using a large b-factor. Often the maximum practical b-factor is limited by the hardware. Also, when time constraints limit the number of b-factors to two, the b-factor should be chosen such that optimal estimate of the ADC-trace map is obtained as discussed in section 4.4.1. However, a higher b-factor may be preferred in order to allow for improved visualization of the lesion on the diffusion weighted image.

After having obtained an estimate of the diffusion, $\tilde{D}$ (or the ADC-trace), it is easy to calculate what the image should look like with arbitrary diffusion weighting b by

$$\tilde{I}(b) = I(0) \cdot \exp(-b\tilde{D}) \tag{4.26}$$

It is interesting to consider the relative noise in $\tilde{I}(b)$, i.e. $\Delta\tilde{I}(b)/\tilde{I}(b)$. If we assume that $\tilde{D}$ is estimated from two measurements with b-values of zero and b_e and that the noise variance in each of these measurements is σ^2, then it is relatively easy to show that

$$\text{std}\left\{\tilde{I}(b)\right\} = \sigma\sqrt{\left(\frac{b}{b_e}+1\right)^2 + \left(e^{b_e D}\frac{b}{b_e}\right)^2}e^{-bD} \tag{4.27}$$

In particular, if the diffusion sensitivity is doubled, then

$$\frac{\Delta\tilde{I}(2b_e)}{\tilde{I}(2b_e)} = \frac{\Delta I(b_e)}{I(b_e)}\sqrt{9+4e^{2b_e D}}e^{-b_e D} \tag{4.28}$$

Therefore, the relative noise increase is in the range from 2 to $\sqrt{13}$ depending on the choice of b_e. Obviously, it is preferable to measure the data with as large b-factor as possible, if artificial diffusion weighting is used because a large $b_e D$ minimizes the noise increase.

A different way to double the diffusion sensitivity is to square the image data. It follows directly from Eq. (4.15), that the relative noise in such power image is twice as large as in the original magnitude image[2]. A drawback to this approach is that it also enhances the T_2 weighting. Furthermore, in this way, it is not possible to weight the data by the trace of the diffusion tensor.

[2]Assuming a good signal-to-noise ratio, i.e. $A \gg \sigma$.

Chapter 5

SSFP Flow and Diffusion Sensitivity

5.1 Introduction

THE steady-state free precession (SSFP) imaging pulse sequence has for long been known for its high sensitivity to flow [102] and diffusion. The diffusion sensitivity of SSFP has been thoroughly investigated [17,65,74,84,146] whereas the sensitivity to both flow and diffusion simultaneously has previously only been studied experimentally [49,53,83]. One of the reasons is, that the approach used by Kaiser *et al.* to obtain a closed form solution for the diffusion sensitivity is not feasible when bulk flow is added to the model. In this chapter we use a partition analysis (PA) to obtain an approximate analytical solution for the simultaneous sensitivity of SSFP to both flow and diffusion. Our approach parallels that of Buxton [15], however, includes the flow as well as the diffusion and is a fourth order instead of a second order approximation. The simulation technique derived in chapter 3 is then use for cases where the PA is inaccurate as well as simulation of pulsatile flow.

The flow sensitivity of SSFP was first described by Patz *et al.* [102] in terms of a gradient dependent scale invariant parameter. Patz [100, 101] also showed how it is possible to suppress the signal from static spins and make the steady-state signal more sensitive to slowly moving spins by using the moving reference frame (MRF) technique. The MRF method was later used by Tyszka *et al.* [129–131] to image very slow fluid flow. The flow sensitivity of SSFP has been used for fast imaging of cerebrospinal fluid motion [63] and has also been applied in the study of renal microcirculation. A strong correlation was shown to exist between the signal in a missing pulse SSFP sequence (MP-SSFP) [103], which has a flow sensitivity similar to the SSFP sequence, and the perfusion rate in kidney [119].

Because SSFP is very sensitive to diffusion and has relatively short acquisition times, it has been proposed for diffusion imaging [26,74] as an alternative to method

such as echo planar imaging (EPI), which require specialized hardware, and to the pulsed gradient spin echo (PGSE) method [117].

The aim here is to analyze the sensitivity of SSFP to both bulk flow and diffusion. It is important to understand this simplified problem in order to gain understanding of more complicated situations that are to be expected *in vivo*. Understanding of the flow sensitivity is also essential in order to maximize or minimize the flow attenuation in SSFP imaging [125, 152].

5.2 Theory

Steady-state free precession (SSFP) sequences involve the application of a stream of RF pulses separated by a time interval, TR, which is less than the time it takes the magnetization to reach its thermal equilibrium. One cycle from a general SSFP imaging pulse sequence is shown in Fig. 5-1. This sequence acquires both the FID and the echo, however, it is also possible to acquire higher order echoes.

The Bloch-Torrey equation can be solved easily for the free induction decay which results after applying a single RF pulse [118]. For a series of RF pulses, like in SSFP, it turns out to be easier to analyze the dynamics of a magnetization located at a specific point in space. The magnetization vector represents an ensemble of spins located in the same region and is usually called an isochromat.

5.2.1 The Steady State of an Isochromat

By assuming that the RF pulses are instantaneous, relaxation can be neglected during the pulse. The dynamics of the isochromat are then described by a RF rotation, precession, and relaxation. Figure 5-2 shows a discrete state model of the Bloch equation for SSFP, where the time increments are TR. The magnetization vector just before the application of the RF pulse (echo) is denoted by $\mathbf{M}^-$ and just after the RF pulse (FID) by $\mathbf{M}^+$. Furthermore, we let α denote the flip angle, $E_1 = \exp(-\mathrm{TR}/T_1)$ and $E_2 = \exp(-\mathrm{TR}/T_2)$. The precession angle is obtained from the Larmor equation (Eq. (2.15)), $\phi = \gamma \mathbf{G}_{\mathrm{eff}}\, \mathbf{r}\mathrm{TR}$ where we define $\mathbf{G}_{\mathrm{eff}}$ as the average gradient strength and $\mathbf{r}$ as the location of the isochromat

$$\mathbf{G}_{\mathrm{eff}} = \frac{1}{\mathrm{TR}} \int_0^{\mathrm{TR}} \mathbf{G}(t)\, dt \tag{5.1}$$

The longitudinal relaxation, $(1 - E_1)$, can be considered as a discrete input to the system, because we are only interested in solving for $\mathbf{M}^+$ and $\mathbf{M}^-$. It is important to realize, that this discrete system is linear and when neither flow nor diffusion is present, its response is also time invariant. Due to relaxation, this system is stable and does therefore reach a steady state.

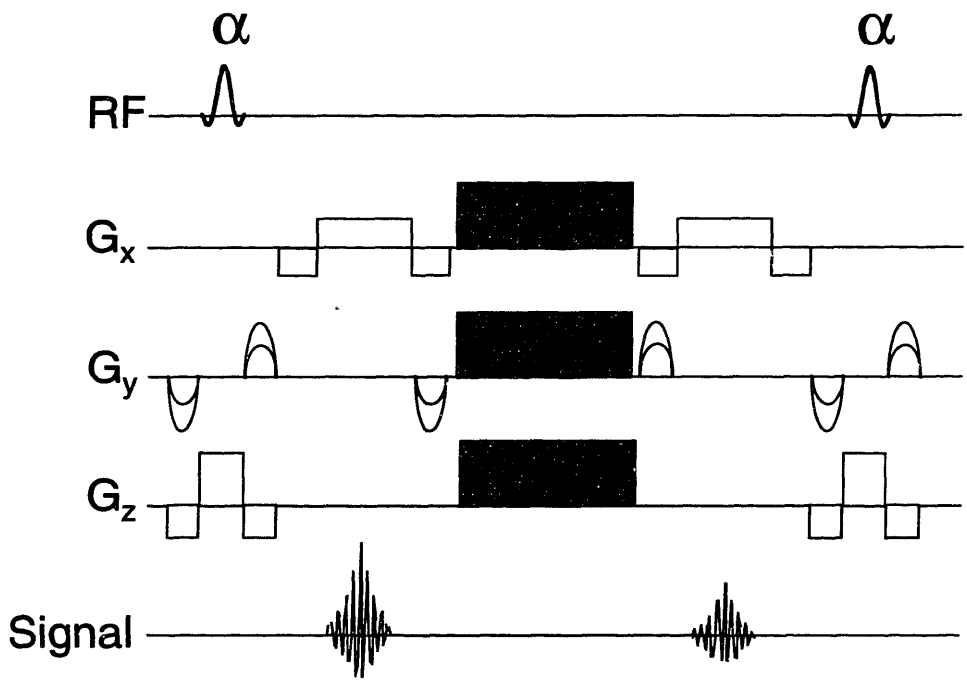

Figure 5-1: An SSFP pulse sequence with flow and diffusion sensitivity in all directions. The effective gradient, which determines the diffusion sensitivity, has to be kept constant in each SSFP cycle to establish a steady state. This is accomplished by rewinding the phase encoding gradient, which amplitude varies from cycle to cycle.

Given the condition of a steady state we can relate $\mathbf{M}^+$ and $\mathbf{M}^-$ by using Eqs. (2.9) and (2.13)

$$\begin{aligned} \mathbf{M}^- &= \mathbf{P}\,\mathbf{M}^+ + \hat{z}(1-E_1)M_0 \\ \mathbf{M}^+ &= \mathbf{R}\,\mathbf{M}^- \end{aligned} \tag{5.2}$$

These two equations can easily be solved to give $\mathbf{M}^- = \mathbf{R}\,(\mathbf{I}-\mathbf{PR})^{-1}\,\hat{z}(1-E_1)M_0$ [34,43]. The expanded solution is given by

$$\begin{aligned} M_x^+ &= \frac{(1-E_1)E_2\sin\alpha\sin\phi}{(1-E_1\cos\alpha)(1-E_2\cos\phi)-(E_1-\cos\alpha)(E_2-\cos\phi)E_2} \\ M_y^+ &= \frac{(1-E_1)(1-E_2\cos\phi)\sin\alpha}{(1-E_1\cos\alpha)(1-E_2\cos\phi)-(E_1-\cos\alpha)(E_2-\cos\phi)E_2} \\ M_z^+ &= \frac{(1-E_1)(E_2(E_2-\cos\phi)+(1-E_2\cos\phi)\cos\alpha)}{(1-E_1\cos\alpha)(1-E_2\cos\phi)-(E_1-\cos\alpha)(E_2-\cos\phi)E_2} \end{aligned} \tag{5.3}$$

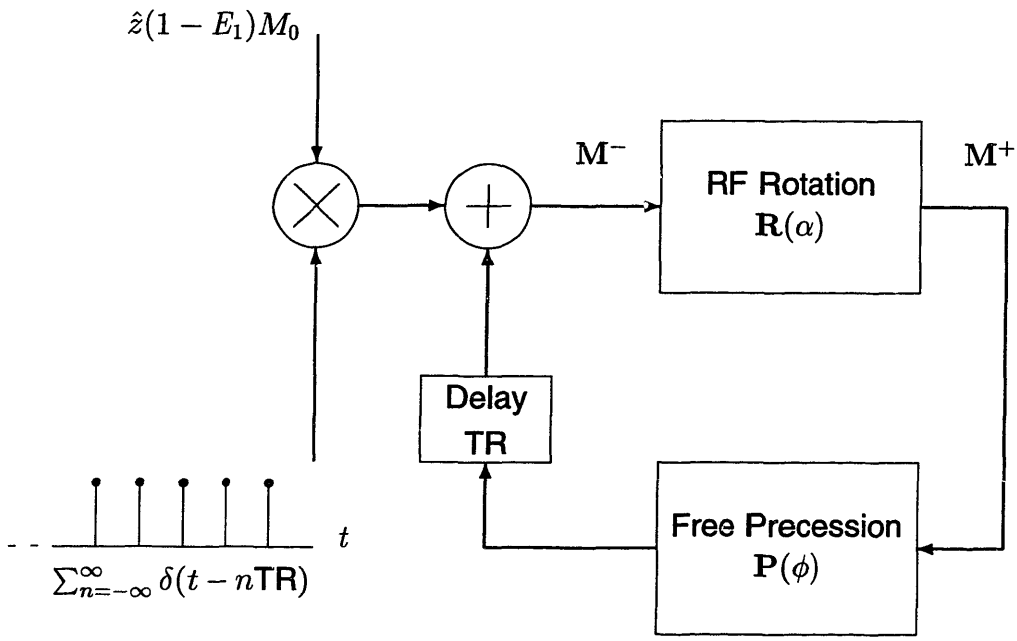

Figure 5-2: Discrete-State model for the Bloch Equation in SSFP. Spin-lattice relaxation can be considered as an input, entering the spin system just before each RF excitation.

The steady-state solution has a much simpler form in the complex notation

$$m_{xy}^{+} = M_0 \frac{ae^{-i\phi} + b}{c\cos\phi + d} \tag{5.4}$$

where

$$\begin{aligned} a &= -(1-E_1)E_2\sin\alpha, \\ b &= (1-E_1)\sin\alpha, \\ c &= E_2(E_1-1)(1+\cos\alpha), \\ d &= 1 - E_1\cos\alpha - (E_1-\cos\alpha)E_2^2 \end{aligned} \tag{5.5}$$

The echo is then calculated as

$$m_{xy}^{-} = m_{xy}^{+}E_2 e^{i\phi} \tag{5.6}$$

In linear gradients, the steady state has a periodic spatial dependence due to its dependence on ϕ. The wavelength, λ, is defined by

$$\lambda\gamma|\mathbf{G}_{\text{eff}}|\text{TR} = \lambda|\mathbf{k}_{\text{eff}}| = 2\pi \tag{5.7}$$

The magnetization will reflect the proton density, $\rho(\mathbf{r})$, modulated with the steady state periodic spatial dependence. Due to the periodicity of the magnetization it can be written as a Fourier series

$$m_{xy}^{+}(\mathbf{r},t) = \rho(\mathbf{r})\exp\left[-t/T_2 + i\mathbf{k}(t)\cdot\mathbf{r}\right]\sum_{n=-\infty}^{\infty} A_n e^{in\mathbf{k}_{\text{eff}}\cdot\mathbf{r}} \tag{5.8}$$

where $t \in (0, \text{TR})$ and $\mathbf{k}(t)$ is given by Eq. (2.16).

Equation (5.8) shows that in an SSFP imaging sequence, the pixel intensity will be influenced by the local magnetic field through the precession angle. Remedies to this problem have been suggested and are commonly used in practice. They involve adjusting the effective gradient such that an integer number of SSFP wavelengths exist within each image voxel [111]. The average FID signal per voxel is then given by

$$\overline{m_{xy}^{+}} = A_0 = \frac{1}{2\pi}\int_0^{2\pi} M_0 \frac{ae^{-i\phi}+b}{c\cos\phi + d}\,d\phi = M_0\left(\frac{a}{c} + \left(\frac{b}{d} - \frac{a}{c}\right)\frac{1}{\sqrt{1-m^2}}\right) \tag{5.9}$$

where $m = -c/d$. General expressions for the coefficients, A_n, in the absence of diffusion and flow can be found in ref. [152] and a solutions which includes diffusion can be found in ref. [65, 146]. In absence of both flow and diffusion the solution is given by

$$A_n = \frac{1}{2\pi}\int_0^{2\pi} M_0 \frac{ae^{-i(n+1)\phi} + be^{-in\phi}}{c\cos\phi + d}\,d\phi \tag{5.10}$$

In particular

$$A_{-1} = M_0\left(\frac{b}{c} + \left(\frac{a}{d} - \frac{b}{c}\right)\frac{1}{\sqrt{1-m^2}}\right) \tag{5.11}$$

and for any n we get [152]

$$\begin{aligned} A_{n+1} &= \frac{1-\sqrt{1-m^2}}{m}A_n, \qquad n \geq 0 \\ A_{n-1} &= \frac{1-\sqrt{1-m^2}}{m}A_n, \qquad n \leq 0 \end{aligned} \tag{5.12}$$

5.2.2 Static Magnetic Field Inhomogeneity Effects

The applied gradient is not solely responsible for precessing the spins and static magnetic field inhomogeneity cannot be neglected in a real imaging experiment. More importantly, one cannot control the phase evolution from static field inhomogeneities the way one controls the gradients. Immediately following the RF pulse the FID is in phase and then it dephases and vanishes as time increases. The echo signal, however, fully dephased initially after the RF pulse excitation will be in focus just before the next RF excitation, i.e. it dephases backwards in time. Because RF excitation and data acquisition cannot occur simultaneously, the gradients are used to refocus these signals at time points just after the RF excitation and before the RF excitation to read the FID and the echo, respectively. This is shown in Fig. 5-1. The time difference between the gradient echoes and the "natural" echo location determines the time interval in which phase evolution due to static inhomogeneities takes place.

Usually it is assumed, that when there is a distribution of static inhomogeneities within each image voxel, the contribution to the natural linewidth can be modeled as an increase in the transverse relaxation, i.e. $1/T_2^* = 1/T_2 + 1/T_2'$ where $1/T_2' = \gamma \Delta B_0/2$. If TE denotes the time from the RF pulse to the gradient echoes, it should be clear from previous discussion that the FID and the echo signals can be written as

$$m_{xy}^{+}(t) = M_0 \left(\frac{a}{c} + \left(\frac{b}{d} - \frac{a}{c} \right) \frac{1}{\sqrt{1-m^2}} \right) \exp\left[-\mathrm{TE} \left(\frac{1}{T_2} + \frac{1}{T_2'} \right) \right] \tag{5.13}$$

$$m_{xy}^{-}(t) = M_0 \left(\frac{b}{c} + \left(\frac{a}{d} - \frac{b}{c} \right) \frac{1}{\sqrt{1-m^2}} \right) \exp\left[\frac{-\mathrm{TE}}{T_2} - \frac{\mathrm{TR} - \mathrm{TE}}{T_2'} \right] \tag{5.14}$$

For a discussion of the effects of static magnetic field inhomogeneity on the higher order echoes see ref. [152].

5.2.3 Optimal Flip Angle

From Eqs. (5.4) and (5.6), we see that the steady-state is only a function of E_1 and E_2, but not T_2^*. Therefore, the flip angle which gives maximum signal[1] is only a function of TR, T_1 and T_2.

When the repetition time is long compared to T_2, i.e. $E_2 \approx 0$, the optimum flip angle for the FID is the *Ernst angle*

$$\alpha_{\mathrm{opt}} = \cos^{-1}(E_1) \tag{5.15}$$

[1] Ignoring flow and diffusion.

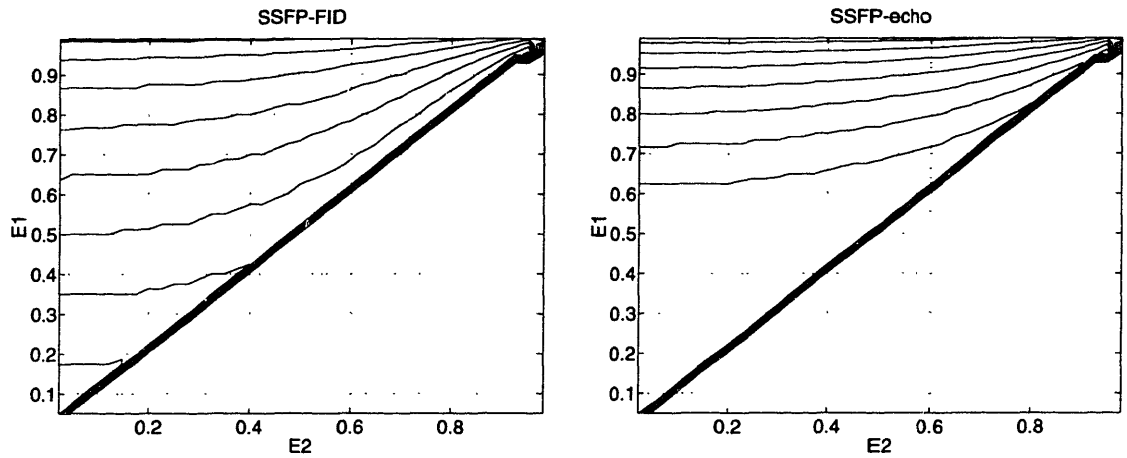

Figure 5-3: Optimum flip angle for SSFP-FID (GRASS) to **left** and SSFP-echo to **right**. Contours at 10°, 20°, ..., 80°. In the lower left corner the angle is 90°.

For the SSFP-FID and the SSFP-echo the relationship is more complex as shown by Fig. 5-3. The optimum flip angle for SSFP-FID at $E_2 = 0$ is however the Ernst angle.

5.2.4 Image Artifacts in SSFP Imaging

A subject related to the uniform pixel intensity is the separation between the FID and the echo as well as the higher order echoes. Several authors have considered this subject [54,67,86,151]; however, their mathematical analysis did not consider an inhomogeneous proton density. A much easier and more intuitive approach is to analyze the magnetization in k-space. Zur *et al.* [151] numerically evaluated the relation between the effective gradient and the readout gradient in order to have uniform pixel intensity. Their analysis is, however, only exact when physical parameters such as the proton density are uniform over the whole field of view. As shown in Eq. (5.8) the magnetization is modulated in space by the SSFP wavelength. The k-space information of the object will therefore be aliased over k-space due to convolution of the spatial frequencies of the object's proton density with the harmonics of the SSFP wave. The separation of these peaks will depend on the effective wavenumber, $\mathbf{k}_{\text{eff}}$, and the amplitude of the harmonics, A_n. Only when $\mathbf{k}_{\text{eff}}$ is two times larger than the highest spatial frequencies of the object, can the echoes be considered fully separated. Whether this is true will depend on the structure of the object. It is, however, always true that the larger the effective gradient, the better is the separation and uniformity of the pixel intensity. This, however, leads to larger flow and diffusion sensitivity as

we will show later.

Examples to clarify previous discussion are shown in Fig. 5-4. In Fig. 5-4a, an attempt is made to visualize the situation where the effective gradient is in the z-direction, i.e. through the rectangular slice profile. The Fourier transform of the slice profile is a sinc function. If the slice thickness is an integer number of SSFP wavelengths, λ_z, then the zeros of the sinc function are located precisely where the adjacent harmonics lie. When the slice is thick and the proton density is nonuniform, the sinc function has to be replaced with the spatial frequencies of the object convolved with a sinc. Hence, it is clear that the more SSFP wavelengths there exist within each image voxel the better separation of the echoes, i.e. more uniform pixel intensity. Figure 5-4b shows the case when the effective gradient is in the image plane. The arrows show how the gradients used in the SSFP pulse sequence in Fig. 5-1 direct the "travel" in k-space.

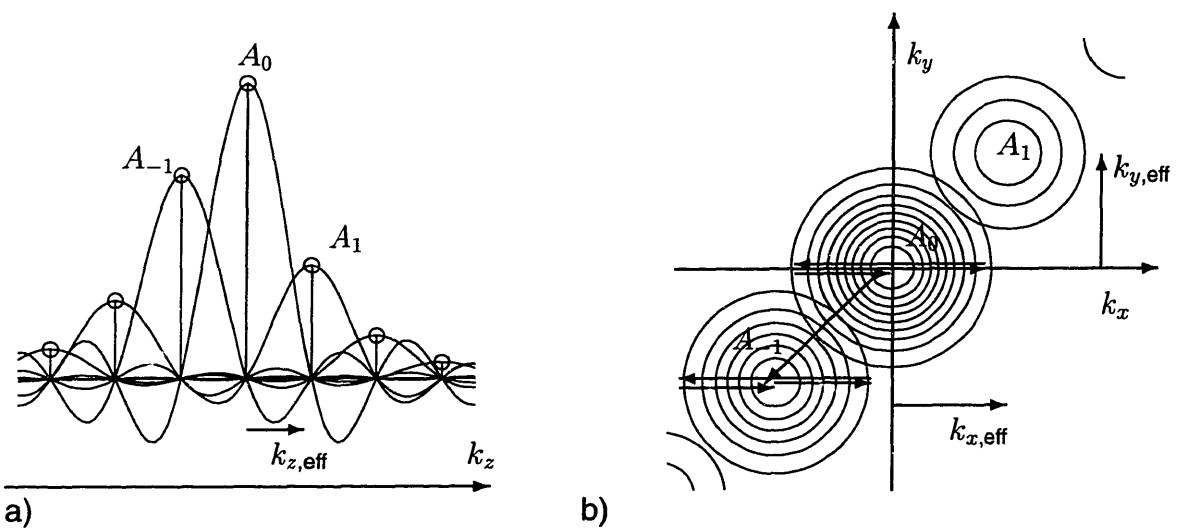

Figure 5-4: a) The harmonics of the magnetization convolved with the Fourier transform of the slice profile whose thickness is exactly λ_z. When the FID is acquired ($k_z(t) = 0$), the contribution from all the harmonics is zero except A_0. Similarly, A_{-1} is the only harmonic which contributes to the signal when $k_z(t) = k_{z,\text{eff}}$, i.e. during the acquisition of the echo. **b)** The aliasing of the objects spatial frequencies depends on $k_{x,\text{eff}}$ and $k_{y,\text{eff}}$ as well as the object itself. The trajectory in the k-space, shown here on top of the contour plot of the spatial frequencies, corresponds to the pulse sequence shown in Fig. 5-1 with no phase encoding.

It has been shown by Zur *et al.* [152], that it is possible to use phase cycling to separate the higher order echoes in SSFP when the effective gradient is small. This is desirable if one wants to reduce the flow sensitivity. Their method resembles the technique used in spectroscopy to select a particular quantum coherence order [115]. It is a subtraction technique that requires several acquisitions. The number of acquisitions is determined by the size of the harmonics, A_n. In practice, as few as 6 acquisitions are sufficient because both the magnetic field inhomogeneities and diffusion-related attenuation significantly reduce the amplitude of higher order harmonics.

5.2.5 Partition Analysis

We present in this section a partition analysis, which, despite being an approximation, provides good insight into the flow and diffusion sensitivity of SSFP. When either flow or diffusion is present, the previous analysis cannot be used because the precession angle of the isochromat will no longer be constant. Indeed, each isochromat will not reach a steady state. As we will show, the ensemble average of isochromats from a voxel with a uniform distribution of precession angles will still reach a steady state. To approximate the steady state, we exploit the fact that the discrete state model for an isochromat shown in Fig. 5-2 is linear. The response to each input impulse can therefore be found separately. Each three dimensional vector can be decomposed into a longitudinal and two transverse components. The input vectors are purely longitudinal but the RF pulses tilt them into the transverse plane. The precession then further decomposes the transverse part into two orthogonal transverse components. At the time when the RF pulses are applied, each of these three vector components are "fed back" and will be decomposed into three new components. This partition continues in each cycle and the number of components grows exponentially. The total contribution from each input vector, or its impulse response, can then be found by adding together all the vector components. It is difficult to keep track of all the components; however, it is easy to approximate the signal by limiting the number of "echo pathways". These echo pathways are shown schematically in Fig. 5-5. They represent the partition of each input vector into longitudinal and transverse components. The longitudinal components do not precess and are represented by horizontal lines; however, the transverse components that precess are represented by sloped lines. The slope indicates the precession of some particular isochromat and will depend on its location. During each longitudinal pathway the signal is attenuated by E_1 and by E_2 during each transverse pathway.

A fourth order approximation in E_2 of the signal strength can be calculated by adding together the signal from all echo pathways with no more than four transverse

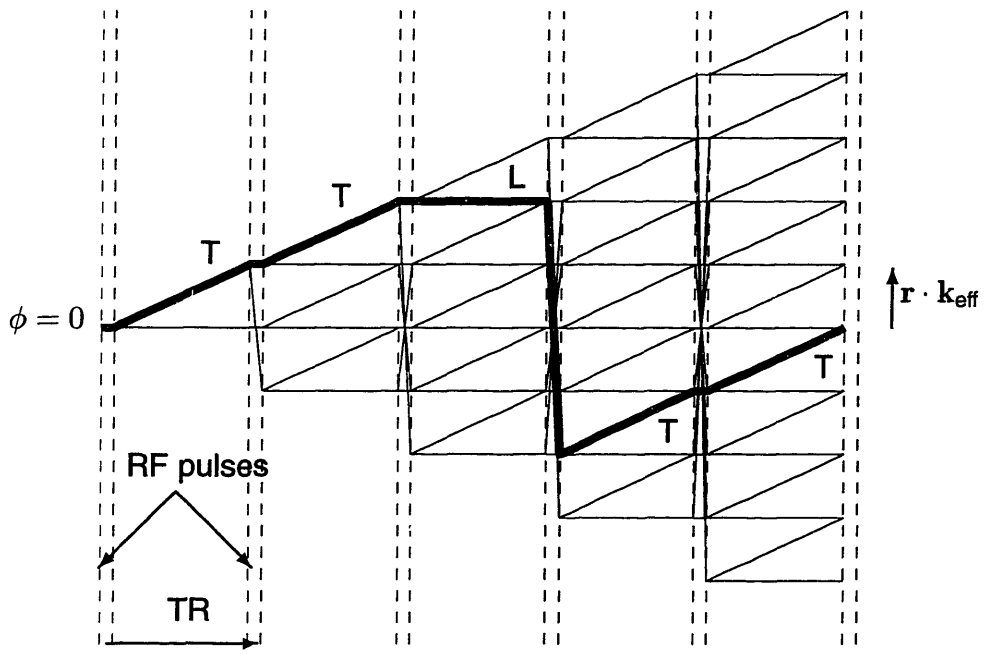

Figure 5-5: This diagram represents the partition of a single vector impulse that enters the system in Fig. 5-2. A particular pathway, TTLTT, is shown with a thicker line. Between the RF pulses the precession angle, ϕ, increases by $\mathbf{r} \cdot \mathbf{k}_{\text{eff}}$. The RF pulse splits each vector into three new vectors. Pathways that cross the zero phase line represent the parts of the original impulse magnetization vector whose phase is reduced to zero. Only those parts contribute to the echo.

pathways:

$$\begin{aligned} \mathrm{M}^- \approx\ & L\ldots LTT + L\ldots LTL\ldots LT \\ +\ & L\ldots LTTTT + L\ldots LTL\ldots LTTT \\ +\ & L\ldots LTTL\ldots LTT + L\ldots LTTTL\ldots LT \\ +\ & L\ldots LTL\ldots LTL\ldots LTT + L\ldots LTL\ldots LTTL\ldots LT \\ +\ & L\ldots LTTL\ldots LTL\ldots LT + L\ldots LTL\ldots LTL\ldots LTL\ldots LT, \end{aligned} \quad (5.16)$$

where $L\ldots L$ represents one or more consecutive longitudinal pathways. Note that we have ignored pathways with an odd number of transverse pathways because according to Fig. 5-5 they can never have zero phase and therefore do not contribute to the echo. An equivalent mathematical expression that proves this statement is Eq. (B.3). One of the reasons why we have chosen to calculate a fourth order partition approximation instead of a second order approximation is that it is more accurate for a wider range of T_2/TR ratios. But more importantly, the fourth order approximation reflects

the behavior of the steady-state signal as a function of E_2 whereas the second order approximation does not. In the second order approximation all the terms are proportional to E_2 and changes therefore only affect the overall amplitude. The fourth order approximation, however, gives more information such as the relation between E_2 and the RF flip angle.

The expression for each component can be found by repeatedly using Eqs. (2.13) and (2.9). Here we will only calculate the magnetization for one type of echo pathway. The calculations are quite tedious but are all "variations on the same theme". Here we will only consider contributions from all echoes of the type:

$$\underbrace{L\ldots L}_{n}T\underbrace{L\ldots L}_{m}T\underbrace{L\ldots L}_{l}T\underbrace{L\ldots L}_{k}T$$

This is the last term in Eq. (5.16). In presence of flow and diffusion, the precession angle will no longer be constant as in Fig. 5-5. The relation between the precession angles in consecutive cycles is given by

$$\phi(n) = \phi(n-1) + \gamma G_{\text{eff}}\,\text{TR}\,[v\text{TR} + \Delta x(n, D, \text{TR})] + \Delta\phi(n, D, G, \text{TR}) \qquad (5.17)$$

The terms in the bracket are the displacement of the isochromat due to the flow velocity, v, and the random variable Δx is due to the diffusion, D. The random variable $\Delta\phi(D, G, \text{TR})$ denotes an additional change in the precession angle, which depends on the shape of the gradient. If we assume the duration of the gradient is much shorter than the repetition time, this term can easily be ignored.

The expression for the x-component of the magnetization can now be written by using Eqs. (2.13) and (2.9).

$$\begin{aligned} M(n,m,l,k)_x &= M_0(1-E_1)(E_1\cos\alpha)^{n+m+l+k-3}E_1^3E_2^4\sin^7\alpha\Big[\\ &\quad \cos(\phi_1)\cos(\phi_2)\cos(\phi_3)\sin(\phi_4)\Big] \end{aligned} \qquad (5.18)$$

where $\phi_1, \ldots, \phi_4$ represent the precession angle of each transverse pathway. Note that the physical significance of this is that longer pathways are better preserved for smaller flip angles than for larger flip angles, because $\cos\alpha$ is closer to one.

As pointed out in a previous section, we are interested in the signal from a uniform distribution of precession angles. The probability distribution of all the random variations in the phase due to diffusion also has to be taken into consideration. The average value, which we represent by $\langle\ \rangle$, is therefore given by

$$\langle M\rangle = \frac{1}{2\pi}\int_0^{2\pi}\int_{-\infty}^{\infty}\int_{-\infty}^{\infty}\int_{-\infty}^{\infty} M(\phi_1,\phi_2,\phi_3,\phi_4)\,\text{Pr}(\phi_1,\phi_2,\phi_3,\phi_4)d\phi_4 d\phi_3 d\phi_2 d\phi_1 \qquad (5.19)$$

For free diffusion, the particle displacement has a Gaussian distribution and these integrals can therefore be evaluated analytically for Eq. (5.18). Unlike the case when only diffusion is present, the flow makes the x-component of Eq. (5.18) nonzero, because the precession angles $\phi_1, \ldots, \phi_4$ are no longer all equal. The details of the integration can be found in the Appendix.

One can assume, that in order to reach a steady state, the system has been excited by infinitely many longitudinal inputs. The transverse signal at any given time can be expressed by adding up all the pathways, from all previous inputs, which are in the transverse plane at the echo time. Hence, the final result for the x-component of the $L \ldots LTL \ldots LTL \ldots LTL \ldots LT$ pathways is given by

$$\begin{aligned}
\langle M_x \rangle = \sum_{n=0}^{\infty}\sum_{m=1}^{\infty}\sum_{l=1}^{\infty}\sum_{k=1}^{\infty} \langle M(n,m,l,k)_x \rangle = \\
M_0(1-E_1)\frac{1}{1-E_1\cos\alpha}E_1^3E_2^4\sin^7\alpha\Bigg[\\
+\frac{1}{8}\frac{A_D^4\left(\sin(4\Delta_v)-\sin(3\Delta_v)A_DE_1\cos\alpha\right)}{D_1^2(1-E_1\cos\alpha)} \\
-\frac{1}{8}\frac{A_DE_1\cos\alpha A_D^4\left(\sin(3\Delta_v)-\sin(2\Delta_v)A_DE_1\cos\alpha\right)}{D_1^2(1-E_1\cos\alpha)} \\
+\frac{1}{8}\frac{A_D^{12}\left(\sin(8\Delta_v)-\sin(6\Delta_v)A_D^4E_1\cos\alpha\right)}{D_1^2D_2} \\
-\frac{2}{8}\frac{A_DE_1\cos\alpha A_D^{12}\left(\sin(7\Delta_v)-\sin(5\Delta_v)A_D^4E_1\cos\alpha\right)}{D_1^2D_2} \\
+\frac{1}{8}\frac{A_D^2E_1^2\cos^2\alpha A_D^{12}\left(\sin(6\Delta_v)-\sin(4\Delta_v)A_D^4E_1\cos\alpha\right)}{D_1^2D_2}\Bigg]
\end{aligned} \tag{5.20}$$

where

$$\begin{aligned}
D_1 &= \left(1-2\cos(\Delta_v)A_DE_1\cos\alpha+A_D^2E_1^2\cos^2\alpha\right) \\
D_2 &= \left(1-2\cos(2\Delta_v)A_D^4E_1\cos\alpha+A_D^8E_1^2\cos^2\alpha\right)
\end{aligned} \tag{5.21}$$

and

$$\Delta_v = \gamma G_{\text{eff}}\, v\text{TR}^2 \qquad \text{and} \qquad A_D = \exp\left[-bD\right] \tag{5.22}$$

where $b = (\gamma G_{\text{eff}}\ \text{TR})^2\ \text{TR}$ is the commonly used diffusion factor.

We notice that the steady-state signal has a complex flow dependence and the diffusion attenuation factor, A_D, appears in many different powers. This is due to the fact that the signal is composed of many different pathways which have different time lengths. The flow dependence is obviously periodic since the flow velocity only enters through trigometric functions. This period can be found from the definition of Δ_v

and agrees with earlier definitions of a gradient dependent scale invariant parameter used to quantify the flow sensitivity of SSFP [101,102]. As expected, the x-component of the signal vanishes when no flow is present. The expression for the y-component resembles Eq. (5.20); however, the flow enters through cosines instead of sinusoids in the nominator. The contribution from the other types of pathways is calculated in exactly the same manner as we have just prescribed.

5.3 Computer Simulation

We did a computer simulation to verify the PA and to evaluate the flow sensitivity for large T_2/TR ratios, where the PA is inaccurate. It is desirable to have a fast simulation technique for SSFP since the magnetization has to form a steady state and that usually takes several RF cycles. When diffusion and flow are included in the simulation model, the conventional Monte Carlo (MC) and finite difference (FD) methods will usually be very slow [17].

Results from a MC simulation of SSFP in the presence of both diffusion and flow have been published earlier by Tyszka *et al.* [129, 131] but they only approximated the effect of diffusion by increasing the transverse relaxation [74]. Wu *et al.* [146] have shown that this approximation does not give the correct flip angle dependence of the diffusion sensitivity.

In chapter 3 we developed a new very fast simulation technique, which correctly simulates the diffusion and flow without sacrificing computation speed [48, 51]. This technique applies to any pulse sequence and is especially useful in simulating the SSFP sequence or other steady-state sequences such as the missing pulse steady-state (MP-SSFP) [103]. Not only does the simulation provide the steady-state value but it also shows how the magnetization evolves into the steady state.

5.3.1 Circular Convolution Method

From Eq. (3.22) we see that the dynamics of spins in the presence of free diffusion can be simulated correctly by first updating the magnetization using the Bloch equation for static spins and then convolving the magnetization with a diffusion propagator, which we call a *correction-kernel*, to account for the movements of the spins [51]. The correction-kernel is then easily modified to include the effects of bulk flow as well. For a constant magnetic field gradient during some time step Δt the correction-kernel is given by

$$c(x, G, \Delta t) = \frac{1}{\sqrt{2\pi \cdot 2D\Delta t}} \exp\left[\frac{-(x - v\Delta t)^2}{2 \cdot 2D\Delta t} - \frac{\gamma^2 G^2 D \Delta t^3}{12} + i\gamma G \frac{x + v\Delta t}{2} \Delta t\right] \tag{5.23}$$

As we know from Eq. (5.8), the magnetization is spatially periodic. We let λ denote the steady-state wavelength which we then discretize with N points. Then we define $m_{xy}[n,t]$ as the transverse magnetization at location $x = n\lambda/N$ at time t and similarly we define $m_z[n,t] = M_z(n\lambda/N, t)$. Although, generally speaking, the spins can diffuse further than one wavelength during the SSFP cycle, we only need to evaluate the magnetization in one wavelength. This is due to the fact that any magnetization which leaves a wavelength-long region from left equals the magnetization which enters from right and *vice versa*. Hence, it is possible to simulate free diffusion by using a N point circular convolution. Between the RF pulses, the simulation algorithm for the transverse magnetization is given by

$$m_{xy}[n, t + \mathrm{TR}] = \left(m_{xy}[n,t] \cdot e^{i2\pi n/N}\right) \textcircled{N} c[n, G_{\mathrm{eff}}, \mathrm{TR}] \cdot E_2 \tag{5.24}$$

The longitudinal magnetization is updated in the same manner but without any precession

$$m_z[n, t + \mathrm{TR}] = m_z[n,t] \textcircled{N} c[n, 0, \mathrm{TR}] \cdot E_1 + (1 - E_1)\, M_0 \tag{5.25}$$

As we showed in section 3.3.2, these calculations are exact for any large simulation time step Δt [51]. In conventional MC and FD methods, however, large simulation time steps cause incorrect phase integration or instability. In practice, both the magnetization and the correction-kernel have to be sampled in space with sufficient density to avoid any aliasing. If we assume the gradient is only on during the first part of the cycle, then two correction-kernels have to be used, the latter with $G = 0$. However, because the magnetization does not precess when the gradient is off, the second simulation step only involves convolution. The two correction-kernels can then be cascaded into a single kernel, that is $c[n, G_{\mathrm{eff}}, \mathrm{TR}] = c[n, G, \Delta t] \textcircled{N} c[n, 0, \mathrm{TR} - \Delta t]$. This reduces the computation time in simulating SSFP with a pulsed gradient. The RF pulses are calculated by Eq. (2.9) and the steps in Eqs. (5.24) and (5.25) are then repeated between the RF pulses.

5.3.2 Discrete Fourier Transform Implementation

In the SSFP pulse sequence, the effective gradient in each TR cycle is always the same as shown in Fig. 5-1. This allows us to exploit the spatial periodicy of the magnetization. Before we describe the simulation algorithm, it is useful to define the following N-point discrete Fourier transform (DFT) pairs [96]

$$\begin{aligned} M_{xy}[k,t] &\overset{\mathcal{DFT}}{\longleftrightarrow} m_{xy}[n,t] \\ M_z[k,t] &\overset{\mathcal{DFT}}{\longleftrightarrow} m_z[n,t] \\ C[k, G, \Delta t] &\overset{\mathcal{DFT}}{\longleftrightarrow} c[n, G, \Delta t] \end{aligned} \tag{5.26}$$

The simulation algorithm represented by Eqs. (5.24) and (5.25) can now be written in the Fourier domain as

$$\begin{aligned} M_{xy}^{-}[k] &= M_{xy}^{+}[k-1] \cdot C[k, G_{\text{eff}}, \text{TR}] \cdot E_2 \\ M_{z}^{-}[k] &= M_{z}^{+}[k] \cdot C[k, 0, \text{TR}] \cdot E_1 + N \cdot \delta[k](1 - E_1) \end{aligned} \tag{5.27}$$

where $\delta[k]$ is the Kronecker-delta function. The precession simply shifts the spatial harmonics of the magnetization and the convolution is replaced by multiplication. The computation time is much reduced because the number of multiplications is $\mathcal{O}(N)$ whereas in convolution the number of multiplications is $\mathcal{O}(N^2)$. The expressions for the RF rotation can be found from Eq. (2.9) and the definition of the DFT [96]:

$$\begin{aligned} M_{xy}^{+}[k] &= \frac{1+\cos\alpha}{2} M_{xy}^{-}[k] + \frac{1-\cos\alpha}{2} \overset{*}{M_{xy}^{-}}[-k] + i \cdot \sin\alpha \, M_{z}^{-}[k] \\ M_{z}^{+}[k] &= \frac{i \cdot \sin\alpha}{2} M_{xy}^{-}[k] - \frac{i \cdot \sin\alpha}{2} \overset{*}{M_{xy}^{-}}[-k] + \cos\alpha \, M_{z}^{-}[k] \end{aligned} \tag{5.28}$$

The asterisk is used to represent the complex conjugate. It should be noted that this DFT simulation algorithm which is expressed by Eqs. (5.27) and (5.28) is in complete harmony with the diagram in Fig. 5-5. The RF rotation mixes the negative and positive magnetization harmonics and between the RF pulses the precession shifts the harmonics up by one.

In the Fourier domain, the initial condition where the magnetization is in thermal equilibrium is given by

$$M_z[k, 0] = N \cdot \delta[k] \cdot M_0 \qquad \text{and} \qquad M_{xy}[k, 0] = 0 \tag{5.29}$$

The simulation steps Eqs. (5.27) and (5.28) are then repeated until the magnetization reaches its steady state. The detected signal is the average of the zeroth order harmonic, $M_{xy}[0]/N$, since the other harmonics integrate to zero. The higher harmonics, however, contain the amplitudes of the higher order echoes which can be acquired in SSFP [54, 67, 86, 152].

5.4 PA and Simulation Results

The fourth order partition approximation was evaluated for a range of different parameters. Figure 5-6 shows how the magnitude of the SSFP-echo behaves as a function of flow and diffusion. The flow sensitivity is periodic and symmetrical. We denote the flow period by the aliasing velocity $V_a = \lambda/\text{TR}$. The magnitude range of the flow sensitivity is then completely described when the velocity ratio v/V_a ranges from zero to $1/2$. The diffusion sensitivity is then plotted as a function of bD. For the

parameters used in Fig. 5-6, we clearly see that SSFP is more sensitive to flow for a 30° than a 90° flip angle. This is comparable with the diffusion sensitivity [15], which is also higher for smaller flip angles. This can be understood from Eq. (5.18). When the flip angle is small, the higher order pathways or stimulated echoes make a significant contribution to the SSFP signal. These echoes are very sensitive to any motion because of their long time path. Hence the steady state is more easily *scrambled* for the smaller flip angles.

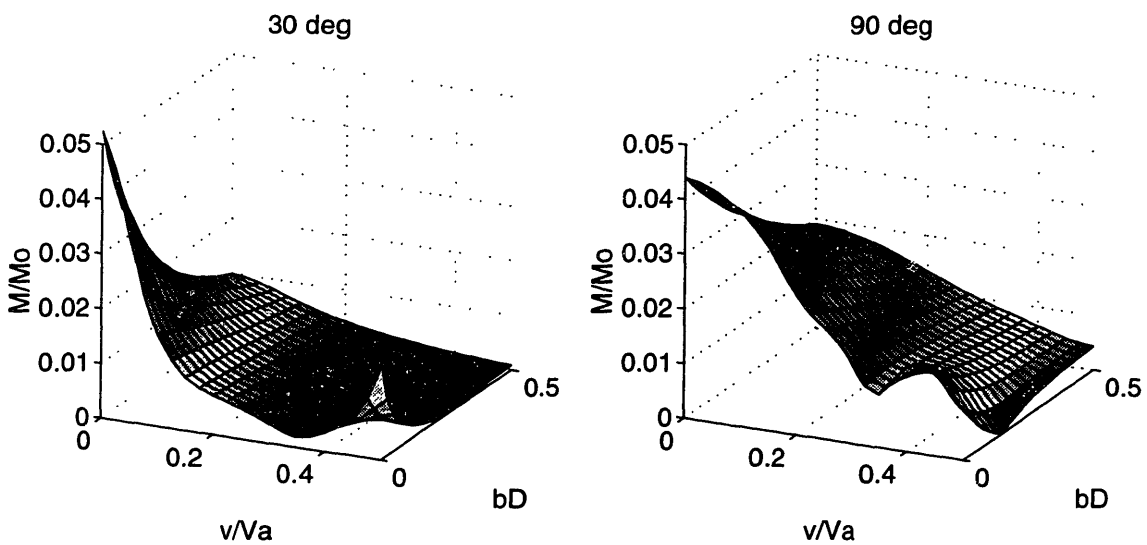

Figure 5-6: The sensitivity of SSFP echo magnitude plotted as a function of diffusion (bD) and flow (v/V_a). At left α = 30° and on the right α = 90°. T_1/TR = 10 and T_2/TR = 2.

We also note that for the 90° flip angle the signal shows a very complex behavior when the diffusion is varied and $v = V_a/2$. At first the signal decreases when the diffusion is increased and reaches a value close to zero. Then, however, increasing diffusion leads to increased signal. Eventually the signal strength will of course start to fall off as the diffusion increases but it is interesting that a certain combination of flow and diffusion causes maximum scrambling of the steady state.

The PA was compared with results from computer simulations. In Fig. 5-7 we see the agreement is very good for T_2/TR ratios as large as 2. We also note that the match is very good for higher ratios of T_2/TR when the diffusion sensitivity is large. This is similar to our observations on the flip angle behavior. Increasing diffusion decreases the higher order pathways significantly so that their contribution to the signal can be neglected.

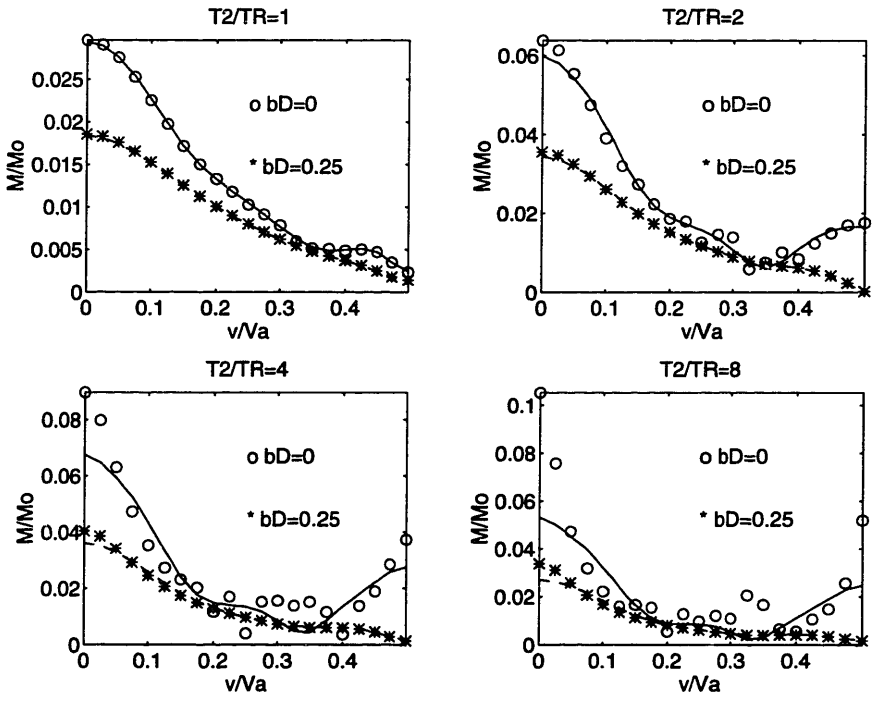

Figure 5-7: The 4'th order partition analysis (PA) compared with results from computer simulation. The solid and dashed lines show the results from the PA without and with diffusion, respectively. The circles and the stars represent the corresponding values from the simulation. $T_1/T_2 = 5$ and $\alpha = 60°$.

5.5 Experimental Methods and Results

5.5.1 Pulse Sequence with a Moving Reference Frame

A 2D SSFP-echo pulse sequence was implemented on a 1.5T GE Signa imager (General Electric Medical Systems, Milwaukee, WI). The imaging pulse sequence is the same as the one shown in Fig. 5-1 but without the acquisition of the FID. The flow and diffusion sensitizing gradients therefore followed the RF excitation. In the sequence we also included the moving reference frame (MRF) by varying the phase of the RF pulses [129]. For a particular value of the RF flip angle, the steady state of the isochromats is only influenced by the relaxation and the precession. If the magnetization is subject to constant bulk flow, it is easy to see from Eq. (5.17) that the change in precession angle between subsequent cycles is given by

$$\Delta\phi = \Delta_v = 2\pi\frac{v}{V_a} \tag{5.30}$$

By synchronizing the RF phase with this phase change, it is possible to make those isochromats which are flowing experience the same RF torque as a stationary isochromat does when the RF phase is kept constant. By similar means, the response of a static isochromat in the MRF will equal the response of an isochromat flowing at the opposite velocity, $-v$, when the RF phase is kept constant.

In our implementation of the MRF technique, we used the following phase program

$$\begin{aligned} i) \quad & \varphi_{n+1} = (\varphi_n + \Delta_v) \bmod 2\pi \\ ii) \quad & \psi_{n+1} = (\psi_n + \varphi_{n+1}) \bmod 2\pi \end{aligned}$$

In this phase program, φ_n and ψ_n are used to represent the precession angle and the total accumulated phase in the n'th SSFP cycle, respectively.

The phase of the n'th RF pulse was set equal to ψ_n; however, the phase of the receiver followed the phase program of the following RF pulse, ψ_{n+1}. This is easy to understand by "thinking backward in time". If the phase of the echo did not follow the phase of the following RF pulse, the torque an isochromats experiences from the RF pulses would not be constant and hence there would not be a steady state.

It is worth noting that our imaging sequence is different from the imaging sequence described by Tyszka *et al.* [129] since we acquired the echo (A_{-1}) whereas they used the FID (A_0), which is much less sensitive to flow.

5.5.2 Measurements

The imaging phantom contained three different liquids: water, doped water and vegetable oil. The longitudinal relaxation, T_1, was estimated by using a fast spin echo inversion recovery imaging sequence (FSE-IR). Several images were acquired with different inversion time, TI. The implementation of FSE we used acquired four k-lines in each RF excitation. The T_1 values were found by fitting the average image intensity from the three regions of interest (ROI) to the theoretical T_1 saturation curve by using nonlinear least-squares. Similarly, the transverse relaxation was obtained by using spin echo (SE) images with different echo time, TE. For all these measurements TR was set to 9 seconds. The results for the best fits can be found in Table 5.1.

To estimate the diffusion constant, a Stejskal-Tanner [118] imaging sequence was used with varied diffusion gradients. The diffusion constant was then estimated from the best least-square fit to the diffusive attenuation as a function of the b value. The diffusion constants for all the ROIs are also given in Table 5.1.

Instead of using a flow phantom, which can be hard to construct to set up a constant bulk flow, we used the MRF principle described above. By varying the RF phase or the MRF velocity, we could therefore simulate the ideal constant bulk flow for the whole phantom.

	ROI no. 1	ROI no. 2	ROI no. 3
T_1/ms	90	2500	190
T_2/ms	75	2050	150
$D/(\mu m^2/ms)$	2.1	2.0	0.02

Table 5.1: Relaxation times and diffusion constants estimated for the different regions of interest (ROI) in the phantom. ROI no. 1 is doped water, ROI no. 2 is water and ROI no. 3 is vegetable oil.

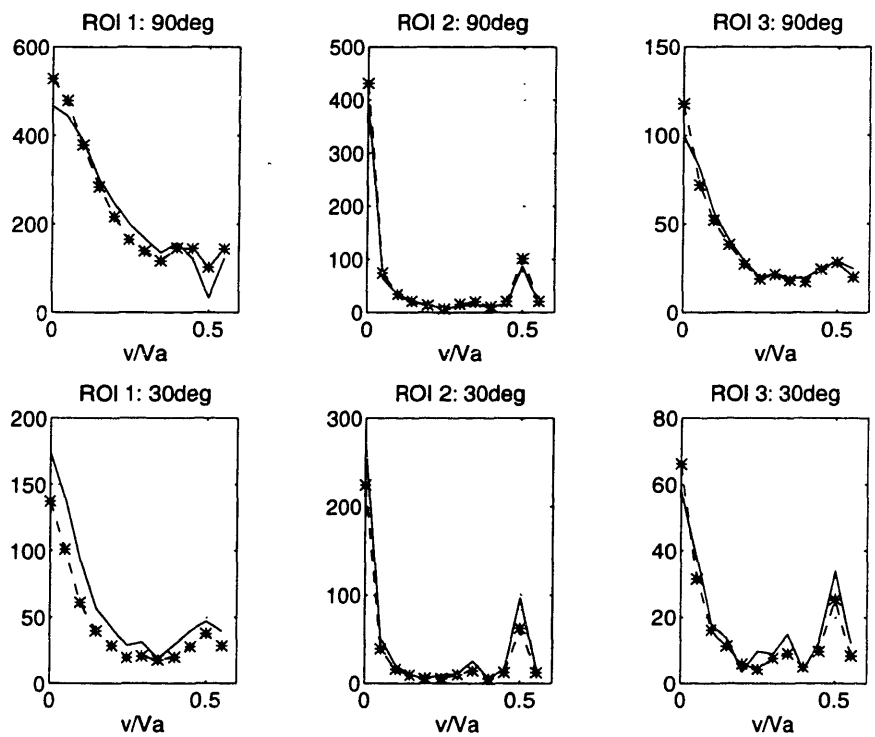

Figure 5-8: The SSFP echo magnitude signal as a function of the MRF velocity for two different flip angles, 30° and 90°. Theory is shown as a solid line and measurements as asterisks. The signal intensity is in arbitrary imager units and the standard deviation of the measurements is less than the size of the asterisks. TR = 30ms and b = 10 s/mm^2.

Magnitude images with a 20cm field of view (FOV) and a 256x256 resolution were reconstructed. Prior to the acquisition, 100 "dummy" cycles were used to allow the magnetization to reach a steady state. For many of the simulated flow rates, low

signal intensity was expected. A 1cm thick slice was therefore used and the number of averages (NEX) ranged from four to eight. The receiver bandwidth was set to be 16kHz. This was found to be sufficient to make almost all the measured signal intensities well above the noise level, therefore neglecting any possible bias due to the *Rician* distribution of the data [52].

Figure 5-8 shows how the magnitude of the SSFP echo changes as a function of the flow rate. As expected from the theory, the flow sensitivity is larger (steeper fall off) for the 30° flip angle than for the 90° flip angle. We also see that the water in ROI No. 2 is most sensitive to the flow because it has the longest relaxation times. The absence of the higher order stimulated echoes, which are easily scrambled by the flow, explains the strong flow sensitivity. In the other regions where the relaxation times are smaller, the reduction in the signal due to the flow is less dramatic. Notice the excellent agreement between the experimental data and the theoretical data, which was calculated by a computer simulation. We also see that the experimental data shows the correct symmetry behavior around $v/V_a = 0.5$. In the computer simulation we did not take into consideration the nonidealities of the slice profile. This could easily be done by averaging the theoretical signal over a range of flip angles, using the flip angle distribution of the slice profile. This would result in a slight increase in the flow and diffusion sensitivity [15].

It should be noted that in order to compare the theoretical and experimental data, the theoretical curve had to be scaled to match with the units of the imager. To do that we used linear least squares to find a single scaling factor which gave the best fit to both the data from the 90° experiment and the 30° experiment. This constant is justified because the amplifier's gain was kept the same for both of the experiments and because the proton density is not subject to change. If each data set had been separately fit, an even better fit could have be obtained, however it would be a "less honest" fit.

We also analyzed the dependence of the signal as a function of flow with variable diffusion sensitivity. In Fig. 5-9 we see the results from measurements with two different b factors, 10sec/mm^2 and 50sec/mm^2. TR was 35ms and the flip angle was set to 30°. It is clear that in regions with large diffusion, ROI No. 1 and 2, the flow sensitivity changes whereas in ROI No. 3 it is much less affected. Again this agrees very well with what is expected from the theory because the flow response simply tells us how the higher order pathways add together. When the diffusion sensitivity is increased, fewer pathways contribute to the signal and therefore there are less variations in the signal due to changes in the flow velocity.

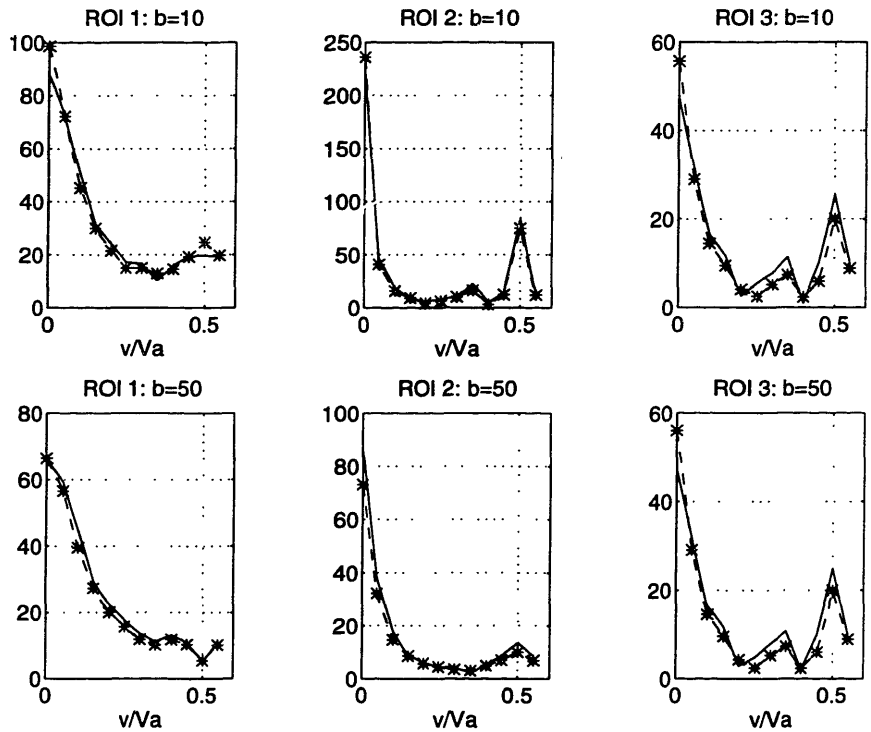

Figure 5-9: The SSFP-echo magnitude signal as a function of the MRF velocity for two different b values, 10 s/mm^2 and 50 s/mm^2. Theory is shown as a solid line and measurements as asterisks. The signal intensity is in arbitrary imager units and the standard deviation of the measurements is less than the size of the asterisks. TR = 35ms and the flip angle is 30°.

5.6 Pulsatile Flow and Diffusion

In this section we will analyze how the pulsatile motion of the brain, due to cardiac action and respiratory events, influences the measurement of diffusion. It is well known that the brain and cerebrospinal fluid exhibit periodic motion, with peak velocities up to 1mm/sec, in the frequency range of a normal heart rate. The maximum displacement of the brain tissue can therefore be as high as 50μm [78].

In order to address the influence of this motion on the diffusion attenuation, we used flow curves, adopted from ref. [78], of tissue located to the left of the ventricles. Note that the bulk motion in the brain is spatially varying and our reference point is chosen arbitrarily. First we simulated a regular SSFP imaging sequence with hardly any diffusion weighting (DW). We assumed the relaxation parameters of the brain

tissue to be $T_1 = 800$ms, $T_2 = 100$ms and the diffusion was assumed to be that of water, $D = 2\mu m^2/ms$. To have a uniform pixel intensity, the SSFP wavelength was set to be slightly smaller than a typical voxel size, 24cm/256. When the repetition time was set to 50ms, the resulting diffusion sensitivity was close to $bD = 0.01$. Both 30° and 90° flip angles were simulated. The results are shown in Fig. 5-10 with the corresponding flow curve at the top of the figure. Note that the flow curve has been normalized to the units of the aliasing velocity, V_a, which depends on the SSFP wavelength and the repetition time. The maximum and minimum of the flow are 0.57mm/sec and -0.89mm/sec, respectively. On the plots the time history of the magnitude of the transverse magnetization is shown with a solid line. For a comparison, we also simulated the signal when flow (dashed line) and when both diffusion and flow (dash-dotted line) are ignored. We see that after the magnetization reaches its steady state, there are only very small perturbations from the response of static spins. For the 90° flip angle case, there is no diffusion or flow sensitivity apparent; however, for the 30° flip angle, there is a small attenuation due to diffusion as well as a tiny flow sensitivity. Figure 5-11 shows the equivalent results when the b factor has been increased to give $bD = 0.2$. Note that this also affects the flow sensitivity and therefore the flow curve has a different amplitude in units of V_a. Now we clearly see a very strong diffusion attenuation for both flip angles, and it is also evident that the bulk motion of the tissue causes extra signal loss. This increased signal loss leads to an overestimation of the diffusion attenuation in DW imaging.

One might speculate whether it is possible to reduce the flow sensitivity while maintaining the diffusion sensitivity. The relation $\Delta_v = \sqrt{v^2 \cdot b \cdot \mathrm{TR}}$ implies that for a given diffusion sensitivity, b, and flow, v, the flow sensitivity could be minimized by using a small TR. This, however, requires a larger effective gradient in order to maintain the fixed diffusion sensitivity. We checked this idea by repeating the simulation with a shorter repetition time, TR = 30ms, but keeping the b factor constant and the results are shown in Fig. 5-12. Our results show that the shorter repetition time not only gives increased flow sensitivity but also diffusion sensitivity especially for the 90° flip angle. This is where one of the complications of SSFP becomes visible, i.e., that the flow and the diffusion sensitivity depend not only on Δ_v and the b factor, respectively, but also on E_1 and E_2.

To make the results shown in Figs. 5-10 - 5-12 more quantitative, we calculated the point spread functions (PSF) one would obtain if the last 128 echoes are used in SSFP Fourier imaging. This is simply done by calculating the discrete Fourier transform of the complex SSFP signal. Figure 5-13 shows the magnitude of the PSFs, in the phase encoding direction, from the simulation with and without flow, for different diffusion sensitivity, TRs and flip angles. The amplitude of the PSF has been normalized with the maximum amplitude of the PSF when both flow and diffusion are ignored. The

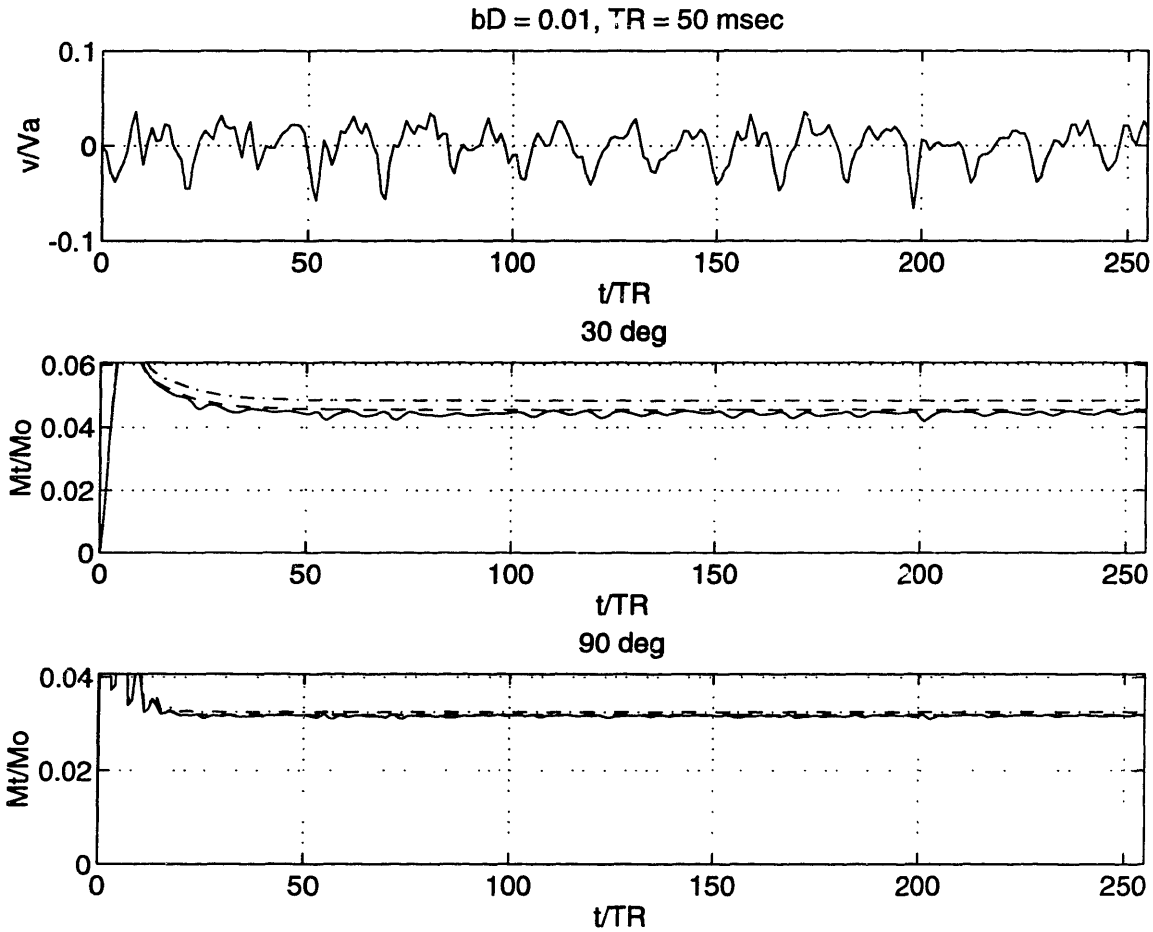

Figure 5-10: Top: *In vivo* motion of brain tissue to the left of the ventricles, adopted from Maier *et al.* Maximum and minimum flow rates are 0.57mm/s and -0.89mm/s, respectively. **Middle**: Results of simulation, showing the magnitude of the transverse magnetization with T_1 = 800ms, T_2 = 100ms, bD = 0.01, TR = 50ms and 30° flip angle. The dot-dashed line shows the results when both diffusion and flow are ignored. The dashed line shows the results when only flow is ignored. The solid line shows the results when both flow and diffusion are taken into account. **Bottom**: Same as above except for a flip angle of 90°.

height of the dashed PSFs is therefore indicative of the theoretical diffusion attenuation.

We see from Fig. 5-13 a) and d) that there is only a small distortion from the brain motion in a non-diffusion-weighted SSFP imaging sequence. In Figs. 5-13 b), c), e), and f) the diffusion sensitivity is $bD = 0.2$ and now it is easy to see the distortion in the PSF. The distortion is more severe for the 30° flip angle in Figs. 5-13 b) and c)

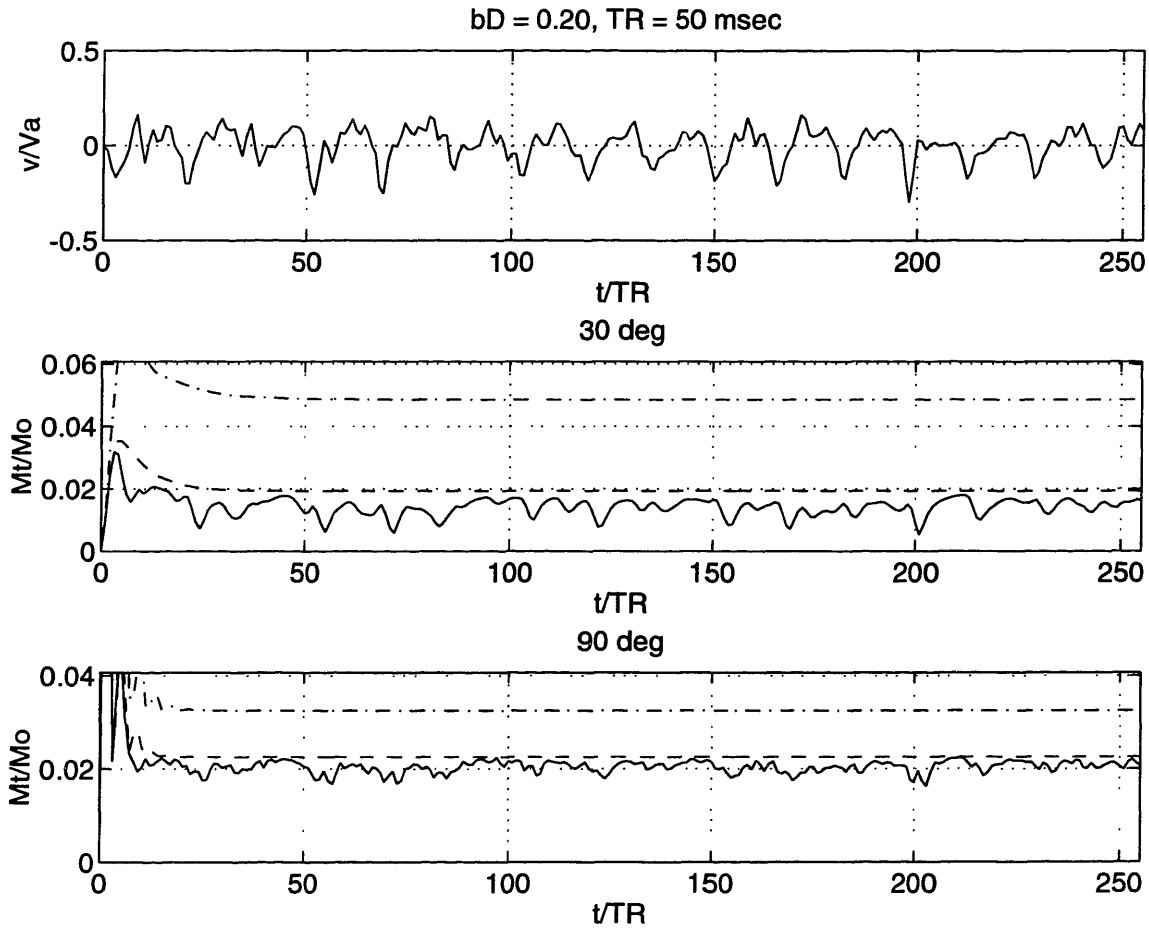

Figure 5-11: Same as in Fig. 5-10 except for a larger b factor, $bD = 0.2$. A 30° flip angle (middle) is compared to a 90° flip angle (bottom).

than for the 90° flip angle in Figs. 5-13 e) and f) because smaller flip angles give more sensitivity to diffusion and flow. When the repetition time is 50ms, as in Figs. 5-13 b) and e), the overestimation of the diffusion attenuation is 61% and 32% for the 30° and the 90° flip angles, respectively. When the repetition time is decreased to 30ms, as in Figs. 5-13 c) and f), the overestimation of the diffusion attenuation is 58% and 33% for 30° and the 90° flip angles, respectively. These results are summarized in Table 5.2. Thus, for this particular flow curve a reduced repetition time does therefore not reduce the flow sensitivity, if the diffusion sensitivity is kept fixed.

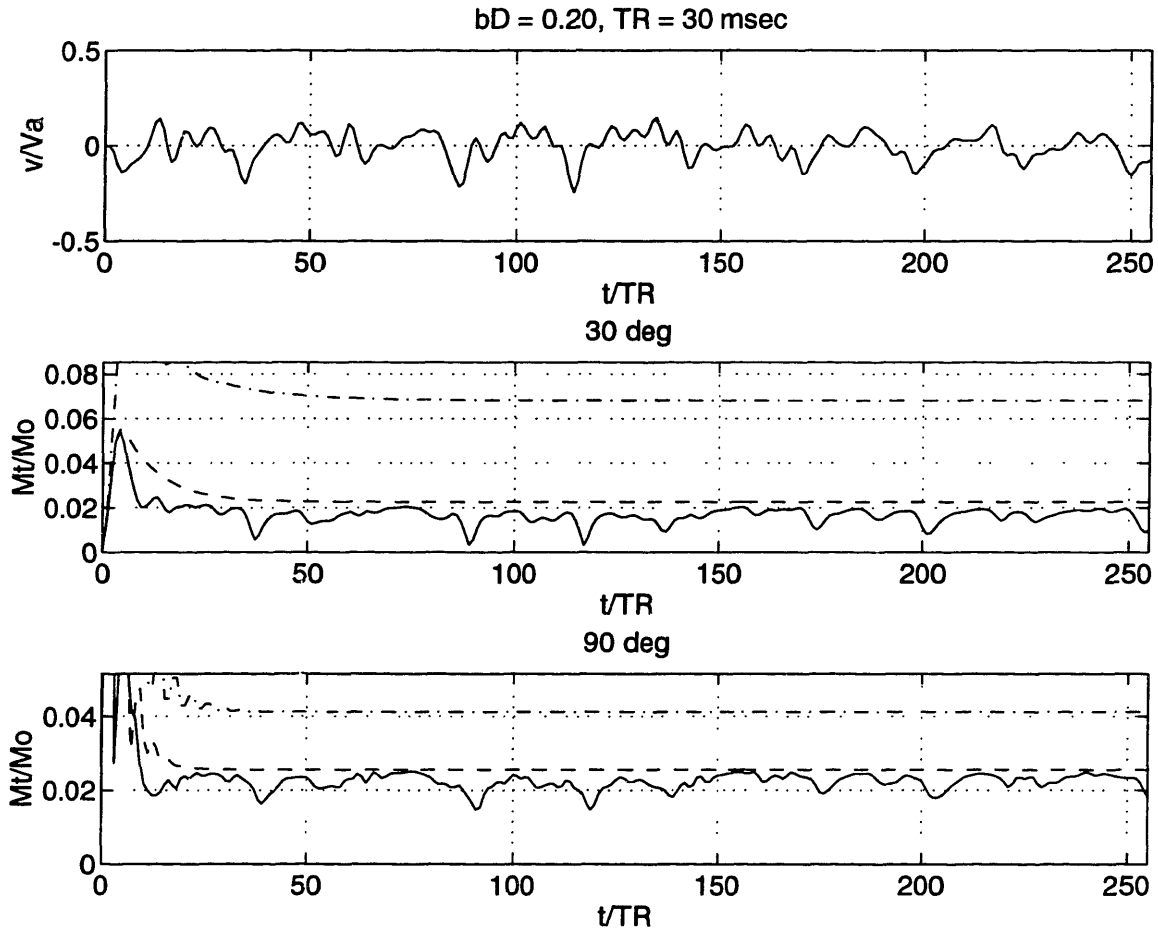

Figure 5-12: Same as in Fig. 5-11 except for a shorter repetition time, TR = 30ms. A 30° flip angle (middle) is compared to a 90° flip angle (bottom).

5.6.1 DW-SSFP versus DW-PGSE

We see from Fig. 5-13 that the overestimation of the diffusion-weighted attenuation is quite severe. It is therefore interesting to compare the artifacts obtained in a DW-SSFP to the artifacts obtained in a diffusion-weighted pulsed gradient spin echo (DW-PGSE) sequence. We assumed the maximum gradient strength to be that of a conventional scanner, 0.01T/m = 1G/cm, and we also assumed the separation of the DW-gradients to be as small as possible. Given these conditions we used the well known Stejskal-Tanner equation [117] to calculate the necessary gradient duration, to achieve the same diffusion attenuation as in Fig. 5-13 a) - f). From this we estimated the image distortion from the pulsatile bulk flow, in exactly the same manner as we

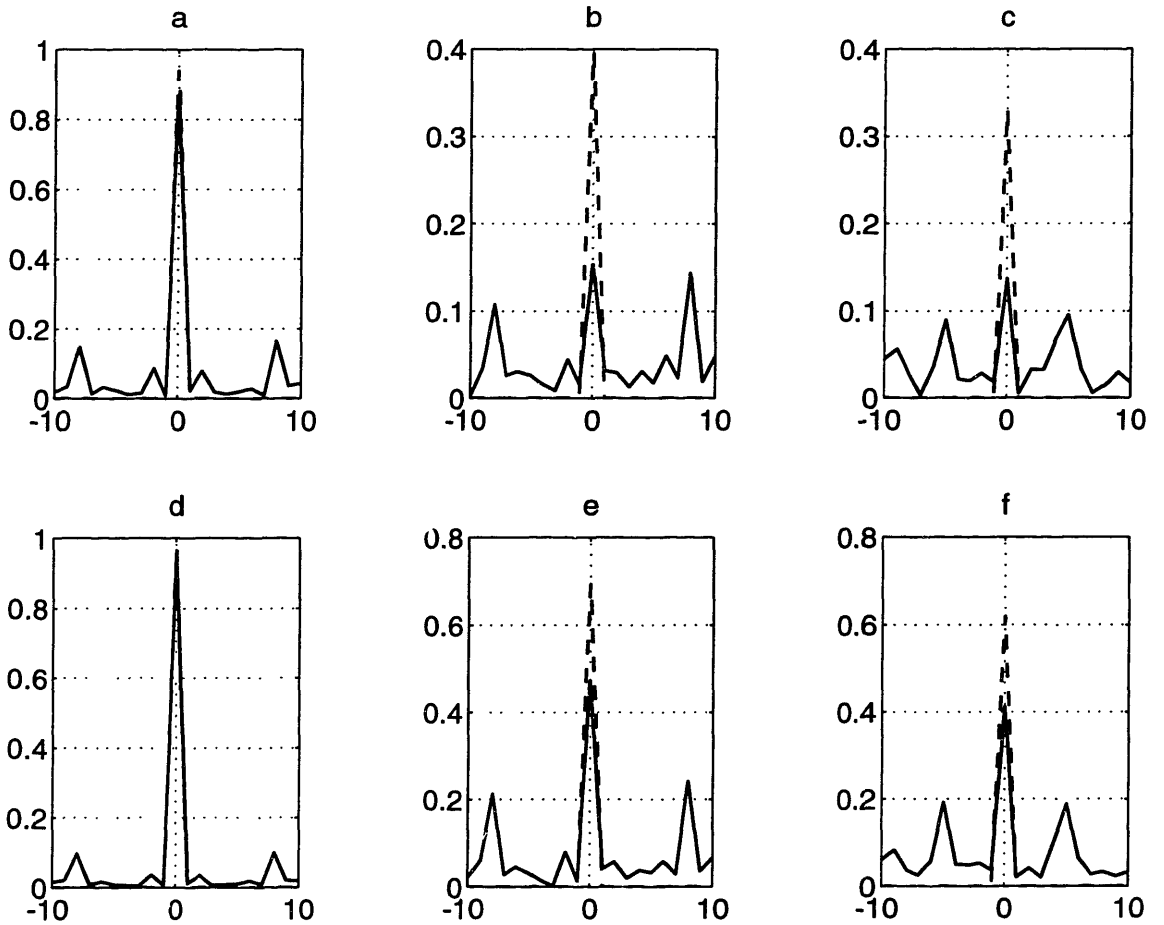

Figure 5-13: The magnitude of the point spread functions in the phase encoding direction, for the cases considered in Figs. 5-10 - 5-12. The dashed line shows the PSF when flow is ignored and the solid line shows the PSF when both flow and diffusion are considered. The PSFs are normalized by the maximum of the PSF when both flow and diffusion are ignored, in order to show the theoretical diffusion attenuation. **a)** $bD = 0.01$, TR = 50ms and $\alpha = 30°$. **b)** $bD = 0.2$, TR = 50ms and $\alpha = 30°$. **c)** $bD = 0.2$, TR = 30ms and $\alpha = 30°$. **d)** $bD = 0.01$, TR = 50ms and $\alpha = 90°$. **e)** $bD = 0.2$, TR = 50ms and $\alpha = 90°$. **f)** $bD = 0.2$, TR = 30ms and $\alpha = 90°$.

did in the SSFP simulation. To simplify the matter we ignore phase artifacts from read and phase encoding gradients, which should be relatively small when the diffusion weighting is considerable, i.e. $bD = 0.2$. The peaks of the PSF functions were used as a measure of the diffusion attenuation and from them the error in the estimation was calculated. Both a regular non-gated PGSE and a cardiac gated (ECG) PGSE were

considered. For the the acquisition of each phase encode, in the non-gated PGSE, we picked an arbitrary flow value frc .n the flow curve in Fig. 5-10. For the ECG simulation we synchronized the acquisition with the large negative peaks of the flow curve. The results are summarized in Table 5.2.

PSF no.	DW att.	SSFP err. %	PGSE err. %	ECG-PGSE error %
a)	0.94	7	3	0.5
b)	0.40	61	64	14
c)	0.33	58	72	18
d)	0.98	2	0.5	0.1
e)	0.69	32	25	5
f)	0.62	33	34	7

Table 5.2: The error in the estimation of the theoretical diffusion attenuation for the cases considered in Fig. 5-13 when using SSFP, spin echo or cardiac gated spin echo.

Table 5.2 shows that the errors in DW-PGSE for *in vivo* diffusion assessment are comparable to SSFP despite the more complicated signal dependence of SSFP. By using cardiac gating, however, it is possible to reduce the errors dramatically. This results in longer acquisition time because of the need for a long repetition time, to minimize artifacts which may arise from variable spin lattice relaxation between RF excitations. Because SSFP is a driven equilibrium technique with RF pulses being applied at a constant rate, cardiac gating is not possible. Even with the ECG in PGSE, we are still left with some errors due to the phase variations in the signal. The only way to avoid this problem is to acquire the image in a single-shot, such as in EPI [128]. The use of a navigator echo has been suggested [2,97] to reduce the phase artifacts in DW-PGSE. The correction scheme used with these navigators, however, assumes the motion of the brain to be that of a rigid object and cannot take into account the more complicated spatial variations of the brain motion [78].

5.7 The Analogy of Flow in SSFP and RF spoiling

The phase program of the MRF turns out to be identical to the phase pattern commonly used to eliminate the transverse magnetization in many fast low flip angle imaging pulse sequences [21,153] such as FLASH. Constant bulk flow, therefore, causes identical spoiling of transverse magnetization as does RF spoiling. On one hand this tells us that when the SSFP-echo signal is totally scrambled due to bulk flow, the

SSFP-FID signal equals the theoretical FLASH signal, which is easily calculated from the steady-state solution by setting E_2 equal to zero. On the other hand, the SSFP-echo flow curves tell us how effective the spoiling of the transverse magnetization is. A phase change increment of 117° is commonly used to do RF spoiling [153]. The effectiveness of the spoiling of the transverse magnetization can be easily seen from Figs. 5-8 and 5-9 where $v/V_a = 117°/360°$. Hence by using the pulse sequence with an MRF, described in this chapter, one can measure whether adequate spoiling can be achieved. The figures clearly indicate that the effectiveness of RF spoiling depends on the flip angle, the tissue relaxation parameters, as well as the diffusion coefficient.

5.8 Bipolar SSFP Sequence

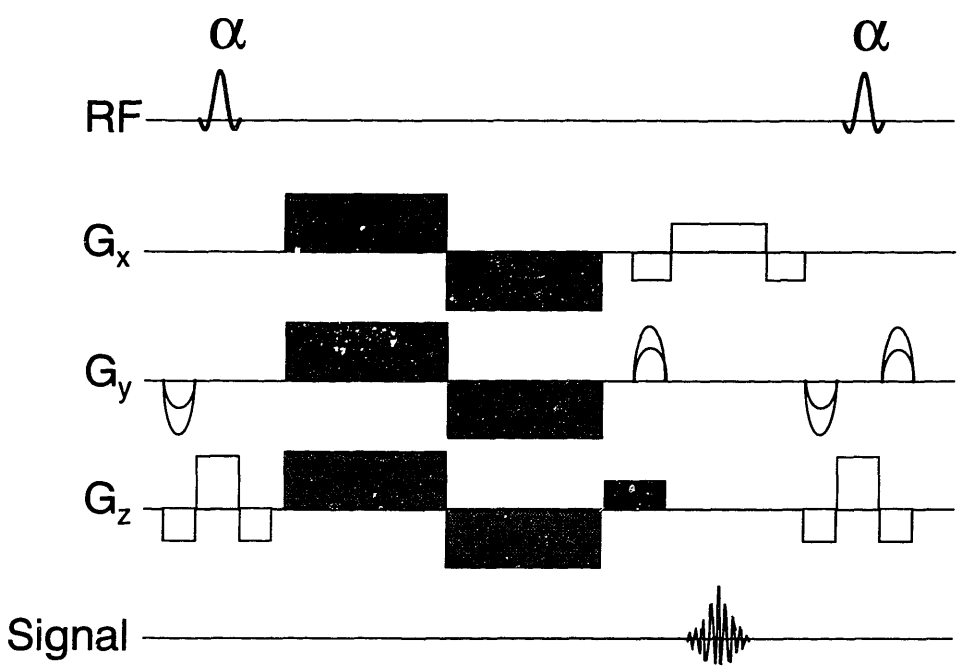

Figure 5-14: A modified SSFP pulse sequence with diffusion sensitivity in all directions. The effective gradient (black) is made as small as possible and the diffusion sensitivity is determined by the bipolar gradients.

A modified diffusion weighted SSFP sequence has recently been suggested where the diffusion attenuation is claimed to be less sensitive to motion and variations in T_1, T_2, and the RF flip angle [28, 150]. The main difference between this modified SSFP

sequence and the SSFP sequence described in previous sections is the use of bipolar diffusion weighting gradients as shown in Fig. 5-14. Ding *et al.* also use a frame-by-frame averaging scheme which has been proposed to reduce motion artifacts in the conventional SSFP sequence [27]. In this section, it will be shown that although this modified SSFP sequence greatly reduces variations in the diffusion attenuation due to relaxation and RF flip angle, it is still sensitive to physiological motion.

The modified SSFP sequence in shown in Fig. 5-14. By making the diffusion sensitizing gradient bipolar its zeroth moment will be zero. The purpose of this is to reduce the motion sensitivity [152]. The major drawback is that very strong gradients are needed to obtain high diffusion sensitivity. The bipolar gradients attenuate the transverse magnetization by $A_D = \exp(-D2\gamma^2 G_{\max}^2 \delta^3/3)$ according to Eq. (3.38). The influence of this bipolar diffusion attenuation is identical to the transverse relaxation, E_2, and the signal can be analyzed by replacing E_2 with $E_2 A_D$ in Eq. (5.3). This is because the moment of the bipolar gradient is zero and displacement of spins in one SSFP-cycle does not influence the precession in the following SSFP-cycles. In other words, the effective gradient and the wavelength, λ, is not affected by the bipolar gradient. Earlier, this same approach has been taken to analyze the diffusion sensitivity of the conventional SSFP sequence [74]. Then, however, this gives incorrect diffusion sensitivity, because it fails to account for the correlation of the diffusion related dephasing in consecutive SSFP-cycles.

To reduce variations in the diffusion attenuation from T_1, T_2, and the RF flip angle, Ding *et al.* suggest to select TR such that the signal can be accurately approximated by a second order approximation in E_2, i.e. contribution from fourth order pathways in Eq. (5.16) can be neglected:

$$\mathbf{M}^- \approx L \ldots LTT + L \ldots LTL \ldots LT \tag{5.31}$$

Clearly, the signal is proportional to E_2^2. From previous discussion on the influence of the bipolar gradients, the diffusion attenuation is $A_D^2 = \exp(-bD)$ independent of the flip angle and the relaxation parameters. Also, the relative accuracy of the second order approximation is on the order of $E_2^2 A_D^2$.

An issue that is not discussed in the paper by Ding *et al.* is the first order moment of the bipolar gradients. It is trivial to show that flowing spins acquire additional phase from the bipolar gradients that is given by

$$\phi_v = \delta^2 v G_{\max} \tag{5.32}$$

If the flow displacement in each cycle is constant and small compared to λ, this does not lead to scrambling of the signal. However, if the flow is pulsatile, the phase from the bipolar gradient is no longer fixed and the signal gets scrambled.

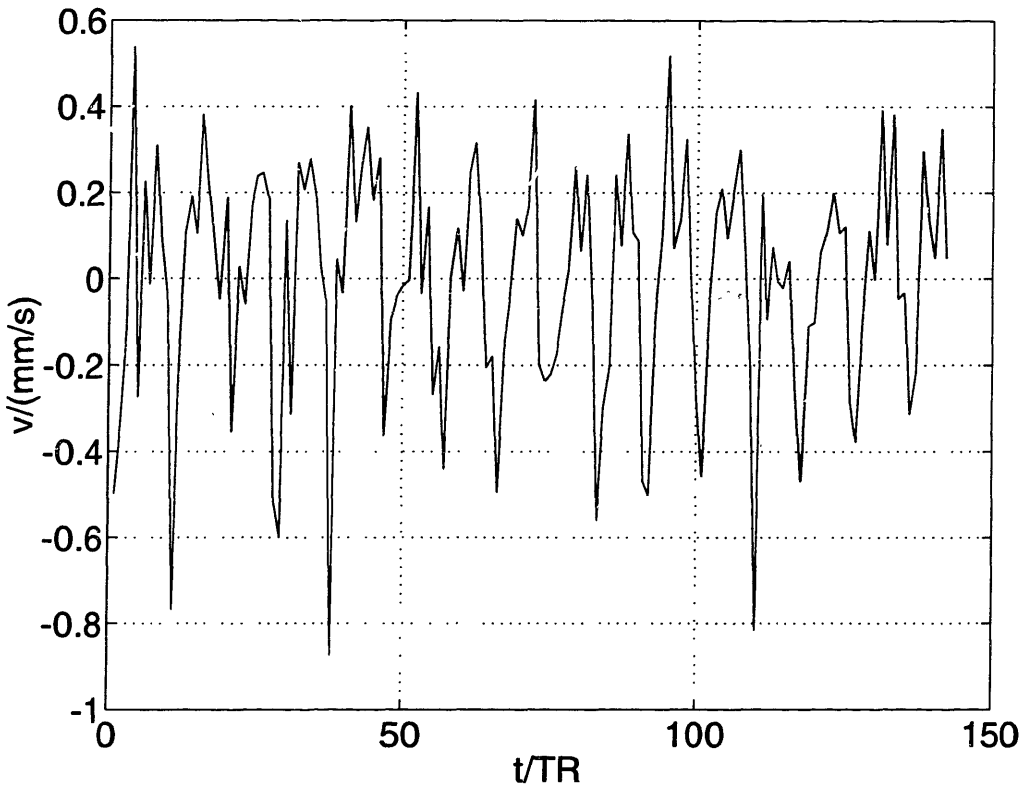

Figure 5-15: *In vivo* motion of brain tissue to the left of the ventricles, adopted from Maier *et al.* The curve is calculated with a spline interpolation of the original data which was sampled at every 50ms. Here, the repetition time is TR = 90ms.

The flow sensitivity of this modified SSFP sequence was studied by a computer simulation analogous to the one described in section 5.6. The influence of the bipolar gradient is modeled by replacing E_2 by $E_2 A_D$ and the flow phase in Eq. (5.32) is added to the precession angle of the transverse magnetization. The effective gradient was set such that the SSFP wavelength was slightly smaller than the pixel size, ca. 1mm. The relaxation parameters of the brain tissue were assumed to be $T_1 = 700$ms, $T_2 = 100$ms, and the diffusion coefficient was set to $D = 1\,\mu\text{m}^2/\text{ms}$. The same flow curve that was used in section 5.6 was used in the simulation and it is shown in Fig. 5-15. Since the flow sensitivity comes from the bipolar gradient and not the SSFP wavelength, the flow curve has not been normalized to the aliasing velocity as in Fig. 5-10. The flow was assumed constant during each bipolar gradient, however, different in each cycle.

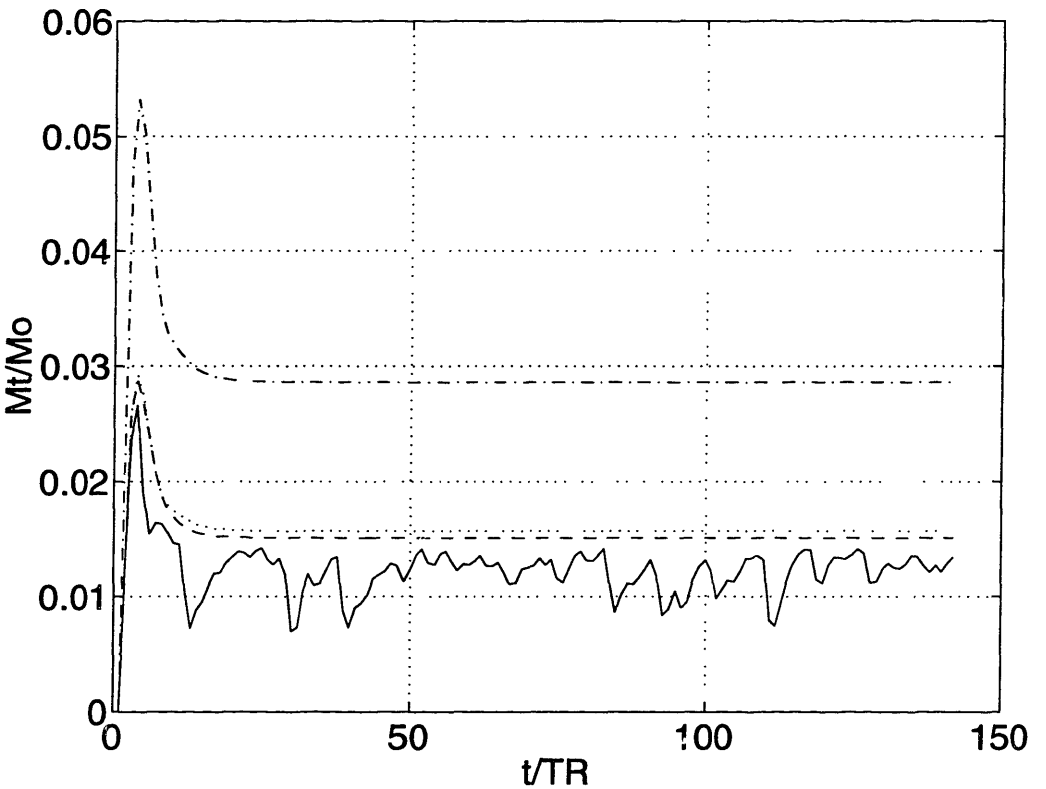

Figure 5-16: The magnitude of the transverse magnetization, in a simulation of the bipolar SSFP sequence with the flow curve in Fig. 5-15. $G_{\max}$ = 1G/cm. The RF flip angle is 50°, b = 600 s/mm^2, TR = 90ms, E_1 = 0.88, E_2 = 0.41, and D = 1 μm^2/ms. The dot-dashed line shows results when diffusion and flow is ignored. The dashed line shows the results when the flow is ignored. The solid line shows the results when both flow and diffusion are taken into account. The dotted line shows the dot-dashed line scaled by $\exp(-bD)$. The difference between the dotted line and the dashed line is due to the contribution from pathways of higher order than two.

The errors from this approximation should be minimal.

Examples of the simulations are shown in Fig. 5-16 and Fig. 5-17 for the maximum gradient strength of 1G/cm and 5G/cm, respectively. In both figures, the repetition time is 90ms and the effective b-factor is 600 s/mm^2. As the solid lines show, the signal is clearly scrambled because of the physiological motion, less though with the stronger gradient.

To analyze the implications of scrambling on the diffusion attenuation, the atten-

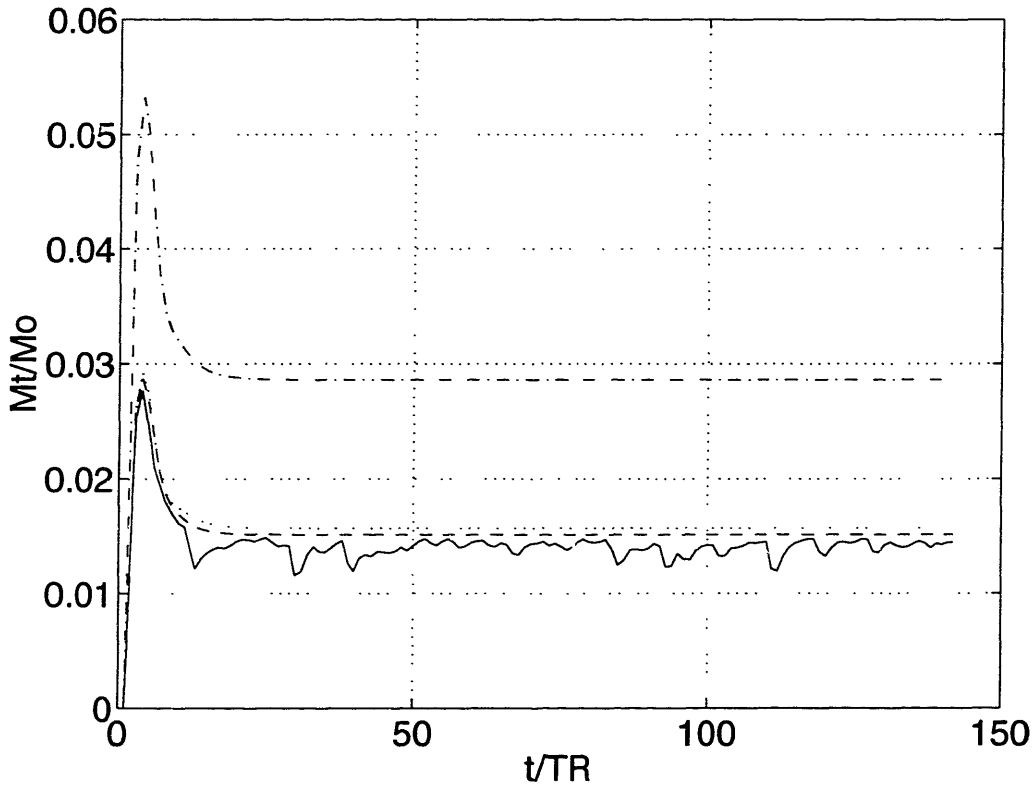

Figure 5-17: Same as in Fig. 5-16 except that $G_{\max}$ = 5G/cm instead of 1G/cm.

uation was estimated from the peak of the PSF as in section 5.6. The computer simulation was repeated for five different b-factors: 200,400,600,800, and 1000 s/mm^2. Log-linear least-squares were then used to estimate the diffusion coefficient from the attenuation curve. These results are shown in Table 5.3.

From Table 5.3 it is clear, that the bipolar SSFP sequence overestimates the diffusion in the brain in regions where there is pulsatile brain motion such as near the ventricles. As expected, stronger gradients reduce the flow sensitivity, because it allows for a shortening of the gradient pulse and therefore reduced phase variations (see Eq. (5.32)). Although a smaller TR makes the flow variations from cycle to cycle smaller, it does not reduce the scrambling of the signal because the higher order pathways become more important, unless of course T_2 is much smaller than TR. Also, the bias in the estimate of the diffusion coefficient becomes larger since it depends on E_2^2. The frame-by-frame averaging scheme does not fix this overestimation of the

TR/ms	50			90		
Flow Curve	v	v/2	v/4	v	v/2	v/4
G_{max}/(G/cm)	$D/(\mu m^2/ms)$			$D/(\mu m^2/ms)$		
1	2.44	1.53	1.25	2.63	1.43	1.14
2	2.02	1.38	1.21	2.00	1.28	1.10
5	1.62	1.27	1.18	1.52	1.16	1.07
10	1.44	1.22	1.17	1.32	1.11	1.06

Table 5.3: Estimates of the diffusion coefficient with the bipolar SSFP sequence using b-factors of 200, 400, 600, 800, and 1000 s/mm^2. The flow curve shown in Fig. 5-15 is denoted by v. Similarly, v/2 and v/4 are this flow curve with scaled amplitude. The RF flip angle is 50°, T_1 = 700ms, T_2 = 100ms, and D = 1 μm^2/ms. With zero flow, the estimates of the diffusion coefficient are 1.05 μm^2/ms and 1.15 μm^2/ms for the 90ms and the 50ms repetition times, respectively.

diffusion coefficient, however, it may reduce the ghost in the phase encoding direction and improve the appearance of the image.

Finally, it is interesting jump ahead and consider the relative signal-to-noise of the modified SSFP sequence and the Line Scan Diffusion imaging sequence which is introduced in chapter 7. This analysis is not supposed to be very formal, but, give a rough idea about the relative SNR of these two techniques. The bipolar SSFP signal, S, was obtained from the simulation described above. The echo time of the LSDI sequence, TE, is found from the maximum b-factor and the gradient strength. The sequences are assumed to have the same repetition time. The SSFP sequence uses 50° flip angle which is close to the optimum flip angle. Analogous with Eq. (7.6), the relative SNR should be approximately

$$\frac{\text{SNR-LSDI}}{\text{SNR-SSFP}} = M_0\sqrt{\frac{1}{N_y}}\exp(-bD - \text{TE}/T_2)/S \tag{5.33}$$

where N_y denotes the resolution in the phase encoding direction or the number of columns in the LSDI sequence. This ratio is evaluated for several gradient strengths in Table 5.4. It is clear from the table, that for brain diffusion imaging, the LSDI sequence has superior SNR.

TR/ms	50	90
G_{max}/(G/cm)	SNR-LSDI / SNR-SSFP	
1	-	1.25
2	1.20	1.93
5	1.68	2.73

Table 5.4: The relative SNR of the LSDI and the bipolar SSFP sequence. The SSFP flip angle is 50°, T_1 = 700ms, T_2 = 100ms, and the maximum b-factor is 1000 s/mm^2.

5.9 Conclusion

In this chapter, we have shown how a partition analysis can be used to obtain an analytical approximation of the simultaneous flow and diffusion sensitivity in SSFP imaging. This approximation was found to be accurate for T_2/TR ratios as large as two and for even larger T_2/TR ratios when diffusion sensitivity is considerable. More significant though is the physical understanding it provides about the signal formation in SSFP.

A 2D SSFP echo imaging pulse sequence with an MRF was implemented on our imaging system, and it was used to obtain experimental data from a phantom. The MRF technique allowed us to make more accurate comparison between our measurements and the theoretical values, because experimental nonidealities due to things such as vortices and laminar flow were avoided. The phantom contained three different solutions with very different relaxation and diffusion properties. An excellent agreement was found between the theory and the experimental data.

Our analysis shows, that the flow sensitivity is larger for smaller flip angles than for larger flip angles. An SSFP imaging pulse sequence that is made maximally sensitive to diffusion [15] is therefore also inherently very sensitive to bulk flow as well. Also, if the tissue undergoes bulk movements, whose size is on the order of the SSFP wavelength, the scrambling of the steady state will lead to additional signal loss and therefore an overestimation of the diffusion-related attenuation. This was demonstrated by using experimental data and the simulation algorithm from chapter 3 to calculate the simultaneous effect of pulsatile *in vivo* brain motion and diffusion. The scrambling of the steady state is not the only source of error when SSFP is used for *in vivo* diffusion measurements. The SSFP imaging sequence uses the phase to encode the spatial location in the y-direction and is therefore very sensitive to phase variations

in the signal. The periodic pulsatile brain motion and the strong diffusion gradient give rise to periodic variations in the signal phase. In Fourier imaging, this appears as a ghost in the y-direction. This ghost is easily seen in Fig. 5-13 as the secondary peaks in the PSF. The PGSE sequence is also sensitive this kind of phase variations. The overestimation in the PGSE was found to be similar to those in the SSFP sequence.

Finally, we showed that the modified SSFP sequence which was recently introduced by Ding *et al.* is also sensitive physiological motion, although, the flow sensitivity is less that in the conventional SSFP sequence if very high gradient amplitude is used.

Chapter 6

Navigator Echoes

6.1 Introduction

IN chapter 5, it was shown that it is impossible to obtain accurate *in vivo* diffusion estimates with the SSFP sequence because of the simultaneously sensitive to diffusion and other physiological motion. The complex nature of the SSFP signal makes it impossible to correct for the motion artifacts. The motion artifacts are easier to study in the PGSE sequence, because, the spin-echo signal does not depend on the transverse magnetization from previous RF pulse.

Navigator echoes have recently been proposed to reduce bulk motion artifacts in diffusion weighted images [2,97] acquired with the PGSE sequence. We have studied the feasibility of this technique and extended it to a fast spin echo sequence, i.e. FSE or RARE. The influence of the echo train length and the order of the navigator in the echo train is studied in terms of how noise and other image artifacts propagate into the image data from the navigator.

6.2 Theory

Diffusion weighting in the PGSE sequence is accomplished by using a pair of strong gradients as shown in Fig. 3-5. Any motion of tissue, between the application of these strong diffusion gradients, will cause a phase change in the signal. The phase variation due to bulk motion can in general be written as [2]

$$\Delta\Phi(\mathbf{r}) = \Delta\Phi_x + \Delta\Phi_y + \Delta\Phi_z + d\mathbf{k}\cdot\mathbf{r} \tag{6.1}$$

where

$$\begin{aligned} d\mathbf{k} &= \gamma \int_0^{\Delta+\delta} \mathbf{G}(t) \times \vec{\theta}(t) dt \\ &= \hat{x}\gamma \int_0^{\Delta+\delta} (G_y(t)\theta_z(t) - G_z(t)\theta_y(t)) dt \\ &+ \hat{y}\gamma \int_0^{\Delta+\delta} (G_z(t)\theta_x(t) - G_x(t)\theta_z(t)) dt \\ &+ \hat{z}\gamma \int_0^{\Delta+\delta} (G_x(t)\theta_y(t) - G_y(t)\theta_x(t)) dt \end{aligned} \tag{6.2}$$

The $\Delta\Phi_x$, $\Delta\Phi_y$, and $\Delta\Phi_z$ phase errors are due translation[1]. The rotation is denoted by $\vec{\theta}$ and $\mathbf{r}$ denotes a location in the image coordinate system[2]. The diffusion gradient, $\mathbf{G}$, is assumed to start at time zero and end at $\Delta+\delta$ as in Fig. 6-1. Since the diffusion gradients are strong enough to sense the microscopic diffusion displacement, it is easy to imagine that the slightest patient motion can produce considerable phase change. When phase encoding is used with repeated RF excitations, this variation in the signal phase causes ghosts and reduced image quality. This can lead to signal loss in one part of the image and signal enhancement in other parts of the image.

Anderson *et al.* [2] have shown, that when the diffusion sensitivity is in the phase encoding direction only, the zeroth and the first order variations in the phase of a navigator echo can be used to correct for phase changes due to rigid bulk displacement and rotation, respectively [2,97]. The principle of this technique is, that the navigator always collects information from the same part of the k-space and individual navigators can therefore be compared.

The navigator echo is simply the baseline signal, i.e. the k-line in the k_x-direction which goes through the center of the k-space. In other words, there is no phase encoding such that $k_y = 0$. Different navigator echoes, that have circular k-space trajectory, have also been proposed for measuring translational and in-plane rotational displacement [44]. These orbital navigators, however, have to be acquired without the diffusion gradients. In contrast, the k-line navigator is acquired with the diffusion gradients on. The purpose is not to correct for displacements of the object which size is on the order of the voxel size, but only artifacts related to some small motion during and in between the very strong diffusion gradients.

The navigator is acquired with the regular frequency encoding gradient but the phase encoding gradient has zero amplitude. Hence, the Fourier transform of the

[1]Even if the patient only rotates his head on top of the scan table, there will still be a phase error in the data from an apparent translation, because the origin of the image coordinates are usually in the middle of the head and, therefore, do not coincide with the axis of rotation.

[2]In Eq. (6.1) it is assumed that the rotation angle is small.

navigator echo gives the projection of the image in the y-direction as a function of x (see Fig.6-7). If the object is displaced during the diffusion gradient pair, we see from Eq. (6.1) that the signal will have additional phase which is a function of the motion. If the object rotates in the image plane and the diffusion gradients are only in the y-direction, the phase change will vary linear with x (the small angle approximation). The image echo will have this same phase variation, however, the image echoes are also phase encoded and therefore it makes no sense to compare the phase of the image echoes. If no motion is present, all the navigator echoes that are acquired with each k-line (view) should have the same phase (and magnitude). By comparing the phase difference between the projections of the navigator echoes, it is possible to estimate the phase distortion in the image echoes and thus correct it. The corrected image will have arbitrary phase which depends on the choice of the reference navigator, however, by forming a magnitude image this phase is irrelevant. For further description of the correction algorithm see ref. [2].

6.3 Methods

Although originally proposed for a single echo PGSE imaging sequence, the navigator correction scheme lends itself to be used for correction of all the echoes in a RARE echo train. This is because, ideally the phase of the odd numbered echoes should simply oppose the phase of the even numbered echoes.

A RARE imaging sequence (FSE) was modified by adding a pair of diffusion gradients between the 90° pulse and the first 180° pulse. In order to get high diffusion weighting on a conventional scanner such as the 1.5T GE Signa which has a maximum gradient strenght of 1G/cm, the time from the 90° pulse to the first echo had to be made larger than the spacing between the following echoes. In inhomogeneous magnetic field, this can lead to problems due to stimulated echoes, which fall into the acquisition window at the later echos. Figure 6-2 shows a pathway diagram for the DW-RARE sequence, taking into consideration the nonidealities of the refocusing pulses. The first two time intervals, i.e. from the 90° pulse to the first 180° pulse and from the 180° to the first echo, differ in length from the other time intervals. Influence from inhomogeneities on the precession angle is therefore different. As shown on the left in Fig. 6-2, this causes the spin echo and the stimulated echo, which form echo no. 2, to refocus at different time. The artifacts resulting from this misalignment of the pathways is shown in Fig. 6-3. The images were reconstructed from the second echo and the diffusion gradients were used to simulate inhomogeneities in the phase encoding direction. By increasing the gradient strength, by a factor of two between Fig. 6-3a) and Fig. 6-3b), the separation of the pathways is doubled and hence the spatial variation of the artifacts. When the separation is high enough, as in Fig. 6-

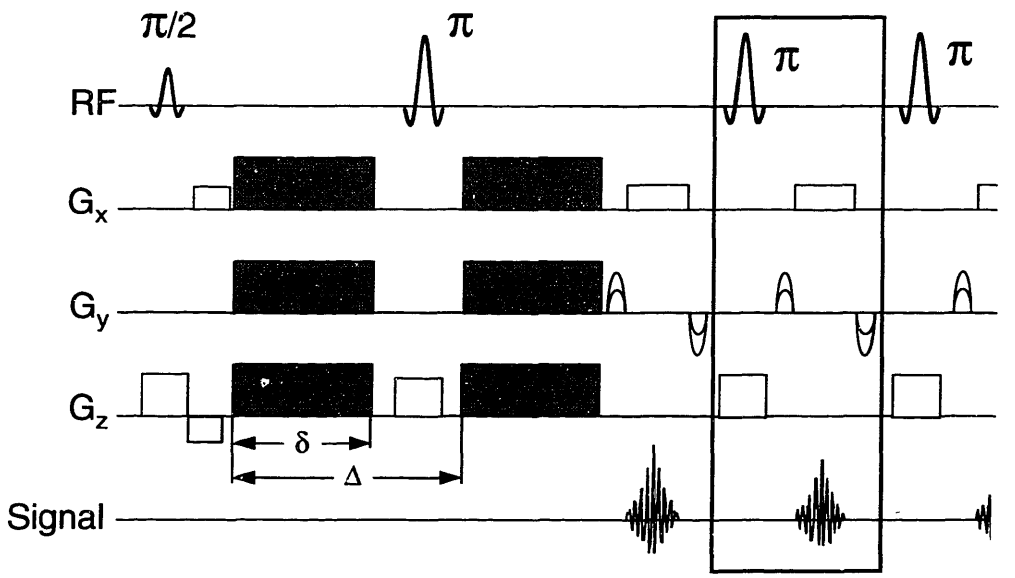

Figure 6-1: DW-RARE imaging sequence. The navigator can be placed anywhere in the echo train by removing the phase encoding gradients at that location.

2c), the stimulated pathway "goes out of the acquisition window" and disappears. In Fig. 6-3d) the resolution in the phase direction has been increased and now the artifacts are visible again.

The RARE technique is well known to be very sensitive to the phase of the image echoes [134]. In order for the correction scheme proposed in ref. [2] to work correctly, all the stimulated echo pathways have to be spoiled, because they will not have the same phase distortion as the principal spin-echo pathway. Also, even in single shot RARE imaging or in single shot GRASE imaging [76], the image would not be free from motion artifacts, because even and odd numbered spin echoes have opposite phase artifacts[3]. For comparison, in EPI all the echoes have the same phase artifact, since EPI uses gradient echoes. Therefore, it is not necessary to correct single shot EPI data from phase artifacts due to the diffusion gradients. The reconstructed EPI image will have an arbitrary phase which is discarded by reconstructing a magnitude image. In short, one can say that EPI is capable of imaging both "real and imagin-

[3]See Eq. (3.31). The 180° pulses conjugates the magnetization. If the magnetization is not purely real, image artifacts are inevitable.

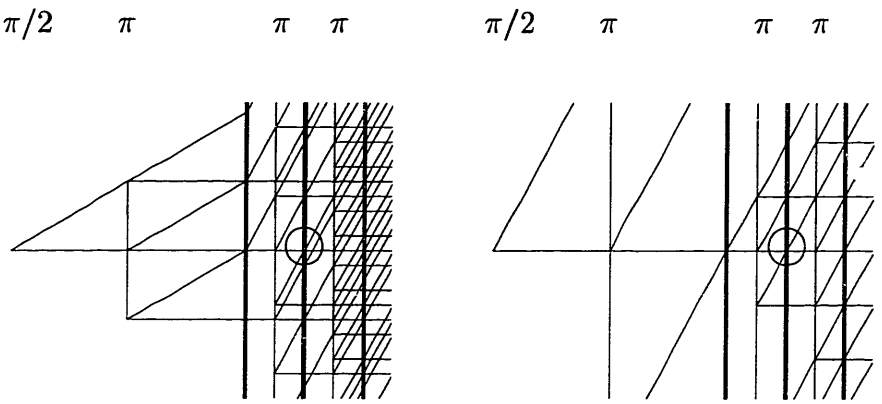

Figure 6-2: Pathway diagrams for the DW-RARE sequence assuming imperfect refocusing pulses. **Left:** Little spoiling or low b-factor. **Right:** Good spoiling or high b-factor. The solid lines show the timing of the echoes and the circles highlight the pathways that fall into the acquisition window of echo no. 2.

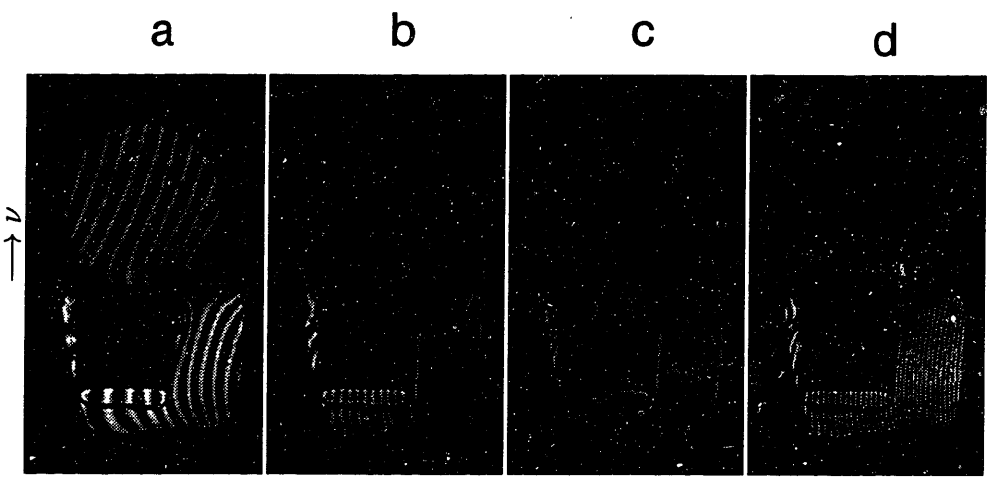

Figure 6-3: Illustration of artifacts from stimulated echoes because of violation of the CPMG condition. These images are formed from echo no. 2 only. **a)** b_y = 0.025 s/mm^2, N_y = 128. **b)** b_y = 0.1 s/mm^2, N_y = 128. **c)** b_y = 0.2 s/mm^2, N_y = 128. **d)** b_y = 0.2 s/mm^2, N_y = 256.

ary magnetization" whereas RARE/FSE and GRASE can only form images of "real magnetization".

6.3.1 Navigators Echo Location

The navigator can be put anywhere in the echo train, however, its position determines the SNR in the final image. Consider the conventional DW-PGSE navigator sequence with single navigator echo followed by the image echo. Let A denote the attenuation between the first and the second echo and σ^2 denote the image noise variance. If the navigator is acquired first, the relative signal loss in the image can be considered to be A. However, if the second echo is used for the navigator, the final image noise will be affected by the noise which propagates from the navigator in the phase correction algorithm described in ref. [2]. According to Eq. (4.10), the corrected image noise can be approximated as

$$\sigma^2_{\text{corr}} \approx \sigma^2 \left(1 + \frac{1}{N_y} \sum_{k=-N_y/2}^{N_y/2-1} \frac{|S(k)|^2}{|S(0)|^2 A^2} \right) \tag{6.3}$$

where $|S(k)|$ denotes the amplitude of the k-lines in the phase encoding direction. The propagation of noise will therefore depend on the object's shape. However, for most large objects the baseline amplitude $|S(0)|$ is by far the largest k-line and the noise increase therefore small. Typically, for A as low as 0.5 this leads to almost no increase in the image noise. When $A = 0.1$ the increase in image noise is ca. 50%. In terms of SNR it should therefore be better to have the navigator in the end of the echo train. Examples of projections reconstructed from navigator echoes are shown in Fig. 6-7.

6.4 Results

Figures 6-4 - 6-6 show DW-RARE images with variable echo train length and diffusion weighting of $b = 400\,\text{s/mm}^2$. Neither head restraints nor cardiac gating was used. Although it is hard to compare these *in vivo* images, because each of them has different motion artifacts, they all show great improvement from the navigator post processing scheme. The images in Fig. 6-4 and Fig. 6-5 seem to have better signal when the navigator is in the end of the echo train, however, in Fig. 6-6 the one with the navigator in the front is better. It is clear from all the images that the correction scheme cannot correct for the strong pulsatile motion in the vicinity of the cerebrospinal fluid (CSF). Close to the CSF, the brain tissue moves radially due to changes in CSF pressure throughout the cardiac and respiratory cycles. The assumption of rigid translational motion and rotation therefore breaks down.

6.5 Conclusion

The initial phantom and *in vivo* experiments show that the navigator correction scheme can in principle be extended from PGSE to DW-RARE imaging if proper spoiling of stimulated echoes is achieved. We have found that the amplitude of the navigator varies most in the center of the brain. This indicaties signal cancellation due to spatially varying motion around the CSF. Therefore, it is clear that cardiac gating is necessary to minimize the influence of pulsatile brain motion. Another limitation is that the navigator technique works only when the diffusion sensitivity is in the phase encoding direction. Our results agree with those in a recent study by Crespigny *et al.* [25] which used the navigated PGSE sequence [2]. They found cardiac gating to be necessary in order to get artifact free images. Furthermore, they blindly applied the diffusion sensitivity in all three directions, however, as to be expected, found least motion artifacts in the corrected images when the diffusion sensitivity was in the phase encoding direction. Crespigny *et al.* found, that in 20 patient examinations, 7 studies had virtually motion free images in all three diffusion directions. Good quality diffusion images were always obtained from at least one direction.

It is clear, from our results and the previous discussion, that the success of the navigator technique relies heavily on cardiac gating and it is not possible to obtain accurate isotropic ADC maps (trace of the diffusion tensor). For that, a sequence that is inherently more robust to motion artifacts is needed, such EPI or the Line Scan Diffusion Imaging technique which is studied in chapter 7.

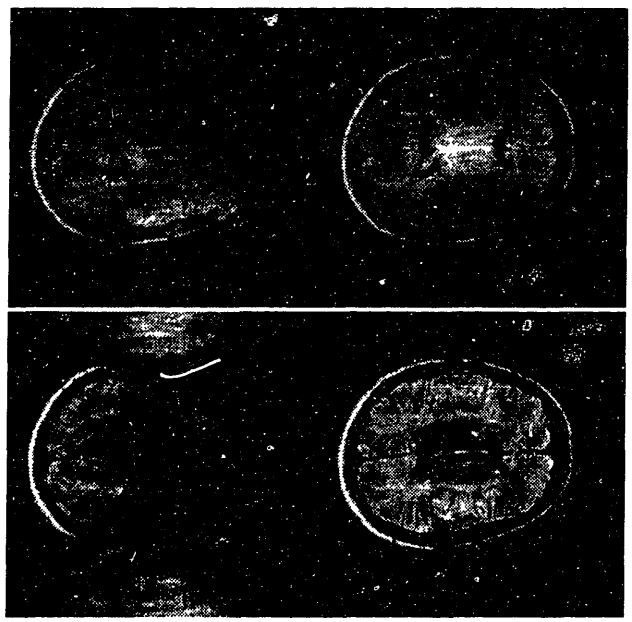

Figure 6-4: The original and the corrected image from an echo train length of **one** plus a navigator. $b = 400\,\mathrm{s/mm^2}$.

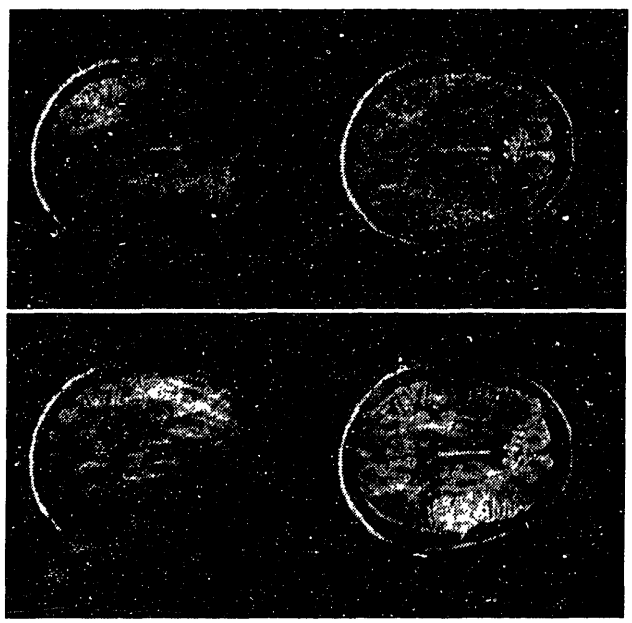

Figure 6-5: The original and the corrected image from an echo train length of **two** plus a navigator. $b = 400\,\mathrm{s/mm^2}$.

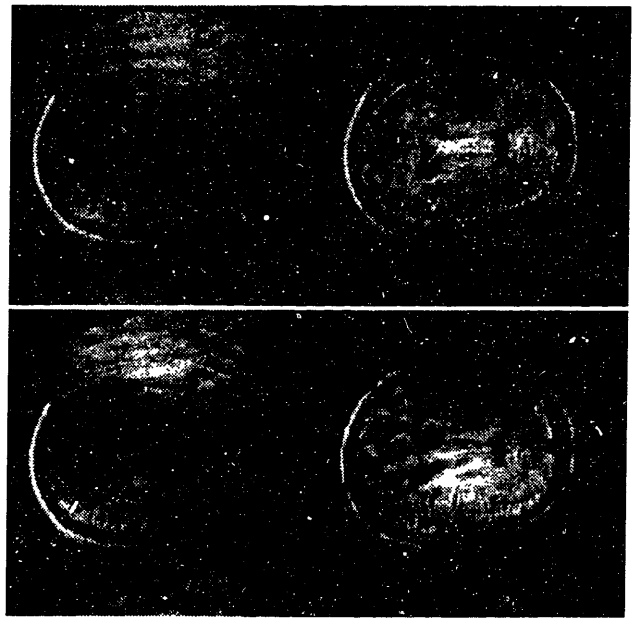

Figure 6-6: The original and the corrected image from an echo train length of **three** plus a navigator. $b = 400\,\mathrm{s/mm^2}$.

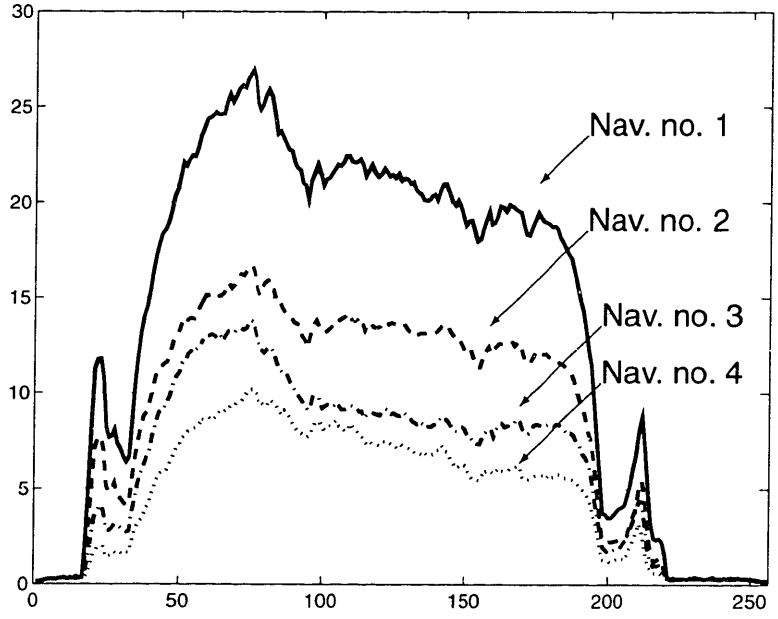

Figure 6-7: A comparison of the projection constructed from the average of the navigators used in Figs. 6-4 - 6-6.

Chapter 7

Line Scan Diffusion Imaging

7.1 Introduction

APPROACHES which offer good immunity to motion artifacts on conventional scanners are volume or column-selective NMR. Column or line scan techniques have been used for *in vivo* spectroscopic studies [91], thermal mapping [56], and for quantitative flow and diffusion measurements [19,37,60,88,89]. However, these 1D-profile techniques lack the anatomic details of 2D methods.

We have extended the column-selective technique into what we call Line Scan Diffusion Imaging (LSDI) [47]. In this chapter, we describe the LSDI sequence as well as some of its intrinsic properties. Diffusion images from the brain and the abdomen of a volunteers are shown as well as images from LSDI stroke studies at both 0.5T and 1.5T. Finally, we compare LSDI with diffusion weighted EPI, which we consider as the technique of reference for *in vivo* diffusion imaging.

7.2 Methods

7.2.1 Line Scan Diffusion Imaging

LSDI uses multiple diffusion weighted spin-echo column excitations to form a two-dimensional image. As shown in Fig. 7-1, the basic sequence is composed of a spatially selective $\pi/2$ and π pulses. The diffusion gradients can be applied in arbitrary directions and are placed on both sides of the refocusing π pulse, followed by a standard frequency encoding readout along the selected column.

The LSDI image is composed of a series of one-dimensional *magnitude* profiles obtained from parallel columns lying in the image plane. The sequential collection of this line data in independent acquisitions makes the sequence largely insensitive to

bulk motion artifacts since no phase encoding is used and shot to shot phase variations are fully removed by calculating the magnitude of the signal.

Each column is formed by the intersection of two planes selected by the two slice selective RF pulses. For the acquisition of one column, the most obvious choice is to select one plane orthogonal to the image plane and the other within the image plane itself. In the repetitive process of line acquisition, this procedure leads to spin saturation and subsequent tissue specific T_1 associated signal loss unless a sufficient period of time between column excitations is permitted. For quantitative diffusion maps composed of 256 lines, this would lead to an unacceptable residence time in the scanner.

To allow for a faster repetition of the excitation without causing spin saturation the excitation scheme shown in Fig. 7-2 is used. The basic principle is to avoid an alignment between the planes excited by the selective pulses and the imaging plane. The selected planes are positioned such that the volume at their intersection forms the column of interest in the imaging plane. The angles α and β between the selected planes and the imaging plane (Fig. 7-2) can be chosen with a certain degree of freedom.

7.2.2 Interleaving Scheme

Dependent on the field of view (FOV), the number of columns (N) and the size of their cross-sections a and b, the selected columns which form the lines in the image may partially overlap. In this case, spin saturation must be avoided by using an interleaved acquisition scheme as shown in Fig. 7-3. For a sufficiently large number of lines, the time period between successive line acquisitions is then restricted primarily by the echo time required for adequate sensitivity to diffusion.

Figure 7-3 shows an example where the image plane is covered by $N = 31$ columns and the column step size, s, is 4. The number of columns per sweep is therefore $\lceil N/s \rceil$. Here $\lceil x \rceil$ denotes the smallest integer which is larger or equal to x. Also shown is the order of the acquired columns for each sweep through the image plane. The column index, c, can in general be expressed as a function of the excitation counter, e, the number of columns, and the step size

$$c = (s \times (e \bmod \lceil N/s \rceil) + \lceil e/\lceil N/s \rceil \rceil) \bmod N \tag{7.1}$$

As shown in Fig. 7-3, during sweep number 0 no data is collected, however, in sweep number 4 the columns excited in sweep 0 are re-excited and data is acquired. The purpose of this extra sweep is to ensure a steady-state magnetization in each column. This is important, when columns overlap and if there is cross-talk due to imperfect slice profiles. It should be noted, that when many images (many b-factors) are acquired from the same slice, this extra sweep needs only to be done once. The

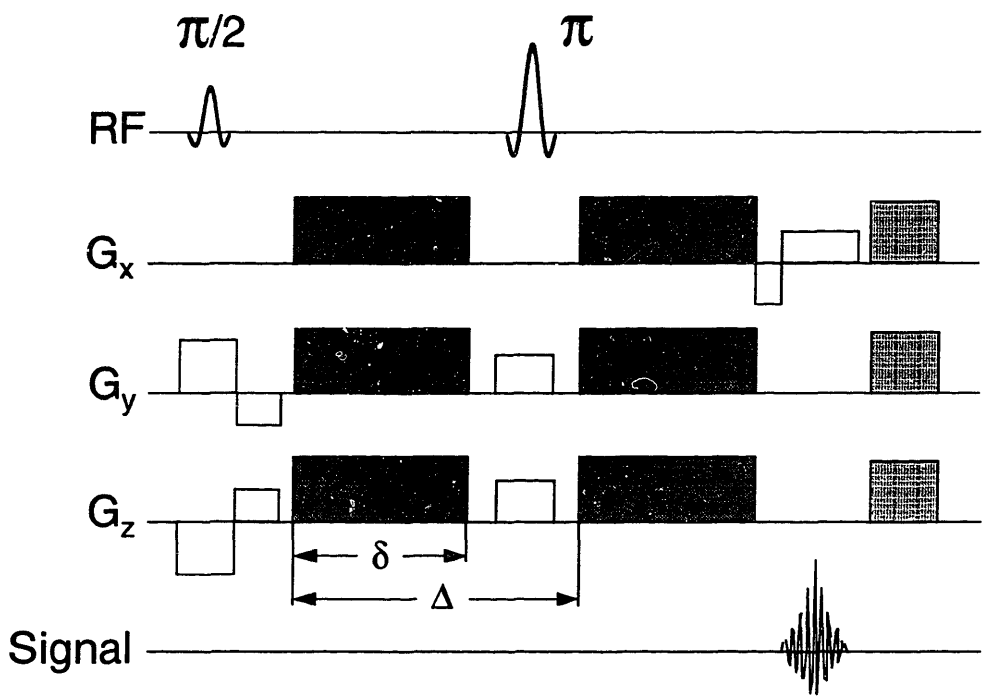

Figure 7-1: The basic LSDI sequence diagram. The dark shaded areas indicate the diffusion gradients and the less dark areas the crusher gradients. RF, radio frequency excitation; x, read-out direction; y and z, select directions.

effective repetition time is defined as the time between the excitation of two adjacent columns. For all columns except number 0 it is given by

$$\mathrm{TR}_{\mathrm{eff}} = \lceil N/s \rceil \cdot \mathrm{TR} \tag{7.2}$$

Here TR refers to the repetition time of the $\pi/2$ excitation pulse. From Fig. 7-3, we see that if the number of columns were 32, the effective repetition time of the columns excited in sweep number 4 would be different from the effective repetition time of the other columns. Therefore, in our images we use odd column numbers, e.g. 255, 127, or 63.

As long as $\mathrm{TR}_{\mathrm{eff}}$ is large enough, signal loss due to spin saturation is avoided. The column step size, s, has to be chosen such that $s \times \mathrm{FOV}/N$ is larger than the column width. Apart from the time spent on the extra steady-state sweep, the total scan time for one image is given by $N \times \mathrm{TR}$.

In the repetitive process of column excitation, the selective π pulses intersect with previous selective $\pi/2$ pulses outside the image plane as shown in Fig. 7-4a. Particularly, if the diffusion gradients are turned off, this leads to secondary echoes and

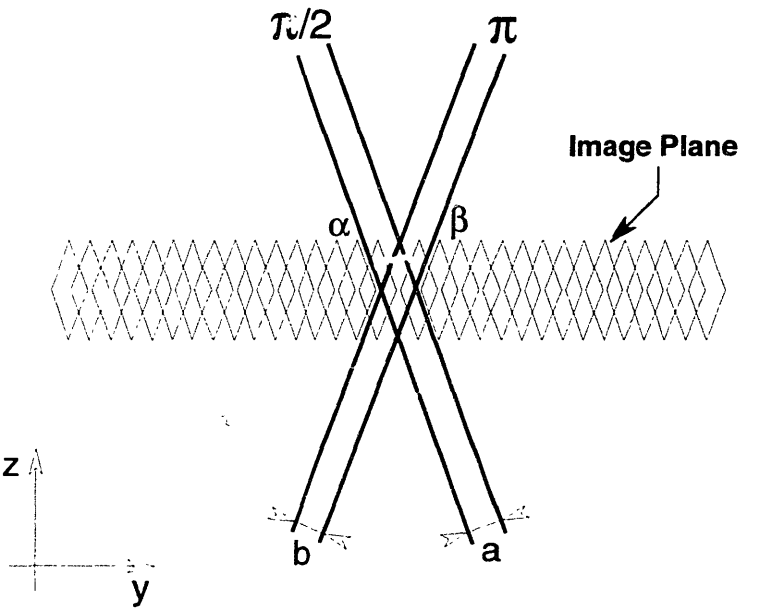

Figure 7-2: The selective excitation produced by the LSDI sequence shown in Fig. 7-1.

ultimately to image artifacts. To some extent these echoes can be reduced by crusher gradients after signal readout. The crusher gradient direction is alternated between each excitation [1], to postpone the refocusing of secondary echoes such that T_2 relaxation and diffusion attenuation renders them insignificant. By alternating the orientation of the selective pulses, as shown in Fig. 7-4b, there is an efficient elimination of the strongest secondary echoes which permits a substantial reduction in duration and amplitude of the crusher gradients.

With short repetition times, the heavy use of diffusion gradients can lead to overheating of the gradient amplifiers. In order to reduce the gradient duty-cycle, we have modified our interleaving scheme such that the sequence alternates between high and low diffusion weighting. Two images, with high and low b-factors, are therefore acquired simultaneously. In this way, when the total number of columns is odd, the subsequent acquisition of each column has a diffusion weighting which is different from its current one. An nice feature of this scheme is, that it totally eliminates any secondary echoes. Furthermore, by making the low b-factor sufficiently high, the FID resulting from imperfections in the refocusing pulse is eliminated. Also, the strongest stimulated echo pathway, $TLLT$, which because of imperfect slice profiles comes from a large fraction of the image volume, is successfully eliminated by alternating between the high and the low b-factor.

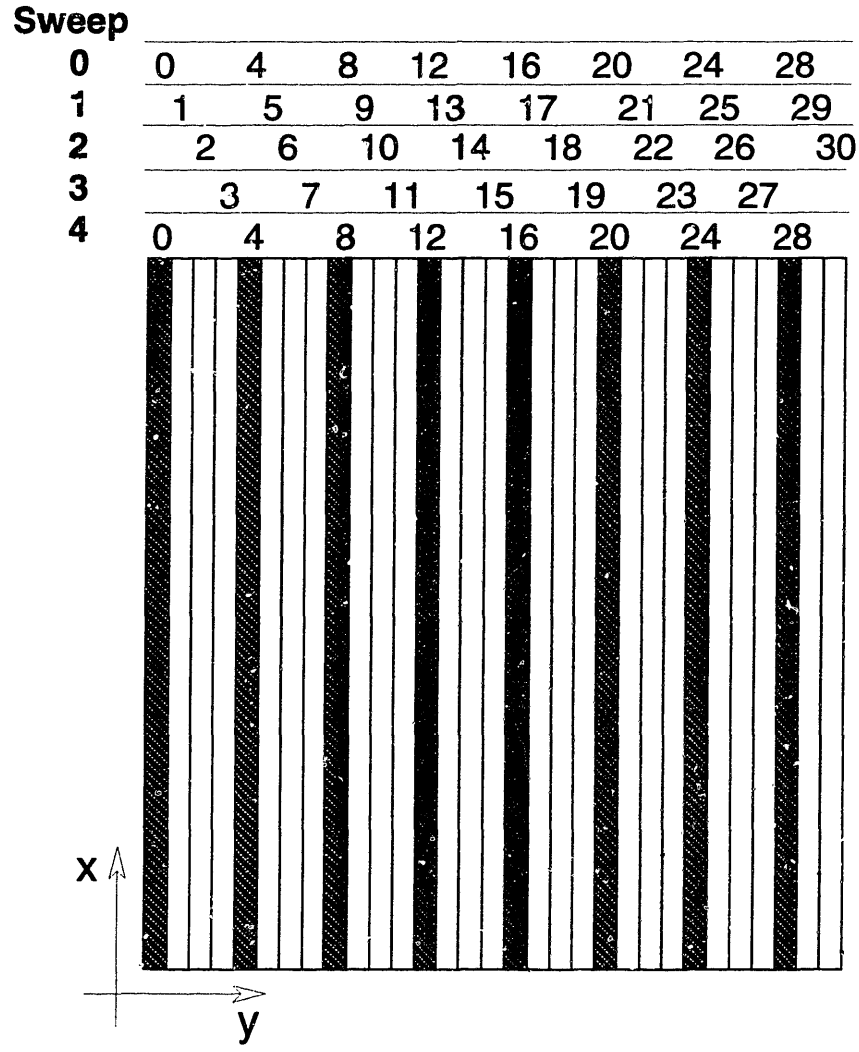

Figure 7-3: Interleaved acquisition scheme, for a line scan image composed of 31 columns. To reach steady state of the magnetization, the first set of columns (hatched columns) is excited twice (sweep 0 and 4), and data is collected at the last excitation only. With the interleaving shown here, the repetition time can be reduced by a factor of ca. 8 without increasing spin saturation.

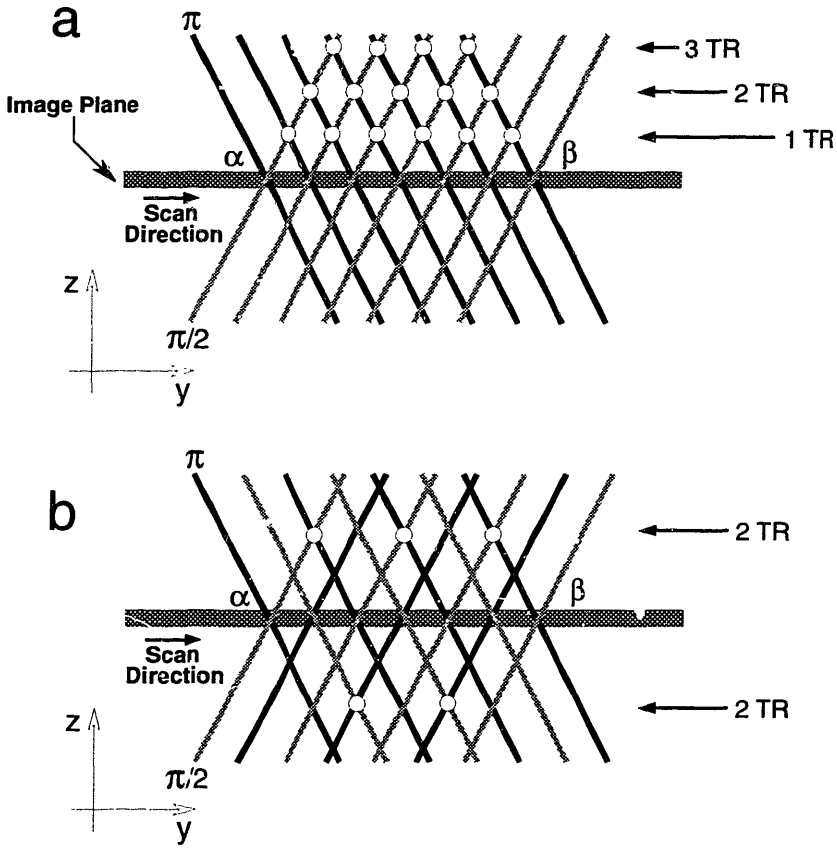

Figure 7-4: Two possible arrangements (**a** and **b**) for the sequence of selective excitations. Selective pulses of $\pi/2$ (grey) and π (black), which define the column in the image plane, are applied sequentially from left to right. The selective π pulse (inversion pulse) intersects with earlier selective $\pi/2$ pulses, outside the image plane. This produces secondary echoes. The strength of these echoes decreases with the delay (number of repetition time intervals TR) between the selective pulses. With arrangement **a**, $\pi/2$ (α) and π (β), for each excitation, all previous $\pi/2$ pulses will contribute to secondary echoes by inversion after 1 TR, 2 TR, 3 TR, etc. With arrangement **b**, $\pi/2$ (α) and π (β), followed by $\pi/2$ (β) and π (α), pulses will contribute to secondary echoes only by inversion after 2 TR, 4 TR, 8 TR, etc. Thus every second and particularly the strongest secondary echo (inversion after 1 TR) is eliminated in arrangement **b**.

7.2.3 The LSDI Point-Spread Function

In order to understand the relation between the object and the reconstructed image, one has to know the point-spread function (PSF) of the imaging technique [66]. By using the interleaving scheme described in the previous section, the PSF is spatially invariant.

The resolution in the frequency encoding direction (x) along the column is determined as in the standard Fourier imaging techniques, by sampling bandwidth, gradient amplitude and duration. Hence, along the column the shape of the point-spread function is the sinc function.

The point-spread function in the two other directions, y and z, is a triangle which geometry is determined by the thickness, a and b, and the angles, α and β, of the selected planes (see Fig. 7-2). The signal strength is then determined by the cross-sectional area of the columns.

For imaging with overlapping columns the symmetric solution ($\alpha = \beta$, $a = b$) is advantageous, because most of the signal derives from the central portion of the cross-section. For each volume element, this results in a signal distribution, that is analogous to conventional Fourier imaging, where the signal contribution of neighboring volume elements decays with the distance from the voxel center. The width of the selected column defines the in-plane resolution and the height defines the image slice thickness. We use the half-maximum of the PSF to define the effective resolution. Hence, for the symmetric case, the effective image plane slice thickness can be defined as $0.5 \times a/\cos\alpha$ and the effective in-plane resolution as $0.5 \times a/\sin\alpha$.

In conventional imaging, the established ratio between slice thickness and in-plane resolution lies in the range of 2:1 and 4:1. This ensures good resolution of anatomic details under the constraints of signal-to-noise ratio (SNR). As shown in Fig. 7-5, for a constant cross-sectional area, inclination angles between 65° and 75° produce a similar range of height to width ratio. Compared to an inclination at 45°, inclination at 70° improves the in-plane resolution by 40%, without reducing the SNR. Because of the reduced overlap it is possible to use smaller column step size and therefore longer effective repetition time.

One can argue that overlapping of the columns is favorable, because it avoids undersampling of the image, or what is usually referred to as aliasing [66]. If the columns overlap substantially, the image can be low-pass filtered without any significant loss in resolution, to improve the SNR.

7.2.4 Signal-to-Noise Considerations

The SNR of the LSDI technique, $\mathrm{SNR}_{\mathrm{lsdi}}$, is naturally lower than the SNR of a regular spin-warp Fourier image, $\mathrm{SNR}_{\mathcal{F}}$. This is because in the LSDI-technique, a column, as

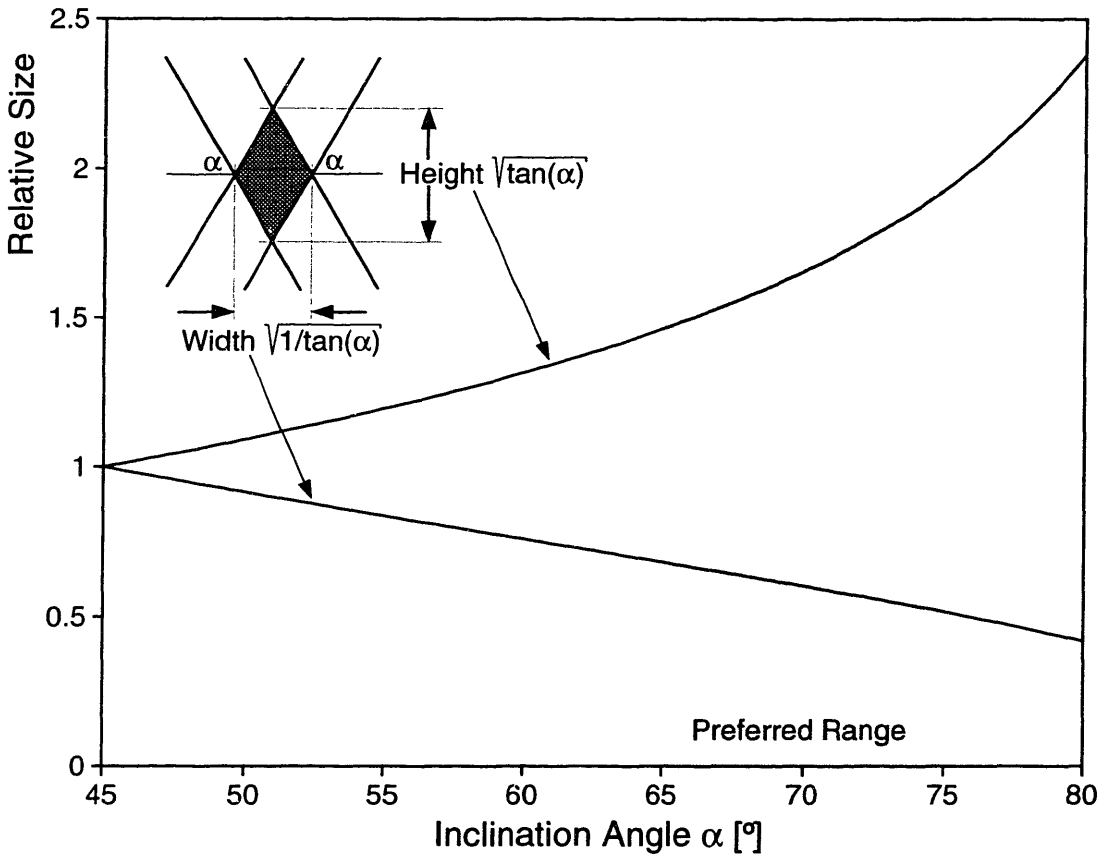

	45°	65°	75°	α
Height/Width	1	2.1	3.7	$\tan\alpha$
Relative Width	1	0.68	0.52	$\sqrt{1/\tan\alpha}$
Rel. Sel. Slice Thickness	1	0.88	0.71	$\sqrt{2\sin\alpha\cos\alpha}$

Figure 7-5: Relation between inclination angle and height and width of columns for a constant cross-sectional area. With inclination angles between 65° and 75°, the height to width ratio of the columns is comparable to the optimal height to width ratio of volume elements in conventional imaging.

opposed to a slice full of spins contributes to the NMR signal. In order to quantitatively compare the two, we assume the same slice thickness for both methods. We then define the effective column width, CW, as the ratio of the cross-sectional area and the slice thickness. By this definition, the actual slice thickness becomes irrelevant.

Consider an ideal uniform phantom which extends over the whole field of view. The signal received from each column excitation is proportional to the column width. The noise we denote by n. When Fourier encoding is used, only the baseline ($k_y = 0$) gives nonzero NMR signal, whose strength is proportional to FOV. For this particular phantom, the other k-lines only contain noise; the same as in the LSDI case. This is because the Fourier transform of this phantom is a sinc function with its zeros located in k-space where the k-lines are acquired. The total noise in the Fourier image will depend on the number of k-lines, i.e., the image resolution N. The noise image intensity in the Fourier image is the square root of the total noise variance, n^2N. For this particular phantom we can therefore write

$$\frac{\mathrm{SNR}_{\mathcal{F}}}{\mathrm{SNR}_{\mathrm{lsdi}}} = \frac{\mathrm{FOV}/\sqrt{n^2N}}{\mathrm{CW}/n} \tag{7.3}$$

It turns out that this equation holds for any object, given that N is high enough such that all the significant spatial frequencies of the object are acquired. This is easily proven by using the scaling property of the Fourier transform. For a "fair" comparison, we will assume the same spatial resolution in both of the imaging techniques. This implies that $N = \mathrm{FOV}/\mathrm{CW}$. Substituting this into Eq. (7.3) gives

$$\frac{\mathrm{SNR}_{\mathcal{F}}}{\mathrm{SNR}_{\mathrm{lsdi}}} = \sqrt{\frac{\mathrm{FOV}}{\mathrm{CW}}} \tag{7.4}$$

This equation ignores the fact that for short repetition times, the influence of relaxation is different in the two methods, because in the LSDI technique it is the effective repetition time that matters. The partial saturation of the equilibrium magnetization in a spin-echo sequence is given by $M_{\mathcal{F}} = M(\mathrm{TR})$, where $M(t)$ is defined as [16]

$$M(t) = M_0(1 - 2\exp(-(t - \mathrm{TE}/2)/T_1) + \exp(-t/T_1)) \tag{7.5}$$

and similarly $M_{\mathrm{lsdi}} = M(\mathrm{TR}_{\mathrm{eff}})$. Equation (7.5) assumes that T_2 is short compared to the effective TR. The echo time, TE, is determined by the diffusion sensitivity needed and the gradient strength. Also, according to Fig. 7-3, the minimum step size needed to avoid saturation of the magnetization in the succeeding column is $s = \mathrm{CW}/(\mathrm{FOV}/N)$. By combining this with our earlier selection of $N = \mathrm{FOV}/\mathrm{CW}$ and Eq. (7.2) we find that $\mathrm{TR}_{\mathrm{eff}} = \mathrm{TR} \times \mathrm{FOV}/\mathrm{CW}$, were TR refers to the repetition time of the LSDI sequence. Finally, we get

$$\frac{\mathrm{SNR}_{\mathcal{F}}}{\mathrm{SNR}_{\mathrm{lsdi}}} = \sqrt{N} \cdot \frac{M_{\mathcal{F}}}{M_{\mathrm{lsdi}}} \tag{7.6}$$

Note that this equation assumes equal imaging time for both techniques. For long TR, the LSDI-technique benefits from shortening the repetition time and the use of averaging. This can be done because of the long effective repetition time, TR_{eff}. We denote the number of excitations (averages) by NEX. Equation (7.6) then becomes

$$\frac{SNR_{\mathcal{F}}}{SNR_{lsdi}} = \sqrt{\frac{N}{NEX}} \cdot \frac{M(TR)}{M(TR_{eff}/NEX)} \tag{7.7}$$

In a cardiac gated PGSE sequence, the repetition time is commonly set to $2 \times RR \approx$ 1500ms. It is possible to use up to 10 NEX if TE allows TR_{lsd} to be less than 150ms. Table 7.1 compares the SNR ratios of the two imaging techniques for single slice imaging.

T_1/ms	TR_{eff}/ms	LSDI-NEX	$SNR_{\mathcal{F}}/SNR_{lsdi}$
500	1500	10	2.4
500	2500	16	2.0
1000	1500	10	1.9
1000	2500	16	1.8
2000	1500	10	1.3
2000	2500	16	1.4

Table 7.1: The SNR ratio of PGSE Fourier imaging versus LSDI according to Eq. (7.7) as a function of several parameters. The resolution is N = 63, and the LSDI repetition time, TR, is assumed less than 150ms allowing 10 NEX when TR_{eff} is 1500ms and 16 NEX for a TR_{eff} of 2500ms. The SNR ratio with N of 127 and 255 can be found by multiplying the values found in the table by 1.4 and 2, respectively.

Finally, it is interesting to compare a single-shot EPI sequence with the LSDI sequence. If we ignore transverse relaxation and assume that the EPI sequence uses the same time for acquiring all the echoes as the LSDI sequence uses for acquiring a single line, i.e. EPI uses N times larger bandwidth, then the sequences should have equal signal-to-noise ratio.

7.2.5 Optimizing the LSDI Sequence

Gradients

Two images with different diffusion weighting are needed to assess the diffusion coefficient in the direction of the diffusion gradient. Because of the microscopic structure of tissues, the diffusion is anisotropic and measurements in three orthogonal directions must be obtained in order to acquire a diffusion map (trace of the diffusion tensor) [6] and information about diffusion anisotropy[1]. To date, this has been done by measuring the diffusion along the MR imager gradient coil principal axes, $\hat{x}$, $\hat{y}$, and $\hat{z}$. Simultaneous use of all three gradients results in a considerably higher gradient amplitude. If the maximal relative gradient amplitude in $\hat{x}$, $\hat{y}$ and $\hat{z}$ direction is equal, we define a new orthogonal coordinate system as

$$\begin{aligned} \hat{x}' &= -\hat{x} + \hat{y} - \hat{z}/2 \\ \hat{y}' &= \hat{x} + \hat{y}/2 - \hat{z} \\ \hat{z}' &= \hat{x}/2 + \hat{y} + \hat{z} \end{aligned} \tag{7.8}$$

The reader can verify that $\hat{x}', \hat{y}'$ and $\hat{z}'$ are mutually orthogonal. Furthermore, this choice of axis gives the maximum gradient strength for three orthogonal directions, $G_{x'}, G_{y'}$ and $G_{z'}$. An identical diffusion gradient scheme has been derived independently by other researchers as well [116]. The amplitude gain is 50% compared to using the conventional gradient axes. For a given diffusion sensitivity, the duration and ultimately the echo time can be reduced by approximately one fourth because the effect of the diffusion gradients is proportional to the square of their amplitude and the cube of their duration. The disadvantage of using this modified gradient axis is that they no-longer coincide with the principal axis of the image. For diffusion tensor trace and anisotropy maps, this does not pose any problems since the trace is rotation invariant.

The LSDI-technique can be made sensitive to diffusion in all three directions at the same time so that the trace of the diffusion tensor can be acquired in only two shots [87, 145]. This, however, leads to longer echo times and increased T_2 decay or low and non-optimal b-factors, as discussed below. Due to the rather limited signal strength of the LSDI technique, our current implementation acquires the trace in either four or six shots.

The diffusion weighting is determined in terms of the b-factor as defined by Eq. (3.4). The signal attenuation is then described as $S(b) = S(0)\exp(-b \cdot \mathrm{ADC})$. The apparent diffusion coefficient can be estimated as the slope of a linear least-squares fit to the logarithm of the signal amplitude.

[1] More measurements are needed to estimate all the coefficients in the diffusion tensor.

The results in section 4.4.1 indicate that the optimum b-factor for brain diffusion maps is close to $750\,\mathrm{s/mm^2}$. However, the improvement in the precision is minimal as b exceeds $500\,\mathrm{s/mm^2}$.

When many averages are used, the polarity of the diffusion gradients is alternated, to reduce the effect of cross-terms from the imaging and slice selective gradients [88]. Any averaging must be done after the calculation of the magnitude of the signal.

Receiver Bandwidth

The optimum bandwidth is found by maximizing the SNR of the spin echo with respect to the sampling rate

$$T_{\mathrm{opt}} = \arg\max_{T} \left\{ \exp\left(-\frac{TN_x}{2T_2}\right) \sqrt{T} \right\} = T_2/N_x \tag{7.9}$$

Note that with this optimal sampling rate, the intrinsic spectral broadening due to T_2 relaxation [16] is not a problem because it is smaller than the voxel width, i.e., $(1/T_{\mathrm{opt}})/N_x = 1/T_2 > 1/\pi T_2$. The PSF will be similar to the regular sinc function but with smaller sidelobes. With 128 samples in the frequency encoding direction, this indicates that the optimal bandwidth for brain imaging is in the range from 640Hz to 1.2kHz. Note that here the bandwidth refers to only half of the frequency passband, i.e., BW=$1/2T$. This low bandwidth makes the image very sensitive to distortions due to field inhomogeneities and chemical shift. For most of our studies on the 1.5T system, we used either 8kHz or 4kHz bandwidth. On the 0.5T system, lower bandwidth can be used since distortions from field inhomogeneities and chemical shift scale with field strength. We found that 2kHz bandwidth gave a good compromise between SNR and short acquisition time[2].

Filtering

Initially, before the two point logarithmic fit, the images were processed with the bias reduction algorithm [52] in chapter 4. This is only important for regions with very low SNR and has no effect on pixels with high SNR. Then the images were low-pass filtered (convolved) [66] in the direction orthogonal to the columns by the kernel $(1, 2, 3, 2, 1)/9$. This improves the SNR by a factor of two without any significant loss of spatial resolution because of the column overlap. Note that the shape and the width of the kernel is chosen according to the way the columns overlap, i.e. almost like a matched filter. When the number of column is less than 255, we interpolate the columns to 255, before we apply the kernel. The SNR improvement from the kernel

[2] A 1kHz bandwidth makes the readout time 128ms. Therefore, the repetition time exceeds 200ms, which we found to be too slow.

specified above is less in this case. For instance, when 127 columns are interpolated into 255 columns, the SNR improvement is only ca. $\sqrt{2}$.

Later, we found that it is better to estimate the ADC map before any filtering or bias reduction. The ADC map can then be filtered by the kernel described above. Figures 7-14 and Figs. 7-16 - 7-18 are processed in this way. See section 4.4.2 for further details.

7.3 Results

The LSDI sequence described in the previous section was implemented on a 1.5T and 0.5T GE Signa whole body scanners (General Electric Medical Systems, Milwaukee, Wisconsin) both equipped with the 5.4 operating system and standard gradient hardware with a maximum gradient strength of 1G/cm. The images were reconstructed on-line with the Signa software, however, diffusion and anisotropy maps were calculated off-line.

7.3.1 Phantom Studies

Diffusion Sensitivity

To verify the diffusion sensitivity of the LSDI sequence, the diffusion coefficient of doped water in a phantom was measured at "room temperature" in all three directions, $\hat{x}'$, $\hat{y}'$ and $\hat{z}'$. The b-factor was stepped through the values of 5, 105, 205, 305, 405 and 505 s/mm^2. For each b-factor an LSDI image was acquired of which a region of interest (ROI) was selected and used to average the signal intensities. For each b-factor, two images were acquired with opposite polarities on the diffusion gradients, as described in the end of the previous section. The results are shown in Fig. 7-6. Clearly, the logarithm of the signal as a function of b fits very well to a straight line. The least-squares fit yielded the following diffusion coefficient: $D_{x'} = 1.82\,\mu$m^2/ms, $D_{y'} = 1.80\,\mu$m^2/ms, and $D_{z'} = 1.78\,\mu$m^2/ms. For comparison, when only a single polarity on the diffusion gradients was used, the best fits were: $D_{x'} = 1.78\,\mu$m^2/ms, $D_{y'} = 1.82\,\mu$m^2/ms, and $D_{z'} = 1.84\,\mu$m^2/ms. The relative precision of the averaged ROIs was from 0.06% to 0.17%, hence, the precision of the estimates is 0.0026 μm^2/ms. Therefore, difference in the estimates of the diffusion coefficients has to be associated with cross-terms and non-idealities in the gradients.

Image Quality

To analyze the image quality of the LSDI technique, a standard image quality phantom was used. Several inclination angles were tried and the thickness of the slices, a, was

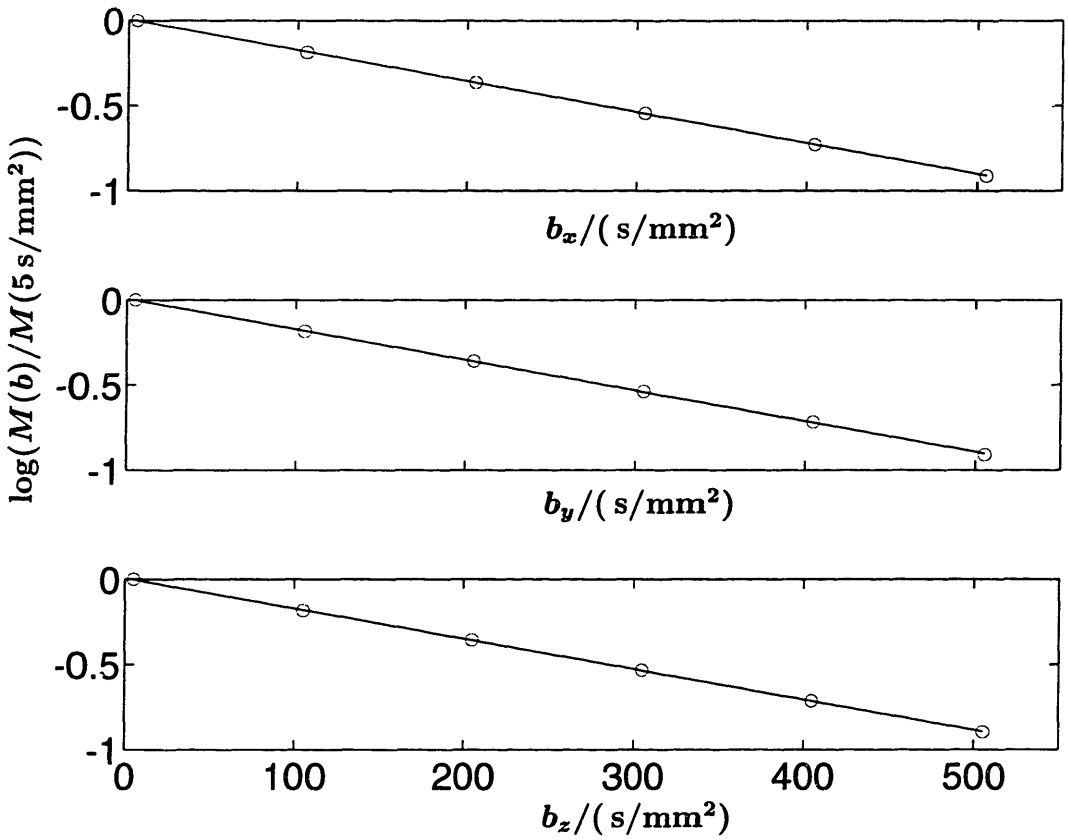

Figure 7-6: The logarithm of the signal diffusion attenuation of doped water plotted against the *b*-factor. The diffusion sensitivity is in direction x (top), y (middle) and z (bottom). The circles represent the means of the ROIs and the lines show the least-square linear fit.

varied. The LSDI images are compared to a regular fast spin-echo image in Fig. 7-7. The LSDI images in Fig. 7-7a) and Fig. 7-7b) should according to Fig. 7-5 have the same SNR, however, because of imperfect slice profiles this is not the case. The LSDI phantom images were acquired with both high and low *b*-factor but Fig. 7-7 shows the images with the low *b*-factor. Because the echo time is not the same in the LSDI sequence and the FSE sequence, it does not make any sense to compare the SNRs. The most important conclusion to be drawn from Fig. 7-7 is, that 70° inclination angle is better than 45° inclination angle since it gives a better compromise between SNR and resolution. Furthermore, apart from noise and some blurring, the image quality of the LSDI images is very good and no artifacts from secondary echoes are present.

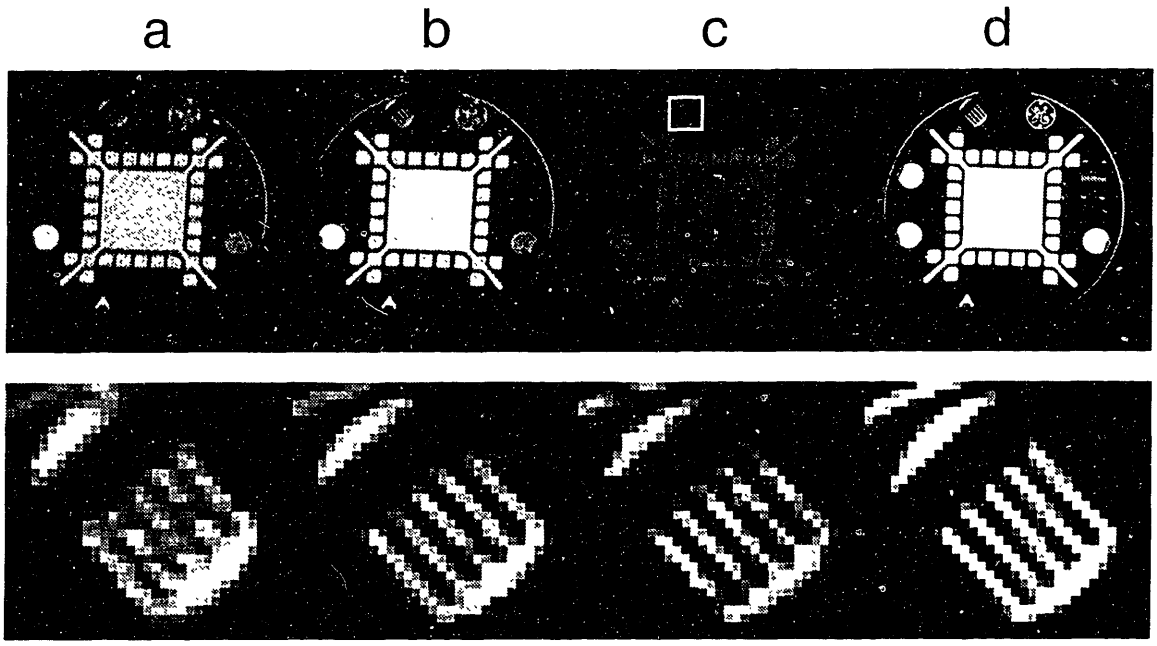

Figure 7-7: Comparing the image quality of three LSDI images, with a different inclination angle (α) and slice thickness (a), to a conventional fast spin-echo image (FSE or RARE) with an echo train length of 8. The resolution of the LSDI images in a-c is 128x256c and the resolution of the FSE image is 256x256p. The images below show the region which is outlined in c). **a)** α = 45°, a = 5mm, and SNR = 16. **b)** α =70°, a = 4mm, and SNR = 22. **c)** α =70°, a = 3mm, and SNR = 13. **d)** Fast spin-echo image with a 7mm slice thickness and SNR = 127.

7.3.2 Diffusion Imaging of the Brain

Healthy Volunteer

To demonstrate the quality and the precision of the LSDI technique, we acquired four sets of coronal ADC maps of a healthy volunteer. No cardiac gating or head constraints were used. The slice selective pulses were chosen such that $a = b = 5$mm, $\alpha = \beta = 70°$ (see Fig. 7-5). With this setting the effective slice thickness is around 7mm. The field of view was set to 24cm and the repetition time used was 130ms. The total number of columns was 255 and the column step size, s, was 16 yielding and effective repetition time of 2.1s. The total acquisition time for each image was therefore approximately 33s. For all the six images used to calculate the ADC-trace the total scan time was 3.5min. The resolution in the frequency encoding direction was set to 128 sample points with a bandwidth of 8kHz. For each direction of the diffusion sensitivity, two b-factors were used: 5 s/mm^2 and 505 s/mm^2. The echo time (TE) was therefore approximately 85ms.

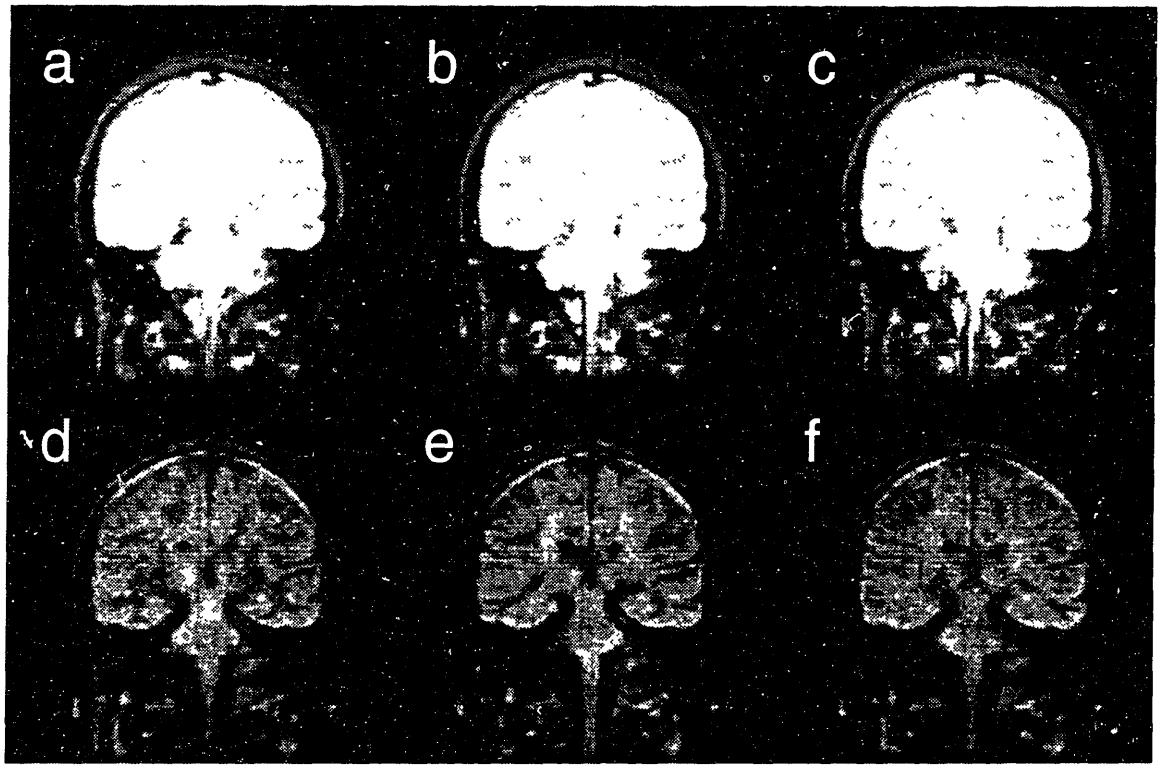

Figure 7-8: Coronal images of an healthy volunteer. FOV = 24cm, TR = 130ms, a = b = 5mm, α = β = 70° (see Fig. 7-5), 255 columns, 8kHz bandwidth, TR_{eff} = 4.2s, TE = 85ms. **a)** b_x = 5 s/mm^2. **b)** b_y = 5 s/mm^2. **c)** b_z = 5 s/mm^2. **d)** b = 505 s/mm^2. **e)** b_y = 505 s/mm^2. **f)** b_z = 505 s/mm^2.

Figure 7-9 shows the resulting ADC-trace map.

In order to estimate the precision of the ADC map, the acquisition described above was repeated 3 more times so that we would have a total of 4 independent ADC maps. A large ROI was defined, which included the whole brain, and for each image pixel we calculated the mean, $M_D = \sum_{i=1}^{4} D_i/4$, and the variance, $\sigma_D^2 = \sum_{i=1}^{4}(D_i - M_D)^2/3$. The mean standard deviation of the whole ROI was found to be $\overline{\sigma_D} = 0.077\,\mu m^2/ms$. Similarly, we calculated the mean relative precision as $\overline{\sigma_D/M_D}$ and found it to be 6%. From two of the four ADC maps a scatter diagram was produced as shown in Fig. 7-9. In the scatter diagram, each pixel in the ROI is given a coordinate according to the two independent ADC maps. Ideally, all the pixels should fall on a straight diagonal line, but due to image noise and possible motion between the two acquisitions, the pixels are spread around the diagonal line.

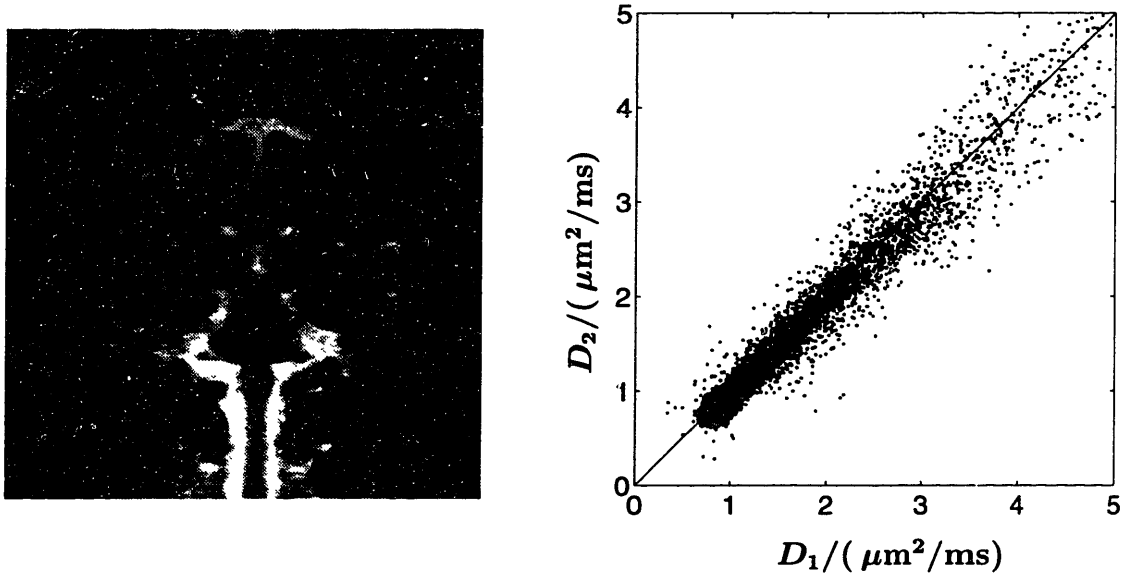

Figure 7-9: Left: Coronal ADC-trace map produced from the images in Fig. 7-8. Relative precision in the ADC-trace map is 6%. **Right:** A scatter diagram in which each pixel in the brain is given a coordinate according to the two independent ADC maps. Ideally, all the pixels should fall on a straight diagonal line.

Stroke Imaging

Figure 7-10 shows the first clinical LSDI images. A 45 year old female patient was imaged eight hours after an acute stroke. Imaging parameters were identical to those used to obtain Fig. 7-8. Minimal head restraints were used and no cardiac gating. The lesion is clearly identified on the diffusion weighted images but hardly seen on the highly T_2 weighted images (those with low b).

Figure 7-11 shows the three orthogonal ADC maps and the corresponding anisotropy map, that is calculated as in ref. [133]. The anisotropy map is inherently much more noisy than the ADC-trace map, however, one can see that anisotropy is highest in the white matter, close to the cerebrospinal fluid. Little difference is seen between the healthy and the affected tissue.

An ADC-trace map was calculated from the three orthogonal diffusion maps and shown in Fig. 7-12. Notice the nonlinear gray scale, used to emphasize the variations in the diffusion map. This gray scale is adapted from histogram equalization [62] of brain diffusion maps. For a comparison, a fast spin-echo image (FSE) of the same plane, with an effective echo time of 68ms is shown. Almost no abnormalities are visible on this image. The images to right, which were acquired four days after the stroke onset, show increased area of decreased ADC.

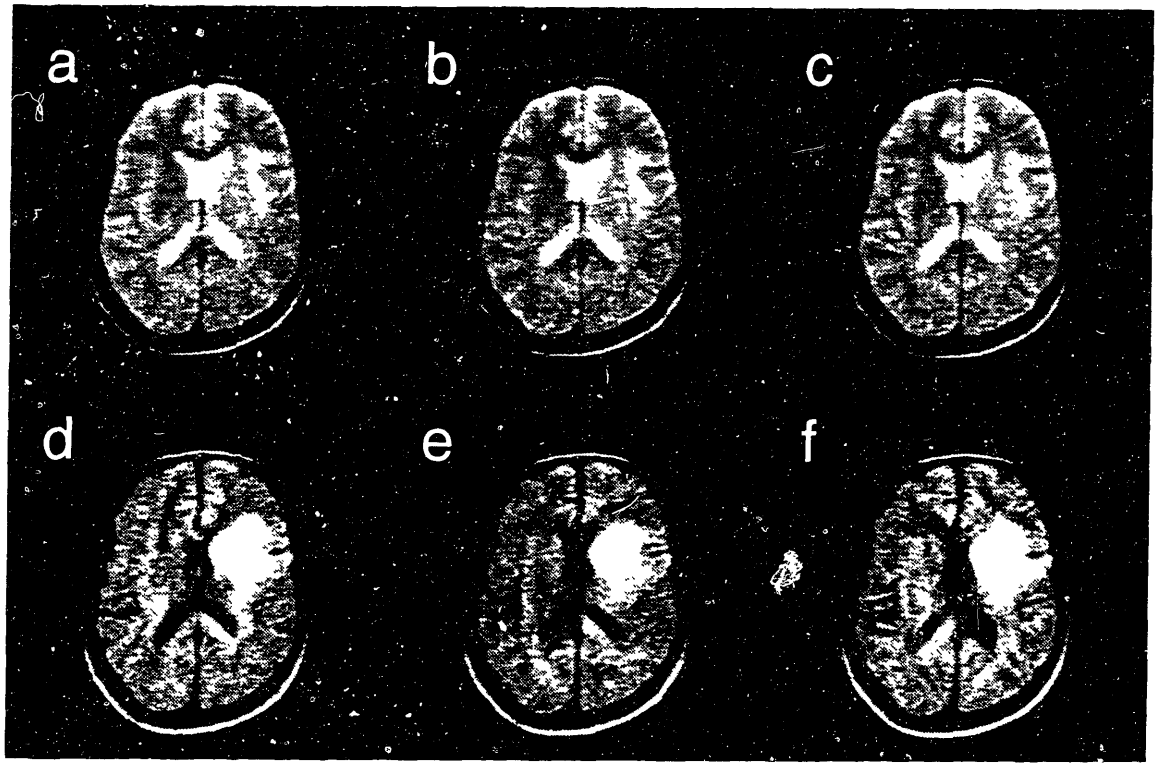

Figure 7-10: Acute stroke 8 hours after onset. Images of a 45 year old female stroke patient with different diffusion weighting. Minimal head restraints were used and no cardiac gating. Imaging parameters were identical to those used to obtain Fig. 7-8. **a)** b_I = 5 s/mm^2. **b)** b_{II} = 5 s/mm^2. **c)** b_z = 5 s/mm^2. **d)** b_I = 505 s/mm^2. **e)** b_{II} = 505 s/mm^2. **f)** b_z = 505 s/mm^2.

Reduced Imaging Time

In previously described images, the number of columns was always 255 and the bandwidth was 8kHz. By lowering the bandwidth to 4kHz and reducing the column number down to 127, we can half the imaging time without sacrificing SNR. Image distortions from chemical shift and field inhomogeneities have to be addressed however. Figure 7-13 shows images with a lower bandwidth. A slight displacement between the skull and the brain along the column direction is visible. Apart from this, the image quality remains very good and the ADC-trace maps compare very well. Both image sets were processed in the same way except that, the 127 columns had to be extrapolated into 255 columns before low-pass filtering. These results show that the LSDI technique is capable of producing high quality diffusion weighted images in only ca. 15 seconds per image. A full ADC-trace map can therefore be acquired in less than 1 minute and 15 seconds per slice.

Figure 7-14 shows two images of acute stroke that were acquired 17 hours after

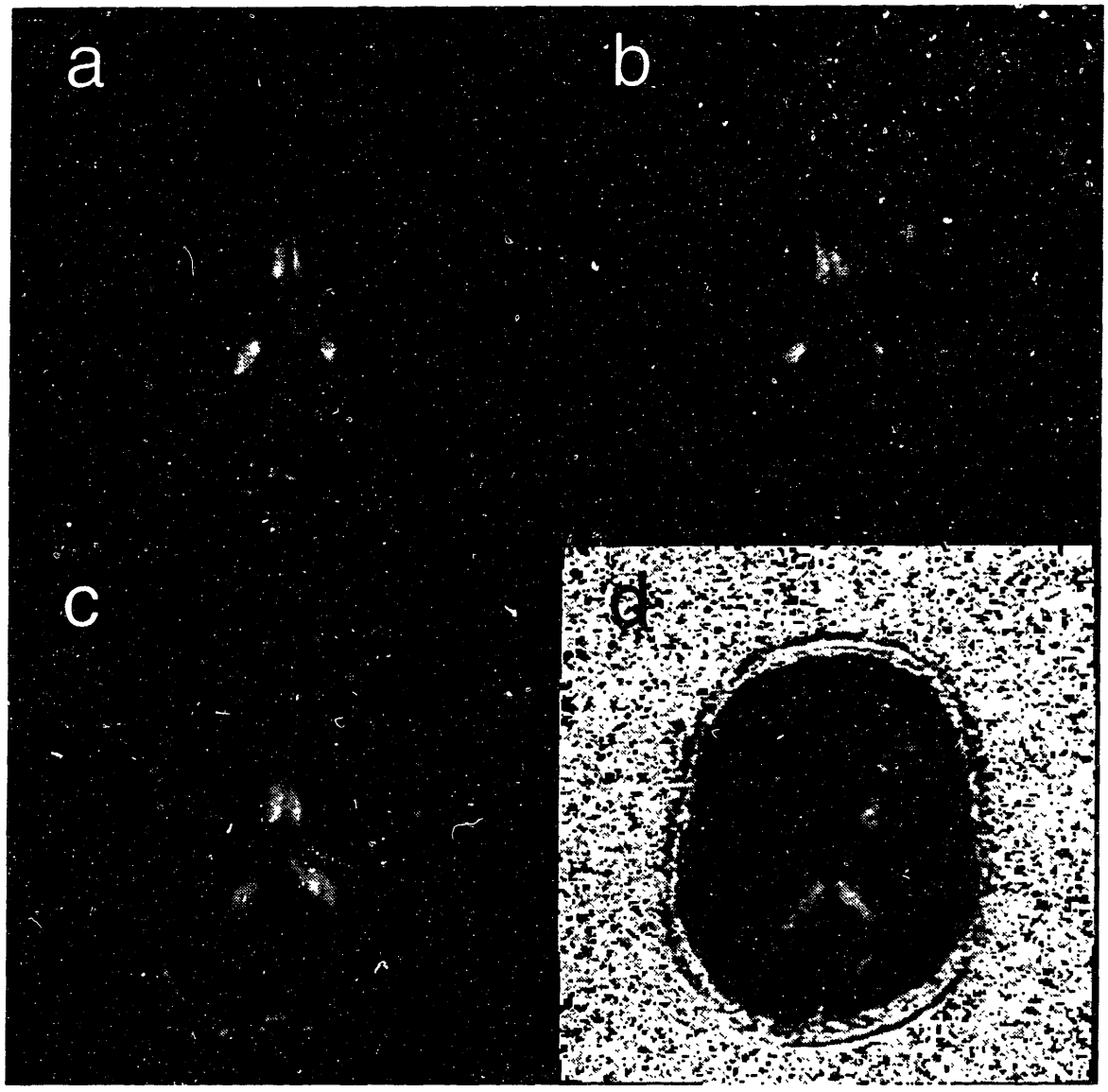

Figure 7-11: Acute stroke 8 hours after onset. **a)** ADC-x. **b)** ADC-y. **c)** ADC-z. **d)** Diffusion anisotropy map calculated as the standard deviation of the three ADC maps.

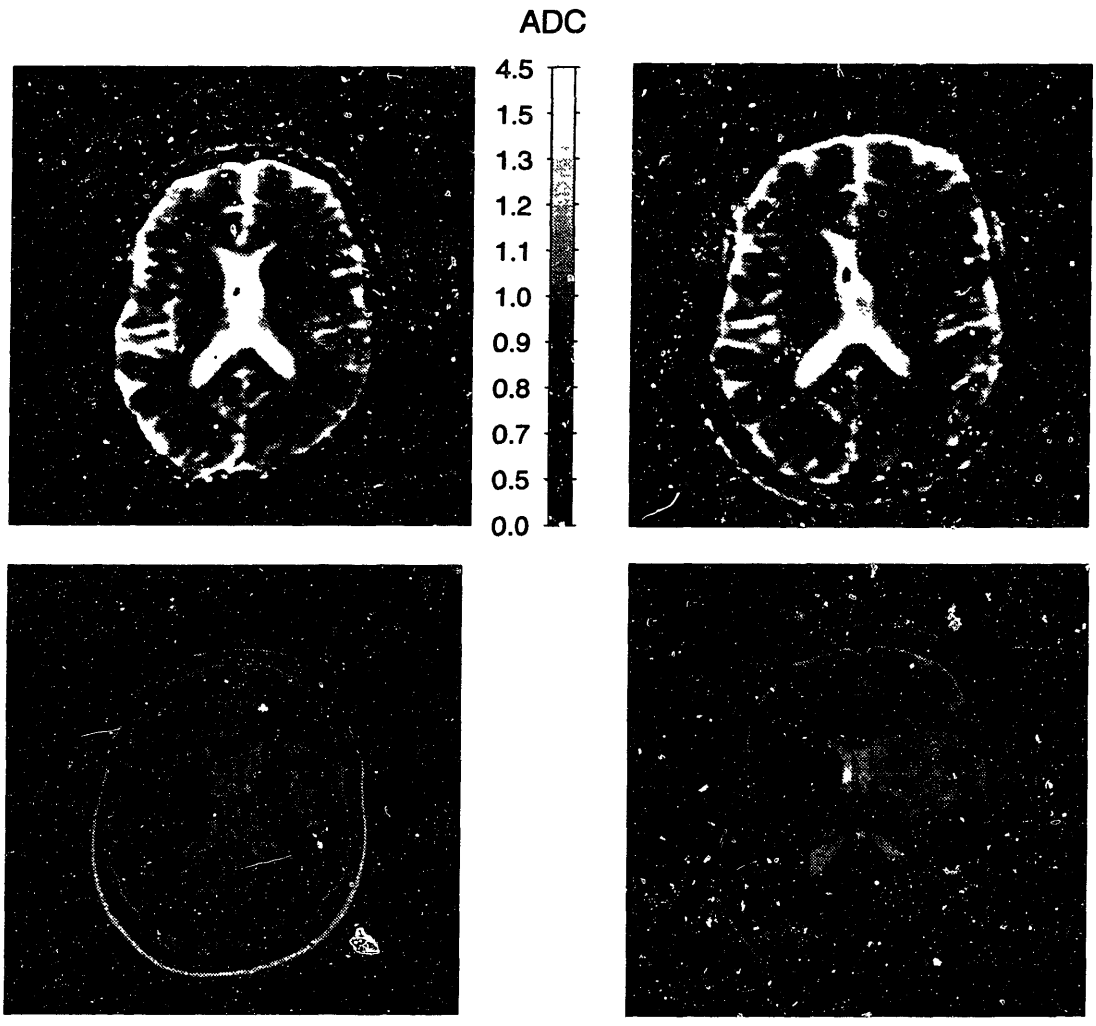

Figure 7-12: Acute stroke. **Left:** 8 hours after onset. FOV = 24cm. **Right:** 4 days after onset. FOV = 22cm. **Above:** ADC-trace map. Notice the nonlinear gray scale which is adapted from histogram equalization of brain diffusion maps. The ADC is in units of $\mu m^2/ms$. **Below:** Fast spin echo image (FSE) of the same slice with an effective echo time of 68ms.

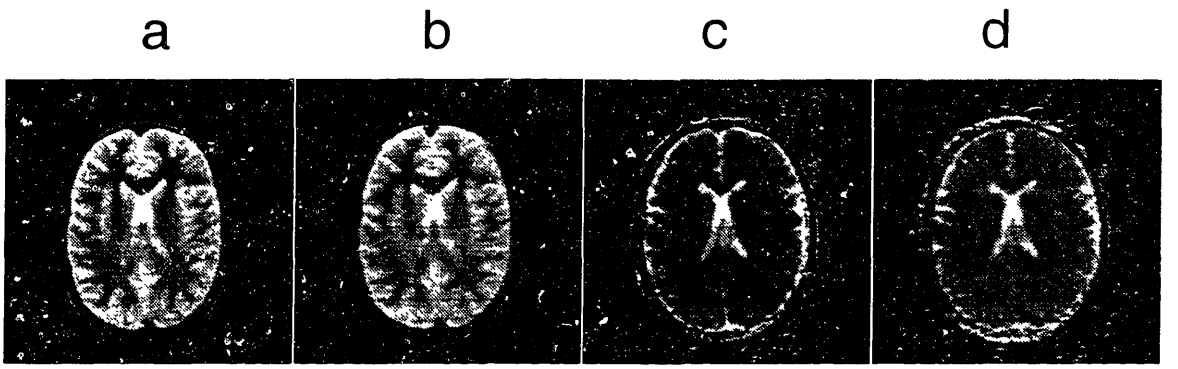

Figure 7-13: FOV = 24cm, TR = 150ms, $a = b$ = 5mm, $\alpha = \beta = 70°$ (see Fig. 7-5). **a)** and **c):** 255 columns, 8kHz bandwidth, TR_{eff} = 4.8s, TE = 85ms. **b)** and **d):** 127 columns, 4kHz bandwidth, TR_{eff} = 2.4s. TE = 90ms. **a)** and **b):** b_1 = 5 s/mm^2. **c)** and **d):** ADC-trace map calculated from six images.

onset on the 1.5T scanner. Neither head restraints nor cardiac gating was used. The bandwidth was 4kHz and the column number was 127. The diffusion weighted image was post-processed as described in section 4.5. The image with the low b-factor, which is highly T_2 weighted, shows no signs of ischemia, whereas, the lesion is clearly depicted on the highly diffusion weighted image.

7.3.3 LSDI at 1.5T versus 0.5T

Accuracy Assessment

To assess and compare the precision of the LSDI diffusion measurements on 1.5T and 0.5T scanners, four sets of diffusion weighted images were acquired from the brain of a healthy volunteer on both scanners. Neither head restraints nor cardiac gating was used. From these images four independent ADC-trace maps were calculated. The imaging parameters and the ADC maps are shown in Fig. 7-15. For each pixel in the region presented in Fig. 7-15, the mean $M_D = \sum_{i=1}^{4} D_i/4$, the variance $\sigma_D^2 = \sum_{i=1}^{4}(D_i - M_D)^2/3$ as well as the relative precision σ_D/M_D was estimated. These statistics we calculated for each voxel and they are presented here as the average over the region of interest.

ADC-trace maps of the identical section in the brain of a volunteer, acquired on 1.5T and 0.5T GE Signa whole body scanners are shown in Fig. 7-15. The scanners have equal gradient systems.

The statistics from the highlighted region are shown in Table 7.2. Clearly, there is an excellent agreement between the 0.5T and the 1.5T maps. The ratio of the relative precision of the 1.5T and the 0.5T ADC-trace map is 1.6. This is lower than the expected ratio of $\sqrt{2/4} \cdot 1.5/0.5 = 2.1$. We associate this discrepancy to the difference

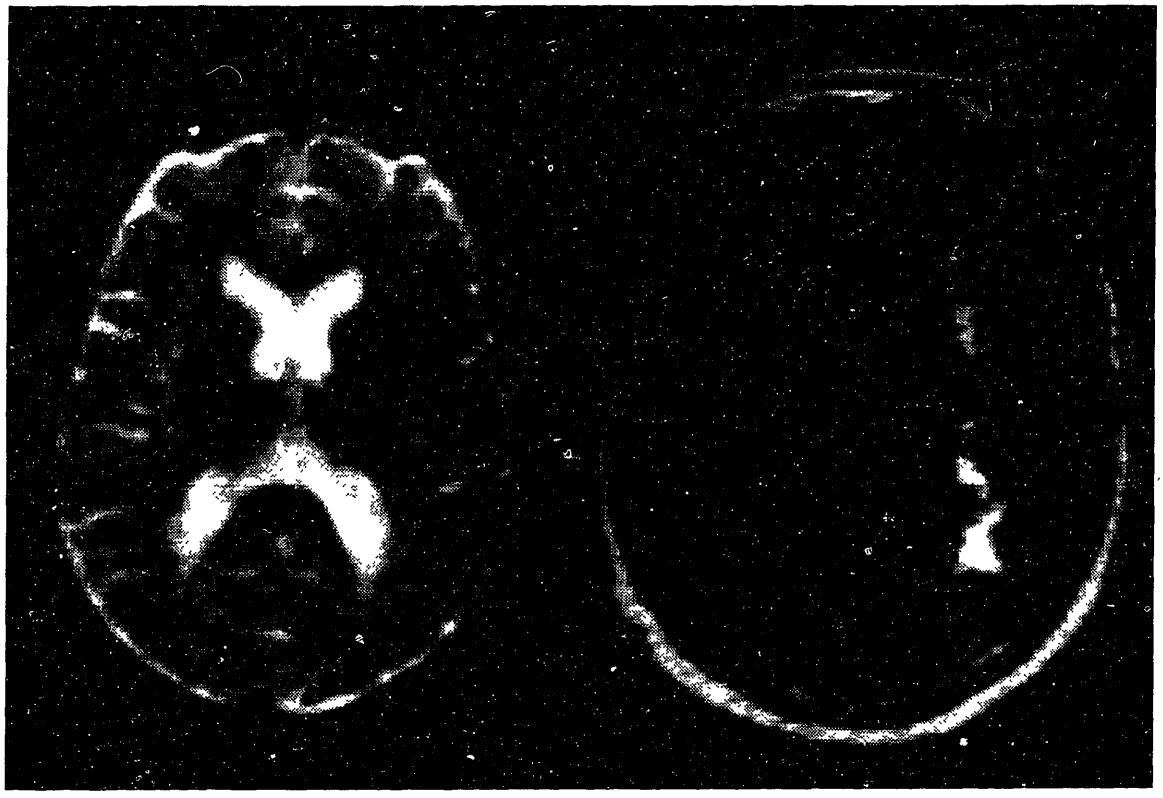

Figure 7-14: Acute stroke, 17 hours after onset. **Left:** T_2 weighted image (low b). **Right:** Post-processed diffusion weighted image with a b = 1500s/mm^2 calculated from the image to the left and the ADC-trace map. FOV = 20cm, 127 columns, TE = 98ms, 4kHz bandwidth, 1.5T field strength. For all three directions, x, y, and z, the b-factors are 5 and 505 s/mm^2. Effective voxel size (freq., col, sl.) is 1.5mm x 2.7mm x 7.3mm. The total acquisition time for the six images was 2min.

in transverse relaxation at the two field strengths and the fact that variations come from both noise and pixel misregistration from small head motion between scans.

The results indicate that it is possible to use the LSDI technique to acquire accurate diffusion maps on 0.5T systems.

Clinical Trial

Figures 7-16 - 7-18 show example of how the LSDI technique can be used in clinical practice. First the patient is screened for stroke with a fast LSDI volume coverage, i.e. a rectangular FOV and with diffusion sensitivity in a single direction, with one

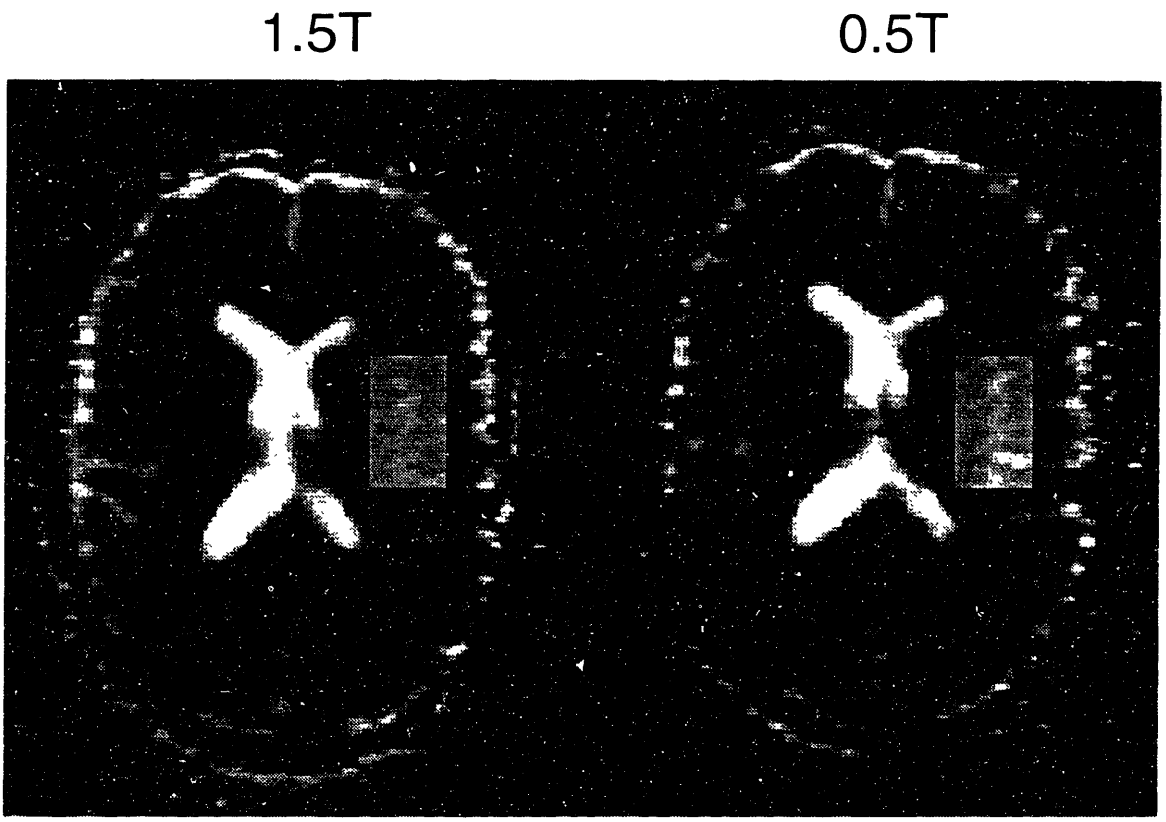

Figure 7-15: Comparison of ADC-trace maps: **1.5T** (4kHz, TE = 105ms, 1.3min scan time) and **0.5T** (2kHz, TE = 121ms, 1.5min scan time). FOV = 30x22.5cm and 95 columns. For all three directions, x, y, and z, the b-factors are 5 and 755 s/mm^2. Effective voxel size (freq., col., sl.) is 2.3mm x 2.7mm x 7.3mm. The highlighted area represents the region used for the analysis in Table 7.2.

low and high b-factor. To minimize the echo time we used all diffusion gradients simultaneously. In this case, 10 slices were acquired in ca. 6 minutes, however, by reducing the number of columns from 127 to 95 as in Fig. 7-15, it is possible to acquire 15 slices in ca. 6.5 minutes.

Once the lesion has been located from the localizers, ADC-trace maps are acquired from the region of interest, i.e. six images per slice. In Fig. 7-16 and Fig. 7-17, we see the localizers from a study of the same patient on 0.5T and 1.5T scanners, respectively. Figure 7-18 shows the axial, sagittal, and coronal images of the region of interest. There is an excellent comparison between the images from the 0.5T and the 1.5T system. Clearly, stroke studies such as this are practical at both 1.5T and 0.5T field strength. Note that in this study, neither cardiac gating nor head restraints were used.

7.3.4 LSDI versus EPI

We compared 1.5T LSDI images with EPI diffusion images on a 1.5T Vista (Siemens Medical Systems, Iselin, NJ) echo planar scanner. The maximum gradient strength on the EPI system was 2G/cm. Scanning was performed on both systems without cardiac gating or head restraints. Diffusion weighted images were obtained from three healthy volunteers. The axial scan plane was defined on a sagittal localizer with the upper rim of the pons as a reference point. With both techniques, four independent ADC-trace maps were acquired from a single slice using typical configuration parameters for each technique[3]. These scans were repeated four times on each system, and the same type of statistical analysis as described in section 7.3.3 was done for 500 pixels regions, right and left to the ventricles. The imaging parameters are shown in Fig. 7-19 and the results from the analysis are given in Table 7.3.

Clearly, there is an excellent agreement between the estimated means, $\overline{M_D} \approx 0.7\,\mu m^2/ms$, and incidentally $\overline{\sigma_D}$ was $0.03\,\mu m^2/ms$ for both techniques. Imaging times were similar for both systems, however, with the echo planar scanner it is possible to acquire multiple slices in the same time it takes to acquire a single slice, by using an interleaved acquisition scheme. This is the main advantage EPI has over LSDI, because with LSDI the acquisition time increases linearly with the number of slices.

From Fig. 7-19 we see that the EPI ADC-trace map has a slightly sharper appearance, however, even though fat suppression was used, chemical shift artifacts are easily visible in the phase encoding direction. We found that images that included the eyeballs had even more artifacts because of susceptibility variations. The LSDI images were free of any such artifacts.

[3]The EPI protocol was multislice, however, only a single slice was used for the analysis.

Field	0.5T		1.5T	
Columns	127	95	127	95
$\overline{M_D}/(\mu m^2/ms)$	0.83	0.86	0.83	0.83
$\overline{\sigma_D}/(\mu m^2/ms)$	0.061	0.067	0.041	0.040
$\overline{\sigma_D/M_D}$	7.4%	7.8%	4.9%	4.8%

Table 7.2: Comparison of the precision of 0.5T and 1.5T ADC-trace maps obtained with LSDI. Imaging parameters are given in Fig. 7-15.

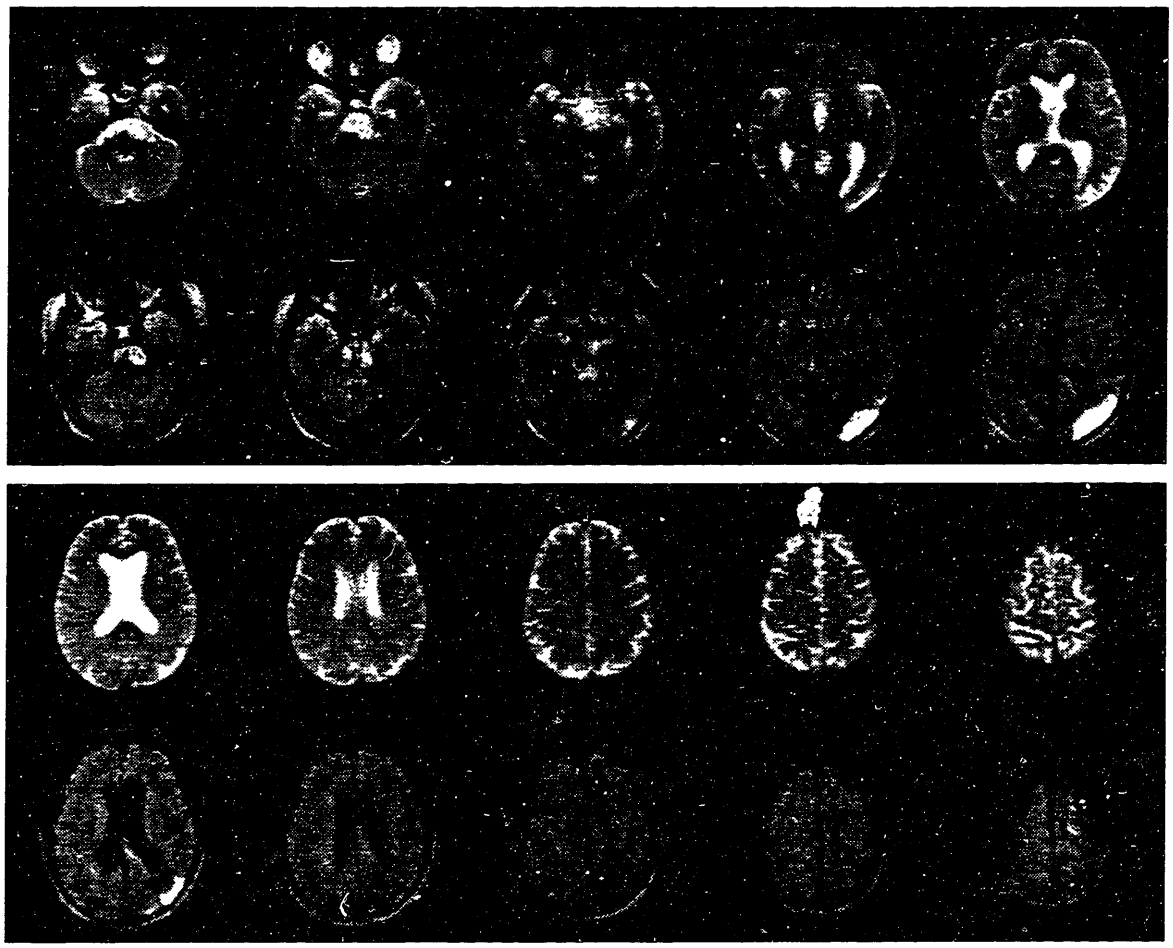

Figure 7-16: Acute stroke 9 hours from onset. **0.5T** LSDI localizer. FOV = 220x165mm, RES = 128x127c, BW = 2kHz, TE/TR = 114/150ms, slice thickness 8.8mm (a = 6mm), scan time 38s/slice, and the b-factors are 5 and 755 s/mm^2. The total imaging time for these 10 slices was 6 minutes and 20 seconds.

7.3.5 Diffusion Imaging of the Abdomen

Some of the most recent applications of diffusion imaging are in the abdomen [94] and the heart [29]. The functional status of the kidney has been explored by means of the ADC [93]. These studies were done with diffusion weighted EPI. Because the LSDI sequence uses spin echoes, it is insensitive to magnetic field inhomogeneities. This, along with its insensitivity to bulk motion makes it an ideal candidate for abdominal diffusion imaging.

Figure 7-20 shows coronal images of a healthy volunteer. The slice selective pulses were chosen such that $a = b = 1$cm and $\alpha = \beta = 70^\circ$ (see Fig. 7-5). The field of view

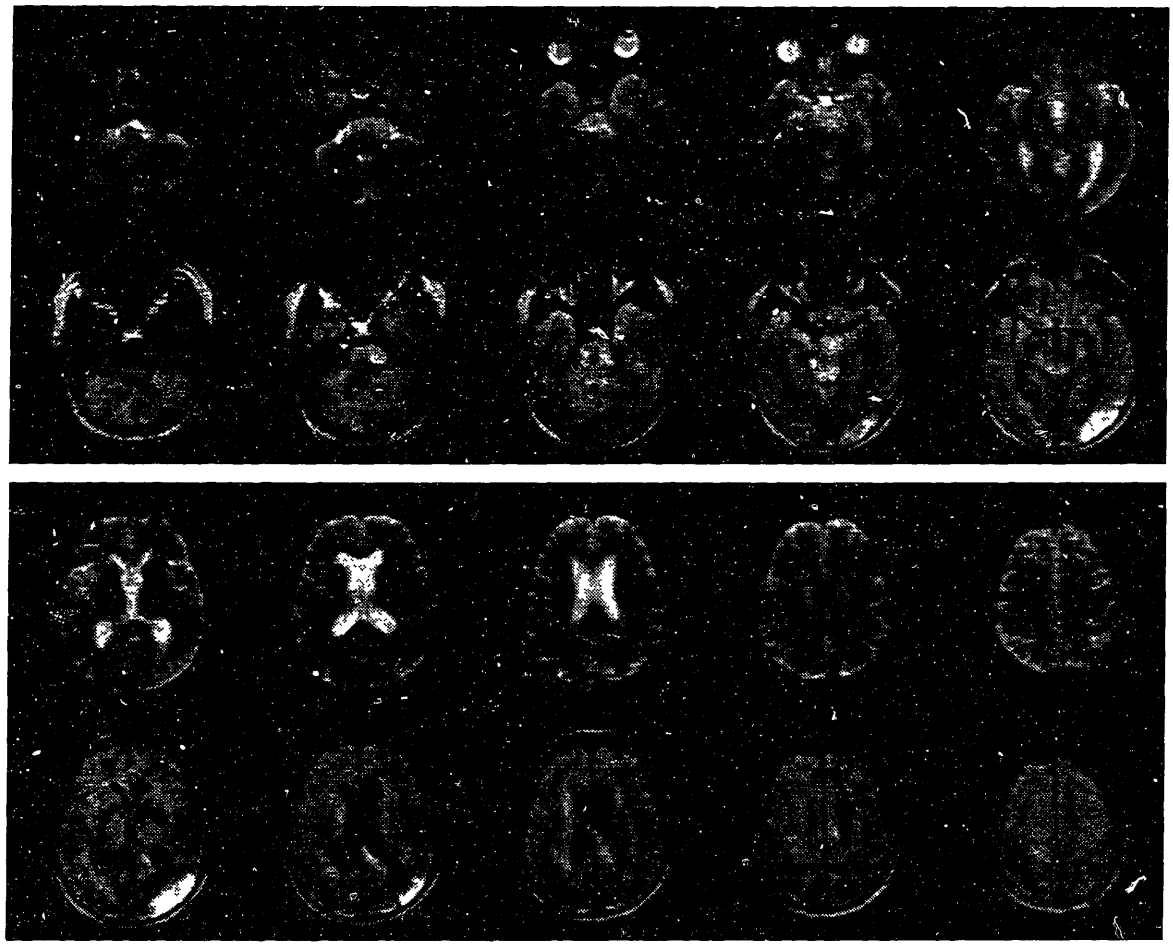

Figure 7-17: Acute stroke 10 hours from onset. **1.5T** LSDI localizer. FOV = 220x165mm, RES = 128x127c, BW = 4kHz, TE/TR = 105/135ms, slice thickness 7.3mm (a = 5mm), scan time 34s/slice, and the b-factors are 5 and 755 s/mm^2. The total imaging time for these 10 slices was 5 minutes and 40 seconds.

was set to 40cm and the repetition time was 150ms. The total number of columns was 255 and with a column step size of 16. The effective repetition time was therefore 2.4s. In order to get high SNR, the bandwidth was set to 4kHz. The image quality is still quite good, although, some chemical shift distortion is visible, e.g. in the spine. Neither breath hold nor cardiac gating was used. The image with the low b-factor (5 s/mm^2) is without any visible motion distortion, however, in the one with the high b-factor (505 s/mm^2), distortion is visible as signal loss in some of the columns.

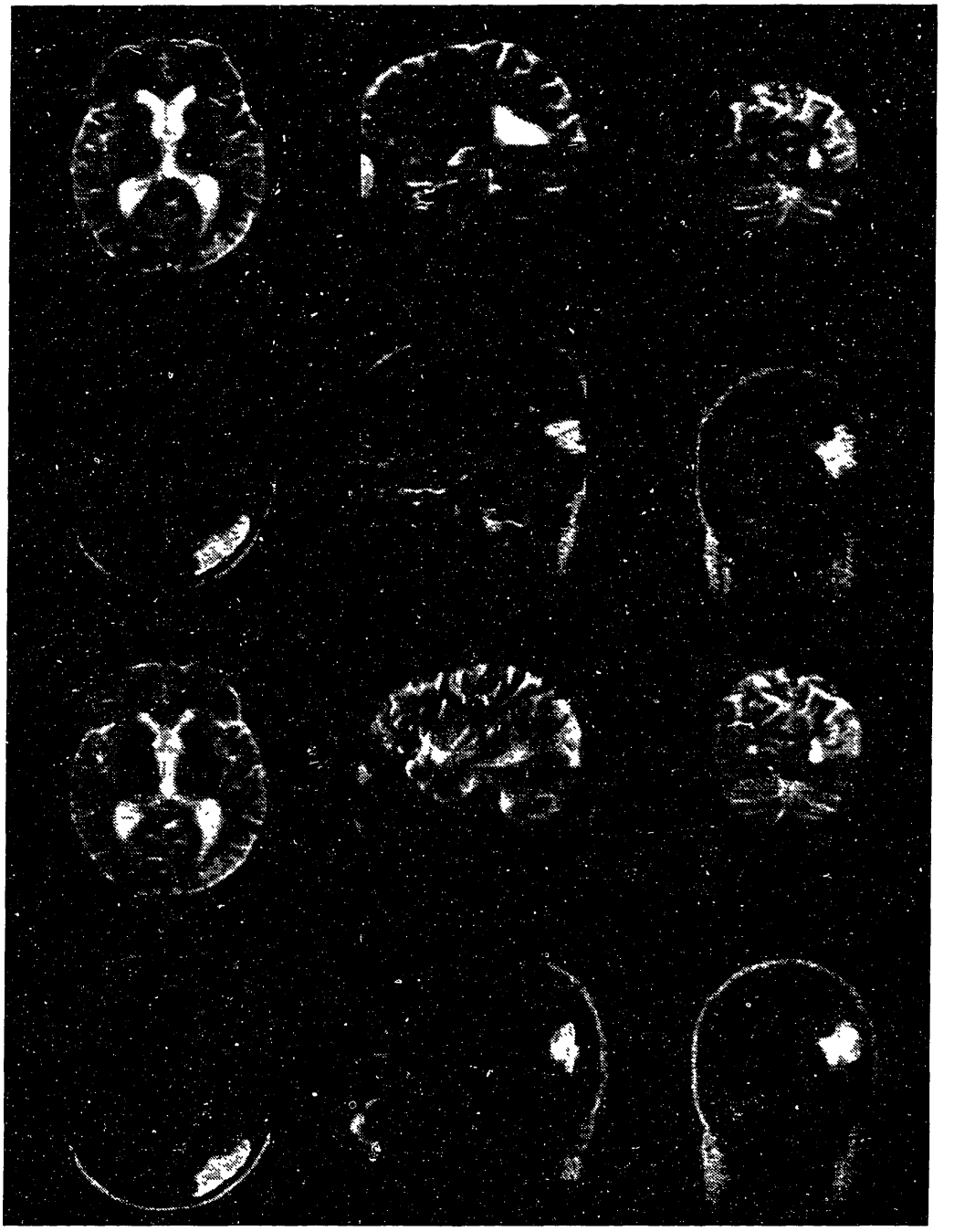

Figure 7-18: Upper six images: 0.5T, 9 hours after onset. **Lower six images:** 1.5T, 10 hours after onset. For each plane, axial, sagittal, and coronal, six images were acquired. For all three directions x, y, and z, the b-factors are 5 and 755 s/mm^2. The diffusion weighted images are post-processed as describe in section 4.5 by using the ADC-trace map and a b-factor of 1500 s/mm^2. The imaging parameters are given in Fig. 7-16 and Fig. 7-17.

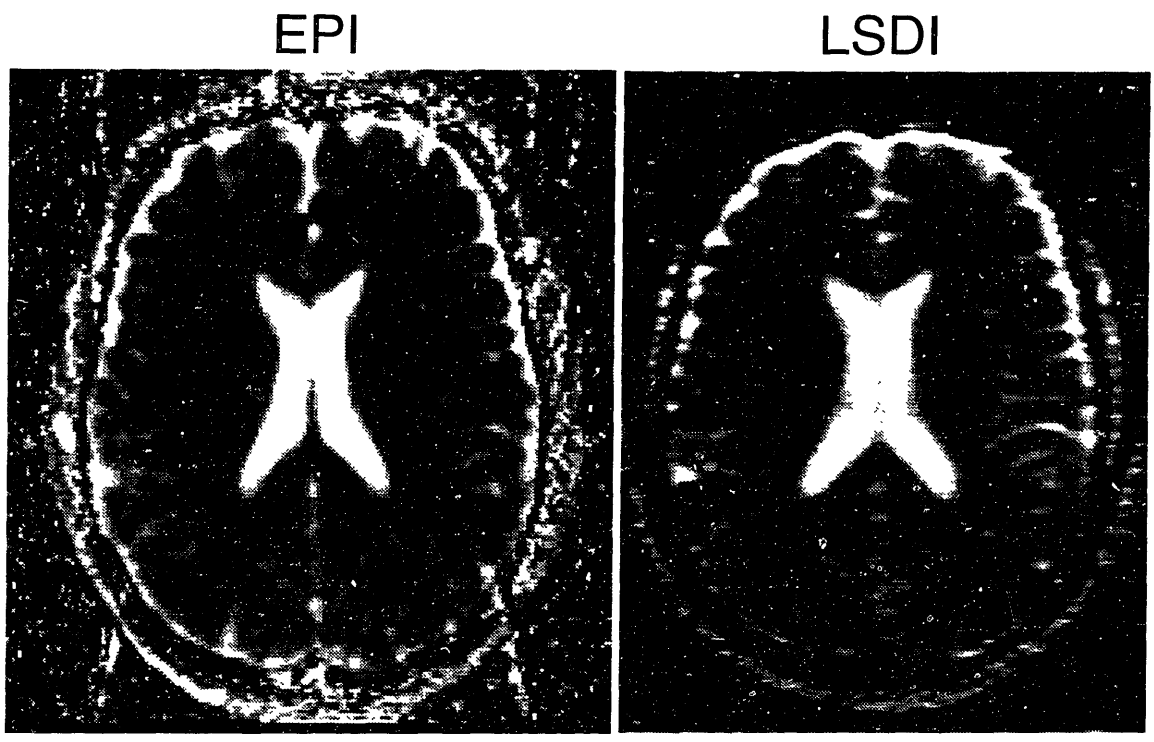

Figure 7-19: a): EPI ADC-trace map. Excitation with fat suppression, TE = 90ms, BW = 160kHz, scan time 84s, effective TR = 6s, FOV = 210x280mm, resolution 128x64p, effective voxel size (freq., ph., sl.) 2.2x3.2x7.0mm, b-factors 0, 160, 340, 600, and 1000 s/mm^2. **b):** LSDI ADC-trace map. TE = 105ms, BW = 4kHz, scan time 100s, TR = 135ms, effective TR = 2s, FOV = 240x180mm, resolution 128x127c, effective voxel size (freq., col., sl.) 1.9x2.7x7.3mm, b-factors 5 and 755 s/mm^2.

7.4 Discussion

In this chapter, we have presented and analyzed the LSDI sequence, which is a novel diffusion imaging technique [47]. A similar diffusion imaging technique was presented simultaneously by other researchers [106] as well. However, their technique shows more resemblance with an older technique, called rapid line scan (RLS) or interleaved line scan (ILS), suggested for the imaging of moving objects [1,113,114]. No application to diffusion was contemplated for the RLS/ILS technique however. Common to LSDI and the RLS/ILS techniques is the use of two slice selective pulses to form columns and the use of time varying crusher gradients, in order to destroy spurious echoes. There are several technical differences that distinguish the LSDI and the RLS/ILS techniques. In the LSDI sequence, a pre-sweep is used to ensure steady-state magnetization across the whole field of view. Also, in the LSDI image neighboring columns overlap. This avoids aliasing and improves image quality. In the LSDI sequence, the novel idea

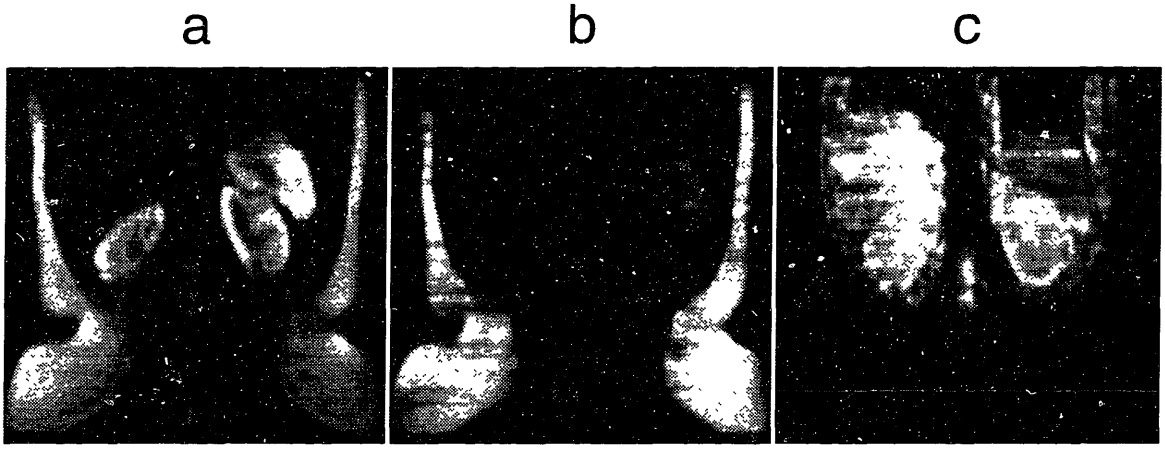

Figure 7-20: FOV = 40cm, TR = 150ms, $a = b = 10$mm, $\alpha = \beta = 70°$ (see Fig. 7-5). 255 columns, 4kHz bandwidth, TR_{eff} = 2.4s, TE = 90ms. **a)** b_x = 5 s/mm^2. **b)** b_x = 505 s/mm^2. **c)** ADC-trace map calculated from six images.

of alternating the slice selection direction is used, that has the distinct advantage of reducing spurious echoes. Furthermore, we show that the inclination angle of 45°, used in the RLS/ILS techniques, is outside of the optimal range from 65° to 75°. For these reasons, the diffusion images presented here are of greatly improved quality and resolution.

It is shown in Figs. 7-10 - 7-12 that LSDI images can clearly identify the ischemic area in the early phase of acute stroke, whereas it is hardly visible on the T_2 weighted images (FSE and those with low b). Because LSDI offers high precision diffusion

	$\overline{M_D}/(\mu m^2/ms)$			
Location	Left		Right	
Technique	LSDI	EPI	LSDI	EPI
subject 1	0.69	0.66	0.69	0.70
subject 2	0.71	0.69	0.70	0.70
subject 3	0.71	0.69	0.71	0.70

Table 7.3: Comparing the mean and the precision of EPI and LSDI. The imaging parameters are given in Fig. 7-19. For both techniques, the mean standard deviation per pixel $\overline{\sigma_D}$ was 0.03 μm^2/ms.

maps, it is possible to accurately monitor the area of reduced ADC. By comparing images at different time points (Fig. 7-12) we see that the area of decreased ADC increases with time from stroke onset. Four days after onset of the acute stroke the ischemic injury becomes more visible on the T_2 weighted image. These findings agree well with previously published studies on stroke [22, 23, 69, 79, 90, 121, 133, 137].

Animal studies indicate that, there is a strong correlation between the regions of hyper-intensity in diffusion weighted images (DWI) and the area at risk for infarction. In a recent study [69], it was found that the regions of hyper-intensity in DWI is similar to that of tissue acidosis but exceeds that for the depletion of energy metabolites, particularly during the early phase of ischemia. However, a study which correlated cerebral blood flow with ADC found that, hyper-intense regions on DWIs are significantly smaller than the area at risk for infarction [79]. The disagreement may be found in the threshold levels used for the planimetric evaluation and therefore the ability of DWI to accurately predict infarct size remains to be demonstrated. LSDI has the potential to make such *in vivo* studies possible on a large number of conventional MR scanners.

LSDI, in contrast to navigated diffusion imaging, is inherently immune to bulk motion artifacts. For imaging tissues other than heart muscle, the LSDI-sequence does therefore not require cardiac gating, which facilitates the technique in the clinical setting. For single slice imaging, the LSDI technique is faster than the navigated PGSE technique. Moreover, unlike the navigated PGSE imaging technique, LSDI does not restrict the diffusion sensitivity to selected spatial directions, which allows accurate assessment of the diffusion tensor trace and anisotropy maps.

The insensitivity of LSDI to bulk motion and susceptibility inhomogeneities makes it applicable for diffusion imaging in the abdomen and the heart. Unlike echo planar diffusion imaging, it does not require any special gradient hardware. Furthermore, arbitrary oblique imaging planes can be defined without any image distortion. In contrast, when oblique imaging planes are defined in EPI, one has to compromise between susceptibility artifact and Maxwell image distortion [141]. In abdominal imaging with a large field of view and severe field inhomogeneities, this may become an issue.

Our initial abdominal diffusion images in Fig. 7-20 show signal loss in some of the columns. This is because of respiratory motion that causes nonuniform motion within each image voxel. When there is nonuniform motion within each image voxel, the phase dispersion will exaggerate the apparent diffusion attenuation. If the phase distribution is known, its influence can be determined from the LSDI point-spread function [139]. By using small voxels, the influence of phase dispersion can be minimized at the cost of reduced SNR. A better way to reduce motion artifacts in the abdomen is to use breath hold imaging. Currently, we have not implemented breath

hold imaging, however, this should be straight forward because with LSDI two images can easily be acquired in a single breath hold. The abdominal diffusion maps compare well with recently published diffusion maps obtained with EPI [94].

As Eq. (6.1) shows, phase dispersion can also come from rotation. Since the shape of the LSDI PSF is not the same in the frequency encoding direction as in the y and z-direction, the influence of rotation related phase dispersion will depend on the direction of the diffusion gradients. Since, the LSDI PSF has a sinc shape in the frequency direction (x) and trapezoidal shape in the y and z-directions, the influence of phase dispersion in the x-direction causes least signal attenuation [139]. Also, usually the voxel size the in x-direction is smaller than in the selective directions. Therefore, instead of applying all three gradients simultaneously, to reduce the echo time for the LSDI localizers, it may be more robust with respect to patient motion, to use only diffusion sensitivity in the y-direction. Further experiments are needed to verify this.

In terms of acquisition speed, the LSDI technique is most competent in single slice imaging. However, volume acquisition can be performed by subsequent acquisition of several image planes. Figures 7-16 and 7-17 shown that volume imaging is still practical with the LSDI technique. Because the SNR does not decrease with a reduced field of view in the y direction, it is possible to cover a volume of interest (e.g. the heart muscle) more efficiently with several rectangular fields of view. Another alternative for volume imaging is to use a two-dimensional selective excitation pulse [105] instead of the one-dimensional $\pi/2$ pulse. This reduces the problem of spin saturation, allows a much more efficient scanning of the imaging volume, and reduces secondary echoes.

7.5 Conclusion

With the LSDI technique, we are able to acquire high quality diffusion images with high and low diffusion sensitivity in scan times of less than thirty seconds per slice. This imaging technique is very robust and easily implemented on conventional scanners. Diffusion maps of the brain that are essentially free of motion artifacts can be obtained without the use of head restraints or cardiac gating. This makes LSDI particularly useful in clinical setting.

Most importantly, we showed that the LSDI technique works well on conventional systems at a field strength of 0.5T and with maximum gradient strength of 1G/cm. Most EPI systems have high field strength and low-field systems are rarely equipped with EPI gradient hardware. The major difference between the utility of the EPI sequence and the LSDI sequence is that multislice imaging is much faster with EPI. By using interleaved multislice acquisition, EPI can image the whole brain volume in only twice the time it takes to acquire a single slice. In contrast, with LSDI the imaging time is directly proportional to the number of slices. We have shown, however,

that it is still possible to screen for stroke with a fast LSDI volume coverage, in less than seven minutes. Then, more accurate LSDI ADC-trace maps can be acquired from the region of interest. A patient study such as this could therefore be completed in approximately ten minutes.

Thus, LSDI should increase the general availability of robust diffusion imaging which does not require specialized hardware. Therefore, LSDI may have considerable impact on the treatment of acute stroke.

Chapter 8

Conclusion

IN this work we have studied the influence of physiological motion on diffusion weighted MR images. In particular, we showed in chapter 5 that techniques based on steady-state free precession (SSFP) cannot provide accurate diffusion maps. The main problem with SSFP is scrambling of the signal and distortions in the 2D phase encoding from brain motion. We have demonstrated this using numerical simulation of the SSFP signal using actual experimentally obtained data for pulsatile brain motion.

Similarly, the navigator technique works only if the diffusion sensitivity is applied in the phase encoding direction and the motion is in the form of bulk motion. As the results in chapter 6 indicate, cardiac gating is therefore necessary to minimize the influence of spatially varying motion around the CSF.

From these experiments, we have concluded that phase encoding is the main problem in diffusion weighted Fourier imaging, unless, it is used with a single shot gradient echo technique such as EPI. More generally we can argue, that imaging techniques which depend highly on the phase of the signal cannot provide accurate diffusion maps when there is spatially varying motion. For instance, if there is spatially varying motion, in projection reconstruction, the amplitude of the projections will be reduced because of signal cancelation from spins with motion related phase artifacts of opposite sign. This results in overestimation of the diffusion attenuation. Also, it is a misconception, that speed is crucial for successful diffusion imaging. According to the discussion in chapter 6, the speed of EPI is not its major advantage for diffusion imaging, but much more importantly the fact, that all the echoes in a single-shot EPI have the same phase artifacts. In contrast we point out, that diffusion imaging with a single shot RARE/FSE or a single-shot GRASE [76] cannot work. This is because these techniques can only form images of real magnetization whereas the single-shot EPI technique can form images of magnetization which has both real and imaginary components.

The major result of this work is the novel line scan diffusion imaging technique

(LSDI). The LSDI technique is inherently insensitive to motion artifacts because it does not use phase encoding. As long as the motion can be considered uniform within the image voxel and the total tissue displacement small compared with the size of the voxel, the LSDI technique should not be affected by the phase variations in the signal. Therefore, we have changed the problem from having uniform motion within the whole field of view into a problem of having uniform motion within a single image voxel. Obviously, the latter is a much easier to achieve.

Line scan and diffusion imaging make a perfect fit, because, problems related to the secondary echoes disappear by alternating between high and low diffusion sensitivity. Then, by using an interleaving scheme with a "dummy sweep", uniform image intensity is ensured. Because the LSDI sequence is based on the spin-echo sequence, it is insensitive to field inhomogeneities and it is easily implemented on conventional scanners. The only real hardware constraint is that a sufficient gradient strength is needed in order to have reasonably short echo times.

We have shown, that high quality diffusion maps can be obtained rapidly with the LSDI technique on both 0.5T and 1.5T systems without the use of head restraints or cardiac gating. Furthermore, we show that these diffusion maps compare very well with diffusion maps obtained using diffusion weighted echo-planar imaging (EPI). In contrast to the EPI technique, LSDI does not require modified gradient hardware, is insensitive to field inhomogeneities, and can easily be implemented on conventional scanners. The main disadvantage of the LSDI technique is that multi-slice imaging is considerably slower than with EPI. However, the feasibility of using the LSDI technique for clinical evaluation of acute ischemic stroke in less than ten minutes is demonstrated in section 7.3.3. It remains to be explored whether the LSDI sequence can be modified in order to reduce imaging time in multi-slice acquisition.

We believe the LSDI technique is an excellent alternative to EPI diffusion imaging. This can have great clinical impact because reliable stroke studies with diffusion imaging, which previously required scanners with expensive gradient hardware for EPI, can now be done on most conventional scanners. Hence, this increases the number of clinical sites capable of doing stroke and other diffusion studies dramatically.

Appendix A

Conditional Random Walk

A.1 Variance Calculation

Here we continue the calculation of the conditional variance. We start by rewriting Eq. (3.14)

$$\overline{\left(ia_i \sum_{j\neq i}^{N} ja_j \mid \mathcal{X}\right)} = i \cdot \left[\frac{\binom{N-1}{\frac{x/\xi+N}{2}-1}\left(\frac{N(N+1)}{2}-i\right)\frac{(x/\xi-1)}{N-1}}{\binom{N}{\frac{x/\xi+N}{2}}} - \frac{\binom{N-1}{\frac{x/\xi+N}{2}}\left(\frac{N(N+1)}{2}-i\right)\frac{(x/\xi+1)}{N-1}}{\binom{N}{\frac{x/\xi+N}{2}}} \right] \tag{A.1}$$

By using the following identity

$$\frac{\binom{N-1}{\frac{x/\xi+N}{2}}}{\binom{N-1}{\frac{x/\xi+N}{2}-1}} = \frac{N-x/\xi}{N+x/\xi} \tag{A.2}$$

Equation (A.1) simplifies to

$$\overline{\left(ia_i \sum_{j\neq i}^{N} ja_j \mid \mathcal{X}\right)} = i\frac{\binom{N-1}{\frac{x/\xi+N}{2}-1}}{\binom{N}{\frac{x/\xi+N}{2}}} \cdot \left(\frac{N(N+1)}{2} - i\right)\left(\frac{(x/\xi-1)}{(N-1)} - \frac{(N-x/\xi)}{(N+x/\xi)}\frac{(x/\xi+1)}{(N-1)}\right) \quad \text{(A.3)}$$

This can be simplified even further by recognizing that

$$\frac{\binom{N-1}{\frac{x/\xi+N}{2}-1}}{\binom{N}{\frac{x/\xi+N}{2}}} = \frac{x/\xi+N}{2N} \quad \text{(A.4)}$$

and Eq. (A.3) reduces to

$$\overline{\left(ia_i \sum_{j\neq i}^{N} ja_j \mid \mathcal{X}\right)} = i\left(\frac{x/\xi+N}{2N}\right)\left(\frac{N(N+1)}{2} - i\right) \cdot \left(\frac{(x/\xi-1)}{(N-1)} - \frac{(N-x/\xi)}{(N+x/\xi)}\frac{(x/\xi+1)}{(N-1)}\right) \quad \text{(A.5)}$$

Finally Eqs. (3.13), (A.5), and (3.11) are plugged into Eq. (3.12) which gives

$$\sigma^2_{\phi|x} = G^2\gamma^2\tau^2\xi^2\left[\frac{N(N+1)(2N+1)}{6} - \left(\frac{N+1}{2}x/\xi\right)^2 + \left(\frac{x/\xi+N}{2N}\right)\left(\left(\frac{N(N+1)}{2}\right)^2 - \frac{N(N+1)(2N+1)}{6}\right) \cdot \left(\frac{(x/\xi-1)}{(N-1)} - \frac{(N-x/\xi)}{(N+x/\xi)}\frac{(x/\xi+1)}{(N-1)}\right)\right] \quad \text{(A.6)}$$

After some algebra this can be expressed as

$$\sigma^2_{\phi|x} = G^2\gamma^2\tau^2\xi^2\left[\frac{N(N+1)(2N+1)}{6} - \left(\frac{N+1}{2}x/\xi\right)^2 + \left(2(x/\xi)^2 - 2N\right)\frac{(N+1)}{(N-1)}\frac{(3N^2-N-2)}{24}\right] \quad \text{(A.7)}$$

A.2 Different Derivation for the Conditional Variance

Now just assume that x and ϕ can be described by a jointly Gaussian distribution

$$\Pr(x,\phi) = \frac{1}{2\pi\sigma_x\sigma_\phi\sqrt{1-r^2}} \exp\left[\frac{-1}{2(1-r^2)}\left(\frac{x^2}{\sigma_x^2} - 2r\frac{x\phi}{\sigma_x\sigma_\phi} + \frac{\phi^2}{\sigma_\phi^2}\right)\right] \tag{A.8}$$

where r is the correlation coefficient defined by

$$r = \frac{\overline{x\phi} - \overline{x}\,\overline{\phi}}{\sqrt{\overline{x^2}\cdot\overline{\phi^2}}} \tag{A.9}$$

Since

$$\Pr(x,\phi) = \Pr(\phi \mid x)\Pr(x) \tag{A.10}$$

it is easy to show that [98]

$$\Pr(\phi \mid x) = \frac{1}{\sigma_x\sqrt{2\pi(1-r^2)}} \exp\left[\frac{-(\phi - r\sigma_x x/\sigma_\phi)^2}{2\sigma_\phi^2(1-r^2)}\right] \tag{A.11}$$

and hence

$$\overline{\phi_{|x}} = r\sigma_\phi x/\sigma_x \tag{A.12}$$

$$\sigma_{\phi|x}^2 = \sigma_\phi^2\left(1-r^2\right) \tag{A.13}$$

Substitution into Eq. (A.9) yields

$$\begin{aligned} r &= \frac{G\xi^2\gamma\tau\frac{N(N+1)}{2}}{\sqrt{G^2\xi^2\gamma^2\tau^2\frac{N(N+1)(2N+1)}{6}\xi^2 N}} \\ &\to \sqrt{\frac{3}{4}} \qquad \text{as} \qquad N\to\infty \end{aligned} \tag{A.14}$$

Using this value in Eqs. (A.12) and (A.13) leads to exactly the same result as obtained in Eqs. (3.17) and (3.18).

A.3 Ramped Gradients

Here we extend the conditional random walk model to include time varying gradients which vary linearly with time.

The difference in the position between a moving and a static spin is defined as

$$x = \xi\sum_{i=1}^{N} a_i \tag{A.15}$$

where $a_i \in (-1, 1)$ is a discrete random variable. From this definition and the definition of $D = \xi^2/2\tau$ and $t = N\tau$ it is straight forward to show that

$$\overline{x(t_1)x(t_2)} = \overline{\xi^2 \left(\min(t_1, t_2)\right)/\tau} = 2D\min(t_1, t_2) \tag{A.16}$$

The gradient is assumed to have the following form

$$G(t) = G_0 + \alpha t \tag{A.17}$$

Hence[1]

$$\begin{aligned}
\sigma_\phi^2 &= \overline{\phi(t)\phi(t)} \\
&= \overline{\int_0^t G(t_1)x(t_1)dt_1 \cdot \int_0^t G(t_2)x(t_2)dt_2} \\
&= G_0^2\gamma^2 2D\frac{t^3}{3} + G_0\alpha\gamma^2 2D\frac{5\cdot t^4}{12} + \alpha^2\gamma^2 2D\frac{2\cdot t^5}{15}
\end{aligned} \tag{A.18}$$

$$\overline{x} = \overline{\phi} = 0 \tag{A.19}$$

$$\begin{aligned}
\overline{x\cdot\phi} &= \overline{x(t)\int_0^t G_0\gamma x(t') + \alpha\gamma t' x(t')dt'} \\
&= G_0\gamma 2D\frac{t^2}{2} + \alpha\gamma 2D\frac{t^3}{3}
\end{aligned} \tag{A.20}$$

$$\begin{aligned}
r &= \frac{\gamma 2D\left(G_0\frac{t^2}{2} + \alpha\frac{t^3}{3}\right)}{\sqrt{2Dt\cdot\gamma^2 2D\left(G_0^2\frac{t^3}{3} + G_0\alpha\frac{5t^4}{12} + \alpha^2\frac{2t^5}{15}\right)}} \\
&= \frac{G_0\frac{1}{2} + \alpha\frac{t}{3}}{\sqrt{G_0^2\frac{1}{3} + G_0\alpha\frac{5t^2}{12} + \alpha^2\frac{2t^2}{15}}}
\end{aligned} \tag{A.21}$$

By substituting into Eqs. (A.12) and (A.13) we get

$$\overline{\phi_{|x}} = \gamma G_0\frac{t}{2}x + \gamma\alpha\frac{t^2}{3}x \tag{A.22}$$

$$\sigma_{\phi|x}^2 = \gamma^2 D\left(\frac{G_0^2 t^3}{6} + \frac{G_0\alpha t^4}{6} + \frac{\alpha^2 2t^5}{45}\right) \tag{A.23}$$

[1]The integral product is evaluated by forming a double integral. The inner integral is then split into two integrals such that Eq. (A.16) can be applied.

The last two equations can be expressed in an alternative form

$$\overline{\phi_{|x}} = \gamma \Delta t \left(\frac{G(t)}{6} + \frac{G(t+\Delta t)}{3} \right) x \tag{A.24}$$

$$\sigma^2_{\phi|x} = \gamma^2 D \Delta t^3 \left(\frac{G(t)G(t+\Delta t)}{6} + \frac{2\left(G(t+\Delta t) - G(t)\right)^2}{45} \right) \tag{A.25}$$

where $G(t)$ and $G(t+\Delta t)$ denote the gradient strength in the beginning and the end of the time step, Δt, respectively. It should be emphasized, that the static precession angle is given by $\gamma \Delta t X \left(G(t) + G(t+\Delta t)\right)/2$, where X is the location of the spin in the beginning of the time step.

A.4 Some Fourier Transform Properties

Transform of a Gaussian

$$\frac{1}{\sqrt{\sigma^2 2\pi}} \int_{-\infty}^{\infty} \exp\left[\frac{-(y-x)^2}{2\sigma^2} + i \cdot a(y-x) \right] dx = \exp\left[\frac{-\sigma^2}{2} a^2 \right] \tag{A.26}$$

Convolution

$$\mathcal{F}\left\{ m(x) * c(x, \Delta t) \right\} = \mathcal{F}\left\{ m(x) \right\} \mathcal{F}\left\{ c(x, \Delta t) \right\} = M(k) C(k, \Delta t) \tag{A.27}$$

Scaling and Modulation

$$\mathcal{F}\left\{ f(bx) e^{iax} \right\} = \frac{1}{b} F\left(\frac{k-a}{b} \right) \tag{A.28}$$

Appendix B

Partition Analysis

By using Eq. (5.17) the precession angle for each of the four transverse pathways can be written as

$$\begin{aligned}
\phi_1 &= \phi \\
\phi_2 &= \phi + ((m+1)\Delta_v + \delta_m + \delta_1) \\
\phi_3 &= \phi + ((m+l+2)\Delta_v + \delta_m + \delta_1 + \delta_l + \delta_2) \\
\phi_4 &= \phi + ((m+l+k+3)\Delta_v + \delta_m + \delta_1 + \delta_l + \delta_2 + \delta_k + \delta_3)
\end{aligned} \tag{B.1}$$

where $\Delta_v = \gamma G_{\text{eff}}\, v\text{TR}^2$ and in general $\delta = \gamma G_{\text{eff}}\text{TR}\Delta x$. The random variables δ_1, δ_2 and δ_3 are changes in the precession angle due to diffusion during only one SSFP cycle. The random variables δ_k, δ_l and δ_k are, however, changes due to k, l and m SSFP cycles, respectively. The variance of δ_k is therefore k times larger than the variance of δ_1 and so on. According to Eq. (3.6) the variance of the particle displacement, Δx, during one SSFP cycle is given by $2D\text{TR}$. For a zero mean Gaussian probability distributions, we find that

$$\begin{aligned}
\frac{1}{2\pi}\int_0^{2\pi}\int_{-\infty}^{\infty}\int_{-\infty}^{\infty}\int_{-\infty}^{\infty}\int_{-\infty}^{\infty}\left(\prod_{i=1}^{4}\cos(\phi+\Delta_i+\delta_i)\Pr(\delta_i)\right)d\delta_1 d\delta_2 d\delta_3 d\delta_4 d\phi = \\
\frac{1}{8}\left[\cos(\Delta_1-\Delta_2-\Delta_3+\Delta_4)\exp\left(-\text{var}(\delta_1-\delta_2-\delta_3+\delta_4)/2\right)\right. \\
+\cos(\Delta_1-\Delta_2+\Delta_3-\Delta_4)\exp\left(-\text{var}(\delta_1-\delta_2+\delta_3-\delta_4)/2\right) \\
\left.+\cos(\Delta_1+\Delta_2-\Delta_3-\Delta_4)\exp\left(-\text{var}(\delta_1+\delta_2-\delta_3-\delta_4)/2\right)\right]
\end{aligned} \tag{B.2}$$

Note that when there is a uniform distribution of precession angles, the signal from an odd number of transverse pathways is always zero because

$$\frac{1}{2\pi}\int_0^{2\pi}\prod_{i=1}^{n}\cos(\phi+\Delta_i)d\phi = 0 \qquad \text{for} \qquad n = 1,3,5,\ldots \tag{B.3}$$

By using the identity in Eq. (B.2), we can evaluate the average magnetization of Eq. (5.18). We see from Eqs. (B.2) and (5.18) that we only need to know the mean and the variance of the three different combinations of the four precession angles, $\phi_1, \ldots, \phi_4$. The mean is only a function of the bulk flow and is deterministic whereas the variance is due to the stochastic nature of the diffusion.

	$\phi_1 - \phi_2$	$\phi_1 - \phi_2 - \phi_3 + \phi_4$	$\phi_1 - \phi_2 + \phi_3 - \phi_4$	$\phi_1 + \phi_2 - \phi_3 - \phi_4$
mean/Δ_v	$-(m+1)$	$-(m-k)$	$-(m+k+2)$	$-(m+2l+k+4)$
var/bD	$m+1$	$m+k+2$	$m+k+2$	$m+4l+k+6$

Table B.1: The accumulated flow phase and the total variance of the phase due to diffusion expressed as functions of k, l, and m.

Table B.1 shows how the mean and the variance add together for the different combinations of the four precession angles. Note that the variances always add, independent of the signs of the angles. Combining Eqs. (5.18) and (B.2) with the results in Table B.1 gives

$$\begin{aligned}\langle M(n,m,l,k)_x\rangle &= M_0(1-E_1)(E_1\cos\alpha)^{n+m+l+k-3}E_1^3E_2^4\sin^7\alpha\Big[\\ &\quad+\frac{1}{8}\Big(\sin(-(m-k)\Delta_v)A_{\mathrm{D}}^{m+k+2}\\ &\quad-\sin(-(m+k+2)\Delta_v)A_{\mathrm{D}}^{m+k+2}\\ &\quad-\sin(-(m+2l+k+4)\Delta_v)A_{\mathrm{D}}^{m+4l+k+6}\Big)\Big] \qquad \text{(B.4)}\end{aligned}$$

where $A_{\mathrm{D}} = \exp[-bD]$ and $b = (\gamma G_{\mathrm{eff}}\ \mathrm{TR})^2\ \mathrm{TR}$.

The total transverse signal at any given time can be expressed by adding up all the pathways from all previous inputs, which are in the transverse plane at the echo time. By using the following two identities repeatedly we find that the final result for the x-component is given by Eq. (5.20).

$$\sum_{m=1}^{\infty}\cos(a(m+b)\Delta_v)(E_1\cos\alpha)^{m-1} = \frac{\cos((b+1)a\Delta_v)-\cos(ba\Delta_v)E_1\cos\alpha}{(1-2\cos(a\Delta_v)E_1\cos\alpha+E_1^2\cos^2\alpha)}$$

$$\sum_{m=1}^{\infty}\sin(a(m+b)\Delta_v)(E_1\cos\alpha)^{m-1} = \frac{\sin((b+1)a\Delta_v)-\sin(ba\Delta_v)E_1\cos\alpha}{(1-2\cos(a\Delta_v)E_1\cos\alpha+E_1^2\cos^2\alpha)}$$

The contribution from other types of pathways is given in the following sections.

B.1 Two Transverse Pathways

B.1.1 $L \ldots LTT$

$$\begin{aligned} M(n)_x &= M_0(1-E_1)(E_1\cos\alpha)^n E_2^2 \sin\alpha \Big[\\ &\quad -\sin(\phi)\cos(\phi+(\Delta_v+\delta_1)) \\ &\quad -\cos\alpha\cos(\phi)\sin(\phi+(\Delta_v+\delta_1))\Big] \end{aligned} \tag{B.5}$$

$$\begin{aligned} \langle M(n)_x\rangle &= M_0(1-E_1)(E_1\cos\alpha)^n E_2^2 \sin\alpha \Big[\\ &\quad -\frac{1}{2}\left(\sin(-\Delta_v)A_{\mathrm{D}}^1\right) \\ &\quad -\cos\alpha\frac{1}{2}\left(-\sin(-\Delta_v)A_{\mathrm{D}}^1\right)\Big] \end{aligned} \tag{B.6}$$

$$\begin{aligned} \langle M_x\rangle &= \sum_{n=0}^{\infty}\langle M(n)_x\rangle \\ &= M_0(1-E_1)\frac{1}{1-E_1\cos\alpha}E_2^2\sin\alpha\Big[\\ &\quad \frac{1}{2}(1-\cos\alpha)\sin(\Delta_v)A_{\mathrm{D}}^1\Big] \end{aligned} \tag{B.7}$$

$$\begin{aligned} M(n)_y &= M_0(1-E_1)(E_1\cos\alpha)^n E_2^2 \sin\alpha \Big[\\ &\quad -\sin(\phi)\sin(\phi+(\Delta_v+\delta_1)) \\ &\quad +\cos\alpha\cos(\phi)\cos(\phi+(\Delta_v+\delta_1))\Big] \end{aligned} \tag{B.8}$$

$$\begin{aligned} \langle M(n)_y\rangle &= M_0(1-E_1)(E_1\cos\alpha)^n E_2^2 \sin\alpha \Big[\\ &\quad -\frac{1}{2}\left(\cos(-\Delta_v)A_{\mathrm{D}}^1\right) \\ &\quad +\cos\alpha\frac{1}{2}\left(\cos(-\Delta_v)A_{\mathrm{D}}^1\right)\Big] \end{aligned} \tag{B.9}$$

$$\begin{aligned}\langle M_y\rangle &= \sum_{n=0}^{\infty}\langle M(n)_y\rangle \\ &= M_0(1-E_1)\frac{1}{1-E_1\cos\alpha}E_2^2\sin\alpha\Big[\\ &\quad -\frac{1}{2}(1-\cos\alpha)\cos(\Delta_v)A_{\mathrm{D}}^1\Big]\end{aligned} \tag{B.10}$$

B.1.2 $L\ldots LTL\ldots LT$

$$\begin{aligned}M(n,m)_x &= M_0(1-E_1)(E_1\cos\alpha)^n(E_1\cos\alpha)^{m-1}E_1E_2^2\sin^3\alpha\Big[\\ &\quad +\cos(\phi)\sin(\phi+((m+1)\Delta_v+\delta_m+\delta_1))\Big]\end{aligned} \tag{B.11}$$

$$\begin{aligned}\langle M(n,m)_x\rangle &= M_0(1-E_1)(E_1\cos\alpha)^n(E_1\cos\alpha)^{m-1}E_1E_2^2\sin^3\alpha\Big[\\ &\quad +\frac{1}{2}\left(-\sin(-(m+1)\Delta_v)A_{\mathrm{D}}^{m+1}\right)\Big]\end{aligned} \tag{B.12}$$

$$\begin{aligned}\langle M_x\rangle &= \sum_{n=0}^{\infty}\sum_{m=1}^{\infty}\langle M(n)_x\rangle \\ &= M_0(1-E_1)\frac{1}{1-E_1\cos\alpha}E_1E_2^2\sin^3\alpha\Big[\\ &\quad +\frac{1}{2}\frac{A_{\mathrm{D}}^2\left(\sin(2\Delta_v)-\sin(\Delta_v)A_{\mathrm{D}}E_1\cos\alpha\right)}{(1-2\cos(\Delta_v)A_{\mathrm{D}}E_1\cos\alpha+A_{\mathrm{D}}^2E_1^2\cos^2\alpha)}\Big]\end{aligned} \tag{B.13}$$

$$\begin{aligned}M(n,m)_y &= M_0(1-E_1)(E_1\cos\alpha)^n(E_1\cos\alpha)^{m-1}E_1E_2^2\sin^3\alpha\Big[\\ &\quad -\cos(\phi)\cos(\phi+((m+1)\Delta_v+\delta_m+\delta_1))\Big]\end{aligned} \tag{B.14}$$

$$\begin{aligned}\langle M(n,m)_y\rangle &= M_0(1-E_1)(E_1\cos\alpha)^n(E_1\cos\alpha)^{m-1}E_1E_2^2\sin^3\alpha\Big[\\ &\quad -\frac{1}{2}\left(\cos(-(m+1)\Delta_v)A_{\mathrm{D}}^{m+1}\right)\Big]\end{aligned} \tag{B.15}$$

$$\begin{aligned}\langle M_y\rangle &= \sum_{n=0}^{\infty}\sum_{m=1}^{\infty}\langle M(n,m)_y\rangle \\ &= M_0(1-E_1)\frac{1}{1-E_1\cos\alpha}E_1E_2^2\sin^3\alpha\Bigg[\\ &\quad -\frac{1}{2}\frac{A_D^2\left(\cos(2\Delta_v)-\cos(\Delta_v)A_DE_1\cos\alpha\right)}{\left(1-2\cos(\Delta_v)A_DE_1\cos\alpha+A_D^2E_1^2\cos^2\alpha\right)}\Bigg]\end{aligned} \tag{B.16}$$

B.2 Four Transverse Pathways

B.2.1 $L\ldots LTTTT$

$$\begin{aligned}\langle M_x\rangle = M_0(1-E_1)\frac{1}{1-E_1\cos\alpha}E_2^4\sin\alpha\Bigg[\\ +\frac{1}{8}(1-3\cos\alpha+3\cos^2\alpha-\cos^3\alpha)A_D^2\sin(2\Delta_v) \\ +\frac{1}{8}(1+\cos\alpha-\cos^2\alpha-\cos^3\alpha)A_D^6\sin(4\Delta_v)\Bigg]\end{aligned} \tag{B.17}$$

$$\begin{aligned}\langle M_y\rangle = M_0(1-E_1)\frac{1}{1-E_1\cos\alpha}E_2^4\sin\alpha\Bigg[\\ +\frac{1}{8}(1-\cos\alpha-\cos^2\alpha+\cos^3\alpha)A_D^2 \\ -\frac{1}{8}(1-3\cos\alpha+3\cos^2\alpha-\cos^3\alpha)A_D^2\cos(2\Delta_v) \\ -\frac{1}{8}(1+\cos\alpha-\cos^2\alpha-\cos^3\alpha)A_D^6\cos(4\Delta_v)\Bigg]\end{aligned} \tag{B.18}$$

B.2.2 $L\ldots LTL\ldots LTTT$

$$\begin{aligned}\langle M_x\rangle = M_0(1-E_1)\frac{1}{1-E_1\cos\alpha}E_1E_2^4\sin^3\alpha\Bigg[\\ +\frac{1}{8}(1-\cos^2\alpha)\frac{A_{\mathrm{D}}^3\left(\sin(\Delta_v)\right)}{(1-2\cos(\Delta_v)A_{\mathrm{D}}E_1\cos\alpha+A_{\mathrm{D}}^2E_1^2\cos^2\alpha)}\\ +\frac{1}{8}(1-2\cos\alpha+\cos^2\alpha)\frac{A_{\mathrm{D}}^3\left(\sin(3\Delta_v)-\sin(2\Delta_v)A_{\mathrm{D}}E_1\cos\alpha\right)}{(1-2\cos(\Delta_v)A_{\mathrm{D}}E_1\cos\alpha+A_{\mathrm{D}}^2E_1^2\cos^2\alpha)}\\ -\frac{1}{8}(1-\cos^2\alpha)\frac{A_{\mathrm{D}}^7\left(\sin(5\Delta_v)-\sin(4\Delta_v)A_{\mathrm{D}}E_1\cos\alpha\right)}{(1-2\cos(\Delta_v)A_{\mathrm{D}}E_1\cos\alpha+A_{\mathrm{D}}^2E_1^2\cos^2\alpha)}\Bigg]\end{aligned} \tag{B.19}$$

$$\begin{aligned}\langle M_y\rangle = M_0(1-E_1)\frac{1}{1-E_1\cos\alpha}E_1E_2^4\sin^3\alpha\Bigg[\\ +\frac{1}{8}(1-\cos^2\alpha)\frac{A_{\mathrm{D}}^3\left(\cos(\Delta_v)-A_{\mathrm{D}}E_1\cos\alpha\right)}{(1-2\cos(\Delta_v)A_{\mathrm{D}}E_1\cos\alpha+A_{\mathrm{D}}^2E_1^2\cos^2\alpha)}\\ -\frac{1}{8}(1-2\cos\alpha+\cos^2\alpha)\frac{A_{\mathrm{D}}^3\left(\cos(3\Delta_v)-\cos(2\Delta_v)A_{\mathrm{D}}E_1\cos\alpha\right)}{(1-2\cos(\Delta_v)A_{\mathrm{D}}E_1\cos\alpha+A_{\mathrm{D}}^2E_1^2\cos^2\alpha)}\\ +\frac{1}{8}(1-\cos^2\alpha)\frac{A_{\mathrm{D}}^7\left(\cos(5\Delta_v)-\cos(4\Delta_v)A_{\mathrm{D}}E_1\cos\alpha\right)}{(1-2\cos(\Delta_v)A_{\mathrm{D}}E_1\cos\alpha+A_{\mathrm{D}}^2E_1^2\cos^2\alpha)}\Bigg]\end{aligned} \tag{B.20}$$

B.2.3 $L\ldots LTTL\ldots LTT$

$$\begin{aligned}\langle M_x\rangle = M_0(1-E_1)\frac{1}{1-E_1\cos\alpha}E_1E_2^4\sin^3\alpha\Bigg[\\ +\frac{1}{8}(1-2\cos\alpha+\cos^2\alpha)\frac{A_{\mathrm{D}}^2\sin(2\Delta_v)}{(1-E_1\cos\alpha)}\\ +\frac{1}{8}(1+2\cos\alpha+\cos^2\alpha)\frac{A_{\mathrm{D}}^{10}\left(\sin(6\Delta_v)-\sin(4\Delta_v)A_{\mathrm{D}}^4E_1\cos\alpha\right)}{(1-2\cos(2\Delta_v)A_{\mathrm{D}}^4E_1\cos\alpha+A_{\mathrm{D}}^8E_1^2\cos^2\alpha)}\Bigg]\end{aligned} \tag{B.21}$$

$$\begin{aligned}\langle M_y\rangle = M_0(1-E_1)\frac{1}{1-E_1\cos\alpha}E_1E_2^4\sin^3\alpha\Bigg[\\ -\frac{1}{8}(1-2\cos\alpha+\cos^2\alpha)\frac{A_D^2}{(1-E_1\cos\alpha)}\\ -\frac{1}{8}(1-2\cos\alpha+\cos^2\alpha)\frac{A_D^2\cos(2\Delta_v)}{(1-E_1\cos\alpha)}\\ -\frac{1}{8}(1+2\cos\alpha+\cos^2\alpha)\frac{A_D^{10}\left(\cos(6\Delta_v)-\cos(4\Delta_v)A_D^4E_1\cos\alpha\right)}{(1-2\cos(2\Delta_v)A_D^4E_1\cos\alpha+A_D^8E_1^2\cos^2\alpha)}\Bigg]\end{aligned} \tag{B.22}$$

B.2.4 $L\ldots LTTTL\ldots LT$

$$\begin{aligned}\langle M_x\rangle = M_0(1-E_1)\frac{1}{1-E_1\cos\alpha}E_1E_2^4\sin^3\alpha\Bigg[\\ -\frac{1}{8}(1-\cos^2\alpha)\frac{A_D^3\left(\sin(\Delta_v)\right)}{(1-2\cos(\Delta_v)A_DE_1\cos\alpha+A_D^2E_1^2\cos^2\alpha)}\\ +\frac{1}{8}(1-2\cos\alpha+\cos^2\alpha)\frac{A_D^3\left(\sin(3\Delta_v)-\sin(2\Delta_v)A_DE_1\cos\alpha\right)}{(1-2\cos(\Delta_v)A_DE_1\cos\alpha+A_D^2E_1^2\cos^2\alpha)}\\ -\frac{1}{8}(1-\cos^2\alpha)\frac{A_D^7\left(\sin(5\Delta_v)-\sin(4\Delta_v)A_DE_1\cos\alpha\right)}{(1-2\cos(\Delta_v)A_DE_1\cos\alpha+A_D^2E_1^2\cos^2\alpha)}\Bigg]\end{aligned} \tag{B.23}$$

$$\begin{aligned}\langle M_y\rangle = M_0(1-E_1)\frac{1}{1-E_1\cos\alpha}E_1E_2^4\sin^3\alpha\Bigg[\\ +\frac{1}{8}(1-\cos^2\alpha)\frac{A_D^3\left(\cos(\Delta_v)-A_DE_1\cos\alpha\right)}{(1-2\cos(\Delta_v)A_DE_1\cos\alpha+A_D^2E_1^2\cos^2\alpha)}\\ -\frac{1}{8}(1-2\cos\alpha+\cos^2\alpha)\frac{A_D^3\left(\cos(3\Delta_v)-\cos(2\Delta_v)A_DE_1\cos\alpha\right)}{(1-2\cos(\Delta_v)A_DE_1\cos\alpha+A_D^2E_1^2\cos^2\alpha)}\\ +\frac{1}{8}(1-\cos^2\alpha)\frac{A_D^7\left(\cos(5\Delta_v)-\cos(4\Delta_v)A_DE_1\cos\alpha\right)}{(1-2\cos(\Delta_v)A_DE_1\cos\alpha+A_D^2E_1^2\cos^2\alpha)}\Bigg]\end{aligned} \tag{B.24}$$

B.2.5 $L\ldots LTL\ldots LTL\ldots LTT$

$$\langle M_x\rangle = M_0(1-E_1)\frac{1}{1-E_1\cos\alpha}E_1^2E_2^4\sin^5\alpha\Bigg[$$
$$-\frac{(1-\cos\alpha)(A_D^3(\sin(\Delta_v))-A_D^3(\sin(3\Delta_v)-\sin(2\Delta_v)A_DE_1\cos\alpha))}{8(1-2\cos(\Delta_v)A_DE_1\cos\alpha+A_D^2E_1^2\cos^2\alpha)(1-E_1\cos\alpha)}$$
$$-\frac{(1+\cos\alpha)(A_D^{11}(\sin(7\Delta_v)-\sin(5\Delta_v)A_D^4E_1\cos\alpha))}{8(1-2\cos(\Delta_v)A_DE_1\cos\alpha+A_D^2E_1^2\cos^2\alpha)(1-2\cos(2\Delta_v)A_D^4E_1\cos\alpha+A_D^8E_1^2\cos^2\alpha)}$$
$$+\frac{(1+\cos\alpha)(A_DE_1\cos\alpha A_D^{11}(\sin(6\Delta_v)-\sin(4\Delta_v)A_D^4E_1\cos\alpha))}{8(1-2\cos(\Delta_v)A_DE_1\cos\alpha+A_D^2E_1^2\cos^2\alpha)(1-2\cos(2\Delta_v)A_D^4E_1\cos\alpha+A_D^8E_1^2\cos^2\alpha)}\Bigg] \tag{B.25}$$

$$\langle M_y\rangle = M_0(1-E_1)\frac{1}{1-E_1\cos\alpha}E_1^2E_2^4\sin^5\alpha\,[$$
$$-\frac{(1-\cos\alpha)(A_D^3(\cos(\Delta_v)-A_DE_1\cos\alpha)+A_D^3(\cos(3\Delta_v)-\cos(2\Delta_v)A_DE_1\cos\alpha))}{8(1-2\cos(\Delta_v)A_DE_1\cos\alpha+A_D^2E_1^2\cos^2\alpha)(1-E_1\cos\alpha)}$$
$$+\frac{(1+\cos\alpha)(A_D^{11}(\cos(7\Delta_v)-\cos(5\Delta_v)A_D^4E_1\cos\alpha))}{8(1-2\cos(\Delta_v)A_DE_1\cos\alpha+A_D^2E_1^2\cos^2\alpha)(1-2\cos(2\Delta_v)A_D^4E_1\cos\alpha+A_D^8E_1^2\cos^2\alpha)}$$
$$-\frac{(1+\cos\alpha)(A_DE_1\cos\alpha A_D^{11}(\cos(6\Delta_v)-\cos(4\Delta_v)A_D^4E_1\cos\alpha))}{8(1-2\cos(\Delta_v)A_DE_1\cos\alpha+A_D^2E_1^2\cos^2\alpha)(1-2\cos(2\Delta_v)A_D^4E_1\cos\alpha+A_D^8E_1^2\cos^2\alpha)}\Bigg] \tag{B.26}$$

B.2.6 $L\ldots LTL\ldots LTTL\ldots LT$

$$\langle M_x\rangle = M_0(1-E_1)\frac{1}{1-E_1\cos\alpha}E_1^2E_2^4\sin^5\alpha\Bigg[$$
$$-\frac{1}{8}(1+\cos\alpha)\frac{A_D^4(\sin(0\Delta_v)-\sin(-1\Delta_v)A_DE_1\cos\alpha)-A_DE_1\cos\alpha A_D^4(\sin(\Delta_v))}{(1-2\cos(\Delta_v)A_DE_1\cos\alpha+A_D^2E_1^2\cos^2\alpha)^2}$$
$$+\frac{1}{8}(1-\cos\alpha)\cdot\Bigg[$$
$$+\frac{A_D^4(\sin(4\Delta_v)-\sin(3\Delta_v)A_DE_1\cos\alpha)-A_DE_1\cos\alpha A_D^4(\sin(3\Delta_v)-\sin(2\Delta_v)A_DE_1\cos\alpha)}{(1-2\cos(\Delta_v)A_DE_1\cos\alpha+A_D^2E_1^2\cos^2\alpha)^2}$$
$$+\frac{A_D^8(\sin(6\Delta_v)-\sin(5\Delta_v)A_DE_1\cos\alpha)-A_DE_1\cos\alpha A_D^8(\sin(5\Delta_v)-\sin(4\Delta_v)A_DE_1\cos\alpha)}{(1-2\cos(\Delta_v)A_DE_1\cos\alpha+A_D^2E_1^2\cos^2\alpha)^2}\Bigg]\Bigg] \tag{B.27}$$

$$\langle M_y \rangle = M_0(1-E_1)\frac{1}{1-E_1\cos\alpha}E_1^2E_2^4\sin^5\alpha\Bigg[$$
$$+\frac{(1+\cos\alpha)}{8}\cdot$$
$$\frac{A_D^4\left(\cos(0\Delta_v)-\cos(-1\Delta_v)A_DE_1\cos\alpha\right)-A_DE_1\cos\alpha A_D^4\left(\cos(\Delta_v)-A_DE_1\cos\alpha\right)}{(1-2\cos(\Delta_v)A_DE_1\cos\alpha+A_D^2E_1^2\cos^2\alpha)^2}$$
$$-\frac{1}{8}(1-\cos\alpha)\cdot\Bigg[$$
$$+\frac{A_D^4\left(\cos(4\Delta_v)-\cos(3\Delta_v)A_DE_1\cos\alpha\right)-A_DE_1\cos\alpha A_D^4\left(\cos(3\Delta_v)-\cos(2\Delta_v)A_DE_1\cos\alpha\right)}{(1-2\cos(\Delta_v)A_DE_1\cos\alpha+A_D^2E_1^2\cos^2\alpha)^2}$$
$$+\frac{A_D^8\left(\cos(6\Delta_v)-\cos(5\Delta_v)A_DE_1\cos\alpha\right)-A_DE_1\cos\alpha A_D^8\left(\cos(5\Delta_v)-\cos(4\Delta_v)A_DE_1\cos\alpha\right)}{(1-2\cos(\Delta_v)A_DE_1\cos\alpha+A_D^2E_1^2\cos^2\alpha)^2}\Bigg]\Bigg] \tag{B.28}$$

B.2.7 $L\ldots LTTL\ldots LTL\ldots LT$

$$\langle M_x \rangle = M_0(1-E_1)\frac{1}{1-E_1\cos\alpha}E_1^2E_2^4\sin^5\alpha\Bigg[$$
$$+\frac{1}{8}(1-\cos\alpha)\frac{A_D^3\left(\sin(\Delta_v)\right)+A_D^3\left(\sin(3\Delta_v)-\sin(2\Delta_v)A_DE_1\cos\alpha\right)}{(1-2\cos(\Delta_v)A_DE_1\cos\alpha+A_D^2E_1^2\cos^2\alpha)(1-E_1\cos\alpha)}$$
$$-\frac{(1+\cos\alpha)(A_D^{11}\left(\sin(7\Delta_v)-\sin(5\Delta_v)A_D^4E_1\cos\alpha\right))}{8(1-2\cos(\Delta_v)A_DE_1\cos\alpha+A_D^2E_1^2\cos^2\alpha)(1-2\cos(2\Delta_v)A_D^4E_1\cos\alpha+A_D^8E_1^2\cos^2\alpha)}$$
$$+\frac{(1+\cos\alpha)(A_DE_1\cos\alpha A_D^{11}\left(\sin(6\Delta_v)-\sin(4\Delta_v)A_D^4E_1\cos\alpha\right))}{8(1-2\cos(\Delta_v)A_DE_1\cos\alpha+A_D^2E_1^2\cos^2\alpha)(1-2\cos(2\Delta_v)A_D^4E_1\cos\alpha+A_D^8E_1^2\cos^2\alpha)}\Bigg] \tag{B.29}$$

$$\langle M_y \rangle = M_0(1-E_1)\frac{1}{1-E_1\cos\alpha}E_1^2E_2^4\sin^5\alpha\Bigg[$$
$$-\frac{1}{8}(1-\cos\alpha)\frac{A_D^3\left(\cos(\Delta_v)-A_DE_1\cos\alpha\right)+A_D^3\left(\cos(3\Delta_v)-\cos(2\Delta_v)A_DE_1\cos\alpha\right)}{(1-2\cos(\Delta_v)A_DE_1\cos\alpha+A_D^2E_1^2\cos^2\alpha)(1-E_1\cos\alpha)}$$
$$+\frac{(1+\cos\alpha)(A_D^{11}\left(\cos(7\Delta_v)-\cos(5\Delta_v)A_D^4E_1\cos\alpha\right))}{8(1-2\cos(\Delta_v)A_DE_1\cos\alpha+A_D^2E_1^2\cos^2\alpha)(1-2\cos(2\Delta_v)A_D^4E_1\cos\alpha+A_D^8E_1^2\cos^2\alpha)}$$
$$-\frac{(1+\cos\alpha)(A_DE_1\cos\alpha A_D^{11}\left(\cos(6\Delta_v)-\cos(4\Delta_v)A_D^4E_1\cos\alpha\right))}{8(1-2\cos(\Delta_v)A_DE_1\cos\alpha+A_D^2E_1^2\cos^2\alpha)(1-2\cos(2\Delta_v)A_D^4E_1\cos\alpha+A_D^8E_1^2\cos^2\alpha)}\Bigg] \tag{B.30}$$

B.2.8 $L\ldots LTL\ldots LTL\ldots LTL\ldots LT$

$$\langle M_x \rangle = M_0(1-E_1)\frac{1}{1-E_1\cos\alpha}E_1^3E_2^4\sin^7\alpha\Bigg[$$
$$+\frac{1}{8}\frac{A_D^4\left(\sin(4\Delta_v)-\sin(3\Delta_v)A_DE_1\cos\alpha\right)}{(1-2\cos(\Delta_v)A_DE_1\cos\alpha+A_D^2E_1^2\cos^2\alpha)^2(1-E_1\cos\alpha)}$$
$$-\frac{1}{8}\frac{A_DE_1\cos\alpha A_D^4\left(\sin(3\Delta_v)-\sin(2\Delta_v)A_DE_1\cos\alpha\right)}{(1-2\cos(\Delta_v)A_DE_1\cos\alpha+A_D^2E_1^2\cos^2\alpha)^2(1-E_1\cos\alpha)}$$
$$+\frac{1}{8}\frac{A_D^{12}\left(\sin(8\Delta_v)-\sin(6\Delta_v)A_D^4E_1\cos\alpha\right)}{(1-2\cos(\Delta_v)A_DE_1\cos\alpha+A_D^2E_1^2\cos^2\alpha)^2(1-2\cos(2\Delta_v)A_D^4E_1\cos\alpha+A_D^8E_1^2\cos^2\alpha)}$$
$$-\frac{2}{8}\frac{A_DE_1\cos\alpha A_D^{12}\left(\sin(7\Delta_v)-\sin(5\Delta_v)A_D^4E_1\cos\alpha\right)}{(1-2\cos(\Delta_v)A_DE_1\cos\alpha+A_D^2E_1^2\cos^2\alpha)^2(1-2\cos(2\Delta_v)A_D^4E_1\cos\alpha+A_D^8E_1^2\cos^2\alpha)}$$
$$+\frac{1}{8}\frac{A_D^2E_1^2\cos^2\alpha A_D^{12}\left(\sin(6\Delta_v)-\sin(4\Delta_v)A_D^4E_1\cos\alpha\right)}{(1-2\cos(\Delta_v)A_DE_1\cos\alpha+A_D^2E_1^2\cos^2\alpha)^2(1-2\cos(2\Delta_v)A_D^4E_1\cos\alpha+A_D^8E_1^2\cos^2\alpha)}\Bigg] \tag{B.31}$$

$$\langle M_y \rangle = M_0(1-E_1)\frac{1}{1-E_1\cos\alpha}E_1^3E_2^4\sin^7\alpha\Bigg[$$
$$-\frac{1}{8}\frac{A_D^4\left(\cos(0\Delta_v)-\cos(-1\Delta_v)A_DE_1\cos\alpha\right)}{(1-2\cos(\Delta_v)A_DE_1\cos\alpha+A_D^2E_1^2\cos^2\alpha)^2(1-E_1\cos\alpha)}$$
$$+\frac{1}{8}\frac{A_DE_1\cos\alpha A_D^4\left(\cos(\Delta_v)-A_DE_1\cos\alpha\right)}{(1-2\cos(\Delta_v)A_DE_1\cos\alpha+A_D^2E_1^2\cos^2\alpha)^2(1-E_1\cos\alpha)}$$
$$-\frac{1}{8}\frac{A_D^4\left(\cos(4\Delta_v)-\cos(3\Delta_v)A_DE_1\cos\alpha\right)}{(1-2\cos(\Delta_v)A_DE_1\cos\alpha+A_D^2E_1^2\cos^2\alpha)^2(1-E_1\cos\alpha)}$$
$$+\frac{1}{8}\frac{A_DE_1\cos\alpha A_D^4\left(\cos(3\Delta_v)-\cos(2\Delta_v)A_DE_1\cos\alpha\right)}{(1-2\cos(\Delta_v)A_DE_1\cos\alpha+A_D^2E_1^2\cos^2\alpha)^2(1-E_1\cos\alpha)}$$
$$-\frac{1}{8}\frac{A_D^{12}\left(\cos(8\Delta_v)-\cos(6\Delta_v)A_D^4E_1\cos\alpha\right)}{(1-2\cos(\Delta_v)A_DE_1\cos\alpha+A_D^2E_1^2\cos^2\alpha)^2(1-2\cos(2\Delta_v)A_D^4E_1\cos\alpha+A_D^8E_1^2\cos^2\alpha)}$$
$$+\frac{2}{8}\frac{A_DE_1\cos\alpha A_D^{12}\left(\cos(7\Delta_v)-\cos(5\Delta_v)A_D^4E_1\cos\alpha\right)}{(1-2\cos(\Delta_v)A_DE_1\cos\alpha+A_D^2E_1^2\cos^2\alpha)^2(1-2\cos(2\Delta_v)A_D^4E_1\cos\alpha+A_D^8E_1^2\cos^2\alpha)}$$
$$-\frac{1}{8}\frac{A_D^2E_1^2\cos^2\alpha A_D^{12}\left(\cos(6\Delta_v)-\cos(4\Delta_v)A_D^4E_1\cos\alpha\right)}{(1-2\cos(\Delta_v)A_DE_1\cos\alpha+A_D^2E_1^2\cos^2\alpha)^2(1-2\cos(2\Delta_v)A_D^4E_1\cos\alpha+A_D^8E_1^2\cos^2\alpha)}\Bigg] \tag{B.32}$$

Bibliography

[1] D. C. Ailion, K. Ganesan, T. A. Case, and R. A. Christman. Rapid line scan technique for artifact-free images of moving objects. *Magn. Reson. Imag.*, 10:747–757, 1992.

[2] A. W. Anderson and J. C. Gore. Analysis and correction of motion artifacts in diffusion weighted imaging. *Magn. Reson. Med.*, 32:379–387, 1994.

[3] B. Authier. Reactive hypertermia monitored on rat muscle using perfluorocarbons and ^{19}F NMR. *Magn. Reson. Med.*, 8:80–83, 1988.

[4] H. R. Avram and L. E. Crooks. Effect of self-diffusion on echo-planar imaging. In *Proc. SMRM 7th Annual Meeting*, volume 1, page 80, Berkeley, CA, August 1988.

[5] B. Balinov, B. Jönsson, P. Linse, and O. Söderman. The NMR self-diffusion method applied to restricted diffusion. simulation of echo attenuation from molecules in spheres and between planes. *J. Magn. Reson.*, 104:17–25, 1993.

[6] P. J. Basser, J. Mattiello, and D. Le Bihan. MR diffusion tensor spectroscopy and imaging. *Biophys. Journal*, 66:259–267, 1994.

[7] C. Beaulieu and P. S. Allen. Determinants of anisotropic water diffusion in nerves. *Magn. Reson. Med.*, 31(4):394–400, 1994.

[8] C. R. Becker, L.R. Schad, T. Hess, and W. J. Lorenz. Intravoxel incoherent motion MR imaging of brain tumors with diffusion sensitized turbo-flash and SSFP sequences. In *Proc. SMRM 12th Annual Meeting*, volume 2, page 599, New York, August 1993.

[9] J. W. Belliveau, B. R. Rosen, H. L. Kantor, R. R. Rzedzian, D. N. Kennedy, R. C. McKinstry, J. M. Vevea, M. S. Cohen, I. L. Pykett, and T. J. Brady. Functional cerebral imaging by susceptibility-contrast NMR. *Magn. Reson. Med.*, 14:538–546, 1990.

[10] M. A. Bernstein, D. M. Thomasson, and W. H. Perman. Improved detectability in low signal-to-noise ratio magnetic resonance images by means of a phase-corrected real reconstruction. *Med. Phys.*, 15(5):813–817, 1989.

[11] M. H. Blees. The effect of finite duration of gradient pulses on the pulsed-field-gradient nmr method for studying restricted diffusion. *J. Magn. Reson.*, 109:203–209, 1994.

[12] S. Brockstedt, C. Thomsen, J. De Poorter, R. Wirestam, C. De Wagter, L. G. Salford, F. Ståhlberg, B. R. R. Persson, and O. Henriksen. Development of a diffusion-sensitive pulse sequence using an enhanced gradient system. application on patients with astrocytomas. In *Proc. SMRM 12th Annual Meeting*, volume 2, page 590, New York, August 1993.

[13] S. Brockstedt, C. Thomsen, R. Wirestam, S. Holtås, and F. Ståhlberg. Development of a diffusion-sensitive fast spin-echo pulse sequence with navigator echo motion correction. In *Third Meeting of the Society of Magnetic Resonance*, volume 2, page 905, Nice, August 1995.

[14] K. Butts, A. de Crespigny, and M. Moseley. Diffusion-weighted interleaved EPI with navigation for stroke imaging. In *Third Meeting of the Society of Magnetic Resonance*, volume 3, page 1386, Nice, August 1995.

[15] R. B. Buxton. The diffusion sensitivity of fast steady-state free precession imaging. *Magn. Reson. Med.*, 29:235–243, 1993.

[16] Paul T. Callaghan. *Principles of Nuclear Magnetic Resonance Microscopy.* Oxford University Press Inc., New York, 1991. ISBN 0-19-853944-4.

[17] C. E. Carney, S. T. S. Wong, and S. Patz. Analytical solution and verification of diffusion effect in SSFP. *Magn. Reson. Med.*, 19:240–246, 1991.

[18] H. Y. Carr and E. M. Purcell. Effect of diffusion on free precession in nuclear magnetic resonance experiments. *Phys. Rev.*, 94:630–636, 1954.

[19] T. L. Chenevert, J. A. Brunberg, and J. G. Pipe. Anisotropic diffusion in human white matter: Demonstration with MR techniques in vivo. *Radiology*, 177:401–405, 1990.

[20] D. Chien, K. Kwong, D. Gress, F. Buonanno, R. Buxton, and B. Rosen. MR diffusion imaging of cerebral infarction in humans. *AJNR*, 13:1097, 1992.

[21] A. P. Crawley, M. L. Wood, and R. M. Henkelman. Elimination of transverse coherences in FLASH MRI. *Magn. Reson. Med.*, 8:248–260, 1988.

[22] B. J. Dardzinski, C. H. Sotak, M. Fisher, Y. Hasegawa, L. Li, and K. Minematsu. Apparent diffusion coefficient mapping of experimental focal cerebral ischemia using diffusion-weighted echo-planar imaging. *Magn. Reson. Med.*, 30(3):318–325, 1993.

[23] D. Davis, J. Ulatowski, S. Eleff, M. Izuta, S. Mori, D. Shungu, and P. C. M. van Zijl. Rapid monitoring of changes in water diffusion coefficient during reversible ischemia in cat and rat brain. *Magn. Reson. Med.*, 31(4):454–460, 1994.

[24] A. J. de Crespigny, M. P. Marks, D. R. Enzmann, and M. E. Moseley. Navigated diffusion imaging of normal and ischemic human brain. *Magn. Reson. Med.*, 33(5):720–728, 1995.

[25] A. J. de Crespigny, T. P. L. Roberts, J. Kucharcyzk, and M. E. Moseley. Improved sensitivity to magnetic susceptibility contrast. *Magn. Reson. Med.*, 30(1):135–137, 1993.

[26] M. Deimling and O. Heid. High resolution SSFP diffusion imaging. In *Second Meeting of the Society of Magnetic Resonance*, volume 2, page 1033, San Francisco, August 1994.

[27] M. Deimling, O. Heid, and U. Böttcher. SSFP imaging with synergistic T_1-T_2-contrast. In *Proc. SMRM 12th Annual Meeting*, volume 3, page 1206, New York, August 1993.

[28] S. Ding, H. Trillaud, M. Yongbi, E. L. Rolett, J. B. Weaver, and J. F. Dunn. High resolution renal diffusion imaging using a modified steady-state free precession sequence. *Magn. Reson. Med.*, 34(4):586–595, 1995.

[29] R. R. Edelman, J. Gaa, V. J. Wedeen, E. Loh, J. M. Hare, P. Prasad, and W. Li. In vivo measurement of water diffusion in the human heart. *Magn. Reson. Med.*, 32:423–428, 1994.

[30] R. R. Edelman, B. Siewert, M Adamis, J. Gaa, G. Laub, and P. Wielopolski. Signal targeting with alternating radiofrequency (STAR) sequences: Application to MR angiography. *Magn. Reson. Med.*, 31(2):233–238, 1994.

[31] W. A. Edelstein, G. H. Glover, C. J. Hardy, and W. Redington. The intrinsic signal-to-noise ratio in nmr imaging. *Magn. Reson. Med.*, 3:604–618, 1986.

[32] R. L. Ehman and J. P. Felmlee and. Adaptive technique for high-definition MR imaging of moving structures. *Radiology*, 173:255, 1989.

[33] A. Einstein. *Investigations on the theory of the Brownian movement.* Dover Publications Inc., 1956. ISBN 0-486-60304-0.

[34] R. R. Ernst and W. A. Anderson. Application of Fourier transform spectroscopy to magnetic resonance. *Rev. Sci. Instr.*, 37(1):93–102, 1966.

[35] R. R. Ernst, G. Bodenhausen, and A. Wokaun. *Principles of Nuclear Magnetic Resonance in One and Two Dimensions.* The international series of monographs on chemistry; 14. Oxford University Press Inc., New York, 1992. ISBN 0-19-855647-0.

[36] T. C. Farrar. *Introduction to Pulse NMR Spectroscopy.* The Farragut Press, Madison, Wisconsin, 1989. ISBN 0-917903-00-5.

[37] D. A. Feinberg and P. D. Jakab. Tissue perfusion in humans studied by Fourier velocity distribution, line scan, and echo-planar imaging. *Magn. Reson. Med.*, 16:280–293, 1990.

[38] R. Feynman, R. B. Leighton, and M. L. Sands. *The Feynman Lectures on Physics: Commemorative Issue.* Addison-Wesley, Reading, Massachusetts, 1989. ISBN 0-201-51003-0.

[39] M. Fischer, K. Bockhorst, M. H. Berlage, B. Schmitz, and K. A. Hossmann. Imaging of the apparent diffusion coefficient for the evaluation of cerebral metabolic recovery after cardiac arrest. *Magn. Reson. Imag.*, 13(6):781–790, 1995.

[40] C. R. Fisel, J. L. Ackerman, R. B. Buxton, L. Garrido, J. W. Belliveau, B. Rosen, and T. J. Brady. MR contrast due to microscopically heterogeneous magnetic susceptibility: Numerical simulations and applications to cerebral physiology. *Magn. Reson. Med.*, 17:336–347, 1991.

[41] M. Forsting, W. Reith, S. Heiland, T. Benner, and K. Sartor. MR-perfusion imaging in cerebrovascular disease: from experimental research to clinical application. *Advances in MRI Contrast*, 3(3):60–69, 1995.

[42] G. F. Franklin, J. D. Powell, and M. L. Workman. *Digital Control of Dynamic Systems.* Addison-Wesley Series in Electrical and Computer Engineering: Control Engineering. Addison-Wesley, Reading, Massachusetts, 2nd edition, 1990. ISBN 0-201-11938-2.

[43] R. Freeman and H. D. W. Hill. Phase and intensity anomalies in Fourier transform NMR. *J. Magn. Reson.*, 4:366, 1971.

[44] Z. W. Fu, Y. Wang, R. C. Grimm, P. J. Rossman, J. P. Felmlee, S. J. Riederer, and R. L. Ehman. Orbital navigator echoes for motion measurements in magnetic resonance imaging. *Magn. Reson. Med.*, 34(5):746–753, 1995.

[45] P. Gillis and S. H. Koenig. Transverse relaxation to solvent protons induced by magnetized spheres: Application to ferrition, erythrocytes, and magnetite. *Magn. Reson. Med.*, 5:323–345, 1987.

[46] A. F. Gmitro and A. L. Alexander. Use of a projection reconstruction method to decrease motion sensitivity in diffusion-weighted MRI. *Magn. Reson. Med.*, 29(6):835–838, 1993.

[47] H. Gudbjartsson, S. E. Maier, R. V. Mulkern, I. A. Morocz, and F. A. Jolesz. Diffusion weighted linescan imaging. In *Third Meeting of the Society of Magnetic Resonance*, volume 2, page 908, Nice, August 1995.

[48] H. Gudbjartsson and S. Patz. Fast time step invariant diffusion simulation. In *Second Meeting of the Society of Magnetic Resonance*, volume 2, page 1053, San Francisco, August 1994.

[49] H. Gudbjartsson and S. Patz. Simultaneous calculation of flow and diffusion sensitivity in SSFP. Oral Presentation. In *First Meeting of the Society of Magnetic Resonance*, volume JMRI 4(P), page 45, Dallas, March 1994.

[50] H. Gudbjartsson and S. Patz. Correction of diffusion weighted RARE images using navigator echoes. In *Third Meeting of the Society of Magnetic Resonance*, volume 2, page 904, Nice, August 1995.

[51] H. Gudbjartsson and S. Patz. NMR diffusion simulation based on conditional random walk. *IEEE Trans. Med. Imag.*, 14(4):636–642, 1995.

[52] H. Gudbjartsson and S. Patz. The Rician distribution of noisy MRI data. *Magn. Reson. Med.*, 34(6):910–914, 1995.

[53] H. Gudbjartsson and S. Patz. Simultaneous calculation of flow and diffusion sensitivity in SSFP. *Magn. Reson. Med.*, 34(4):567–579, 1995.

[54] M. L. Gyngell. The steady-state signals in short-repetition-time sequences. *J. Magn. Reson.*, 81:474–483, 1989.

[55] E. L. Hahn. Spin echoes. *Phys. Rev.*, 80:580–594, 1950.

[56] C. J. Hardy, H. E. Cline, and R. D. Watkins. One-dimensional NMR thermal mapping of focused ultrasound surgery. *JCAT*, 18(3):476–483, 1994.

[57] P. Hardy and R. M. Henkelman. On the transverse relaxation rate enhancement induced by diffusion of spins through inhomogeneous fields. *Magn. Reson. Med.*, 17:348–356, 1991.

[58] R. M. Henkelman. Measurement of signal intensities in the presence of noise in mr images. *Med. Phys.*, 12:232–233, 1985. Erratum in 13:544, 1986.

[59] A. L. Hopkins, E. M. Haacke, J. Tkach, et al. Improved sensitivity of proton mr to oxygen-17 as a contrast agent using fast-imaging detection in brain. *Magn. Reson. Med.*, 7:222, 1988.

[60] M. A. Horsfield, G. J. Barker, and W. I. McDonald. Self-diffusion in CNS tissue by volume-selective proton NMR. *Magn. Reson. Med.*, 31(6):637–644, 1994.

[61] D. I. Hoult and P. C. Lauterbur. The sensitivity of the zeugmatographic experiment involving human samples. *J. Magn. Reson.*, 34:425–433, 1979.

[62] A. K. Jain. *Fundamentals of Digital Image Processing.* Prentice Hall, Englewood Cliffs, New Jersey 07632, 1989. ISBN 0-13-336165-9.

[63] F. A. Jolesz, S. Patz, R. C. Hawkes, and I. Lopez. Fast imaging of CSF flow/motion patterns using steady-state free precession (SSFP). *Invest. Radiology*, 22:761–771, 1987.

[64] K. J. Jung and Z. H. Cho. Reduction of flow artifacts in NMR diffusion imaging using new angle tilted line-integral projection reconstruction. *Magn. Reson. Med.*, 19:349–360, 1991.

[65] R. Kaiser, E. Bartholdi, and R. R. Ernst. Diffusion and field-gradient effects in NMR Fourier spectroscopy. *J. Chem. Phys.*, 60(8):2966–2979, 1974.

[66] A. C. Kak and M. Slaney. *Principle of Computerized Tomographic Imaging.* IEEE Press, 345 East 47th Street, New York, NY 10017-2394, 1988. ISBN 0-87942-198-3.

[67] D. J. Kim and Z. H. Cho. Analysis of the higher-order echoes in SSFP. *Magn. Reson. Med.*, 19:20–30, 1991.

[68] J. E. Kirsch, L. Hilaire, D. Hucaby, and V. M. Runge. Preliminary studies towards quantitative perfusion using dynamic contrast enhanced MRI. In *Proc. SMRM 12th Annual Meeting*, volume 2, page 627, New York, August 1993.

[69] K. Kohno, M. Hoehn-Berlage, G. Mies, T. Back, and K. A. Hossman. Relationship between diffusion-weighted MR images, cerebral blood flow, and energy state in experimental brain infarction. *Magn. Reson. Imag.*, 13:73–80, 1995.

[70] B. P. Lathi. *Modern Digital and Analog Communication Systems.* ,Hault-Saunders International Edition. Hault-Saunders, Japan, 1983. ISBN 4-83337-0156-1.

[71] D. Le Bihan. Intravoxel incoherent motion imaging using steady-state free precession. *Magn. Reson. Med.*, 7:346–351, 1988.

[72] D. Le Bihan, E. Breton, D. Lallemand, P. Grenier, E. A. Cabanis, and M. Laval-Jeantet. MR imaging of intravoxel incoherent motions: application to diffusion and perfusion in neurologic disorders. *Radiology*, 161:401–407, 1986.

[73] D. Le Bihan, E. Breton, and A. Syrota. Imagerie de diffusion par résonance magnétique nucléaire. *C R Acad Sci.*, 301:1109–1112, 1985.

[74] D. Le Bihan, R. Turner, and J. R. MacFall. Effects of intravoxel incoherent motions (IVIM) in steady-state free precession (SSFP) imaging: Application to molecular diffusion imaging. *Magn. Reson. Med.*, 10:324–337, 1989.

[75] R. L. Liboff. *Quantum Mechanics.* Addison-Wesley, Reading, Massachusetts, 2nd edition, 1991. ISBN 0-201-54715-5.

[76] G. Liu, P. van Gelderen, and C. T. W. Moonen. Single-shot diffusion MRI on a conventional clinical instrument. In *Second Meeting of the Society of Magnetic Resonance*, volume 2, page 1034, San Francisco, August 1994.

[77] X. Ma, G. T. Gullberg, and D. L. Parker. The effect of flow rate of externally tagged endogenous protons on the MRI signal intensity. In *Proc. SMRM 12th Annual Meeting*, volume 2, page 616, New York, August 1993.

[78] S. E. Maier, C. J. Hardy, and F. A. Jolesz. Brain and cerebrospinal fluid motion: Real-time quantification with M-mode MR imaging. *Radiology*, 193:447–483, 1994.

[79] A. Mancuso, H. Karibe, W. D. Rooney, G. J. Zarow, S. H. Graham, M. W. Weiner, and P. R. Weinstein. Correlation of early reduction in the apparent diffusion coefficient of water with blood flow reduction during middle cerebral artery occlusion in rats. *Magn. Reson. Med.*, 34:368–377, 1995.

[80] I. Mano, R. M. Levy, L. E. Crooks, and A. Hosobuchi. Proton nuclear magnetic resonance imaging of acute experimental cerebral ischemia. *Investigative Radiology*, 18:345–351, 1983.

[81] G. McGibney and M. R. Smith. An unbiased signal-to-noise ratio measure for magnetic resonance images. *Med. Phys.*, 20(4):1077–1078, 1993.

[82] R. S. Menon, S. Ogawa, D. W. Tank, and K. Uğurbil. Tesla gradient recalled echo characteristics of photic stimulation-induced signal changes in the human primary visual cortex. *Magn. Reson. Med.*, 30:380–386, 1993.

[83] K. D. Merboldt, W. Hänicke, M. L. Gyngell, J. Frahm, and H. Bruhn. The influence of flow and motion in MRI of diffusion using a modified CE-FAST sequence. *Magn. Reson. Med.*, 12:198–208, 1989.

[84] K. D. Merboldt, W. Hänicke, M. L. Gyngell, J. Frahm, and H. Bruhn. Rapid NMR imaging of molecular self-diffusion using a modified CE-FAST sequence. *J. Magn. Reson.*, 82:115–121, 1989.

[85] A. J. Miller and P. M. Joseph. The use of power images to perform quantitative analysis on low snr mr images. *Magn. Reson. Imag.*, 11:1051–1056, 1993.

[86] C. T. Mizumoto and E. Yoshitome. Multiple echo SSFP sequences. *Magn. Reson. Med.*, 18:244–250, 1991.

[87] S. Mori and P. C. M. van Zijl. Diffusion weighting by the trace of the diffusion tensor within a single scan. *Magn. Reson. Med.*, 33:41–52, 1995.

[88] D. Morvan. In vivo measurement of diffusion and pseudo-diffusion in skeletal muscle at rest and after exercise. *Magn. Reson. Imag.*, 13:193–199, 1995.

[89] D. Morvan, A. Leroy-Willig, A. Malgouyres, C. A. Cuenod, P. Jehenson, and A. Syrota. Simultaneous temperature and regional blood volume measurements in human muscle using an MRI fast diffusion technique. *Magn. Reson. Med.*, 29(3):371–377, 1993.

[90] M. E. Moseley, J. Kucharczyk, J. Mintorovitch, Y. Cohen, J. Kurhanewicz, N. Derugin, H. Asgari, and D. Norman. Diffusion-weighted MR imaging of acute stroke: correlation with T2-weighted and magnetic suceptibility-enhanced MR imaging in cats. *AJNR*, 11:423, 1990.

[91] R. V. Mulkern, J. Meng, K. Oshio, C. R. G. Guttmann, and D. Jaramillo. Bone marrow characterization in the lumbar spine with inner volume spectroscopic CPMG imaging studies. *J. Magn. Reson. Imag.*, 4:585–589, 1994.

[92] R. V. Mulkern and R. G. S. Spencer. Diffusion imaging with paired CPMG sequences. *Magn. Reson. Imag.*, 6:623–631, 1988.

[93] M. F. Müller, P. V. Prasad, D. Bimmler, A. Kaiser, and R. Edelman. Funcional imaging of the kidney by means of measurement of the apparent diffusion coefficient. *Radiology*, 193:711–715, 1994.

[94] M. F. Müller, P. V. Prasad, B. Siewert, M. A. Nissenbaum, V. Raptopoulos, and R. R. Edelman. Abdominal diffusion mapping with use of a whole-body echo-planar system. *Radiology*, 190:475–478, 1994.

[95] S. Ogawa, T. M. Lee, A. S. Nayak, and P. Glynn. Oxygenation-sensitive contrast in magnetic resonance image of rodent brain at high magnetic fields. *Magn. Reson. Med.*, 14:68, 1990.

[96] A. V. Oppenheim and R. W. Schafer. *Discrete-Time Signal Processing.* Prentice Hall, Englewood Cliffs, New Jersey 07632, 1989. ISBN 0-13-216292-X.

[97] R. J. Ordidge, J. A. Helpern, Z. X. Qing, R. A. Knight, and V. Nagesh. Correction of motional artifacts in diffusion-weighted MR images using navigator echoes. *Magn. Reson. Imag.*, 12:455–460, 1994.

[98] A. Papoulis. *Probability, Random Variables, and Stochastic Processes.* McGraw-Hill Inc., 3rd edition, 1991. ISBN 0-07-048477-5.

[99] R. K. Pathria. *Statistical Mechanics.* Pergamon Press, 1984.

[100] S. Patz. Zero velocity suppression using steady state free precession. In *Proc. SMRM 6th Annual Meeting*, Montreal, August 1986.

[101] S. Patz. Some factors that influence the steady state in steady-state free precession. *Magn. Reson. Imag.*, 6:405–413, 1988.

[102] S. Patz and R. C. Hawkes. The application of steady-state free precession to the study of very slow fluid flow. *Magn. Reson. Med.*, 3:140–145, 1986.

[103] S. Patz, T. S. Wong, and M. S. Roos. Missing pulse steady-state free precession. *Magn. Reson. Med.*, 10:194–209, 1989.

[104] L. Pauling and C. Coryell. The magnetic properties and structure of hemoglobin, oxyhemoglobin and carbon monooxyhemoglobin. *Proc. Natl. Acad. Sci. (USA)*, 22:210–216, 1936.

[105] J. Pauly, D. Nishimura, and A. Macovski. A k-space analysis of small-tip-angle excitation. *J. Magn. Reson.*, 81:43–56, 1989.

[106] J. De Poorter, Y. De Deene, R. Van de Walle, C. De Wagter, C. Thomsen, S. Brockstedt, F. Ståhlberg, and E. Achten. An improved line-scanning technique for in vivo diffusion imaging without motion artifacts. In *Third Meeting of the Society of Magnetic Resonance*, volume 2, page 907, Nice, August 1995.

[107] W. H. Press, S. A. Teukolsky, W. T Vetterling, and B. P. Flannery. *Numerical Recipes in C: the art of scientific computing.* Cambridge University Press, 2nd edition, 1992. ISBN 0-521-43108-5.

[108] S. O. Rice. *Mathematical Analysis of Random Noise.* Dover Publication, 1954. Reprinted by N. Wax, Selected Papers on Noise and Stochastic Process, *Bell System Tech. J.*, 23:282, 1944.

[109] B. Robertson. Spin-echo decays of spins diffusion in a bounded region. *Phys. Rev.*, 151:273, 1966.

[110] B. R. Rosen, W. Belliveau, J. M. Vevea, and T. J. Brady. Perfusion imaging with NMR contrast agents. *Magn. Reson. Med.*, 14:249–265, 1990.

[111] K. Sekihara. Steady-state magnetization in rapid NMR imaging using small flip angles and short repetition intervals. *IEEE Trans. Med. Imag.*, MI-6(2):157–164, June 1987.

[112] K. Seong-Gi and J. J. H. Ackerman. Multicompartment analysis of blood flow and tissue perfusion employing D_2O as a freely diffusible tracer: A novel deuterium NMR techinique demonstrated via application with muring RIF-1 tumors. *Magn. Reson. Med.*, 8:410–426, 1988.

[113] S. Shioya, R. Christman, and D. C. Ailion. An in vivo NMR imaging determination of multiexponential Hahn T2 of normal lung. *Magn. Reson. Med.*, 16:49–56, 1990.

[114] S. Shioya, R. Christman, D. C. Ailion, A. G. Cutillo, and K. C. Goodrich. Nuclear magnetic resonance Hahn spin-echo decay T_2 in live rats with endotoxin lung injury. *Magn. Reson. Med.*, 29(4):441–445, 1993.

[115] C. P. Slichter. *Principles of Magnetic Resonance.* Springer series in solid-state sciences. Springer-Verlag, New York, Berlin, Heidelberg, 3rd edition, 1990. ISBN 0-387-50157-6.

[116] A. G. Sorensen, R. M. Weisskoff, T. R. Reese, and B. R. Rosen. Optimization of diffusion-weighted MR imaging for evaluation of acute stroke. In *Third Meeting of the Society of Magnetic Resonance*, volume 3, page 1383, Nice, August 1995.

[117] E. O. Stejskal. Use of spin echoes in a pulsed magnetic-field gradient to study anisotropic, restricted diffusion and flow. *J. Chem. Phys.*, 43:3597–3602, 1965.

[118] E. O. Stejskal and J. E. Tanner. Spin diffusion measurements: Spin echoes in the presence of a time-dependent field gradient. *J. Chem. Phys.*, 42:288–292, 1965.

[119] M. E. Stromski, H. R. Brady, S. R. Gullans, and S. Patz. Application of missing pulse steady state free precession to the study of renal microcirculation. *Magn. Reson. Med.*, 20:66–77, 1991.

[120] A. Szafer, J. Zhong, and J. C. Gore. Theoretical model for water diffusion in tissues. *Magn. Reson. Med.*, 33(5):697–712, 1995.

[121] M. Takahashi, B. Fritz-Zieroth, T. Chikugo, and H. Ogawa. Differentiation of chronic lesions after stroke in stoke-prone spontaneously hypertensive rats using diffusion weighted MRI. *Magn. Reson. Med.*, 30(4):485–488, 1993.

[122] The National Institute of Neurological Disorders and Stroke rt-PA Stroke Study Group. Tissue plasminogen activator for acute ischemic stroke. *The New England Journal Medicine*, 333(24):1581–1587, 1995.

[123] C. Thomsen, O. Henriksen, and P. Ring. In vivo measurement of water self-diffusion in the human brain by magnetic resonance imaging. *Acta Radiol.*, 28:353–361, 1987.

[124] K. Thulborn, J. Waterton, P. Matthews, and G. Radda. Oxygenation dependence of the transverse relaxation time of water protons in whole blood at high field. *Biochem. Biophys. Acta.*, 714:265–270, 1982.

[125] R. D. Tien, M. Bernstein, and J. MacFall. Pulsatile motion artifact reduction in 3D steady-state-free-precession-echo brain imaging. *Magn. Reson. Imag.*, 11(2):175–181, 1993.

[126] H. C. Torrey. Bloch equations with diffusion terms. *Phys. Rev.*, 104:563–565, 1956.

[127] T. Tsukamoto, K. King, T. K. F. Foo, and E. Yoshitome. Diffusion imaging with spiral scans. In *Second Meeting of the Society of Magnetic Resonance*, volume 2, page 1032, San Francisco, August 1994.

[128] R. Turner, D. Le Bihan, J. Maier, et al. Echo-planar imaging of intravoxel incoherent motions. *Radiology*, 177:407, 1990.

[129] M. Tyszka, R. C. Hawkes, and L. D. Hall. New method for moving reference frame generation under steady-state free precession. *J. Magn. Reson.*, 92:183–188, 1991.

[130] M. Tyszka, R. C. Hawkes, and L. D. Hall. Three-dimensional magnetic resonance imaging of very slow coherent motion in complex flow systems. *Flow Meas. Instrum.*, 2:4, 1991.

[131] M. Tyszka, R. C. Hawkes, and L. D. Hall. Moving-reference-frame imaging under steady-state free precession. *J. Magn. Reson.*, B 101:158–164, 1993.

[132] A. M. Uluğ, P. B. Barker, and P. C. M. van Zijl. Correction of motional artifacts in diffusion-weighted images using a reference phase map. *Magn. Reson. Med.*, 34:476–480, 1995.

[133] P. van Gelderen, M. H. M. de Vleeschouwer, D. DesPres, J. Pekar, and P. C. M. van Zijl. Water diffusion and acute stroke. *Magn. Reson. Med.*, 31(2):154–163, 1994.

[134] X. Wan, D. L. Parker, J. N. Lee, H. R. Buswell, and G. T. Gullberg. Reduction of phase error ghosting artifacts in thin slice fast spin-echo imaging. *Magn. Reson. Med.*, 34(4):632–638, 1995.

[135] S. Warach, D. Chien, W. Li, M. Ronthal, and R. R. Edelman. Fast magnetic resonance diffusion-weighted imaging of acute stroke. *Neurology*, 42:1717–1723, 1992.

[136] S. Warach, J. F. Dashe, and R. R. Edelman. Clinical outcome in ischemic stroke predicted by early diffusion-weighted and perfusion magnetic resonance imaging: a preliminary analysis. *J. Cereb. Blood Flow Metab.*, 1995. In Press.

[137] S. Warach, J. Gaa, B. Siewert, P. Wielopolski, and R. R. Edelman. Acute human stroke studied by whole brain echo planar diffusion-weighted magnetic resonance imaging. *Annals of Neurology*, 37(2):231–242, 1995.

[138] S. Webb, editor. *The Physics of Medical Imaging.* IOP Publishing Inc., Philadelphia, PA, 1992. ISBN 085274-349-1.

[139] V. J. Wedeen, R. M. Weisskoff, and B. P. Poncelet. MRI signal void due to in-plane motion is all-or-none. *Magn. Reson. Med.*, 32:116–120, 1994.

[140] R. M. Weisskoff, D. Chesler, J. L. Boxerman, and Bruce Rosen. Pitfalls in MR measurement of tissue blood flow with intravascular tracers: Which mean transit time. *Magn. Reson. Med.*, 29(4):553–559, 1993.

[141] R. M. Weisskoff and M. S. Cohen. Nonaxial whole-body instant imaging. *Magn. Reson. Med.*, 29(6):796–803, 1993.

[142] R. M. Weisskoff, C. S. Zuo, J. L. Boxerman, and B. R. Rosen. Microscopic susceptibility variation and transverse relaxation: Theory and experiment. *Magn. Reson. Med.*, 31(6):601–610, 1994.

[143] D. S. Williams, D. J. Grandis, W. Zhang, and A. P. Koretsky. Magnetic resonance imaging of perfusion in the isolated rat heart using spin inversion of arterial water. *Magn. Reson. Med.*, 30(3):361–365, 1993.

[144] E. C. Wong and P. A. Bandettini. A deterministic method for computer modelling of diffusion effects in MRI with application to BOLD contrast imaging. In *Proc. SMRM 12th Annual Meeting*, volume 1, page 10, New York, August 1993.

[145] E. C. Wong, R. W. Cox, and A. W. Song. Optimized isotropic diffusion weighting. *Magn. Reson. Med.*, 34:139–143, 1995.

[146] Ed X. Wu and R. B. Buxton. Effect of diffusion on the steady-state magnetization with pulsed field gradients. *J. Magn. Reson.*, 90:243–253, 1990.

[147] Y. Yang, S. Xu, and M. J. Dawson. Measurement of water diffusion in hormone-treated rat uteri by diffusion-weighted magnetic resonance imaging. *Magn. Reson. Med.*, 33(5):732–735, 1995.

[148] W. Zhang, D. S. Williams, and A. P. Koretsky. Measurement of rat brain perfusion by NMR using spin labeling of arterial water: *In Vivo* determination of the degree of spin labeling. *Magn. Reson. Med.*, 29(3):416–421, 1993.

[149] G. Z. Zientara and J. H. Freed. Spin-echoes for diffusion in bounded, heterogeneous media: Numerical study. *J. Chem. Phys.*, 72:1285–1292, 1980.

[150] Y. Zur, E. Bosak, and N. Kaplan. A new diffusion ssfp imaging technique. In *Third Meeting of the Society of Magnetic Resonance*, volume 2, page ?, Nice, August 1995.

[151] Y. Zur, S. Stokar, and P. Bendel. An analysis of fast imaging sequences with steady-state transverse magnetization refocusing. *Magn. Reson. Med.*, 6:175–193, 1988.

[152] Y. Zur, M. L. Wood, and L. J. Neuringer. Motion-insensitive, steady-state free precession imaging. *Magn. Reson. Med.*, 16:444–459, 1990.

[153] Y. Zur, M. L. Wood, and L. J. Neuringer. Spoiling of transverse magnetization in steady-state sequences. *Magn. Reson. Med.*, 21:251–263, 1991.

THESIS PROCESSING SLIP

FIXED FIELD: ill. _____ name _____

index _____ biblio _____

▶ COPIES: (Archives) Aero Dewey (Eng) Hum

Lindgren Music Rotch Science

TITLE VARIES. ▶☐ _____

NAME VARIES: ▶☐ _____

IMPRINT: (COPYRIGHT) _____

▶COLLATION: 180p

▶ADD. DEGREE: _____ ▶DEPT.: _____

SUPERVISORS: _____

NOTES:

cat'r: date:

page: F52

▶DEPT: E.E.

▶YEAR: 1996 ▶DEGREE: Ph.D.

▶NAME: GUDBJARTSSON, Hakon